Université de Liège

Aerospace and Mechanical Engineering Department
Computational & Multiscale Mechanics of Materials

Stochastic multi-scale modelling of MEMS

Thesis submitted in fulfilment of the requirements for the degree of
Doctor in Engineering Sciences

by

Vincent Lucas, Ir.

July 2016

Members of the Examination Committee

Prof. Jean-Claude GOLINVAL (President of the Committee)
University of Liège (Liège, Belgium)
Email: jc.golinval@ulg.ac.be

Prof. Ludovic NOELS (Advisor)
University of Liège (Liège, Belgium)
Email: l.noels@ulg.ac.be

Prof. Julien YVONNET
Université Paris-Est Marne-La-Valle (Paris, France)

Prof. Dirk VANDEPITTE
Katholieke Universiteit Leuven (Leuven, Belgium)

Prof. Maarten ARNST
University of Liège (Liège, Belgium)

Dr. Ling WU (guest Professor at Vrije Universiteit Brussel (VUB), Brussels, Belgium)
University of Liège (Liège, Belgium)

Abstract

When studying Micro-Electro-Mechanical Systems (or MEMS) made of polycrystalline materials, as the size of the device is only one or two orders of magnitude higher than the size of the grains, the structural properties exhibit a scatter at the macro-scale due to the existing randomness in the grain size, grain orientation, surface roughness... In order to predict the probabilistic behaviour at the structural scale, we investigated the recourse to a stochastic 3-scale approach in this thesis dissertation.

Estimating the scatter in the response of the structure is studied at macro-scale based on stochastic finite elements along with Monte-Carlo simulations. To produce accurate results, the mesh size of the finite element approach should be small enough so that the heterogeneities can be captured. This can lead to overwhelming computation if the microstructure is directly considered, thus justifying the recourse to stochastic homogenisation to define a meso-scale random field. Based on a stochastic model of this random field, the variability of the response of the structure can be computed.

In this work, the micro-scale uncertainties are modelled based on measurements provided by the IMT-Bucharest institute. These uncertainties are then propagated towards the macro-scale for 3 different problems. The first one serves the purpose of verification. The variability of the resonance frequency of a micro-beam is computed and compared to a reference numerical solution. The second problem extends the 3-scale approach to the thermo-elastic case. Thus the uncertainties of the quality factor of 3D beams are studied with a modelling of the anchor. Finally, the third problem aims at propagating surface roughness uncertainties on the resonance frequency of thin plates.

Acknowledgements

First, I want to thank Professors Jean-Claude Golinval, Dirk Vandepitte, Julien Yvonnet, Maarten Arnst, Ling Wu and Ludovic Noels who accepted to participate in the examination committee of this doctoral thesis.

The research has been funded by the Walloon Region under the agreement no 1117477 (CT-INT 2011-11-14) in the context of the ERA-NET MNT framework. Computational resources have been provided by the supercomputing facilities of the Consortium des Équipements de Calcul Intensif en Fédération Wallonie Bruxelles (CÉCI) funded by the Fond de la Recherche Scientifique de Belgique (FRS-FNRS).

I wish to thank all the members of the 3SMVIB project. I am truly grateful to Zygmunt for the warm welcome he granted us in Poland. I would like to thank Open-Engineering for welcoming me in their office, and more particularly, Stéphane, for his patience while I was loading. I am sure he will understand.

I also want to acknowledge Vinh for all the bedroom sharing, Van Dung for being so helpful, and Ling for surviving in the mess I had established in our office and of course for her everlasting invaluable help. I also want to acknowledge the help of Prof. Maarten Arnst and Prof. Jean-Claude Golinval for their good advice. Many thanks must go to my advisor, Prof. Ludovic Noels. This thesis would never have seen the light of day without him. Ludovic grants his students a considerable amount of time, which is, I believe, the most precious resource of all.

I wish to thank my friends for their never-ending support. Archimede needed a lever, I needed their smiles. Finally, my thoughts go to my family who coped with me all these years. And I won't forget Delphine who supported me against all tides.

Contents

Chapter 1

Introduction

1.1 Background and motivation

Nowadays, MEMS, or microelectromechanical systems, are well-established devices which involve low fabrication costs, large volume production, light and small products with a reasonable energy consumption. They can thus be found in many different applications, ranging from vehicles to medicine technology. Producing reliable MEMS can however be a challenging task when, for example, a high quality factor[1] (and thus a higher accuracy) is sought. This is the case for RF-MEMS filters or resonant sensors. To produce such MEMS with a high quality factor, the different mechanisms which involve energy dissipation need to be properly identified. While some dissipation mechanisms can be reduced through proper operating conditions, such as air damping, other mechanisms rely solely on the design, such as thermoelastic damping. A proper modelling of such intrinsic loss mechanisms would allow to define an efficient MEMS design process.

An efficient deterministic design however can be hazardous. From the desired design to produced MEMS, a non-negligible scatter in the device properties can be seen which can result in unusable MEMS. Such uncertainties, through the quality factor of micro-beams, are inevitable in MEMS design. Indeed, as MEMS involve small dimensions as well as complex systems, geometric uncertainties are unavoidable. The roughness of the different surfaces of the MEMS imply uncertainty. The material itself can also be subjected to uncertainties. For example it can be expressed through grain orientation of poly-crystalline materials with anisotropic crystals or through amorphous phase distribution when the crystallinity is not perfect. Fig. 1.1 illustrates such micro-beams, produced at the IMT institute in Bucharest.

With the help of uncertainty quantification (UQ) in MEMS design, parameters whose uncertainty should be controlled rigorously can be identified. Consid-

---

[1] A dimensionless parameter which characterises the bandwidth of a resonator as well as its energy loss

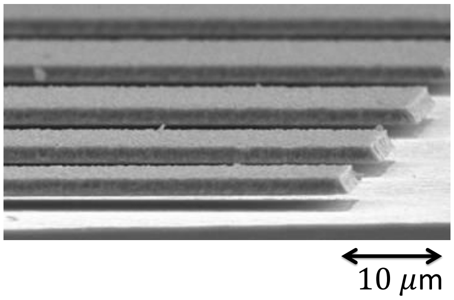

Figure 1.1: Samples of micro-beams, courtesy of IMT institute in Bucharest

ering UQ in the pre-design phase can lead to an efficient design whose success rate is satisfactory. However, the straightforward UQ method that could be applied, the Monte-Carlo procedure on the beam where each heterogeneities is modelled and meshed, is overwhelming in terms of computational resources. Therefore there are increasing interests into solving this problem in a more efficient way with a multi-scale method propagating the uncertainty. Investigating such an approach in the frame of MEMS design is the objective of this work.

1.2 Overview of the dissertation

In the micro-electromechanical systems (MEMS) community, there are increasing demands in developing reliable micro-structures with very high quality factors (Q). These micro-structures constitute the essential active part of applications such as resonant sensors and RF-MEMS filters, for which increasing the sensitivity and resolution (a higher quality factor implies a lower bandwidth at resonant peaks) of the devices is a critical issue. In order to obtain high-Q micro-resonators, all dissipation mechanisms that contribute to decreasing the quality factor have to be identified and well considered at the design stage. The energy dissipation mechanisms of micro-resonators can be classified into two categories [100]. On the one hand, the majority of dissipation mechanisms are extrinsic, which means that they can be minimised by a proper design and operating conditions, such as by minimising the air damping effect. Intrinsic losses, on the other hand, cannot be controlled as easily as extrinsic ones. Thermo-elastic damping has been identified as one kind of important intrinsic loss in high-Q micro-resonators [16, 34].

Thermo-elastic damping is an intrinsic energy dissipation mechanism which occurs due to heat conduction. In a thermo-elastic solid, the thermal and mechanical fields are strongly coupled through the thermal expansion effect. MEMS resonators generally contain elements which vibrate in flexural modes and can be approximated by beams. In a vibrating beam in its first flexural mode, the two opposite sides undergo opposite deformations. When one side is compressed and its temperature increases consequently, the other side is stretched with a decrease in the temperature. Thus temperature gradients are generated and an energy dissipation occurs. However, this dissipation has a measurable influence only when the vibration frequency is of the order of the thermal relaxation rate. On the one hand, when the vibration frequency is much lower than the thermal relaxation rate, the vibrations are isothermal since the solid is always in thermal equilibrium. On the other hand, when the vibration frequency is much higher than the thermal relaxation rate, the vibrations are adiabatic since the system has no time for thermal relaxation. In MEMS, due to the small dimensions involved, the relaxation times of both the mechanical and thermal fields have a similar order of magnitude and hence, thermo-elastic damping becomes important. Therefore, accurate modelling and prediction of energy loss due to the thermo-elastic effects becomes a key requirement in order to improve the performance of high-Q resonators.

The early studies of thermo-elastic damping were mainly based on analytical models, which were derived for very simple structures and are subject to very restrictive assumptions. Zener [104] has developed the so-called Zener's standard model to approximate thermo-elastic damping for flexural vibrations of thin rectangular beams. Based on an extension of Hooke's law to the "Standard Anelastic Solid", which involves the stress σ, strain ε as well as their first time derivatives $\dot{\sigma}$, $\dot{\varepsilon}$, the vibration characteristics of the solid are analysed with the harmonic stress and strain. However Zener's theory [104] does not provide the estimation of the frequency shift induced by thermo-elastic effects. For this purpose, Lifshitz and Roukes have developed in [50] the thermo-elastic equations of a vibrating beam based on the same fundamental physics than Zener, which model more accurately the transverse temperature profile. The analytical models can be used to obtain the complex thermo-elastic resonant pulsation ϖ_n and its corresponding quality factor Q for simplified cases only. The limitation of analytical models and the complexity of the real micro-structures (i.e. non rectangular geometry, complex 3-D structures, anisotropic material,...) have motivated the development of numerical models [48],[81], and the application of the finite element method to study the thermo-elastic damping has been validated by the comparisons of numerical results with analytical results.

However, deterministic finite element models are not accurate enough to obtain a reliable analysis of the performance of micro-resonators [48]. Indeed, MEMS are subject to inevitable and inherent uncertainties in their dimensional parameters and material properties which lead to variability in their performance and reliability. Due to the small dimensions of MEMS, manufacturing processes leave substantial variability in the shape and geometry of the device, while the material properties of a component are inherently subject to a scatter. The effects of these variations have to be considered and a stochastic modelling methodology is needed in order to ensure the required MEMS performance under uncertainties.

Sources of uncertainties are most of the time neglected in numerical models. However they can affect the structural behaviour, in which case it is important to consider them. This is why nowadays a lot of efforts are spent on improving uncertainty quantification procedures. Dealing with uncertainties can be done in different ways, but this work focuses on the propagation of micro-scale material and geometrical uncertainties up to the structural response. Micro-scale material uncertainties result from spatially varying material properties. The structural behaviour is thus non-deterministic as the material properties are not homogeneous over the structure. This structure can be modelled using the finite element method, in which case a full description of the material heterogeneities and of their variations is required. Using Monte-Carlo simulations on such a fine discretization to estimate the uncertainties in the structural behaviour, *i.e.* performing direct Monte Carlo simulations, can however involve overwhelming computation cost as the finite element mesh should capture the micro-scale uncertainties. The purpose of this work is to investigate the recourse to stochastic methods to study the probabilistic behaviour of MEMS.

Stochastic Finite Elements methods, referred to as SFEM and described in [24, 47, 88], as a non exhaustive list, are relevant tools to study uncertainty quantification at a reasonable cost. In the case of MEMS, this was illustrated by considering thermoelastic stochastic finite elements in [48]. SFEM to study the stochastic behaviour of shells whose thickness and material properties are random was also used in [89]. However, with those approaches, the random field used to describe the spatially varying material properties and thickness was not obtained directly from micro-structure resolutions. Thus the recourse of SFEM approaches alone does not overcome the problem of modelling the material heterogeneities. Indeed, to be able to propagate the uncertainties from the micro-structure itself using SFEM, as the involved uncertainties are characterised by a small correlation length, the finite element size should be drastically reduced [84]. According to [28], accurate results are obtained when the finite element size is smaller than at least one half of the correlation length, which would lead to unreachable computational resources to capture the micro-scale heterogeneities uncertainties. However, this limitation can be overcome thanks to multi-scale approaches as the introduction of an intermediate scale implies a larger correlation length, and thus reduces the computation cost of the SFEM procedure [52].

Multi-scale approaches are an efficient, convenient and elegant way to deal with complex heterogeneous materials. The rise of composites, among other progresses in material science, led to an the extensive use of complex materials. The micro-structure of such materials can involve a mixture of different materials arranged according to a complex geometry. The numerical simulation of structures made of such materials requires insights of the behaviour of the micro-structure to produce accurate results. Including the modelling of the micro-structure in the frame of a direct simulation has a cost which can lead to an unaffordable computational burden. This is the starting point of multi-scale approaches where the macro scale simulation does not model the micro-structure directly but is informed of analyses performed at the micro-scale.

In such an analysis, three scales are defined, see Fig. 1.2. The micro-scale is the characteristic size of the micro-structure. A volume element made of the material of interest defines an intermediate scale: the meso-scale. The macro-

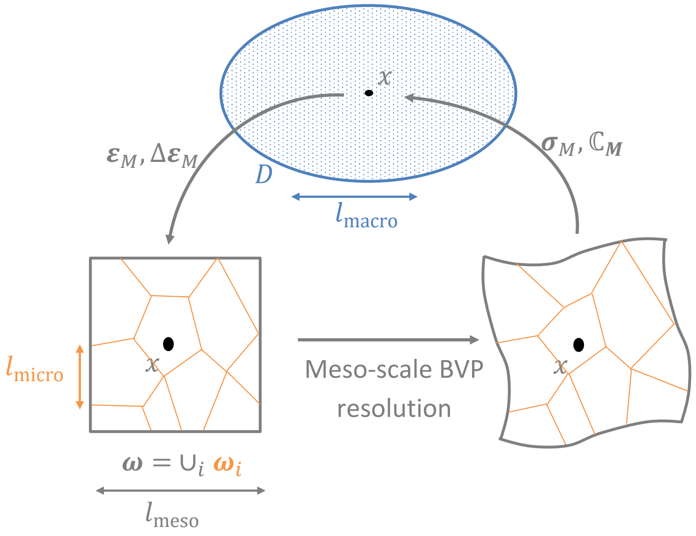

Figure 1.2: Homogenisation-based multi-scale method with 1^{st}-order homogenisation for classical macro-scale continuum.

scale is the characteristic size of the whole structure, based on the gradient of the structural loading. A macro-scale problem is defined and solved numerically with usual methods such as an FE analysis. The resolution of this problem requires micro-scale information through homogenised properties at the meso-scale. Therefore the homogenisation itself is the cornerstone of several multi-scale approaches. On the one hand, when the homogenisation is done *a priori*, one refers to a sequential approach. On the other hand, when an homogenisation procedure is called at various steps of the macro-scale solver, thus involving a coupling between the two problems, one refers to a concurrent approach. In a concurrent approach, the strain information at any point of the macro-scale model can be down-scaled, analysed at the micro-scale to estimate a homogenised stress counterpart, which is then up-scaled to the macro-scale problem.

The multi-scale approach produces relevant results when some hypotheses are fulfilled. First, the method needs to be consistent: the deformation energy should be the same at both the micro and macro-scales. This condition is referred to as the Hill-Mandel condition. Second, the length scale separation which can be expressed as

$$l_{\text{meso}} << l_{\text{macro}}, \text{ and} \tag{1.1}$$

$$l_{\text{micro}} << l_{\text{meso}} \;, \tag{1.2}$$

should be satisfied.

The first equation (1.1) guarantees the accuracy of the procedure: accurate results are obtained when the homogenisation is applied on meso-scale volume elements whose size is much smaller than the characteristic length on which the macro-scale loading varies in space [21]. The second one, Eq. (1.2), ensures the RVE existence. RVE stands for representative volume element. A volume element is said to be representative when it is large enough to statistically represent the material of interest. In other words, the homogenised properties do not depend on the choice of volume element as well as they do not depend on the type of energetically consistent boundary conditions.

Following an energetically consistent approach and owing to both scale-separations, relevant results can be obtained with multi-scale methods. However, the homogenisation procedure still needs to be defined. The homogenisation step can be done in many different ways. For example, semi-analytical methods exist, such as the mean-field homogenisation (MFH), whose starting point is Eshelby's eigenstrains [18]. When the micro-structure is made of repetitive unit cells, asymptotic homogenisation can be used to state the equations at different orders corresponding to the ratio between scales, and the resolution of the corresponding lower scale equations usually follows a unit cell resolution. The FE^2 and FFT methods are numerical approaches which can compute homogenised properties in a wide range of applications. A more detailled review of the state of the art is given in Section 3.1. Moreover, reviews of the different multi-scale approaches can be found in [40] for a general overview, in [22] for an emphasis on numerical approaches and in [51] for multi-scale approaches in the frame of damage.

When dealing with reduced size structures, the characteristic size of the micro-scale heterogeneities can be too close to the macro-scale to respect both scale separations (1.1) and (1.2). The first one, Eq. (1.1), guarantees the accuracy of the procedure. Therefore, it should be satisfied. The second scale separation, Eq. (1.2), will thus not be respected. This implies that volume elements are not representative and they are referred to as Statistical Volume Elements (SVEs) [70]. Indeed, on the one hand, the meso-scale boundary value problem over an SVE is boundary condition dependent, and on the other hand, different homogenised properties are obtained for different realisations of the SVEs, even under a unique case of BCs. Although it is possible to address the lack of representativity by statistical considerations of the homogenised properties for different SVE sizes/realisations [39, 32] in order to extract mean homogenised properties or to define minimum RVE size, such a method does not allow to up-scale the uncertainties. This has motivated the development of stochastic multi-scale methods.

Stochastic multi-scale analyses have been developed based on order reduction of asymptotic homogenisation [20] to account for micro-scale material uncertainties in the form of random variables –and random fields in particular cases. However, accounting for general fine-scale random fields would require the nested solution of micro-scale problems during the structural-scale analysis, leading to a prohibitive cost. Local effects can be treated using Monte-Carlo simulations: the brittle failure of MEMS made of a poly-silicon material was studied by considering several realisations of a critical zone [55] on which the relevant loading was applied. An alternative to these approaches is to introduce in the stochastic multi-scale method a meso-scale random field, obtained from a multi-scale analysis, in order to conduct the stochastic finite element method at the structural scale in an uncoupled way.

For this purpose, statistics and homogenisation were coupled to investigated the probability convergence criterion of RVE for masonry [27], to obtain the property variations due to the grain structure of poly-silicon film [54], to extract the stochastic properties of the parameters of a meso-scale porous steel alloy material model [101], to evaluate open foams meso-scale properties [49], to extract probabilistic meso-scale cohesive laws for poly-silicon [65], to extract effective properties of random two-phase composites [90], to study the scale-dependency of homogenisation for matrix-inclusion composites [92, 93], or again to consider the problem of composite materials under finite strains [53]. In this last reference, a particular attention was drawn on the correlation between the different sources of uncertainty. In most of the previously cited works, the stochastic homogenisation on SVEs was mainly achieved by a combination of computational homogenisation with Monte Carlo simulation. In the recent works of [73], the stochastic homogenisation was achieved by using a modified version of the SFEM (here applied on the meso-scale boundary value problem), leading to a more efficient resolution. The problem of high-dimensionality was investigated in [9], in which the resolution of composite material elementary cells was used to explicitly define a meso-scale potential with the aim of studying the uncertainties in the fibers geometry/distribution in the case of finite elasticity.

The meso-scale uncertainties can then be up-scaled to study the probabilistic macro-scale behaviour. Based on their stochastic properties identification of the meso-scale porous steel alloy material model [101], Yin *et al.* [102] have generated a random field based on Karhunen-Loève expansion to study the macro-scale behaviour. A similar approach was applied to study the dynamic behaviour of open-foamed structures [49].

The purpose of this thesis dissertation is to develop a stochastic 3-scale method applied on MEMS vibrating beams. The main steps of this approach can be summarised as (i) the definition of micro-scale SVEs with a random structure; (ii) at the meso-scale, finite-element simulations on different SVEs, defined from a larger material sample by using the moving window technique, lead to the distribution of the homogenised poly-crystalline material properties and their spatial correlation; (iii) a random field of the meso-scale homogenised properties is generated based on the information obtained from the SVE simulations; and (iv) the generated meso-scale random fields are used in the frame of a stochastic finite element method to predict the statistical distribution of MEMS macro scale properties of interest such as their resonant frequencies or their thermoelastic damping. In particular, by comparison with direct Monte-Carlo simulations, it will be shown that the generation of a spatially correlated random field allows predicting macro-scale statistical distributions which do not depend on the SVE size and macro-scale mesh sizes, as long as the distance between macro-scale integration points remains lower than the correlation length of the meso-scale random field.

In the first step, (i), actual measurements are considered on poly-silicon samples to define the uncertainties of the micro-structure. These measurements were provided by the IMT institute in Bucharest in the frame of an MNT ERA-NET project. The micro-structure being made of an anisotropic poly-crystalline material, *i.e.* poly-silicon, the randomness in the grain size distribution and in their orientation –with or without preferred orientations– induce uncertainties. The grain size distribution is studied for different manufacturing temperatures by Low Pressure Vapour Chemical Deposition (LPCVD) based on Scanning Electron Microscope (SEM) images while the distribution of orientations, when considered, is obtained using X-Ray Diffraction (XRD) measurements. Another source of scatter is the surface profile of the MEMS structure as its roughness is of comparable size to the structure thickness in case of a thin device. The surface topology, when considered, is obtained thanks to Atomic Force Microscopy (AFM) measurements. Both the roughness and the grain structure are correlated as it is noted in [105].

To achieve the second step of the method, *i.e* the homogenisation of the micro-structure over a volume element, the choice of the method depends on the macro-scale problem of interest. In this work, three cases will be considered. First order computational homogenisation, as described in [43], is used to study the mechanical material behaviour of the volume element. As we are interested in poly-silicon structures, the anisotropy of the grain crystal induces material uncertainties through the randomness of their orientation. These meso-scale uncertainties can be captured with first-order computational homogenisation. If the thermo-elastic damping is of interest at the macro-scale, the homogenisation procedure will consider the thermo-mechanical coupling as described in [48]. If uncertainties of the geometry, such as roughness, are to be taken into account, second-order gradient-enhanced homogenisation procedures are carried out on Rough Statistical Volume Elements (RSVEs) which would consider the material profile uncertainties. With a view toward macro-scale plate simulations, second-order homogenisation allows capturing the roughness effect on the bending behaviour of the meso-scale volume element as it provides a bridge not only between the in-plane stress and the in-plane strain, but also between the higher-order stress –*i.e.* bending moment– and the higher-order strain –*i.e.* curvature– as illustrated in Fig. 1.3. Second-order homogenisation was described for small strains in [37], and for finite strains in [45]. The method was adapted for shells in [10] or again in [11], where the method was applied to study the buckling of heterogeneous shells. Owing to the computational homogenisation process, the stochastic meso-scale information, *i.e.* the elasticity tensor or the shell-like resultant membrane, bending, and coupled material tensors, see Fig. 1.3, are then gathered following a simple Monte-Carlo scheme applied on (R)SVEs realisations.

Although by performing homogenisation on several (R)SVE realisations the marginal distribution of the different homogenised properties can be obtained, in order to propagate the uncertainties to the macro-scale, the spatial correlation has also to be evaluated. To obtain the spatial correlation between neighbouring (R)SVEs, a moving-window technique [5] is used on a sufficiently large material sample, thus estimating a discrete correlation function of the (R)SVEs proper-

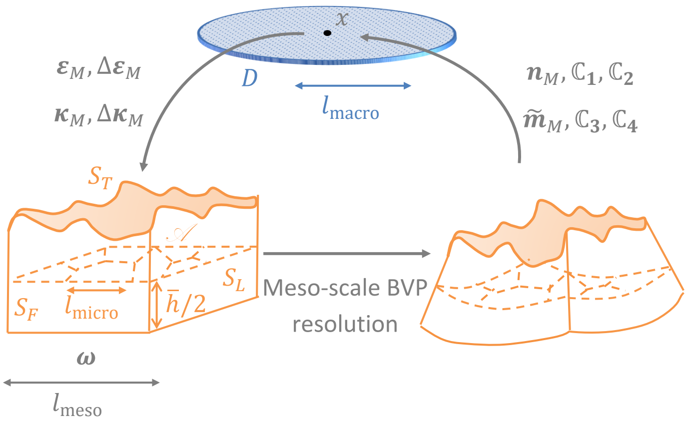

Figure 1.3: Homogenisation-based multi-scale method with 2^{nd}-order homogenisation for macro-scale Kirchhoff-Love plates.

ties. The cross-correlation between the different meso-scale properties is also computed. Indeed, as stated in [89], the influence of the cross-correlation between the Young's modulus and the Poisson ratio on the response variability is negligible in case of a static problem but this assumption is not valid when a dynamic problem is involved.

Once the stochastic behaviour of the meso-scale (R)SVEs is evaluated using a sufficient number of realisations, a random field can be defined, which is the third step of the method. The two main approaches usually considered to build a random field are the Karhunen-Loève expansion, which was used in the recent work [8] for example, and the spectral representation method which was developed in [83, 85]. The latter procedure allows computing the discrete spectral density from the discrete correlation function evaluated by the stochastic homogenisation by recourse to Fast Fourier Transforms and is therefore chosen in this work. The spectral representation generates Gaussian fields, but non-Gaussian fields can be retrieved through an appropriate mapping technique [74, 98, 13]. As the non-linear mapping from Gaussian to non-Gaussian changes the spectral density, an iterative procedure is required to obtained both the desired spectral density and non-Gaussian probability distribution. Moreover, in order to ensure the existence of the expectation of the norm of the inverse of the material tensors, a lower bound is introduced during the generation process [12].

With the possibility of generating random fields, the fourth step can be performed *i.e.* the uncertainties at the meso-scale are then propagated up to the macro-scale. On the one hand, a unique stochastic approach will be used at the macro-scale: the Monte-Carlo procedure. On the other hand, different macro-scale analyses will be performed so that different problems can be studied.

The first problem studied is the uncertainty propagation of the elasticity tensor in linear elasticity towards the scatter in a MEMS resonator resonance frequency, the quantity of interest in this case. For the sake of simplicity, beam elements are considered at the macro-scale. This problem is used to verify the 3-scale procedure as a reference solution can be estimated. The reference solution is obtained using full direct numerical simulations, *i.e.* for which the grains are meshed, in linear elasticity combined to a Monte-Carlo method, which allows the probability density function to be computed. This methodology is computationally expensive due to the number of degrees of freedom required to study one sample. Nevertheless, it is a convenient approach to show that the stochastic multi-scale approach yields the same marginal distribution of the quantity of interest as the direct approach. The advantage of the multi-scale strategy is the use of coarser finite elements at the structural-scale which reduces the computational costs. In the context of the 3-scale method, different SVE sizes and different structural-scale finite element meshes are successively considered to demonstrate that by accounting for the spatial correlation of the meso-scale homogenised properties, correct predictions are obtained if the distance between integration points of the finite-element mesh remains smaller than the mesoscopic correlation length.

The second studied problem consists in estimating the uncertainties of the quality factor, the quantity of interest in this case, of a micro-beam modelled with 3D finite elements. Modelling both the resonator and its clamp will be performed. The thermo-elastic quality factor for micro-resonators can be extracted by recourse to multi-physics finite elements which considers the influence of the homogenised elasticity tensors, conductivity tensors and thermal expansion tensors.

Finally, the last problem focuses on the influence of the roughness on the resonance frequency, the quantity of interest in this case, of thins plates. To propagate roughness uncertainties, a more general macro-scale approach than the use of beam elements is considered. To take into account most of the available information at the meso-scale, such as the resultant bending material tensor (obtained thanks to the second-order homogenisation procedure), Kirchhoff-Love plate elements are considered. In particular, the plate elements are formulated using a displacement-only discretization by recourse to a Discontinuous Galerkin method [95, 68].

For each problem, the variability of the macro-scale quantity of interest can be captured using a Monte-Carlo (MC) procedure. However, compared to the direct MC simulations, the recourse to the meso-scale random field obtained from the stochastic homogenisation allows the use of coarser macro-scale finite elements, reducing the total computational cost. The MC approach is an accurate, straightforward, non-intrusive tool to study complicated systems even if it involves a high random dimensionality. It is commonly used in many applications, such as in engineering or finance. The recourse to MC is here acceptable provided that it is coupled with the 3-scale approach.

To summarise, volume elements representing the uncertainty of the microstructure are generated based on experimental measurements. An homogenisation procedure allows computing the stochastic behaviour of the meso-scale

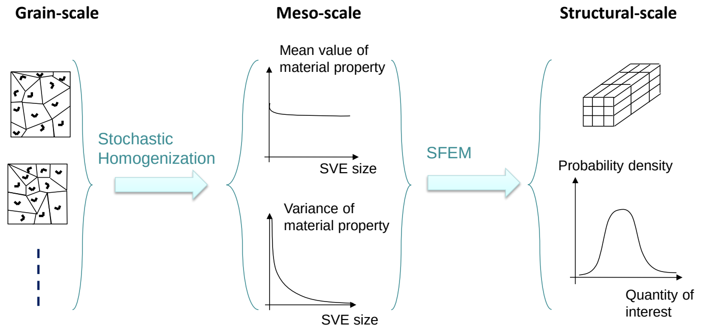

Figure 1.4: The 3-scale procedure

properties. The resulting random field description of the meso-scale material properties can be used with stochastic finite element methods to predict the probabilistic behaviour at the structural-scale. With this multi-scale method the meso-scale random field is smooth and has a correlation length larger than when considering explicitly the grain discretization. Hence coarser meshes can be used in the framework of the stochastic finite-element methods, eventually reducing the computational cost. The procedure is illustrated in Fig. 1.4. This process will be applied in linear elasticity for 1D free-clamped beams, for thermo-elastic 3D beams, and for rough thin plates.

1.3 Contributions

Both multi-scale methods and uncertainty quantification procedures are well established in the scientific community nowadays. In this thesis dissertation, we investigate the integration of uncertainties in the frame of multi-scale analyses to propagate uncertainties from the microstructure up to the quantity of interest at the scale of the structure. In particular, we develop an original stochastic 3-scale methodology which is verified by direct MC simulations. This stochastic 3-scale approach has been developed in the context of (i) linear elasticity, (ii) linear thermo-elasticity, (iii) second-order homogenisation combined to Kirchhoff-Love plate formulation. Also the uncertainties of the microstructure are defined based on experimental measurements on poly-silicon films performed by IMT-Bucharest.

We published the following papers:

- Vincent Lucas, Ling Wu, Maarten Arnst, Jean-Claude Golinval, Stéphane Paquay, Van Dung Nguyen, and Ludovic Noels. *Prediction of macroscopic mechanical properties of a polycrystalline microbeam subjected to material uncertainties.* In Proceedings of the 9th International Conference on Structural Dynamics, EURODYN 2014, pages 2691-2698, 2014.

- Vincent Lucas, J-C Golinval, Stéphane Paquay, V-D Nguyen, Ludovic Noels, and Ling Wu. *A stochastic computational multiscale approach; application to MEMS resonators.* Computer Methods in Applied Mechanics and Engineering, 294:141-167, 2015.

- Ling Wu, Vincent Lucas, Van-Dung Nguyen, Jean-Claude Golinval, Stéphane Paquay, and Ludovic Noels. *A stochastic multi-scale approache for the modeling of thermo-elastic damping in micro-resonators.* Computer Methods in Applied Mechanics and Engineering, under revision.

- Vincent Lucas, Jean-Claude Golinval, Rodica Voicu, M. Danila, Raluca Müller, M. Danila, Adrian Dinescu, Ludovic Noels, and Ling Wu. *Propagation of material and surface profile uncertainties on MEMS microresonators using a stochastic second-order computational multi-scale 3 approach.* International Journal for Numerical Methods in Engineering, Submitted.

1.4 Outline

This work is divided into the following chapters:

- Chapter 2, **SFEM in the frame of macro-scale simulations**, focuses on the use of stochastic finite elements methods to solve problems at the structural scale. First, uncertainty quantification procedures are introduced. Afterwards, the SFEM approach is described and applied on 3 problems: the first one deals with beam finite elements, the second one extends the problem to 3D thermo-elastic cases, and the last one tackles the problem of thin plates.

- Chapter 3, **Meso-scale material characterisation by computational homogenisation**, describes the homogenisation procedure considered to capture the micro-scale uncertainties at the meso-scale. At first, a review of homogenisation procedure is done. Afterwards, the computational homogenisation considered in this work is described for the 3 distinct problems (first order homogenisation in linear elasticity, extension to the thermo-elastic case, and second-order homogenisation in linear elasticity).

- Chapter 4, **Stochastic model of the meso-scale properties**, focuses on the meso-scale random fields. First, random fields notions are introduced. Afterwards, the case of positive-definite matrix is investigated. Finally, the spectral representation method is considered. It is used to generate random fields based on the results computed in Chapter 3. The generated samples are the input of the SFEM approach in Chapter 2. The implementation of the random field generation and its extension to the non-Gaussian case are described.

- Chapter 5, **Application to MEMS**, deals with the application of the procedure on MEMS micro-beams. First, modelling the micro-structure based on measurements is considered. Afterwards, the meso-scale homogenised properties are extracted using the methods described in Chapter 3. Finally, the random fields are generated using the process described in Chapter 4 and used as input for the SFEM described in Chapter 2 to study the variability of the response of structures. This 3-scale procedure is applied for 3 cases. The first one, based on beam finite elements, is used to verify the procedure. A direct monte-carlo approach is considered to estimate the reference solution. The second problem considers the uncertainties in the thermo-elastic damping of MEMS micro-beam. Finally, the third problem focuses on rough thin plates and their variability in terms of resonance frequency.

- Chapter 6, **Conclusions and perspectives**, conclude the dissertation and present the perspectives.

Chapter 2

SFEM in the frame of macro-scale simulations

The problem of uncertainty quantification is first investigated in the opening of this chapter. Afterwards, the stochastic finite element approach is introduced in Section 2.2. It is applied for 3 different problems in the last 3 sections of this chapter: beam elements in linear elasticity, the extension to 3D thermo-elastic problems and the case of Kirchhoff-Love plates.

2.1 Uncertainty Quantification

Nowadays, there is no need to defend the use of numerical simulations. At any design phase of a product, the recourse to numerical analyses is a very useful tool for the engineers. Often, numerical simulations allow engineers to avoid costly experiments. Deterministic models are mainly considered in industrial applications. Sometimes, the model is such that uncertainties can be neglected. Sometimes, it is not the case and an uncertainty quantification procedure should be considered. As described in [47], uncertainties can be classified in 3 categories:

- **Model errors:** when performing simulations, a mathematical model is used to represent reality. The assumptions considered to describe a physical phenomenon induce unavoidable uncertainties. For example, the motion of a spacecraft around the earth can be simulated based on a 2-body mathematical model with perturbation forces. This does not exactly represent reality, nevertheless the results are very useful. Modelling errors are thus an unavoidable sources of uncertainties and the error resulting from the assumptions behind the mathematical model should be rigorously assessed.

- **Numerical errors:** when a mathematical model can not be solved analytically, numerical approaches are considered. However, the recourse to numerical approaches inherently implies uncertainties, due to discretization steps, iterative algorithms, finite number representation for a computer, ... When performing numerical analyses, uncertainties are unavoidable and should be lowered at most. However, there is always a trade-off between accuracy and computational efficiency (in terms of memory usage, CPU time, ...).

- **Data errors:** a mathematical model needs parameters and data to represent the physical characteristics of the system of interest. Such parameters, *i.e.* the geometry, material properties or external forces, are sometimes deterministic and sometimes subjected to variability. These variabilities can take many forms. The uncertainty of some parameters can be inherently random. For example, this is the case for environmental effects (wind,...). This is also the case when the manufacturing process of a system involve a scattering based on design tolerance. The variabilities can come from an uncertain knowledge of some parameters, such as uncertain experimental measurements. Finally, the variabilities can also be present during the early design phase of a system: some parameters of the design may not yet be fixed and are subjected to uncertainty. Such uncertainties, unavoidable when present, cannot be reduced but they can be considered and modelled.

The focus of this work concerns this last source of uncertainty. Due to the fabrication process of MEMS and due to the intrinsic uncertainty involved in poly-crystalline anisotropic materials, macro-scale quantities of interest are subjected to scatter. This scatter can be studied at an early-design phase following an appropriate uncertainty modelling strategy. It is assumed that data errors are the most important source of variability and therefore the two other sources of uncertainties are not modelled.

The modelling of uncertainty can be done in many different ways. In the case of interval analysis, only extreme values of uncertain inputs are considered and represented with interval numbers which possess their own algebra. The interval analysis can be used to study uncertain structural systems, *e.g.* [77] or [78].

The fuzzy logic, first introduced by Zadeh [103], can be seen as an extension of the interval analysis where a membership function is considered for each interval. This fuzziness represents how much the uncertain property is in one interval. While in interval analyses the membership with respect to an interval was a Boolean value (either it is in the interval or it is not), it is a real value between 0 and 1 in the fuzzy logic. This logic, often seen in linguistic applications, can be used in engineering numerical analysis. As an example, Fuzzy sets are used in [61] to study a dynamical system subjected to fuzzy uncertainties.

Even though interval analyses or fuzzy logic are possible ways to treat uncertainty, the recourse to the probabilistic formalism is much more common in the literature. While the membership function of a fuzzy set defines how much a variable is in an interval, a probability defines how likely the variable is in an interval. Probabilities can be associated to discrete and continuous quantities. In the continuous case, a probability density function is assigned to the randomness. The domain of definition of the randomness is divided into infinitesimal intervals. The probability density function provides the probability associated to each interval.

The evidence theory, also named Dempster-Shafer theory (DST) can be seen as an extension of the probability theory where the probability is bounded with a belief (lower bound) and a plausibility (upper bound). The evidence theory can be used to study epistemic uncertainty (uncertainty due to a lack of knowledge).

Finally, Bayesian statistics can be used to draw *a priori* estimation enhanced afterwards with new information. Such an approach, based on Bayes theorem which states the conditional probability of an event, can lead to efficient uncertainty analyses when only few samples are available. As no hypotheses are required *a priori*, it is useful in data mining. When the number of samples is high, the results are similar to those obtained with the probabilistic formalism. However, the Bayesian approach is computationally more expensive. Thus it is not a convenient approach when samples can be easily obtained.

The approach mostly encountered in the literature is the probabilistic formalism and it will be used in this work. It is a convenient way to deal with uncertainties and a lot a tools are available in the frame of the probabilistic approach, which is not the case of evidence theory for example. Furthermore, regarding data availability, as we are dealing with numerical observations, we can compute enough samples to obtain convergence.

In the probabilistic approach, one can first define a probability space $(\Omega, \mathcal{T}, P)$ where:

- Ω is the sample space, which contains all possible outcomes of a random physical or virtual experiment;
- $\mathcal{T}$ is the event space, which contains all possible subsets of Ω;
- P is the probability measure, each event possessing a probability which defines its likelihood.

The probability measure P is defined so that the Kolmogorov axioms are satisfied. These 3 axioms are the following. The first axiom states that the probability P is a non-negative real number. The second axiom can be written as: $P(\Omega) = 1$. Thus the probability of the whole sample space is defined. It can be seen as a normalisation condition. The third axiom states that, for any events $\mathcal{B}$ and $\mathcal{C}$, if $\mathcal{B} \cap \mathcal{C} = \emptyset$, then $P(\mathcal{B} \cup \mathcal{C}) = p(\mathcal{B}) + p(\mathcal{C})$.

A random quantity, defined over a continuous space $\mathbb{R}$, can be modelled with a random variable X with a probability density function f_u, referred to as PDF, so that the probability of u being in the interval $[a, b]$ is:

$$P\left(a \leqslant u \leqslant b\right) = \int_a^b f_u\left(u\right) du\,. \tag{2.1}$$

From the Kolmogorov second axiom, the probability density function of u defined over the space Ω satisfies $\int_\Omega f_u\left(u\right) du = 1$.

The cumulative distribution function, or CDF, noted $F_u\left(u\right) \in [0,1]$, is defined as:

$$F_u\left(u\right) = \int_{-\infty}^{u} f_u\left(v\right) dv\,. \tag{2.2}$$

The PDF (or the CDF) contains all the information about an independent random variable. However, it is convenient to define scalar parameters to ease the representation of a random variable. Let us introduce a function g of the random variable u. Therefore the expectation operator $\mathbb{E}$ over $g(u)$ is established following:

$$\mathbb{E}\left[g(u)\right] = \int_{-\infty}^{\infty} g(u) f_u\left(u\right) du\,. \tag{2.3}$$

The mean $\bar{u}$ is obtained for $g\left(u\right) = u$. It is a measure of the central tendency of the random variable. It is also the first moment of u. The moments are obtained by considering $g\left(u\right) = u^n$ where n is the moment's order. Central moments are defined by considering $g\left(u\right) = \left(u - \mathbb{E}\left[u\right]\right)^n$. The first central moment is 0. The second central moments is the variance $\mathbb{V}\left[u\right]$. The standard deviation σ is defined as $\sigma_u = \sqrt{\mathbb{V}\left[u\right]}$. It is a measure of the dispersion of the distribution about the mean value. A convenient way to represent this dispersion is the coefficient of variation, or COV. It is expressed in percent as $\mathrm{COV}\left(u\right) = \frac{\sigma_u}{\bar{u}} \cdot 100$. The skewness, based on the third central moment, is a measure of the asymmetry of the distribution. A distribution with a positive (negative) skewness possesses a longer right (left) tail while most of the density of the distribution is concentrated on its left (right) side. The skewness γ_1 of u is ${\gamma_1}_u = \frac{\mathbb{E}\left[\left(u - \mathbb{E}[u]\right)^3\right]}{\sigma_u^3}$. The fourth central moment is the basis of the kurtosis. The kurtosis is defined as: ${\beta_2}_u = \frac{\mathbb{E}\left[\left(u - \mathbb{E}[u]\right)^4\right]}{\sigma_u^4}$. It is a measure of the "peakedness" of the distribution.

A random variable can follow any distribution function (as long as the latter is normalised). In practice however, it is common to consider parametrised density functions. Classified in different families, these density functions are fully characterised by a finite number of parameters. Among all the parametrised density functions, the most famous one is undoubtedly the Gaussian distribution, also known as normal distribution. The Gaussian distribution relies on 2 parameters, the mean $\bar{u}$ and the standard deviation σ_u, and follows the probability density function (2.4).

$$f_u(u) = \frac{1}{\sigma_u \sqrt{2\pi}} e^{\frac{(u-\bar{u})^2}{2\sigma_u^2}}\,. \tag{2.4}$$

Although most uncertainties that engineers are dealing with are not Gaussian, the Gaussian assumption is still often used. To understand the hegemony of the Gaussian distribution, two concepts must be introduced: the central limit theorem (CLT) and the maximum entropy principle (maxEnt).

In its general form, the central limit theorem states that the sum of a sufficiently high number of terms, each term being independent and identically distributed with a well-defined mean and variance, follow a Gaussian distribution. The extension to non-identically distributed terms can be made under certain conditions. Thus a Gaussian distribution naturally occurs.

The maximum entropy can be briefly described in the following way. Based on Shannon entropy, the entropy of a random variable can be defined based on its probability density function. The higher the entropy, the higher the uncertainty on the random variables. This can be used to estimate a probability distribution with the maximum entropy principle. The latter states that, to avoid introducing bias and unknown information, the PDF to consider is the one maximising entropy as what is not known is uncertain. The PDF will be evaluated using all the information available and only the information available. When the only available information is the mean and the variance (e.g. few experimental samples), the Gaussian distribution is once again obtained. The maximum entropy principle will be described in Section 4.2.1.

Finally, many tools are available to deal with Gaussian distributions. Thus, these facts explain the recurrence of the Gaussian assumption.

As many engineering applications involve non-Gaussian distributions (e.g. Young's modulus, which is by definition a strictly positive value), a mapping from Gaussian samples towards a non-Gaussian set of realisations is commonly used. A set of samples u following a distribution f_u can be mapped to another known distribution f_v according to:

$$v = F_v^{-1}\left(F_u\left(u\right)\right) \,, \tag{2.5}$$

where v are the mapped samples following the distribution f_v.

A system can involve more than one random variable. The joint probability density function is an extension to higher dimensions of the PDFs, the joint probability density function being defined in an analogous way to the uni-variate case. In the context of a multivariate random space, a 1D probability density function for one random variable can still be defined through the marginal distribution (without reference to the value of other variables) or through the conditional distribution (the other variables are considered to be known). In the remaining of this work, marginal probability density functions are considered if not stressed otherwise.

Two random variables u and v are independent if their joint probability respects:

$$P(u \cup v) = P(u)P(v) \,. \tag{2.6}$$

If u and v do not respect Eq. (2.6), u and v are dependent, correlated. If two random variables u and v are correlated (e.g., the age and weight of a human being are correlated), one realisation of u depends on the corresponding realisation of v. The correlation is a measure of such dependency. Even though many ways to measure dependency exist, the most common way to compute the correlation is to study the linear relationship between the two variables (Pearson correlation). From now on, the correlation will refer to the measure of the linear link between the random variables through the covariance. The covariance R is a measure of their cumulative deviation with respect to their means:

$$R_u^v = \mathbb{E}\left[\left(u - \bar{u}\right)\left(v - \bar{v}\right)\right] . \tag{2.7}$$

The correlation is the covariance scaled by the standard deviation of both random variables. Its values can range from $[-1, 1]$. It can be defined as in Eq. (2.8) where $\underline{R}_u^v$ represents the correlation.

$$\underline{R}_u^v = \frac{R_u^v}{\sigma_u \sigma_v} . \tag{2.8}$$

Let us stress the fact that only the linear correlation is estimated in this case. Therefore, while two independent variables show a correlation of 0, two variables with a zero (linear) correlation are not necessarily independent. For example, if u defines uniformly distributed variables in the range $[a, b]$, the linear correlation of v defined as $v = u^2$ is 0. Let us note that, in the case of normal distributions, a zero linear correlation implies independence. One should also keep in mind that correlation does not necessarily imply causation. Relationships can be coincidental or a third factor can be present, and therefore correlated variables should be treated with care. For example the number of firemen requested for fire fighting is correlated with the amount of damage. This does not mean less firemen should be called[1]. Furthermore, since mid 20th century, the CO_2 level in the atmosphere, the usage of computer resources and obesity all increased and are correlated[2]. It does not mean there is a true link between them.

Dependency between variables can happen, dependency between the same variables located at different spatial position exists too. This correlation is referred to as spatial correlation and it is the key ingredient behind a random field. The same can be said with time and a random process.

A random process $a\left(t\right)$ consists of a set of realisations of a at different time t. It can be continuous with respect to t (and thus the set of realisations is infinite) or discrete. A random process is said to be stationary if its stochastic behaviour does not depend on the time t. In other words, the correlation between two variables of the process only depends on their time interval δt and not on the absolute time t. As an example, stock market can be modelled with random processes.

A random field can be seen as an extension of a random process, defined over time, to a randomness defined over any manifold of dimension n. Let us focus on random fields defined over the 3D spatial space. Such a random field, denoted $a\left(\boldsymbol{x}\right)$, consists of a set of realisations of a over a domain of interest $\boldsymbol{D}$

---

[1] `www.stat.ncsu.edu/people/reiland/courses/st350/correl.ppt`

[2] `https://en.wikipedia.org/wiki/Correlation_does_not_imply_causation`

spaced by $\boldsymbol{x}$. The random field can be continuous if the random variables are continuously distributed over the domain or discrete if a finite set of variables are defined over the domain. The spatial domain can be of any dimensions. In simple words, random fields are generally considered to stress the fact that the scatter between nearby values is smaller than the scatter between variables further apart. The random field is said homogeneous if its properties do not depend on the spatial position. In other words, one can write for a homogeneous field:

$$f_{a(\boldsymbol{x})}\left(a\left(\boldsymbol{x}\right)\right) = f_{a(\mathbf{0})}\left(a\left(\mathbf{0}\right)\right) \, \forall \boldsymbol{x} \in \boldsymbol{D} \, . \tag{2.9}$$

The spatial correlation is defined as the correlation between the same random variable at different spatial positions. It can be defined as:

$$\underline{R}\left(\boldsymbol{x}, \boldsymbol{y}\right) = \frac{\mathbb{E}\left[\left(a\left(\boldsymbol{x}\right) - \bar{a}\right)\left(a\left(\boldsymbol{y}\right) - \bar{a}\right)\right]}{\sigma_a^2} \, . \tag{2.10}$$

In the case of a homogeneous random field, it solely depends on the spatial distance between the random variables $\boldsymbol{\tau}$, $\underline{R}\left(\boldsymbol{x}, \boldsymbol{y}\right) = \underline{R}\left(\boldsymbol{x} - \boldsymbol{y}\right) = \underline{R}\left(\boldsymbol{\tau}\right)$. Let us note that $\boldsymbol{\tau}$ is a vector, the direction being of interest for a homogeneous random field. It is not the case any more for an isotropic homogeneous random field. If the field is isotropic, the stochastic behaviour of the field is the same in any direction. Therefore, the correlation solely depends on the scalar norm of $\boldsymbol{\tau}$, $\underline{R}\left(\boldsymbol{x}, \boldsymbol{y}\right) = \underline{R}\left(||\boldsymbol{\tau}||\right)$.

The correlation length is a measure of the spatial correlation of a field. For a homogeneous field, it can be defined by [84]:

$$l_{\mathbf{C}} = \frac{\int_{-\infty}^{\infty} R(\tau)\mathrm{d}\tau}{R(0)} \, . \tag{2.11}$$

Many examples of random fields exist. The landscape can be seen as a random field over the spatial domain. The ocean, whose height variations are time dependent, can be seen as a random field defined over both the spatial domain and the time t. An extensive review concerning random fields can be found in [94]. More consideration concerning random fields can be found in Chapter 4.

This section introduced uncertainty quantification, or UQ. Using UQ in an engineering simulation analysis involves three main steps.

- **Assessing**: the input uncertainty, its stochastic behaviour, has to be evaluated. This involves PDFs, spatial correlations and cross-correlations. This can be achieved by numerical simulations, experiments, or measurements. Assessing the stochastic behaviour of homogenised material properties using numerical simulations is the focus of Chapter 3.

- **Modelling**: a stochastic model encompassing the assessed stochastic behaviour has to be developed. Often, this involves random fields. A stochastic model of the homogenised properties has to be built which would allow generating random fields of those properties. The problem can be tackled in many ways and the use of a spectral generator combined to a non-Gaussian mapping is the focus of Chapter 4.

- **Computing**: once a stochastic model of the random inputs is defined, the uncertainty of the system response can be computed. The Stochastic Finite Element Method is a common way to compute the stochastic response using the generated random fields as input and is the topic of this chapter.

2.2 SFEM overview

The propagation of uncertainties towards a stochastic response (*e.g.* resonance frequencies or quality factors) of a system is mainly carried out today with the help of SFEM approaches [88],[24],[47]. SFEM stands for stochastic finite element method and consists of an extension of the deterministic finite element framework for stochastic problems, both in statics and in dynamics. By using finite elements whose properties are random, SFEM can propagate the uncertainties through the mechanical system and evaluate its stochastic response. To analyse an uncertain system, the very first thing to consider is the representation of the stochastic uncertainties. In this work, the stochastic input is represented by a continuous random field defined over the domain of interest $\boldsymbol{D}$. The generation of this random field will be carried out in Chapter 4, based on samples computed in Chapter 3. For now on, the procedure being generic, let us assume that all the stochastic input, which corresponds to the material parameters at each point of interest of the FE model, are gathered in a vector $\mathcal{U}$. This vector is defined for each spatial position $\boldsymbol{x}$ of the domain of interest $\boldsymbol{D}$. It is thus a field and each realisation of the field is based on the multidimensional random vector $\boldsymbol{\theta}$[3]. Thus the continuous random vector field $\mathcal{U}\left(\boldsymbol{x}, \boldsymbol{\theta}\right)$ is defined. The use of this field towards the evaluation of a stochastic response of interest, with the help of SFEM, involves three basic steps, as recalled in [88].

- *Discretization of the stochastic fields representing the uncertain system properties*,
- *the formulation of the stochastic matrix*,
- *response variability calculation.*

2.2.1 Discretization of the stochastic fields

The discretization step is the approximation of the continuous random field $\mathcal{U}\left(\boldsymbol{x}, \boldsymbol{\theta}\right)$ by a discrete field involving a finite number of random variables $\hat{\mathcal{U}}\left(\boldsymbol{x}, \boldsymbol{\theta}\right)$. The discretization methods can be classified into three categories [48],[88]:

---

[3] In the remaining sections of this work, a variable depending on θ is random based, the random space being uni-dimensional. A variable depending on $\boldsymbol{\theta}$ is also subjected to randomness, the random space being multidimensional.

- **point discretization methods** where the continuous random field is modelled by its values at some given points;
- **average-type discretization methods** where the continuous random field is represented by weighted integrals over specified domains;
- **series expansion methods** where the continuous random field is modelled by a truncated series whose spatial functions are deterministic and its random space is defined by a finite set of variables.

The point discretisation method is often used due to its simplicity. Furthermore, the distribution of the discretised field is the same as the distribution of the continuous field. The choice of the points of interest still needs to be carried out. Many possibilities exist such as considering the middle point of the finite elements, the nodal points, the integration points, the interpolation methods, or the optimal linear estimation. As shown in [14], the midpoint discretization method tends to over-represent the uncertainties in each element. The midpoint discretization method is easy to implement but its accuracy depends on the mesh discretization: the mesh elements must be small enough compared to the correlation length so that the properties can be considered constant over the mesh elements [48].

While the uncertainties tend to be overestimated with the midpoint discretisation approaches, they are underestimated in the case of average-type discretisations [14]. Among the average discretisations, the local approach is the simplest one. The local average method approximates the random values associated to a mesh element as a constant which is the average of the original field over the element. It can be written as:

$$\hat{\mathcal{U}}_i\left(\boldsymbol{\theta}\right) = \frac{\int_{\boldsymbol{D}_i} \mathcal{U}\left(\boldsymbol{x}, \boldsymbol{\theta}\right) d\boldsymbol{x}}{\int_{\boldsymbol{D}_i} d\boldsymbol{x}} \,, \tag{2.12}$$

where the domain of interest $\boldsymbol{D}$ is discretised with a finite set of mesh elements $\boldsymbol{D}_i$ and $\hat{\mathcal{U}}_i\left(\boldsymbol{\theta}\right)$ is the random vector associated to the finite element $\boldsymbol{D}_i$. Note that there exist other average discretisation procedures such as the weighted integral method.

Series expansion methods can be written in a general way as:

$$\hat{\mathcal{U}}\left(\boldsymbol{x}, \boldsymbol{\theta}\right) = \sum_{i=1}^{N} \boldsymbol{\alpha}_i\left(\boldsymbol{\theta}\right) \boldsymbol{\phi}_i\left(\boldsymbol{x}\right) \,, \tag{2.13}$$

where $\boldsymbol{\phi}_i\left(\boldsymbol{x}\right)$ are deterministic spatial functions and the $\boldsymbol{\alpha}_i\left(\boldsymbol{\theta}\right)$ are parameters representing the randomness. The point discretisation and the local average methods can be seen as particular cases of the series expansion method. Spectral expansion methods can be based on the Karhunen-Loève decomposition, polynomial chaos expansion or on a spectral decomposition. The recourse to spectral decomposition can lead to a reduction of the random space [48].

Let us note that the random field mesh is not necessarily the same as the finite element mesh, even though it is often the case as it eases the problem.

Actually, the accuracy of the discretisation of both meshes are based on different criteria. The discretisation of the random field is linked to the correlation length while the finite element mesh is based on the geometry of the structure or on the stress gradients. In some cases, it may be advantageous to consider different meshes. For example, if the random field is highly correlated (compared to the mesh size of the required finite element mesh), the stochastic mesh can be coarser to its corresponding finite element mesh so that the random space is reduced.

2.2.2 The formulation of the stochastic matrix

The aim of this section is to integrate the discretised stochastic fields defined in Section 2.2.1 in the finite element framework. This first requires to set up the deterministic problem. For example, for a static problem, the system of equations can be written as:

$$\boldsymbol{K}\mathbf{u} = \boldsymbol{f} \,, \tag{2.14}$$

where $\boldsymbol{K}$ is the stiffness matrix, $\mathbf{u}$ the displacement, and $\boldsymbol{f}$ the external forces. Afterwards, the randomness can be added. In this example, uncertainties can come from the material and thus will be reflected on $\boldsymbol{K}$ or from random external loading, thus involving $\boldsymbol{f}$, or both. If the stochastic response of a static structure experiencing random external loading through wind load is sought, the problem becomes:

$$\boldsymbol{K}\mathbf{u} = \boldsymbol{f}\left(\boldsymbol{\theta}\right) \,. \tag{2.15}$$

In the frame of non-intrusive procedures, the stochastic problem is fully formulated at this stage. Non-intrusive procedures compute the stochastic response of the structure based on a set of samples of the response of the deterministic problem with random inputs. Non-intrusive procedures are convenient as the deterministic solver underlying the problem can be used as a black box.

2.2.3 Response variability calculation

Once the stochastic problem is defined, the variability of its response can be estimated. The most common way to deal with the response variability calculation is the Monte-Carlo (MC) simulation. Other methods exist, such as the perturbation approach or the spectral stochastic finite element approach (SSFEM).

The Monte-Carlo simulation is a straight-forward non-intrusive approach which is very often used due to its simplicity and accuracy. From one realisation of the stochastic input, one sample of the structure response can be extracted based on a deterministic approach. From a set of realisations, the variability of the stochastic response of the structure can be estimated with statistical tools. To achieve a given accuracy, the system must be solved a sufficient number of times. This method is accurate as long as enough samples are computed (law of large numbers[4]). It does not suffer from the *curse of dimensionality*[5], even though the generation of an high number of random variables can still be costly. Monte-Carlo simulations are computationally heavy. However, as deterministic algorithms are more robust and efficient, as the computational power always increases, as parallel computing is more affordable, time enables the cost of MC simulations on realistic structures to become reasonable.

Nevertheless the computational cost of MC approaches can be reduced using appropriate strategies such as with importance sampling (the considered samples are concentrated in a low probability region which corresponds to a failure domain for example), stratified sampling (instead of taking randomly generated samples from a random variable, the random space is stratified and samples are taken in each subspace) or Latin hypercube sampling (a generalisation of stratified sampling in which the random space is divided in hypercubes with a particular generation strategy).

The perturbation stochastic finite element approach (PSFEM), described in [42], is a simple procedure applicable to many problems which gives an estimate of the solution at a low cost. However, the accuracy of the method, especially in non-linear cases, is not always ensured. A deterministic analysis is first performed as well as a sensitivity analysis with respect to the random inputs. A Taylor series expansion of the response can be performed to compute first and second order moments of the desired output based on both the sensitivities and the correlation information of the stochastic input. First order and second order approximations of the response variability can be retrieved. Accurate results can only be computed for small variability and for nearly linear problems.

To study high variability, it can be convenient to use the Spectral Stochastic Finite Element procedure (SSFEM). This procedure is based on the spectral discretisation of both the random field input (*i.e.* with a Karhunen-Loève expansion for a Gaussian field) and of the response field (*i.e.* with polynomial chaos expansion). Even though more costly than PSFEM, SSFEM can handle large variabilities and the stochastic behaviour of the response can be studied more accurately (as PSFEM computes only the first two moments). The SSFEM can however result in computationally expensive solutions, especially for large scale problems. The spectral stochastic approach is described in [24, 47]. It was used in many different applications and examples can be found in [48, 88]. As stated in [88], *as a conclusion, it can be stated that SSFEM is a rather new but promising technique and many advances remain to be achieved for its successful and computationally efficient application to nonlinear and inverse problems with stochastic data as well as to cases with time dependence.*

---

[4] The law of large number in probability states that statistical results obtained over a large number of trials should be close to the actual ones and will be closer with an increasing number of samples

[5] The curse of dimensionality refers to stochastic approaches which do not scale well with high-dimensional stochastic space. The computational burden involved when the stochastic problem possesses a high number of random input is unaffordable.

2.3 Linear elasticity: Timoshenko beams

The SFEM approach will now be applied on our first problem: estimating the uncertainty of the resonance frequency of a 1D micro-beam based on randomly and spatially varying material properties. This case is considered to demonstrate the accuracy of the methodology with a simple problem as the stochastic 3-scale method can be verified numerically with direct MC simulations.

2.3.1 The stochastic field and its discretisation

The material properties are represented by a random field of the elasticity tensor. Let $\boldsymbol{C}(\boldsymbol{x}, \boldsymbol{\theta}) : \boldsymbol{D} \times \boldsymbol{\Omega} \rightarrow \boldsymbol{M}_6^+(R)$ be a random field of the elasticity tensor, in its Voigt notation, over the spatial domain $\boldsymbol{D}$, which is a function of the spatial coordinate $\boldsymbol{x}$. $\boldsymbol{\theta} \in \boldsymbol{\Omega}$ denotes the elements in the sample space involving random quantities and $\boldsymbol{M}_n^+(R)$ refers to the set of all symmetric positive-definite real matrices of size $n \times n$. In this 1D beam problem, stated in linear elasticity, only the Young's modulus E_x in the x direction, extracted from the elasticity tensor, is propagated at the macro-scale with the finite element procedure.

In order to evaluate the different elementary stiffness matrices of the finite elements, the discretization of the elasticity tensor random field is now taken into account. The point discretization method is considered to solve this problem, see Section 2.2.1. With the point discretization method, the random field $E_x(x, \boldsymbol{\theta}) : D \times \boldsymbol{\Omega} \rightarrow R^+$ is evaluated at some integration points x_i, leading to the random field $E_x\left(x_i, \boldsymbol{\theta}\right)$. The integration points considered in this work are the mid-points of each beam finite element[6] (mid-point discretisation).

2.3.2 Formulation of the stochastic matrix through the problem definition

The deterministic problem of an un-damped mechanical structure can be discretised using the finite element method. To this end the spatial domain D is discretised into beam finite elements D_i, such that $D = \bigcup_i D_i$, where D_i includes the finite element boundary. The finite element model is based on the equilibrium of forces and moments. To express this equilibrium, for the sake of simplicity, we only consider the deflection along z at first. While the Euler-Bernoulli formulation assumes that the cross-section remains planar and normal to the neutral fibres after deformation and thus no shear strain are considered, the Timoshenko beam theory considers shear strain and beams cross-sections remain planar but no longer normal to the neutral fibres after deformation. The following displacements field is assumed:

$$\boldsymbol{u}^{(x)}\left(x, z\right) = z\phi\left(x\right) , \tag{2.16}$$

$$\boldsymbol{u}^{(z)}\left(x, z\right) = \upsilon\left(x\right) , \tag{2.17}$$

---

[6] the stochastic mesh matching the finite element mesh

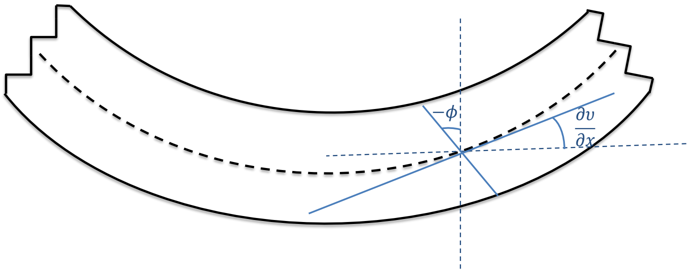

Figure 2.1: Timoshenko beam theory. Euler-Bernoulli is retrieved when $-\phi = \frac{\partial \upsilon}{\partial x}$.

where υ is the deflection in the thickness direction of the neutral fibres of the beam and ϕ is the rotation of the cross-section around the y-direction, as can be seen in Figure 2.1. Let us note that $\phi = -\frac{\partial \upsilon}{\partial x}$ for the Euler-Bernoulli beam element. Following the definition of the Cauchy strains and assuming a linear relationship between stress and strain, the internal moment $M(x)$ and the internal transverse force $Q(x)$ can be written as:

$$M(x) = \int_A z\sigma_{xx} dA = EI\frac{\partial \phi}{\partial x}\,, \tag{2.18}$$

$$Q(x) = K_s \int_A \sigma_{xz} dA = GAK_s \left(\phi + \frac{\partial \upsilon}{\partial x}\right)\,, \tag{2.19}$$

where G is the shear modulus, I is the inertia of the beam, A is the area of the cross section, and K_s is the shear correction coefficient[7] which accounts for the fact that the cross-sections do not remain plane in reality.

The equilibrium between both the moments and the transverse forces, in the absence of external forces, and in the dynamic case, leads to the following system of equations ([79] where inertia terms were added):

$$\rho I\frac{\partial^2 \phi}{\partial t^2} - \frac{\partial}{\partial x}\left(EI\frac{\partial \phi}{\partial x}\right) + GAK_s\left(\frac{\partial \upsilon}{\partial x} + \phi\right) = 0\,, \tag{2.20}$$

$$\rho A\frac{\partial^2 \upsilon}{\partial t^2} - \frac{\partial}{\partial x}\left[GAK_s\left(\frac{\partial \upsilon}{\partial x} + \phi\right)\right] = 0\,. \tag{2.21}$$

To define the finite element model over the structure, 2 kinematically admissible weight functions w_ϕ and w_υ are respectively multiplied with Eqs. (2.20) and (2.21) and the resulting equations are integrated over the domain D to finally obtain the weak form of the governing equations. After integrating by parts, the weak form of the equilibrium equations over a finite element defined over $[x_a, x_b]$ are written as [79]:

---

[7] 5/6 for rectangular cross-sections

$$\rho I \int_{x_a}^{x_b} \frac{\partial^2 \phi}{\partial t^2} w_\phi \mathrm{d}x - M(x_b) w_\phi(x_b) + M(x_b) w_\phi(x_b) + \\ EI \int_{x_a}^{x_b} \frac{\partial \phi}{\partial x} \frac{\partial w_\phi}{\partial x} \mathrm{d}x + GAK_s \int_{x_a}^{x_b} \left(\frac{\partial \upsilon}{\partial x} w_\phi + \phi w_\phi \right) \mathrm{d}x = 0 \,, \quad (2.22)$$

$$\rho A \int_{x_a}^{x_b} \frac{\partial^2 \upsilon}{\partial t^2} w_\upsilon \mathrm{d}x - Q(x_b) w_\upsilon(x_b) + Q(x_a) w_\upsilon(x_a) + \\ GAK_s \int_{x_a}^{x_b} \left(\frac{\partial \upsilon}{\partial x} \frac{\partial w_\upsilon}{\partial x} + \phi \frac{\partial w_\upsilon}{\partial x} \right) \mathrm{d}x \,. \quad (2.23)$$

Both ϕ and υ(as well as their derivatives) can be approximated based on their nodal values $\boldsymbol{\phi}$ and $\boldsymbol{\upsilon}$ following:

$$\phi = \boldsymbol{N}_\phi \boldsymbol{\phi} \,, \quad (2.24)$$

$$\upsilon = \boldsymbol{N}_\upsilon \boldsymbol{\upsilon} \,, \quad (2.25)$$

where $\boldsymbol{N}_\phi$ and $\boldsymbol{N}_\upsilon$ are shape functions for respectively ϕ and υ.

However, the different Timoshenko beam theories that can be found in the literature are usually different due to their particular choice of shape functions. In this work, we consider the locking free interdependent interpolation element described in [79] whose shape functions are based on the solution of the homogeneous differential equations and on the nodal values. In the case of absence of external forces, this results in the system:

$$\boldsymbol{M}\ddot{\mathbf{u}} + \boldsymbol{K}\mathbf{u} = \mathbf{0} \,, \quad (2.26)$$

where $\boldsymbol{M}$ and $\boldsymbol{K}$ are respectively the assembled mass and stiffness matrices, $\mathbf{u}$ is the assembled vector of the degrees of freedom ϕ and υ, and no external forces are considered. The elementary mass and stiffness matrices can be found in Appendix A. The case of deflections in the other plane is directly deduced by considering the beam in its cross sectional principle axes.

As the uncertainties result from the elasticity tensor, the stiffness matrix of the finite element discretization is subjected to uncertainties and the non-deterministic problem is thus stated by:

$$\boldsymbol{M}\ddot{\mathbf{u}} + \boldsymbol{K}(\boldsymbol{\theta})\mathbf{u} = \mathbf{0} \,. \quad (2.27)$$

The resonance frequency can be computed by considering the case of harmonic vibrations:

$$\mathbf{u} = \mathbf{u}_0 e^{i\varpi t} \,, \quad (2.28)$$

where ϖ is the angular frequency and $\mathbf{u}_0$ is the mode of vibration. Using Eq. (2.28) in Eq. (2.27), the following system is obtained:

$$\lambda^2 \boldsymbol{M}\mathbf{u}_0 = -\boldsymbol{K}(\boldsymbol{\theta})\mathbf{u}_0 \tag{2.29}$$

where $\lambda = i\varpi$.

2.3.3 Response variability calculation

Finally, Monte Carlo simulations can be used to compute the variability of the response of the structure, which in this case are the resonant frequencies. The computational cost required to solve this system of equations highly depends on the involved mesh size, which needs to be chosen carefully. As discussed before, there exists a strong link between the spatial correlation length (2.11) of the random field and the mesh size: the mesh size should be sufficiently small compared to the correlation length. As for a structure made of a poly-crystalline material the random field of the material properties corresponds to a noise field (as opposed to a smooth field), the SFEM described previously cannot be applied directly [56, 5] and the structural finite element problem would thus have to be solved based on the realisations of micro-structures such that each grain is meshed with several finite elements. This motivates the introduction of an intermediate scale, the meso-scale, which represents an aggregate of several grains. At this scale, the random field description for the material properties has a correlation length larger than when considering explicitly the grain discretization, allowing the use of coarser elements in the SFEM at the structural-scale. The material characterisation at meso-scale is the focus of Chapter 3 and the resulting meso-scale stochastic model is described in Chapter 4.

2.4 Thermo-elasticity

The second problem on which SFEM is applied, is a thermo-elastic problem. The objective is to characterise the uncertainty of the quality factor of micro-beams modelled using 3D FEM.

2.4.1 The stochastic field and its discretisation

First, the sources of uncertainty for the thermo-mechanical problem need to be identified. The material properties which are assumed to exhibit a scatter are the elastic tensor $\boldsymbol{C}$, the heat conductivity tensor $\boldsymbol{\kappa}$, and the thermal expansion tensor $\boldsymbol{\alpha}$. The heat conductivity is a material property which links heat flux and temperature gradient through Fourier's law. The higher the conductivity, the higher the rate of heat transfer. The thermal expansion is a material property which represents the deformation due to a change of temperature. The 3 random tensors $\boldsymbol{C}$, $\boldsymbol{\kappa}$, and $\boldsymbol{\alpha}$ can be represented under the form of a random field. Using the Voigt notations for the different tensors, we have the random fields of the elasticity tensor, heat conductivity tensor, and thermal expansion tensor

$\boldsymbol{C}(\boldsymbol{x},\boldsymbol{\theta}) : \boldsymbol{D}\times\boldsymbol{\Omega}\rightarrow\boldsymbol{M}_6^+(R)$, $\boldsymbol{\kappa}(\boldsymbol{x},\boldsymbol{\theta}) : \boldsymbol{D}\times\boldsymbol{\Omega}\rightarrow\boldsymbol{M}_3^+(R)$ and $\boldsymbol{\alpha}(\boldsymbol{x},\boldsymbol{\theta}) : \boldsymbol{D}\times\boldsymbol{\Omega}\rightarrow\boldsymbol{M}_3(R)$ respectively, over the spatial domain $\boldsymbol{D}$, which are functions of the spatial coordinate $\boldsymbol{x}$. $\boldsymbol{M}_n(R)$ refers to the set of all symmetric real matrices of size $n\times n$ in order to keep $\boldsymbol{\alpha}(\boldsymbol{x},\boldsymbol{\theta})$ more general (negative thermal expansion is possible for some materials).

Because all these three tensors relate to the heterogeneities or micro structures of materials, it is not proper to write them as three uncorrelated random fields. Therefore, one random field is considered so that the cross-correlation between $\boldsymbol{C}$, $\boldsymbol{\kappa}$, and $\boldsymbol{\alpha}$ is taken into account as will be seen in Chapter 4.

Once again, the random field can be discretised with the integration point method, see Section 2.2.1. Let us recall that an accurate SFEM analysis with the simple point discretization of the random field requires that the mesh elements are small enough compared to the correlation length [14].

2.4.2 Formulation of the stochastic matrix through the problem definition

Governing equations for the thermo-elastic solids

The equations that govern the motion of thermo-elastic solids include the balance laws for mass, momentum, and energy [96]. The weak form for linear coupled thermo-elastic problems can be derived from two governing equations. The first governing equation is the linear momentum balance equation. The second governing equation is derived from the balance of energy and the Clausius-Duhem inequality. Here we just give the resulting equations, more details can be found in [48] and [96].

The first governing equation is the linear momentum balance equation, which reads

$$\rho\ddot{\boldsymbol{u}} = \nabla\cdot\boldsymbol{\sigma} + \rho\boldsymbol{b}\,, \tag{2.30}$$

where ρ is the mass density, $\boldsymbol{u}$ is the displacement vector, $\boldsymbol{\sigma}$ is the Cauchy stress tensor, and $\boldsymbol{b}$ is the body force density vector. The dot on top of a variable refers to its time derivative.

The second governing equation is obtained based on the balance of energy and the Clausius-Duhem inequality, which is stating the irreversibility of a natural process when energy dissipation is involved. When the only dissipation mechanism involved results from the heat conductivity, and no heat source is considered in the body, the balance of energy and the Clausius-Duhem relation lead to

$$\dot{\mathcal{S}} = -\frac{\nabla\cdot\boldsymbol{q}}{T}\,, \tag{2.31}$$

where $\mathcal{S}$ is the entropy per unit volume of the body, T is the absolute temperature, and $\boldsymbol{q}$ is the thermal flux vector, as detailed in B.1. In a general form, the Helmholtz free energy of the body per unit volume is expressed in terms of the elastic potential $\psi(\boldsymbol{\varepsilon})$ per unit volume and satisfies

$$\boldsymbol{\sigma}(\boldsymbol{\varepsilon}, T) = \left(\frac{\partial \mathcal{F}}{\partial \boldsymbol{\varepsilon}}\right)_T \quad \text{and} \quad \mathcal{S}(\boldsymbol{\varepsilon}, T) = -\left(\frac{\partial \mathcal{F}}{\partial T}\right)_{\boldsymbol{\varepsilon}}, \tag{2.32}$$

where $\boldsymbol{\varepsilon}$ is the Cauchy strain tensor.

In the case of the absence of external force and of heat source, and at a temperature T different from the reference temperature T_0, the Helmholtz free energy $\mathcal{F}$ accounting for the thermal expansion reads

$$\mathcal{F}(\boldsymbol{\varepsilon}, T) = \mathcal{F}_0(T) - \boldsymbol{\varepsilon} : \frac{\partial^2 \psi}{\partial \boldsymbol{\varepsilon} \partial \boldsymbol{\varepsilon}} : \boldsymbol{\alpha}(T - T_0) + \psi(\boldsymbol{\varepsilon}), \tag{2.33}$$

where $\boldsymbol{\alpha} = \frac{\partial \boldsymbol{\varepsilon}}{\partial T}$ is the thermal expansion tensor assumed to be constant with the temperature.

From Eqs. (2.32), we have

$$\boldsymbol{\sigma}(\boldsymbol{\varepsilon}, T) = \left(\frac{\partial \mathcal{F}}{\partial \boldsymbol{\varepsilon}}\right)_T = \frac{\partial^2 \psi}{\partial \boldsymbol{\varepsilon} \partial \boldsymbol{\varepsilon}} : \boldsymbol{\varepsilon} - \frac{\partial^2 \psi}{\partial \boldsymbol{\varepsilon} \partial \boldsymbol{\varepsilon}} : \boldsymbol{\alpha}(T - T_0), \tag{2.34}$$

and

$$\mathcal{S}(\boldsymbol{\varepsilon}, T) = -\left(\frac{\partial \mathcal{F}}{\partial T}\right)_{\boldsymbol{\varepsilon}} = \mathcal{S}_0(T) + \boldsymbol{\varepsilon} : \frac{\partial^2 \psi}{\partial \boldsymbol{\varepsilon} \partial \boldsymbol{\varepsilon}} : \boldsymbol{\alpha}, \tag{2.35}$$

where $\mathcal{S}_0(T) = \partial \mathcal{F}/\partial T$ is the entropy at $\boldsymbol{\varepsilon} = \mathbf{0}$, i.e. at zero-deformation. Moreover, we can write $\partial \mathcal{S}_0/\partial t = (\partial \mathcal{S}_0/\partial T) \cdot (\partial T/\partial t)$, where the derivative $(\partial \mathcal{S}_0/\partial T) = \rho C_v/T$ with C_v the heat capacity per unit mass at constant volume. Taking the derivative with respect to time t of Eq. (2.35) and using Eq. (2.31) lead to the second governing equation, which reads

$$\rho C_v \frac{\partial T}{\partial t} + T\boldsymbol{\alpha} : \frac{\partial^2 \psi}{\partial \boldsymbol{\varepsilon} \partial \boldsymbol{\varepsilon}} : \frac{\partial \boldsymbol{\varepsilon}}{\partial t} = \boldsymbol{\kappa} : \frac{\partial^2 T}{\partial \boldsymbol{x} \partial \boldsymbol{x}}, \tag{2.36}$$

where $\boldsymbol{\kappa}$ is the second-order tensor called thermal conductivity, which satisfies $\boldsymbol{q} = -\boldsymbol{\kappa} \cdot \nabla T$.

Finite element discretization

We assume that the temperature change corresponding to the mechanical loading is relatively small compared to the reference temperature T_0. Then we define $\vartheta = T - T_0$ and rewrite the two governing equations as

$$\begin{aligned} \rho \ddot{\boldsymbol{u}} - \nabla \cdot \boldsymbol{\sigma} - \rho \boldsymbol{b} &= 0, & (2.37)\\ \rho C_v \dot{\vartheta} + T_0 \boldsymbol{\alpha} : \mathbb{C} : \dot{\boldsymbol{\varepsilon}} - \boldsymbol{\kappa} : \frac{\partial^2 \vartheta}{\partial \boldsymbol{x} \partial \boldsymbol{x}} &= 0, & (2.38) \end{aligned}$$

where $\mathbb{C} = \frac{\partial^2 \psi}{\partial \boldsymbol{\varepsilon} \partial \boldsymbol{\varepsilon}}$ is the tensorial notation of the elasticity tensor $\boldsymbol{C}$ and we use the approximation $T \approx T_0$ in the second term $T\boldsymbol{\alpha} : \mathbb{C} : \dot{\boldsymbol{\varepsilon}}$ of the second governing equation for the purpose of linearization. Indeed, as we intend to perform modal analyses, linear equations are required. This set of equations is completed by the mechanical boundary conditions enforced on $\partial \boldsymbol{D} = \partial \boldsymbol{D}_u \cup \partial \boldsymbol{D}_{\mathcal{T}}$

$$\begin{aligned} \boldsymbol{u} = \underline{\boldsymbol{u}} \quad & \text{on} \quad \partial \boldsymbol{D}_u \,, \\ \boldsymbol{\sigma} \cdot \boldsymbol{n} = \boldsymbol{\mathcal{T}} \quad & \text{on} \quad \partial \boldsymbol{D}_{\mathcal{T}} \,, \end{aligned} \tag{2.39}$$

and by the thermal boundary conditions enforced on $\partial \boldsymbol{D}^T = \partial \boldsymbol{D}_T^T \cup \partial \boldsymbol{D}_q^T$

$$\begin{aligned} T = \underline{T} \quad & \text{on} \quad \partial \boldsymbol{D}_T^T \,, \\ \nabla T \cdot \boldsymbol{\kappa} \cdot \boldsymbol{n} = -\boldsymbol{q} \cdot \boldsymbol{n} = -\mathcal{Q} \quad & \text{on} \quad \partial \boldsymbol{D}_q^T \,, \end{aligned} \tag{2.40}$$

where $\underline{\boldsymbol{u}}$ is the constrained displacement field, $\boldsymbol{\mathcal{T}}$ is the constrained surface traction, $\underline{T}$ is the constrained temperature, $\mathcal{Q}$ is the constrained thermal surface flux, and where $\boldsymbol{n}$ is the outward unit normal vector.

The weak form of the set of governing equations is established using kinematically admissible weight functions defined in the $n+1$ dimensional spaces:

$$\begin{aligned} \boldsymbol{w}_u \in [C^0]^n \quad & \text{The weight function of the displacement field} \,, \\ w_\vartheta \in [C^0] \quad & \text{The weight function of the temperature field} \,. \end{aligned} \tag{2.41}$$

Multiplying the governing equation (2.37) by the displacement weight function $\boldsymbol{w}_u$ and integrating the result over the domain $\boldsymbol{D}$ yields

$$\int_{\boldsymbol{D}} \boldsymbol{w}_u \cdot [\rho \ddot{\boldsymbol{u}} - \nabla \cdot \boldsymbol{\sigma} - \rho \boldsymbol{b}] \mathrm{d}V = 0 \,. \tag{2.42}$$

Applying the divergence theorem, the natural boundary conditions on $\partial \boldsymbol{D}_{\mathcal{T}}$, the essential boundary conditions on $\partial \boldsymbol{D}_u$, and the symmetry property of the Cauchy stress tensor leads to

$$\int_{\boldsymbol{D}} \{ \boldsymbol{w}_u \cdot \rho \ddot{\boldsymbol{u}} + [\nabla \boldsymbol{w}_u]^{\mathrm{T}} : \boldsymbol{\sigma} \} \mathrm{d}V = \int_{\boldsymbol{D}} \boldsymbol{w}_u \cdot \rho \boldsymbol{b} \mathrm{d}V + \int_{\partial \boldsymbol{D}_{\mathcal{T}}} \boldsymbol{w}_u \cdot \boldsymbol{\mathcal{T}} \mathrm{d}\Gamma \,. \tag{2.43}$$

The same method is used to treat the second PDE (2.38), which results into

$$\int_{\boldsymbol{D}} \{ \rho C_v \dot{\vartheta} w_\vartheta + T_0 \boldsymbol{\alpha} : \mathbb{C} : \dot{\boldsymbol{\varepsilon}} w_\vartheta + \nabla w_\vartheta \cdot \boldsymbol{\kappa} \cdot \nabla \vartheta \} \mathrm{d}V = - \int_{\partial \boldsymbol{D}_q^T} \mathcal{Q} w_\vartheta \mathrm{d} \partial \boldsymbol{D}^T . \tag{2.44}$$

The third term on the left-hand side of Eq. (2.44), *i.e.* $\int_\Omega \nabla w_\vartheta \cdot \boldsymbol{\kappa} \cdot \nabla \vartheta \mathrm{d}\Omega$, is responsible for the thermo-elastic damping when the thermal relaxation time $\tau = \frac{\rho C_v l_\tau^2}{\|\boldsymbol{\kappa}\|_\infty \pi^2}$ is close to the deformation period. In this relation l_τ is the characteristic length characterizing the conduction, typically the device thickness. When the thermal relaxation time τ is small (large) compared to the deformation period, the process is quasi-isothermal (quasi-adiabatic) and the thermo-elastic damping is negligible.

The finite element discretization is straightforwardly formulated using the Galerkin approach. Toward this end, the displacement field $\boldsymbol{u}$ and the relative temperature field ϑ can be interpolated in each element $\boldsymbol{D}^{\mathrm{e}}$ using traditional shape function matrices $\boldsymbol{N}_u$ and $\boldsymbol{N}_\vartheta$ as follows:

$$\boldsymbol{u} = \boldsymbol{N}_u \mathbf{u}, \quad \text{and} \quad \vartheta = \boldsymbol{N}_\vartheta \boldsymbol{\vartheta}\,, \tag{2.45}$$

where the vectors $\mathbf{u}$ and $\boldsymbol{\vartheta}$ contain the assembled nodal values of the displacements and of the relative temperature field, respectively. Similarly, the weight functions are interpolated using the same shape functions

$$\boldsymbol{w}_u = \boldsymbol{N}_u \mathbf{du}, \quad \text{and} \quad w_\vartheta = \boldsymbol{N}_\vartheta \mathbf{d}\boldsymbol{\vartheta}\,, \tag{2.46}$$

where $\mathbf{du}$ and $\mathbf{d}\boldsymbol{\vartheta}$ are arbitrary values fulfilling the essential boundary conditions.

The strain tensorial field and the gradient field of the relative temperature can easily be deduced, in terms of the problem unknowns, from

$$\boldsymbol{\varepsilon} = \boldsymbol{B}_u \mathbf{u}, \quad \text{and} \quad \nabla\vartheta = \nabla \boldsymbol{N}_\vartheta \boldsymbol{\vartheta} = \boldsymbol{B}_\vartheta \boldsymbol{\vartheta}\,, \tag{2.47}$$

where $\boldsymbol{B}_u$ and $\boldsymbol{B}_\vartheta$ represent the matrix strain operator and the matrix operator for the temperature gradient, respectively. The related derivatives with respect to time are

$$\ddot{\boldsymbol{u}} = \boldsymbol{N}_u \ddot{\mathbf{u}}, \quad \dot{\boldsymbol{\varepsilon}} = \boldsymbol{B}_u \dot{\mathbf{u}} \quad \text{and} \quad \dot{\vartheta} = \boldsymbol{N}_\vartheta \dot{\boldsymbol{\vartheta}}\,. \tag{2.48}$$

We recall the expression of stress, Eq. (2.34), in linear thermo-elasticity

$$\boldsymbol{\sigma} = \mathbb{C} : \boldsymbol{\varepsilon} - \mathbb{C} : \boldsymbol{\alpha}\vartheta\,. \tag{2.49}$$

Therefore, using the arbitrary nature of $\mathbf{du}$ and $\mathbf{d}\boldsymbol{\vartheta}$, the Eq. (2.43) and (2.44) become

$$\int_{\boldsymbol{D}} \{\rho \boldsymbol{N}_u^{\mathrm{T}} \boldsymbol{N}_u \ddot{\mathbf{u}} + \boldsymbol{B}_u^{\mathrm{T}} \boldsymbol{C} \boldsymbol{B} \mathbf{u} - \boldsymbol{B}_u^{\mathrm{T}} \boldsymbol{C} \boldsymbol{\alpha} \boldsymbol{N}_\vartheta \boldsymbol{\vartheta}\} \mathrm{d}V = \int_{\boldsymbol{D}} \boldsymbol{N}_u^{\mathrm{T}} \rho \boldsymbol{b} \mathrm{d}V + \int_{\partial \boldsymbol{D}_{\mathcal{T}}} \boldsymbol{N}_u^{\mathrm{T}} \boldsymbol{\mathcal{T}} \mathrm{d}\partial \boldsymbol{D}\,, \tag{2.50}$$

$$\int_{\boldsymbol{D}} \{\rho C_v \boldsymbol{N}_\vartheta^{\mathrm{T}} \boldsymbol{N}_\vartheta \dot{\boldsymbol{\vartheta}} + T_0 \boldsymbol{N}_\vartheta^{\mathrm{T}} \boldsymbol{\alpha} \boldsymbol{C} \boldsymbol{B}_u \dot{\mathbf{u}} + \boldsymbol{B}_\vartheta^{\mathrm{T}} \boldsymbol{\kappa} \boldsymbol{B}_\vartheta \boldsymbol{\vartheta}\} \mathrm{d}V = - \int_{\partial \boldsymbol{D}_q^T} \boldsymbol{N}_\vartheta^{\mathrm{T}} \mathcal{Q} \mathrm{d}\partial \boldsymbol{D}^T\,, \tag{2.51}$$

where $\boldsymbol{C}$ is the matrix form of the fourth-order tensor $\mathbb{C}$.

The equations above can be stated in the following matrix form:

$$\begin{bmatrix} \boldsymbol{M} & \mathbf{0} \\ \mathbf{0} & \mathbf{0} \end{bmatrix} \begin{bmatrix} \ddot{\mathbf{u}} \\ \ddot{\boldsymbol{\vartheta}} \end{bmatrix} + \begin{bmatrix} \mathbf{0} & \mathbf{0} \\ \boldsymbol{D}_{\vartheta u} & \boldsymbol{D}_{\vartheta\vartheta} \end{bmatrix} \begin{bmatrix} \dot{\mathbf{u}} \\ \dot{\boldsymbol{\vartheta}} \end{bmatrix} + \begin{bmatrix} \boldsymbol{K}_{uu} & \boldsymbol{K}_{u\vartheta} \\ \mathbf{0} & \boldsymbol{K}_{\vartheta\vartheta} \end{bmatrix} \begin{bmatrix} \mathbf{u} \\ \boldsymbol{\vartheta} \end{bmatrix} = \begin{bmatrix} \boldsymbol{f}_u \\ \boldsymbol{f}_\vartheta \end{bmatrix}\,, \tag{2.52}$$

where the definitions of all the sub-matrices can be found in Appendix B.2.

Based on the randomness defined in Section 2.4.1, the finite element formulation (2.52) can be restated in the probabilistic form as:

$$\begin{bmatrix} \boldsymbol{M} & \mathbf{0} \\ \mathbf{0} & \mathbf{0} \end{bmatrix} \begin{bmatrix} \ddot{\mathbf{u}} \\ \ddot{\boldsymbol{\vartheta}} \end{bmatrix} + \begin{bmatrix} \mathbf{0} & \mathbf{0} \\ \boldsymbol{D}_{\vartheta u}\left(\boldsymbol{\theta}\right) & \boldsymbol{D}_{\vartheta\vartheta}\left(\boldsymbol{\theta}\right) \end{bmatrix} \begin{bmatrix} \dot{\mathbf{u}} \\ \dot{\boldsymbol{\vartheta}} \end{bmatrix} + \begin{bmatrix} \boldsymbol{K}_{uu}\left(\boldsymbol{\theta}\right) & \boldsymbol{K}_{u\vartheta}\left(\boldsymbol{\theta}\right) \\ \mathbf{0} & \boldsymbol{K}_{\vartheta\vartheta}\left(\boldsymbol{\theta}\right) \end{bmatrix} \begin{bmatrix} \mathbf{u} \\ \boldsymbol{\vartheta} \end{bmatrix} = \begin{bmatrix} \boldsymbol{f}_u \\ \boldsymbol{f}_\vartheta \end{bmatrix} . \tag{2.53}$$

Numerical evaluation of the quality factor

In a wide variety of MEMS devices, such as in accelerometers, gyrometers, sensors, charge detectors, radio-frequency filters, magnetic resonance force microscopes, or again torque magnetometers, the resonator part is a critical component for which a high quality factor Q is sought[48]. The Q factor is defined by the ratio of the stored energy in the resonator W and the total dissipated energy ΔW per cycle of vibration

$$Q = 2\pi \frac{W}{\Delta W} , \tag{2.54}$$

The thermo-elastic damping represents the energy loss associated to an entropy rise caused by the coupling between the heat transfer and strain rate. In solids with a positive thermal expansion effect, an increase of temperature induces a dilatation and inversely, a decrease of temperature produces a compression. Similarly, a dilatation lowers the temperature and a compression raises it. Therefore, when a thermo-elastic solid is in motion and taken out of equilibrium, the energy dissipates through the irreversible flow of heat driven by local temperature gradients that are generated by the strain field through its coupling with the temperature field.

Thermo-elastic coupling induces damping whose effect is characterised by a resonance frequency shift [50]. The quality factor can be computed through solving the eigenvalues of the coupled problem using the finite element model (2.53). The dissipation of the resonating beam is measured by the fraction of energy loss per cycle, which is the inverse of the quality factor, Q^{-1}, and can be expressed in terms of the imaginary and real parts of the pulsation as

$$Q^{-1} = \frac{2|\mathrm{Im}(\varpi_n)|}{\sqrt{\mathrm{Re}^2(\varpi_n) + \mathrm{Im}^2(\varpi_n)}} , \tag{2.55}$$

where ϖ_n is the thermo-elastic resonant pulsation. As the imaginary part of the resonant pulsation considered is much smaller than the real part, the approximated inverse of the quality factor reads

$$Q^{-1} \approx 2 \left| \frac{\mathrm{Im}(\varpi_n)}{\mathrm{Re}(\varpi_n)} \right| . \tag{2.56}$$

Equation (2.53) can be rewritten in general for the thermo-elastic case as

$$\mathbb{M}\ddot{\boldsymbol{v}} + \mathbb{D}\left(\boldsymbol{\theta}\right)\dot{\boldsymbol{v}} + \mathbb{K}\left(\boldsymbol{\theta}\right)\boldsymbol{v} = \mathbb{F} , \tag{2.57}$$

where $\boldsymbol{v} = \{\mathbf{u}, \boldsymbol{\vartheta}\}^{\mathrm{T}}$. To calculate the effect of thermo-elastic coupling on the vibrations of a structure, we solve the coupled thermo-elastic equations (2.57) for the case of harmonic vibrations, and we set

$$\boldsymbol{v} = \boldsymbol{v}_0 e^{i\varpi t}\,, \tag{2.58}$$

in order to obtain the normal modes of vibration and their corresponding frequencies. In general the frequencies are complex, the real part $\mathrm{Re}(\varpi)$ giving the new eigenvalue frequencies of the structure in the presence of thermo-elastic coupling, and the imaginary part $\mathrm{Im}(\varpi)$ giving the attenuation of the vibration. The quality factor, Eq. (2.56), can be computed from the eigenvalue of the coupled problem as

$$Q = \frac{1}{2}\left|\frac{\mathrm{Re}(\varpi)}{\mathrm{Im}(\varpi)}\right|. \tag{2.59}$$

The general quadratic eigenvalue problem to solve results from Eq. (2.57) without considering external force and external heat exchange. For simplicity, we rewrite $\lambda = i\varpi$. Submitting Eq. (2.58) into Eq. (2.57) and setting its right hand side to be zero results in

$$\left(\mathbb{M}\lambda^2 + \mathbb{D}\left(\boldsymbol{\theta}\right)\lambda + \mathbb{K}\left(\boldsymbol{\theta}\right)\right)\boldsymbol{v} = \mathbf{0}\,. \tag{2.60}$$

A generation transformation is applied to convert the original quadratic problem into a first-order problem as

$$\begin{bmatrix} -\mathbb{K}\left(\boldsymbol{\theta}\right) & \mathbf{0} \\ \mathbf{0} & \mathbb{I} \end{bmatrix} \begin{bmatrix} \boldsymbol{v} \\ \dot{\boldsymbol{v}} \end{bmatrix} = \lambda \begin{bmatrix} \mathbb{D}\left(\boldsymbol{\theta}\right) & \mathbb{M} \\ \mathbb{I} & \mathbf{0} \end{bmatrix} \begin{bmatrix} \boldsymbol{v} \\ \dot{\boldsymbol{v}} \end{bmatrix}\,. \tag{2.61}$$

Expanding all the entries of this compact allows this last equation to be written under the form

$$\begin{bmatrix} -\boldsymbol{K}_{uu}\left(\boldsymbol{\theta}\right) & -\boldsymbol{K}_{u\vartheta}\left(\boldsymbol{\theta}\right) & \mathbf{0} & \mathbf{0} \\ \mathbf{0} & -\boldsymbol{K}_{\vartheta\vartheta}\left(\boldsymbol{\theta}\right) & \mathbf{0} & \mathbf{0} \\ \mathbf{0} & \mathbf{0} & \boldsymbol{I} & \mathbf{0} \\ \mathbf{0} & \mathbf{0} & \mathbf{0} & \boldsymbol{I} \end{bmatrix} \begin{bmatrix} \mathbf{u} \\ \boldsymbol{\vartheta} \\ \dot{\mathbf{u}} \\ \dot{\boldsymbol{\vartheta}} \end{bmatrix} = \\ \lambda \begin{bmatrix} \mathbf{0} & \mathbf{0} & \boldsymbol{M} & \mathbf{0} \\ \boldsymbol{D}_{\vartheta u}\left(\boldsymbol{\theta}\right) & \boldsymbol{D}_{\vartheta\vartheta}\left(\boldsymbol{\theta}\right) & \mathbf{0} & \mathbf{0} \\ \boldsymbol{I} & \mathbf{0} & \mathbf{0} & \mathbf{0} \\ \mathbf{0} & \boldsymbol{I} & \mathbf{0} & \mathbf{0} \end{bmatrix} \begin{bmatrix} \mathbf{u} \\ \boldsymbol{\vartheta} \\ \dot{\mathbf{u}} \\ \dot{\boldsymbol{\vartheta}} \end{bmatrix}, \tag{2.62}$$

where the eigenvalues associated with the fourth matrix equation are independent of the three other ones and can be eliminated without affecting the eigenvalue problem. The problem that needs to be solved is thus

$$\begin{bmatrix} -\boldsymbol{K}_{uu}\left(\boldsymbol{\theta}\right) & -\boldsymbol{K}_{u\vartheta}\left(\boldsymbol{\theta}\right) & \mathbf{0} \\ \mathbf{0} & -\boldsymbol{K}_{\vartheta\vartheta}\left(\boldsymbol{\theta}\right) & \mathbf{0} \\ \mathbf{0} & \mathbf{0} & \boldsymbol{I} \end{bmatrix} \begin{bmatrix} \mathbf{u} \\ \boldsymbol{\vartheta} \\ \dot{\mathbf{u}} \end{bmatrix} = \lambda \begin{bmatrix} \mathbf{0} & \mathbf{0} & \boldsymbol{M} \\ \boldsymbol{D}_{\vartheta u}\left(\boldsymbol{\theta}\right) & \boldsymbol{D}_{\vartheta\vartheta}\left(\boldsymbol{\theta}\right) & \mathbf{0} \\ \boldsymbol{I} & \mathbf{0} & \mathbf{0} \end{bmatrix} \begin{bmatrix} \mathbf{u} \\ \boldsymbol{\vartheta} \\ \dot{\mathbf{u}} \end{bmatrix}, \tag{2.63}$$

which can be written under the simpler form

$$\boldsymbol{A}(\boldsymbol{\theta})\,\boldsymbol{p} = \lambda \boldsymbol{B}(\boldsymbol{\theta})\,\boldsymbol{p}\,, \tag{2.64}$$

where $\boldsymbol{p} = \{\mathbf{u}, \boldsymbol{\vartheta}, \dot{\mathbf{u}}\}^{\mathrm{T}}$. The details on how to solve this eigenvalue problem were discussed in [46] and [48].

After solving this eigenvalue problem, the quality factor realisations can thus be computed from equation (2.59) using the relation of ϖ and λ, which gives

$$Q(\boldsymbol{\theta}) = \frac{1}{2}\left|\frac{\mathrm{Im}(\lambda)}{\mathrm{Re}(\lambda)}\right|. \tag{2.65}$$

2.4.3 Response variability calculation

The variability of the macro-scale thermoelastic problem is computed with a Monte-Carlo procedure as for the linear elastic 1D beam problem. However this time a 3D FEM is required to extract the thermo-elastic damping. From samples of micro-beams, samples of the quality factor can be computed and analysed using appropriate statistical tools. Once again, particular attention must be drawn on the finite element mesh which should be small enough compared to the correlation length of the input random field.

In Section 3.3, we introduce an intermediate scale, the meso-scale, and detail how to extract the meso-scale random field of vector $\mathcal{U}$ from the finite element resolution of meso-scale volume elements. The obtained smooth random field description for the material properties has a correlation length larger than the characteristic length of the micro-structure, which allows the use of coarser elements in the SFEM at the structural-scale.

2.5 Kirchhoff-Love plates

The estimation of the probability density function of the resonance frequency of a thin MEMS subjected to uncertainties is the objective of this third problem. In order to treat more general problems than 1D beams, we consider a plate approximation. As shown in Chapter 5, this allows considering uncertainties in the profile of the MEMS surface. Once again, the SFEM approach is used.

2.5.1 The stochastic field and its discretisation

First the properties exhibiting uncertainties must be identified. Some sources of uncertainty are material related such as the grain sizes and grain orientations for poly-crystalline materials. Other sources come from the geometry, such as the surface roughness. To account for both the material uncertainty and the roughness, we use a resultant stress-strain relation formulated for thin structures in a stochastic way. Toward this end, we consider the plate representation illustrated in Fig. 2.2. The domain $\boldsymbol{D}$ of the plate is discretised in a Cosserat plane $\mathcal{A}$, assumed to be lying in the plane $\mathrm{O}\boldsymbol{E}_x\boldsymbol{E}_y$ for simplicity, and in the

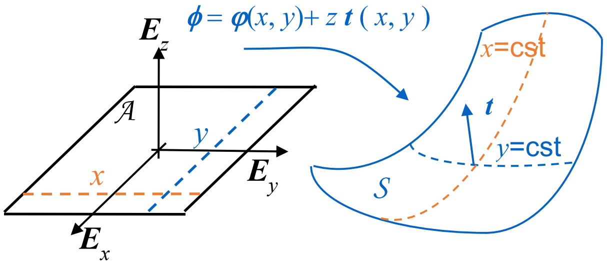

Figure 2.2: Representation of the plate discretization in a Cosserat plane $\mathcal{A}$ and along the thickness direction $\boldsymbol{E}_z$

thickness direction along $\boldsymbol{E}_z$. The deformation mapping $\boldsymbol{\phi}$ maps the neutral surface, represented by the Cosserat plane $\mathcal{A}$, to the deformed neutral-surface $\mathcal{S}$, and the thickness direction to the deformed unit direction $\boldsymbol{t}$, see Fig. 2.2. The displacement of the neutral surface is denoted by $\boldsymbol{u}$, and the change of the unit out-of-plane direction $\boldsymbol{t}$ by $\boldsymbol{\Delta t}$. In small deformations, considering Reissner-Mindlin plates, one can extract from those displacement fields, the kinematic membrane field $\boldsymbol{\varepsilon}^*$, the bending field $\boldsymbol{\kappa}^*$, and the out-of-plane shearing field $\boldsymbol{\gamma}^*$, following respectively

$$\boldsymbol{\varepsilon}^*_{\alpha\beta} = \frac{1}{2}\left(\boldsymbol{u}_{\alpha,\beta} + \boldsymbol{u}_{\beta,\alpha}\right) \,, \tag{2.66}$$

$$\boldsymbol{\kappa}^*_{\alpha\beta} = \frac{1}{2}\left(\boldsymbol{\Delta t}_{\alpha,\beta} + \boldsymbol{\Delta t}_{\beta,\alpha}\right) \,, \text{ and} \tag{2.67}$$

$$\gamma^*_{\alpha} = \boldsymbol{u}_{z,\alpha} + \boldsymbol{\Delta t}_{\alpha} \,, \tag{2.68}$$

where $\alpha = x,\, y$ and $\beta = x,\, y$ correspond to the in-plane directions, and where the notation $a_{,i}$ denotes the derivatives of a with respect to direction i.

These kinematic fields are related to the resultant membrane stresses $\boldsymbol{n}^*$,[8]

$$\boldsymbol{n}^{*\,\alpha} = \tilde{\boldsymbol{n}}^{*\,\alpha\beta}\boldsymbol{E}_\beta + \tilde{\boldsymbol{q}}^{*\,\alpha}\boldsymbol{E}_z \,, \tag{2.69}$$

to the resultant bending stresses $\tilde{\boldsymbol{m}}^*$,

$$\tilde{\boldsymbol{m}}^{*\,\alpha} = \tilde{\boldsymbol{m}}^{*\,\alpha\beta}\boldsymbol{E}_\beta \,, \tag{2.70}$$

and to the shear resultant stresses $\boldsymbol{n}^{*\,z}$

$$\boldsymbol{n}^{*\,z} = \tilde{\boldsymbol{q}}^{*\,\alpha}\boldsymbol{E}_\alpha \,. \tag{2.71}$$

---

[8] All along this section we use the classical notations for plates and shells described in a non-orthonormal referential with superscripts for stress related fields, although in this work the basis remains orthonormal. Similarly, we use the $\tilde{}$ notation to refer to the uncoupled in-plane/out-of-plane components, although for plate they are naturally uncoupled.

The different components of those vectors result from the integration of the stress tensor over the thickness h, with

$$\tilde{\boldsymbol{n}}^{*\,\alpha\beta} = \int_h \boldsymbol{\sigma}^{\alpha\beta} dz \,, \tag{2.72}$$

$$\tilde{\boldsymbol{m}}^{*\,\alpha\beta} = \int_h \boldsymbol{\sigma}^{\alpha\beta} z dz \,, \text{ and} \tag{2.73}$$

$$\tilde{\boldsymbol{q}}^{*\,\alpha} = \int_h \boldsymbol{\sigma}^{\alpha z} dz \,. \tag{2.74}$$

In elasticity, the linear relationships between the resultant kinematic fields and the resultant stresses can be expressed as

$$\tilde{\boldsymbol{n}}^{*} = \mathbb{C}_1^* : \boldsymbol{\varepsilon}^* + \mathbb{C}_2^* : \boldsymbol{\kappa}^* + \mathbb{C}_5^* \cdot \boldsymbol{\gamma}^*, \tag{2.75}$$

$$\tilde{\boldsymbol{m}}^{*} = \mathbb{C}_3^* : \boldsymbol{\varepsilon}^* + \mathbb{C}_4^* : \boldsymbol{\kappa}^* + \mathbb{C}_6^* \cdot \boldsymbol{\gamma}^*, \tag{2.76}$$

$$\tilde{\boldsymbol{q}}^{*} = \mathbb{C}_7^* : \boldsymbol{\varepsilon}^* + \mathbb{C}_8^* : \boldsymbol{\kappa}^* + \boldsymbol{C}_9^* \cdot \boldsymbol{\gamma}^*, \tag{2.77}$$

with, in all generalities the fourth order tensors $\mathbb{C}_1^*$, $\mathbb{C}_2^*$, $\mathbb{C}_3^*$, and $\mathbb{C}_4^*$, the third order tensors $\mathbb{C}_5^*$, $\mathbb{C}_6^*$, $\mathbb{C}_7^*$, and $\mathbb{C}_8^*$, and the second order tensor $\boldsymbol{C}_9^*$ in $\mathbb{R}^2$.

In this dissertation, we consider only the Kirchhoff-Love plate theory, which implies that $\boldsymbol{\Delta t}_\alpha = -\boldsymbol{u}_{z,\alpha}$, $\boldsymbol{\kappa}^*_{\alpha\beta} = -\boldsymbol{u}_{z,\alpha\beta}$, and $\tilde{\boldsymbol{q}}^{*\,\alpha} = 0$. In other words, the section of the plate remains perpendicular to the membrane after deformation. As a result, the set of Eqs. (2.75-2.77) simplifies into

$$\tilde{\boldsymbol{n}}^{*} = \mathbb{C}_1^* : \boldsymbol{\varepsilon}^* + \mathbb{C}_2^* : \boldsymbol{\kappa}^* \,, \tag{2.78}$$

$$\tilde{\boldsymbol{m}}^{*} = \mathbb{C}_3^* : \boldsymbol{\varepsilon}^* + \mathbb{C}_4^* : \boldsymbol{\kappa}^* \,. \tag{2.79}$$

Those last expressions can be rewritten under the matrix form

$$\boldsymbol{\psi}_\sigma^\star = \boldsymbol{U} \boldsymbol{\chi}_\epsilon^\star, \tag{2.80}$$

where $\boldsymbol{\chi}_\epsilon^\star$ corresponds to the resultant kinematic fields ordered in a vector notation and $\boldsymbol{\psi}_\sigma^\star$ corresponds to the resultant stresses ordered in a vector notation. The corresponding resultant material operator $\boldsymbol{U}$ defines the shell-like material behaviour.

In Chapter 3, the resultant material operator is computed through a multiscale procedure: a volume element is associated to each position $\boldsymbol{x}$ for a sample $\boldsymbol{\theta}$ thus forming a boundary value problem (BVP). As small scale volume elements are considered, they are not representative and therefore referred to as SVE or Statistical Volume Elements. The solution of the stochastic BVP determines $\boldsymbol{U}(\boldsymbol{x}, \boldsymbol{\theta})$. A random field is thus defined so that $\boldsymbol{U}(\boldsymbol{x}, \boldsymbol{\theta}) : \mathcal{A} \times \boldsymbol{\Omega} \rightarrow \boldsymbol{M}_6^+(\mathbb{R})$. The demonstration that $\boldsymbol{U} \in \boldsymbol{M}_n^+(\mathbb{R})$ can be proven in the following way.

First, let us show that the generalised tangent is symmetric. The matrix $\boldsymbol{U}$ can be written as:

$$\boldsymbol{U}^{(ij)} = \frac{\partial \boldsymbol{\psi}_{\sigma_{\text{plate}}}^{\star(i)}}{\partial \boldsymbol{\chi}_\epsilon^{\star(j)}} \,. \tag{2.81}$$

The stress vector $\boldsymbol{\psi}^{\star}_{\sigma_{\text{plate}}}$ can be obtained from the plate energy:

$$\boldsymbol{\psi}_{\sigma}^{\star(i)} = \frac{\partial W}{\partial \boldsymbol{\chi}_{\epsilon}^{\star(i)}} \,. \tag{2.82}$$

Using Eq. (2.82) into (2.81) gives:

$$\boldsymbol{U}^{(ij)} = \frac{\partial W}{\partial \boldsymbol{\chi}_{\epsilon}^{\star(i)} \partial \boldsymbol{\chi}_{\epsilon}^{\star(j)}} \,, \tag{2.83}$$

thus ensuring the symmetry of $\boldsymbol{U}$.

Second, we can investigate the positive-definiteness of $\boldsymbol{U}$. It can be proved based on the plate energy once again. The plate energy, which is strictly positive, is defined as:

$$W = \frac{1}{2} \boldsymbol{\psi}^{\star T}_{\sigma_{\text{plate}}} \boldsymbol{\chi}^{\star}_{\epsilon} = \frac{1}{2} \boldsymbol{\chi}_{\epsilon}^{\star T} \boldsymbol{U} \boldsymbol{\chi}^{\star}_{\epsilon} \,, \tag{2.84}$$

thus ensuring the positive-definiteness of $\boldsymbol{U}$.

Besides the material uncertainties, the influence of the roughness is also studied. Rough SVEs are referred to as RSVEs. When both cases, rough or flat, are possible, the volume elements are referred to as (R)SVEs. The roughness influences the mechanical behaviour of the volume element, thus affecting $\boldsymbol{U}(\boldsymbol{x}, \boldsymbol{\theta})$. It also influences the distribution of mass over the macro-scale structure and thus another random field must be defined. Therefore the mass per membrane unit area random field $\bar{\rho}(\boldsymbol{x}, \boldsymbol{\theta}) : \mathcal{A} \times \boldsymbol{\Omega} \to \mathbb{R}^{+}$ is now introduced as it is commonly done for plate elements. Note that plate elements also involve the cross section inertia I_p. However the contribution to the mass matrix of this last term being much smaller than the contribution from $\bar{\rho}$ (the ratio between the two being of the order of h/l_{macro}, we actually approximate the uncertainty effect in I_p by approximating the term as $I_p = \frac{\bar{\rho}^3}{12\rho^2}$).

In order to evaluate the random fields, the point discretization method, see Section 2.2.1, is also considered for this third problem. At each integration point $\boldsymbol{x}_i$ of the plate finite elements, the correlated random fields are evaluated thus leading to the mass per membrane unit area $\bar{\rho}(\boldsymbol{x}_i, \boldsymbol{\theta})$ and the resultant material operator $\boldsymbol{U}(\boldsymbol{x}_i, \boldsymbol{\theta})$.

2.5.2 Formulation of the stochastic matrix through the problem definition

The second step is the formulation of the stochastic matrices which define the problem: the mass and the stiffness matrix. They must be defined from the governing equations which are, for a thin body $\boldsymbol{D}$, the equilibrium of forces and moments, respectively

$$\rho \ddot{\boldsymbol{u}} = \rho \boldsymbol{b} + \boldsymbol{\nabla} \cdot \boldsymbol{\sigma} \quad \text{in}\, \boldsymbol{D} \,, \text{ and} \tag{2.85}$$

$$\boldsymbol{\phi} \wedge \rho \ddot{\boldsymbol{u}} = \boldsymbol{\phi} \wedge \rho \boldsymbol{b} + \boldsymbol{\phi} \wedge \boldsymbol{\nabla} \cdot \boldsymbol{\sigma} \quad \text{in}\, \boldsymbol{D} \,, \tag{2.86}$$

where $\rho\boldsymbol{b}$ represents the external forces and $\boldsymbol{\phi}$ is the position mapping. The input values of this mapping are the Cosserat plane $\mathcal{A}$ coordinates of the thin body and the coordinate along the normalised thickness. The output of the mapping is the actual current configuration. The main idea behind plate elements is to avoid the discretization along the thickness direction by considering the thin body assumption. Therefore the governing equations for plates are obtained after integration of Eqs. (2.85) and (2.86) over the thickness, which results in the strong form of the Reissner-Mindlin plates, respectively

$$\bar{\rho}\ddot{\boldsymbol{u}} = \boldsymbol{n}^{*\,\alpha}_{,\alpha} + \bar{\boldsymbol{n}} \quad \text{in } \mathcal{A}, \text{ and} \tag{2.87}$$

$$I_p\ddot{\boldsymbol{t}} = \bar{\tilde{\boldsymbol{m}}} - (\boldsymbol{n}^{*\,z} - \lambda\boldsymbol{E}_z) + \tilde{\boldsymbol{m}}^{*\alpha}_{,\alpha} \quad \text{in } \mathcal{A}, \tag{2.88}$$

where I_p is the mass inertia per unit width, $\boldsymbol{t}$ is the direction of the membrane plane, λ is an undefined pressure applied along the thickness direction, $\bar{\boldsymbol{n}}$ and $\bar{\tilde{\boldsymbol{m}}}$ are respectively the resultant external surface traction per unit length and the resultant external torque per unit length.

As previously stated, the Kirchhoff-Love plate theory is considered. Furthermore, small deformations/rotations and plane-stress state are assumed. The Cosserat plane $\mathcal{A}$ of the plate can be divided into finite elements $\mathcal{A}^e$, such that $\mathcal{A} = \bigcup_e \mathcal{A}^e$. Under these assumptions, to derive the weak form corresponding to the set of Eqs. (2.87-2.88), the equations (2.87-2.88) are first multiplied by respectively $\delta\boldsymbol{u}$ and $-\delta\boldsymbol{u}_{z,\alpha}\boldsymbol{E}_\alpha$, are integrated on the sum of the elements $\mathcal{A}^e$, and the resulting virtual energies are added, leading to

$$\begin{aligned}\sum_e \int_{\mathcal{A}^e} \bar{\rho}\ddot{\boldsymbol{u}}_\alpha \delta\boldsymbol{u}_\alpha d\mathcal{A}^e + \sum_e \int_{\mathcal{A}^e} \bar{\rho}\ddot{\boldsymbol{u}}_z \delta\boldsymbol{u}_z d\mathcal{A}^e + \sum_e \int_{\mathcal{A}^e} I_p \ddot{\boldsymbol{u}}_{z,\alpha} \delta\boldsymbol{u}_{z,\alpha} d\mathcal{A}^e = \\ \sum_e \int_{\mathcal{A}^e} \tilde{\boldsymbol{n}}^{*\,\alpha\beta}_{,\alpha} \delta\boldsymbol{u}_\beta d\mathcal{A}^e - \sum_e \int_{\mathcal{A}^e} \left(\tilde{\boldsymbol{m}}^{*\,\alpha\beta}_{,\alpha} \delta\boldsymbol{u}_{z,\beta}\right) d\mathcal{A}^e + \\ \sum_e \int_{\mathcal{A}^e} \bar{\boldsymbol{n}}^\alpha \delta\boldsymbol{u}_\alpha d\mathcal{A}^e + \sum_e \int_{\mathcal{A}^e} \bar{\boldsymbol{n}}^z \delta\boldsymbol{u}_z d\mathcal{A}^e - \sum_e \int_{\mathcal{A}^e} \bar{\tilde{\boldsymbol{m}}}^\alpha \delta\boldsymbol{u}_{z,\alpha} d\mathcal{A}^e \,,\end{aligned} \tag{2.89}$$

where we have used the Kirchhoff-Love relation $\ddot{\boldsymbol{t}} = -\ddot{\boldsymbol{u}}_{z,\alpha}$. Isolating the virtual contributions in the Cosserat plane ($\delta\boldsymbol{u}_\alpha$) and along the out-of-plane direction ($\delta\boldsymbol{u}_z$), which can be done as the test functions are arbitrary, yields the system

$$\sum_e \int_{\mathcal{A}^e} \bar{\rho}\ddot{\boldsymbol{u}}_\alpha \delta\boldsymbol{u}_\alpha d\mathcal{A}^e \;=\; \sum_e \int_{\mathcal{A}^e} \tilde{\boldsymbol{n}}^{*\,\alpha\beta}_{,\alpha} \delta\boldsymbol{u}_\beta d\mathcal{A}^e + \sum_e \int_{\mathcal{A}^e} \bar{\boldsymbol{n}}^\alpha \delta\boldsymbol{u}_\alpha d\mathcal{A}^e \,, \tag{2.90}$$

$$\begin{aligned}\sum_e \int_{\mathcal{A}^e} \bar{\rho}\ddot{\boldsymbol{u}}_z \delta\boldsymbol{u}_z d\mathcal{A}^e + \sum_e \int_{\mathcal{A}^e} I_p \ddot{\boldsymbol{u}}_{z,\alpha} \delta\boldsymbol{u}_{z,\alpha} d\mathcal{A}^e = \\ -\sum_e \int_{\mathcal{A}^e} \left(\tilde{\boldsymbol{m}}^{*\,\alpha\beta}_{,\alpha} \delta\boldsymbol{u}_{z,\beta}\right) d\mathcal{A}^e + \sum_e \int_{\mathcal{A}^e} \bar{\boldsymbol{n}}^z \delta\boldsymbol{u}_z d\mathcal{A}^e - \sum_e \int_{\mathcal{A}^e} \bar{\tilde{\boldsymbol{m}}}^\alpha \delta\boldsymbol{u}_{z,\alpha} d\mathcal{A}^e \,.\end{aligned} \tag{2.91}$$

The final expression of the weak form is obtained by integrating by parts on each element $\mathcal{A}^e$ the resultant stress terms, and by applying the Gauss theorem [6]. Omitting the external forces contributions for conciseness, this results into

$$\sum_e \int_{\mathcal{A}^e} \bar{\rho}\ddot{\boldsymbol{u}}_\alpha \delta\boldsymbol{u}_\alpha d\mathcal{A}^e + \sum_e \int_{\mathcal{A}^e} \tilde{\boldsymbol{n}}^{*\,\alpha\beta}\delta\boldsymbol{u}_{\beta,\alpha} d\mathcal{A}^e = \sum_e \int_{\partial\mathcal{A}^e} \tilde{\boldsymbol{n}}^{*\,\alpha\beta}\delta\boldsymbol{u}_\beta \boldsymbol{\nu}_\alpha d\partial\mathcal{A}^e\,, \tag{2.92}$$

$$\sum_e \int_{\mathcal{A}^e} \bar{\rho}\ddot{\boldsymbol{u}}_z \delta\boldsymbol{u}_z d\mathcal{A}^e + \sum_e \int_{\mathcal{A}^e} I_p \ddot{\boldsymbol{u}}_{z,\alpha}\delta\boldsymbol{u}_{z,\alpha} d\mathcal{A}^e + \sum_e \int_{\mathcal{A}^e} \left(-\tilde{\boldsymbol{m}}^{*\,\alpha\beta}\delta\boldsymbol{u}_{z,\alpha\beta}\right) d\mathcal{A}^e$$
$$= \sum_e \int_{\partial\mathcal{A}^e} \left(-\tilde{\boldsymbol{m}}^{*\,\alpha\beta}\delta\boldsymbol{u}_{z,\beta}\right)\boldsymbol{\nu}_\alpha d\partial\mathcal{A}^e\,, \tag{2.93}$$

where $\boldsymbol{\nu}$ is the outward unit normal to the elements contour $\partial\mathcal{A}^e$ (in the Cosserat plane). In these expressions, we have kept the boundary contribution of each element. Indeed, those terms vanish in Eq. (2.92) by continuity of the kinematically admissible displacement $\delta\boldsymbol{u}_\beta$, but as the gradient $\delta\boldsymbol{u}_{z,\alpha}$ of the kinematically admissible displacement is not continuous across element interfaces, these terms have to be kept in the weak form (2.93).

By defining $(\partial_I\mathcal{A})^s$ an interface between two plate elements, $\langle\ \rangle$ the average operator obtained from the two values of the neighbouring elements and $[\![\ ]\!]$ the jump operator obtained from the two values of the neighbouring elements[9], we have the following relation

$$\sum_e \int_{\partial\mathcal{A}^e} \left(-\tilde{\boldsymbol{m}}^{*\,\alpha\beta}\delta\boldsymbol{u}_{z,\beta}\right)\boldsymbol{\nu}_\alpha d\partial\mathcal{A}^e = -\sum_s \int_{(\partial_I\mathcal{A})^s} [\![-\tilde{\boldsymbol{m}}^{*\,\alpha\beta}\delta\boldsymbol{u}_{z,\beta}\boldsymbol{\nu}_\alpha]\!] d\partial\mathcal{A}^e =$$
$$-\sum_s \int_{(\partial_I\mathcal{A})^s} \left\langle\tilde{\boldsymbol{m}}^{*\,\alpha\beta}\right\rangle [\![-\delta\boldsymbol{u}_{z,\beta}\boldsymbol{\nu}_\alpha]\!] d\partial\mathcal{A}^e - \sum_s \int_{(\partial_I\mathcal{A})^s} \left[\!\!\left[\tilde{\boldsymbol{m}}^{*\,\alpha\beta}\right]\!\!\right] \langle-\delta\boldsymbol{u}_{z,\beta}\boldsymbol{\nu}_\alpha\rangle d\partial\mathcal{A}^e\,, \tag{2.94}$$

as $[\![ab\boldsymbol{\nu}]\!] = [\![a\boldsymbol{\nu}]\!]\langle b\rangle + \langle a\rangle[\![b\boldsymbol{\nu}]\!]$, and where we have omitted the boundary terms for simplicity. However, the term in $\left[\!\!\left[\tilde{\boldsymbol{m}}^{*\,\alpha\beta}\right]\!\!\right]$ in Eq. (2.94) can be removed without losing the consistency of the method as the exact solution $\tilde{\boldsymbol{m}}^{*\,\alpha\beta}$ is continuous. In order to ensure the compatibility of the method, the continuity of $\boldsymbol{u}_{z,\alpha}$ accross the element interfaces is weakly enforced by considering, on the one hand a symmetrization term ensuring the symmetry of the stiffness matrix, and a stabilization term ensuring the stability of the method [95, 68]. The

---

[9] Considering two adjacent elements "+" and "-", the average operator of a field $\bullet$ is defined as $\langle\bullet\rangle = \frac{1}{2}\left(\bullet^+ + \bullet^-\right)$, and the jump operator of a field $\bullet$ as $[\![\bullet\boldsymbol{\nu}]\!] = \left(\bullet^+ - \bullet^-\right)\boldsymbol{\nu}^-$, where the superscript "±" refers to the field evaluated on element "±".

interface term of Eq. (2.94) is thus substituted as

$$
\begin{aligned}
\sum_e \int_{\partial\mathcal{A}^e} \left(-\tilde{\boldsymbol{m}}^{*\,\alpha\beta}\delta\boldsymbol{u}_{z,\beta}\right)\boldsymbol{\nu}_\alpha d\partial\mathcal{A}^e \to & -\sum_s \int_{(\partial_I\mathcal{A})^s} \left\langle \tilde{\boldsymbol{m}}^{*\,\alpha\beta}\right\rangle [\![-\delta\boldsymbol{u}_{z,\beta}\boldsymbol{\nu}_\alpha]\!]\, d\partial\mathcal{A}^e \\
& -\sum_s \int_{(\partial_I\mathcal{A})^s} \left\langle \delta\tilde{\boldsymbol{m}}^{*\,\alpha\beta}\right\rangle [\![-\boldsymbol{u}_{z,\beta}\boldsymbol{\nu}_\alpha]\!]\, d\partial\mathcal{A}^e \\
& -\sum_s \int_{(\partial_I\mathcal{A})^s} [\![-\boldsymbol{u}_{z,\beta}\boldsymbol{\nu}_\alpha]\!] \left\langle \frac{\beta_s}{h_s}\frac{\partial\delta\tilde{\boldsymbol{m}}^{*\,\alpha\beta}}{\partial\left(-\delta\boldsymbol{u}_{z,\gamma\delta}\right)}\right\rangle [\![-\delta\boldsymbol{u}_{z,\gamma}\boldsymbol{\nu}_\delta]\!]\, d\partial\mathcal{A}^e\,, \qquad (2.95)
\end{aligned}
$$

where β_s is the stabilisation parameter that has to be larger than a value depending on the polynomial approximation only, h_s is the mesh size, and where $\delta\tilde{\boldsymbol{m}}^{*\,\alpha\beta}$ is obtained from the constitutive relation (2.79).

Using this last substitution and the continuity in $\delta\boldsymbol{u}_\beta$, the weak form (2.92-2.93) results in a Continuous/Discontinuous Galerkin formulation of the plate equations similar to the ones developed in [95, 68][10], which reads

$$
\sum_e \int_{\mathcal{A}^e} \bar{\rho}\ddot{\boldsymbol{u}}_\alpha\delta\boldsymbol{u}_\alpha d\mathcal{A}^e \quad + \quad \sum_e \int_{\mathcal{A}^e} \tilde{\boldsymbol{n}}^{*\,\alpha\beta}\delta\boldsymbol{u}_{\beta,\alpha} d\mathcal{A}^e \qquad = \qquad 0\,, \qquad (2.96)
$$

$$
\begin{aligned}
&\sum_e \int_{\mathcal{A}^e} \bar{\rho}\ddot{\boldsymbol{u}}_z\delta\boldsymbol{u}_z d\mathcal{A}^e + \sum_e \int_{\mathcal{A}^e} I_p\ddot{\boldsymbol{u}}_{z,\alpha}\delta\boldsymbol{u}_{z,\alpha} d\mathcal{A}^e + \sum_e \int_{\mathcal{A}^e} \left(-\tilde{\boldsymbol{m}}^{*\,\alpha\beta}\delta\boldsymbol{u}_{z,\alpha\beta}\right) d\mathcal{A}^e + \\
&\sum_s \int_{(\partial_I\mathcal{A})^s} \left\langle \tilde{\boldsymbol{m}}^{*\,\alpha\beta}\right\rangle [\![-\delta\boldsymbol{u}_{z,\beta}\boldsymbol{\nu}_\alpha]\!]\, d\partial\mathcal{A}^e + \\
&\sum_s \int_{(\partial_I\mathcal{A})^s} \left\langle \mathbb{C}_3^{*\,\alpha\beta\gamma\delta}\delta\boldsymbol{\varepsilon}^*_{\gamma\delta} + \mathbb{C}_4^{*\,\alpha\beta\gamma\delta}\delta\boldsymbol{\kappa}^*_{\gamma\delta}\right\rangle [\![-\boldsymbol{u}_{z,\beta}\boldsymbol{\nu}_\alpha]\!]\, d\partial\mathcal{A}^e + \\
&\sum_s \int_{(\partial_I\mathcal{A})^s} [\![-\delta\boldsymbol{u}_{z,\beta}\boldsymbol{\nu}_\alpha]\!] \left\langle \frac{\beta_s}{h_s}\mathbb{C}_4^{*\,\alpha\beta\gamma\delta}\right\rangle [\![-\boldsymbol{u}_{z,\gamma}\boldsymbol{\nu}_\delta]\!]\, d\partial\mathcal{A}^e = 0\,, \qquad (2.97)
\end{aligned}
$$

In such a framework, the problem is formulated in terms of the sole displacement field $\boldsymbol{u}$ of the Cosserat plane. We refer to [95, 68, 6] for more details and the demonstration of the numerical properties.

Finally, the finite element discretization is obtained using the polynomial interpolation

$$
\boldsymbol{u} = \boldsymbol{N}_u\mathbf{u}\,, \qquad (2.98)
$$

where $\boldsymbol{N}_u$ is the shape function matrix and $\mathbf{u}$ are the nodal displacements of the Cosserat surface $\mathcal{A}$. The assembled mass and stiffness matrices can thus be computed, following Appendix C.1, resulting in the system of equations

$$
\boldsymbol{M}\left(\boldsymbol{\theta}\right)\ddot{\mathbf{u}} + \boldsymbol{K}\left(\boldsymbol{\theta}\right)\mathbf{u} = 0\,. \qquad (2.99)
$$

---

[10] Continuous as $\boldsymbol{u}_z$ is continuous and discontinuous as $\boldsymbol{u}_{z,\alpha}$ is such.

2.5.3 Response variability calculation

The third step of SFEM involves the response variability calculation. Toward this end, a Monte-Carlo simulation is used once more. If the input random field is known, the stochastic behaviour of the quantity of interest can be estimated. As already discussed, the finite element mesh size should be small enough with respect to the correlation length. Modelling each grain results in an expensive analysis. However, the recourse to multi-scale approach enables an important computational cost reduction so that Monte-Carlo simulations remain affordable. A meso-scale random field, which possesses a much bigger correlation length, is therefore defined and enables a computationally efficient approach.

2.6 Conclusion

Throughout this chapter, the SFEM approach was applied on different problems aiming at the uncertainty characterisation of macro-scale quantities of interest. Such approaches require random fields as input. The computational cost of the overall procedure can be reduced by considering random fields with a larger correlation length. This can be obtained owing to the recourse to stochastic homogenisation over an intermediate scale, the meso-scale. Assessing the stochastic behaviour of these meso-scale random fields is the focus of Chapter 3.

Chapter 3

Meso-scale material characterisation by computational homogenisation

To estimate the uncertainties of a structure, we investigated the recourse to SFEM methods in the previous chapter. SFEM requires a random field as input. The purpose of this chapter is to define those RF from stochastic homogenisation

3.1 General overview

Materials can possess complex micro-structures, sometimes tailored with a view towards improved strength, electrical permittivity, negative Poisson ratio, both a high stiffness and a high damping, ... When one wants to perform numerical analyses on a structure made of such a complex material, the micro-structure must be taken into account. In the frame of a finite element analysis, this implies meshing the details of the micro-structure over the whole structure which leads to overwhelming computations. The recourse to multi-scale approaches is an elegant way to compute the behaviour of the structure at a reasonable cost while accounting for the micro-structure.

Commonly, in multi-scale approaches, 3 scales are defined as shown in Fig. 3.1: l_{micro} is the size of the microscopic heterogeneities, l_{macro} represents the size of the whole structure, and l_{meso} is an intermediate size. The whole structure is modelled without its microscopic heterogeneities and a finite element analysis can be applied. At each point of interest, the deformation state (or the stress state in stress-driven procedure) can be downscaled to a new problem involving the micro-structure. The stress state (the deformation state) corresponding to the meso-scale volume, computed with an homogenisation procedure, can then

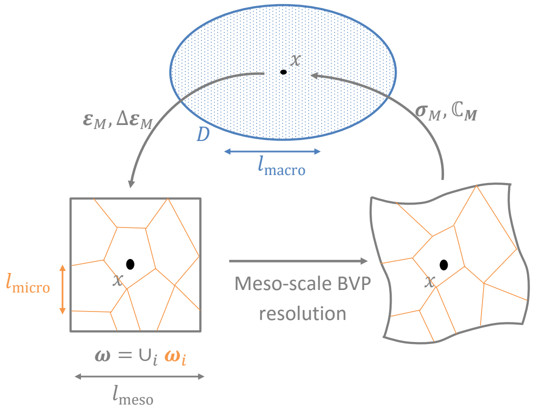

Figure 3.1: The multi-scale procedure. At each macro-scale point of interest, the deformation state is down-scaled to a meso-scale boundary value problem whose resolution brings the stress state which thus can be up-scaled.

be up-scaled to the finite element analysis at the scale of the structure and the analysis can continue. This corresponds to a multi-scale analysis performed with a concurrent[1] approach. In a sequential approach, the homogenisation procedures involving the micro-structure are performed *a priori* and only the up-scaling is required.

Consistent results are only obtained when energetically consistent boundary conditions are applied over the meso-scale volume element. This ensures that the deformation energy at the macro-scale corresponds to the deformation energy at the micro-scale. Another important requirement is the scale separation which can be written as:

$$l_{\text{micro}} << l_{\text{meso}} << l_{\text{macro}} \,. \tag{3.1}$$

The meso-scale should be much bigger than the micro-scale so that the meso-scale volume element is representative. Therefore it does not depend on the boundary condition applied over it neither on the volume element ω itself. The volume element ω is then said representative. The macro-scale should be much bigger than the meso-scale so that accurate results can be computed. In this work this first condition will be relaxed, thus introducing uncertainties.

The main procedure to consider in such a multi-scale analysis is the homogenisation step. It can be done in many ways and some of them will be briefly recalled in the following. Reviews concerning the multi-scale approaches can be found in [22, 40, 51].

When the micro-structure consists of many repetitive unit cells so that the structure can be considered periodic, the asymptotic homogenisation can be

---

[1] some authors call concurrent multi-scale, non-homogenisation-based multi-scale approaches such as domain decomposition

used. Although this method is mainly used for linear two-scales problems, its extension to non-linear problems and to several scales analysis is possible. A review of the method can be found in [38] and a rigorous formulation of the problem can be found in [7]. Briefly, the method consists in expanding the variables of the problem, whose perturbation field is assumed periodical, with respect to ϵ, a small dimensionless parameter representing the length scale separation. A decomposition of the field is done based on this latter parameter. The periodicity of the perturbation fields is assumed. Using partial derivatives with respect to the stretch coordinate representing the micro-structure, and splitting the equations based on their order with respect to ϵ, a numerical procedure can be settled and homogenised properties can be obtained.

Semi-analytical approaches are efficient methods as they provide homogenised properties at a low computational cost. To model multi-phase composites, a commonly used method is the mean-field homogenisation (MFH). The basic idea behind the MFH method is that the local micro strain can be linked to the macroscopic strain through a concentration tensor. The concentration tensor relates the relative average strains between the phases. Therefore, in deformation driven macro-scale procedures, the homogenised stress is the average of the local stress which can be related to the macroscopic strain with the concentration tensor. The definition of the concentration tensor can be done in many different ways. When the volume fraction of inclusions is low, the interaction between inclusions can be neglected and each inclusion can be considered as single inclusion in an infinite matrix (extension of the solution of Eshelby [18]). Considering the interaction between inclusions can be done based on the Mori-Tanaka model [62] (one inclusion is interacting with a homogeneous medium undergoing the matrix deformation) or the self-consistent scheme [31] (one inclusion is embedded in a fictitious matrix possessing the homogenised material stiffness which is sought). In the non-linear case, the behaviour of the constituents are linearised at particular strain states.

Other semi-analytical methods exist, such as the TFA (transformation field analysis) approach [17] or the generalised methods of cells [1] but their description falls outside the scope of this work as we will consider a numerical approach for the homogenisation process.

Computational homogenisation methods are expensive methods but they can provide solutions for more general geometries and constitutive behaviours. The basic idea behind computational homogenisation is the following: at each integration point of the macro-scale procedure, the macro-scale constitutive behaviour is obtained through a meso-scale boundary value problem resolution over a representative volume element ω. Therefore a finite element problem has to be solved at each integration point of the macro scale procedure and as it has to be done iteratively in the non-linear range, the method is computationally expensive. Interested readers are referred to [19, 43, 59] for a non-exhaustive list of references. A review of the method can be found in [22]. The first-order and second-order homogenisation methods are described throughout this chapter.

In computational homogenisation, the meshing procedure required when dealing with complex micro-structures can be difficult. An alternative method

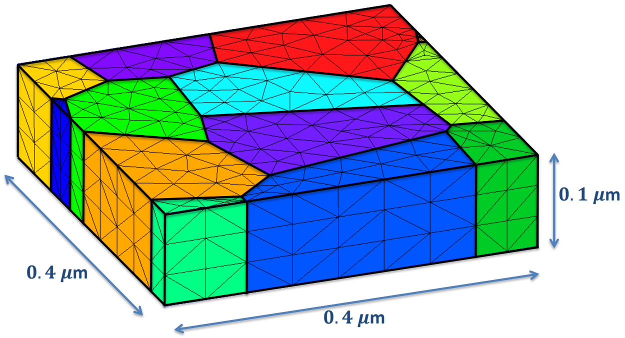

Figure 3.2: A sample of the meso-scale volume element ω. One colour is associated to each grain.

exists which allows the user to directly use images of the micro-structure, thus avoiding the meshing procedure as the RVE is discretised based on data sampled from a regular grid. This method is based on Fast Fourier Transform and is introduced in [64].

3.2 First-order computational homogenisation theory

Based on SVE samples, we are now extracting the meso-scale random field $\boldsymbol{C}_{\mathrm{M}}(x, \boldsymbol{\theta})$ which is used as input of the SFEM defined in Chapter 2.

3.2.1 Generalities on Representative and Statistical Volume Elements

The aim of this section is to define the scale transition from the micro-scale up to an intermediate scale: the meso-scale, see Fig. 1.2. As this work focuses on polycrystalline materials, the micro-scale is characterised by the grain distribution. The grain size is assumed to be large enough (> 100 nm) so that grain boundary (of nm size) mechanics can be neglected. A meso-scale volume element ω is depicted in Fig. 3.2. At first, only flat SVEs are considered (the roughness is not taken into account).

Within a multi-scale framework, one can define macro-scale values as the volume average of a micro-scale field on the meso-scale volume-element ω, following

$$a_{\mathrm{M}} = < a_{\mathrm{m}} > = \frac{1}{V(\omega)} \int_{\omega} a_{\mathrm{m}} dV \,, \tag{3.2}$$

where the subscript m refers to the micro-scale, the subscript M refers to the homogenised value, $\langle \bullet \rangle$ is the volume average, and $V(\omega)$ is the volume of the meso-scale volume element ω. In particular, the macro-stress tensor $\boldsymbol{\sigma}_{\mathrm{M}}$ and the macro-strain tensor $\boldsymbol{\varepsilon}_{\mathrm{M}}$ are defined as

$$\begin{aligned} \boldsymbol{\sigma}_{\mathrm{M}} &= \langle \boldsymbol{\sigma}_{\mathrm{m}} \rangle = \frac{1}{V(\omega)} \int_{\omega} \boldsymbol{\sigma}_{\mathrm{m}} dV \,, \qquad (3.3) \\ \boldsymbol{\varepsilon}_{\mathrm{M}} &= \langle \boldsymbol{\varepsilon}_{\mathrm{m}} \rangle = \frac{1}{V(\omega)} \int_{\omega} \boldsymbol{\varepsilon}_{\mathrm{m}} dV \,. \qquad (3.4) \end{aligned}$$

First of all, for the separation of scales to be valid, the volume element ω should be small enough compared to the wavelength of the deformation mode so that the time for the strain wave to propagate in the SVE remains negligible. Therefore the equivalence of the micro and macro-strain is instantaneous. This allows writing the equilibrium equation in the absence of external forces:

$$\boldsymbol{\nabla}_{\mathrm{m}} \cdot \boldsymbol{\sigma}_{\mathrm{m}} = \mathbf{0} \,. \qquad (3.5)$$

In the elastic regime, the micro-stress tensor is related to the micro-strain tensor through the material fourth-order tensor $\mathbb{C}_{\mathrm{m}}$ with

$$\boldsymbol{\sigma}_{\mathrm{m}} = \mathbb{C}_{\mathrm{m}} : \boldsymbol{\varepsilon}_{\mathrm{m}} \,. \qquad (3.6)$$

When performing the homogenisation, the relative size of the meso-scale volume element with respect to the micro-structure size is of prime importance. If the volume-element on which the averaging is performed is large enough, it is called Representative Volume Element (RVE). To be considered as an RVE, the volume-element should be statistically representative so that it is *entirely typical of the whole mixture on average* [30]. Moreover the volume element is representative when the effective constitutive response is independent with respect to the energetically consistent boundary conditions, as it will be discussed later.

Assuming ω is an RVE, a unique effective material tensor $\mathbb{C}_{\mathrm{M}}^{\mathrm{eff}}$ can be defined such that

$$\boldsymbol{\sigma}_{\mathrm{M}} = \mathbb{C}_{\mathrm{M}}^{\mathrm{eff}} : \boldsymbol{\varepsilon}_{\mathrm{M}} \,, \qquad (3.7)$$

for any RVE ω [35]. Defining as a'_{m} the perturbation of the micro-scale field a_{m} around its average value $\langle a_{\mathrm{m}} \rangle$, and combining Eqs. (3.3-3.7) lead to

$$\begin{aligned} \mathbb{C}_{\mathrm{M}}^{\mathrm{eff}} : \boldsymbol{\varepsilon}_{\mathrm{M}} = \boldsymbol{\sigma}_{\mathrm{M}} = \frac{1}{V(\omega)} \int_{\omega} \left(\langle \mathbb{C}_{\mathrm{m}} \rangle + \mathbb{C}'_{\mathrm{m}} \right) : \left(\langle \boldsymbol{\varepsilon}_{\mathrm{m}} \rangle + \boldsymbol{\varepsilon}'_{\mathrm{m}} \right) dV = \\ \langle \mathbb{C}_{\mathrm{m}} \rangle : \boldsymbol{\varepsilon}_{\mathrm{M}} + \langle \mathbb{C}'_{\mathrm{m}} : \boldsymbol{\varepsilon}'_{\mathrm{m}} \rangle \,, \qquad (3.8) \end{aligned}$$

which shows that the effective material tensor is not equal to $\langle \mathbb{C}_{\mathrm{m}} \rangle$, the meso-scale volume average of the micro-scale material tensor. This last expression corresponds to the Voigt upper bound $\bar{\mathbb{C}}_{\mathrm{M}}$ of the effective material tensor. In all generalities, an upper (lower) bound $\mathbb{C}_{\mathrm{U}}$ ($\mathbb{C}_{\mathrm{L}}$) of the tensor $\mathbb{C}$ is defined such that $\boldsymbol{\varepsilon} : (\mathbb{C}_{\mathrm{U}} - \mathbb{C}) : \boldsymbol{\varepsilon} \geqslant 0$ ($\boldsymbol{\varepsilon} : (\mathbb{C} - \mathbb{C}_{\mathrm{L}}) : \boldsymbol{\varepsilon} \geqslant 0$) for any non-zero deformation tensor $\boldsymbol{\varepsilon}$, and we use the notation $\mathbb{C}_{\mathrm{U}} \geqslant \mathbb{C} \geqslant \mathbb{C}_{\mathrm{L}}$. Applying the same relations by considering the compliance tensor $\mathbb{S}$ leads to a similar conclusion: the effective compliance tensor $\mathbb{S}_{\mathrm{M}}^{\mathrm{eff}}$ such that

$$\boldsymbol{\varepsilon}_{\mathrm{M}} = \mathbb{S}_{\mathrm{M}}^{\mathrm{eff}} : \boldsymbol{\sigma}_{\mathrm{M}} \,, \tag{3.9}$$

is different from $\langle \mathbb{S}_{\mathrm{m}} \rangle$, the meso-scale volume average of the micro-scale compliance tensor. The inverse of this last expression corresponds to the Reuss lower bound $\underline{\mathbb{C}}_{\mathrm{M}}$ of the effective material tensor.

To be energetically consistent, the effective tensor $\mathbb{C}_{\mathrm{M}}^{\mathrm{eff}}$ should satisfy the Hill-Mandel principle, which implies the equality of the internal energy at both scales, *i.e.*

$$\boldsymbol{\sigma}_{\mathrm{M}} : \boldsymbol{\varepsilon}_{\mathrm{M}} = \frac{1}{V(\omega)} \int_{\omega} \boldsymbol{\sigma}_{\mathrm{m}} : \boldsymbol{\varepsilon}_{\mathrm{m}} dV \,. \tag{3.10}$$

Using Eqs. (3.3-3.7), this equation reduces to

$$\begin{aligned} \boldsymbol{\varepsilon}_{\mathrm{M}} : \mathbb{C}_{\mathrm{M}}^{\mathrm{eff}} : \boldsymbol{\varepsilon}_{\mathrm{M}} = \frac{1}{V(\omega)} \int_{\omega} \boldsymbol{\sigma}_{\mathrm{m}} : \boldsymbol{\varepsilon}_{\mathrm{m}} dV = \\ \frac{1}{V(\omega)} \int_{\omega} \left(\langle \boldsymbol{\sigma}_{\mathrm{m}} \rangle + \boldsymbol{\sigma}'_{\mathrm{m}} \right) : \left(\langle \boldsymbol{\varepsilon}_{\mathrm{m}} \rangle + \boldsymbol{\varepsilon}'_{\mathrm{m}} \right) dV = \boldsymbol{\varepsilon}_{\mathrm{M}} : \mathbb{C}_{\mathrm{M}}^{\mathrm{eff}} : \boldsymbol{\varepsilon}_{\mathrm{M}} + \langle \boldsymbol{\sigma}'_{\mathrm{m}} : \boldsymbol{\varepsilon}'_{\mathrm{m}} \rangle \,. \end{aligned} \tag{3.11}$$

Therefore the resolution of the meso-scale boundary value problem should satisfy

$$\int_{\omega} \boldsymbol{\sigma}'_{\mathrm{m}} : \boldsymbol{\varepsilon}'_{\mathrm{m}} dV = 0 \,. \tag{3.12}$$

This condition is satisfied for the Voigt and Reuss assumptions, which respectively state a constant strain field, *i.e.* $\boldsymbol{\varepsilon}'_{\mathrm{m}} = 0$, and a constant stress field, *i.e.* $\boldsymbol{\sigma}'_{\mathrm{m}} = 0$, which lead to the upper and lower bounds of the effective tensor, respectively.

The displacement at micro-scale $\boldsymbol{u}_{\mathrm{m}}$ can be decomposed into an $\boldsymbol{\varepsilon}_{\mathrm{M}} \cdot \boldsymbol{x}$ and into a fluctuation field $\boldsymbol{u}'_{\mathrm{m}}$:

$$\boldsymbol{u}_{\mathrm{m}} = \boldsymbol{\varepsilon}_{\mathrm{M}} \cdot \boldsymbol{x} + \boldsymbol{u}'_{\mathrm{m}} \,, \tag{3.13}$$

$\boldsymbol{x}$ being the position vector.

Following the Gauss theorem and the equilibrium equation (3.5), the Hill-Mandel condition (3.10) can be written as [43, 59, 66]:

$$\begin{aligned} \boldsymbol{\sigma}_{\mathrm{M}} : \boldsymbol{\varepsilon}_{\mathrm{M}} &= \frac{1}{V(\omega)} \int_{\omega} \boldsymbol{\sigma}_{\mathrm{m}} : \boldsymbol{\varepsilon}_{\mathrm{M}} dV + \frac{1}{V(\omega)} \int_{\omega} \boldsymbol{\sigma}_{\mathrm{m}} : \boldsymbol{\nabla}_{\mathrm{m}} \boldsymbol{u}'_{\mathrm{m}} dV \,, & (3.14) \\ &= \frac{1}{V(\omega)} \int_{\omega} \boldsymbol{\sigma}_{\mathrm{m}} dV : \boldsymbol{\varepsilon}_{\mathrm{M}} + \frac{1}{V(\omega)} \int_{\omega} \left(\boldsymbol{\sigma}_{\mathrm{m}} \cdot \boldsymbol{n}_{\mathrm{m}} \right) \cdot \boldsymbol{u}'_{\mathrm{m}} dV \,, & (3.15) \end{aligned}$$

or again,

$$\int_{\partial\omega} \boldsymbol{t}_{\mathrm{m}} \cdot \boldsymbol{u}'_{\mathrm{m}} dS = 0 \,, \tag{3.16}$$

where $\partial\omega$ is the boundary of the meso-scale volume ω, S is its surface, $\boldsymbol{t}_{\mathrm{m}} = \boldsymbol{\sigma}_{\mathrm{m}} \cdot \boldsymbol{n}_{\mathrm{m}}$ is the surface traction, and $\boldsymbol{n}_{\mathrm{m}}$ is its outward unit normal.

In order to estimate the effective material tensor $\mathbb{C}_{\mathrm{M}}^{\mathrm{eff}}$ from the resolution of the meso-scale BVP, boundary conditions should be applied on the RVE ω. These boundary conditions should satisfy the Hill-Mandel condition (3.16) so that the scale transition is energetically consistent.

The four main BCs satisfying this equation are

- The Kinematic Uniform Boundary Conditions (KUBCs) for which there is no fluctuation on the boundary, *i.e.*
$$\boldsymbol{u}'_{\mathrm{m}} = 0 \text{ on } \partial\omega\,; \tag{3.17}$$
- The Static Uniform Boundary Conditions (SUBCs) for which $\boldsymbol{t}_{\mathrm{m}} = \boldsymbol{\sigma}_{\mathrm{M}} \cdot \boldsymbol{n}_{\mathrm{m}}$ on $\partial\omega$; In the case of parallelepiped RVEs for which the boundary can be separated in opposite faces $\partial\omega^-$ and $\partial\omega^+$, this also corresponds to the minimal kinematic boundary conditions (*i.e.* zero average fluctuation field) [59], *i.e.*
$$\int_{\partial\omega^\pm} \left(\boldsymbol{u}'_{\mathrm{m}} \otimes \boldsymbol{n}_{\mathrm{m}}\right) dS = 0\,; \tag{3.18}$$
- The Orthogonal Uniform Mixed Boundary Conditions (OUMBCs), for which a combination of constrained displacements in one direction and surface tractions in the other directions is used[2];
- The Periodic Boundary Conditions (PBCs) for which one has on the opposite faces
$$\boldsymbol{u}'_{\mathrm{m}}\left(\boldsymbol{x}^+\right) = \boldsymbol{u}'_{\mathrm{m}}\left(\boldsymbol{x}^-\right) \forall \boldsymbol{x}^+ \in \partial\omega^+ \text{ and corresponding } \boldsymbol{x}^- \in \partial\omega^-\,, \tag{3.19}$$
$$\boldsymbol{t}'_{\mathrm{m}}\left(\boldsymbol{x}^+\right) = -\boldsymbol{t}'_{\mathrm{m}}\left(\boldsymbol{x}^-\right) \forall \boldsymbol{x}^+ \in \partial\omega^+ \text{ and corresponding } \boldsymbol{x}^- \in \partial\omega^-\,, \tag{3.20}$$
  with $\int_{\partial\omega^\pm} \boldsymbol{u}'_{\mathrm{m}} dS = 0$ to remove the rigid mode motion. An alternative to this last constraint to impose a macro-scale deformation, is to directly constrain the corner nodes by $\boldsymbol{u}_{\mathrm{m}} = \boldsymbol{\varepsilon}_{\mathrm{M}} \cdot \boldsymbol{x}$.

As previously stated, if the meso-scale volume-element ω on which the averaging is performed is large enough, the so-called RVE is statistically representative and a unique material tensor $\mathbb{C}_{\mathrm{M}}^{\mathrm{eff}}$ can be obtained for these different "energetically consistent" boundary conditions. If the volume element is not large

---

[2] Although not true for general MBCs, particular MBCs such as the orthogonal uniform ones can be defined in a particular way as to satisfy the Hill-Mandel condition (3.16), see the discussion in [29]. Assuming a rectangular parallelepiped RVE, on every face we constrain along one direction –says x– the displacements to $u_{\mathrm{m}x} = \sum_{i=x}^{z} \varepsilon_{\mathrm{M}xi} x_i$, so that $u'_{\mathrm{m}x} = 0$, and along the two other directions $t_{\mathrm{m}j} = \sum_{k=x}^{z} \sigma_{\mathrm{M}jk} n_{\mathrm{m}k}$, $j = y$, z. As a result, since $u'_{\mathrm{m}x} = 0$, the Hill-Mandel Eq. (3.16) is rewritten $\sum_{j=y}^{z} \sum_{k=x}^{z} \sigma_{\mathrm{M}jk} \int_{\partial\omega^\pm} n_{\mathrm{m}k} \boldsymbol{u}'_{\mathrm{m}j} dS$, which vanishes by constraining $\int_{\partial\omega^\pm} n_{\mathrm{m}k} \boldsymbol{u}'_{\mathrm{m}j} dS = 0$ for $j = y$, z and $k = x$, y, z.

enough the homogenisation provides an apparent material tensor $\mathbb{C}_{\mathrm{M}}$, which depends on the applied boundary conditions, but also on the particular realisation of the micro-structure considered. In this case, the meso-scale volume-element ω is called Statistical Volume Element (SVE) [71].

Therefore the material tensors obtained using SVEs face two sources of uncertainties: one contribution resulting from the applied boundary conditions and the other one from the uncertainties in the material micro-structure. However as it will be seen in Section 5.2.1, the uncertainties resulting from the micro-structure randomness, the grain distribution and orientation, is more important than the ones resulting from the applied BCs in the case of the studied poly-crystalline material.

In the next section we discuss how this apparent material tensor $\mathbb{C}_{\mathrm{M}}$ is computed in the computational homogenisation framework before detailing the process to generate the different SVEs.

3.2.2 Evaluation of the apparent meso-scale material tensor

Computing the apparent meso-scale material tensor from the finite element resolution of a meso-scale volume-element ω can be done in different ways. In [26] and [69], it was achieved with the help of a minimisation procedure and Huet's partition theorem [35]. It can also be estimated directly from the stiffness matrix of the FE model following the developments in [43, 59]. This last method is adopted herein. Based on the equilibrium equation (3.5), the static linear system $\boldsymbol{K}\mathbf{u} = \boldsymbol{f}$ can be constructed.

In the absence of body forces, the macro-stress tensor (3.3) can be rewritten with the Gauss theorem as

$$\boldsymbol{\sigma}_{\mathrm{M}} = \frac{1}{V(\omega)} \int_{\partial\omega} \boldsymbol{t}_{\mathrm{m}} \otimes \boldsymbol{x} dS \,. \tag{3.21}$$

When considering a finite element discretization of the SVE and when applying one of the energetically consistent boundary conditions (3.17-3.19), there are N_{nd} nodes with prescribed displacements on the boundary $\partial\omega$, N_{nd} depending on the type of boundary conditions. Let $\boldsymbol{x}^p$ be the position vector of these nodes. The discretised form of Eq. (3.21) thus reads

$$\boldsymbol{\sigma}_{\mathrm{M}} = \frac{1}{V(\omega)} \sum_{p=1}^{N_{\mathrm{nd}}} \boldsymbol{f}^p \otimes \boldsymbol{x}^p \,, \tag{3.22}$$

where $\boldsymbol{f}^p$ corresponds to the resulting external nodal forces at the prescribed nodes. In linear elasticity, the equilibrium between external and internal forces can be written as

$$\sum_{q=1}^{N_{\mathrm{nd}}} \boldsymbol{K}^{pq} \cdot \mathbf{u}^q = \boldsymbol{f}^p \,, \tag{3.23}$$

where p and q correspond to the different N_{nd} prescribed nodes, and where $\boldsymbol{K}_{\text{M}}^{pq}$ is the stiffness tensor at nodes p and q obtained following the condensation of the internal nodes [43]. The general process for arbitrary BCs is given for thermo-mechanical problems in Section 3.3.3. Here we assume a direct relation between the constraint nodes and $\boldsymbol{\varepsilon}_{\text{M}}$ ($\mathbf{u}^q = \boldsymbol{\varepsilon}_{\text{M}} \cdot \boldsymbol{x}^q$) as for KUBCs, and substituting Eq. (3.23) in Eq. (3.22) results in

$$\boldsymbol{\sigma}_{\text{M}} = \frac{1}{V(\omega)} \sum_{p=1}^{N_{\text{nd}}} \sum_{q=1}^{N_{\text{nd}}} \left(\boldsymbol{K}^{pq} \cdot \mathbf{u}^q\right) \otimes \boldsymbol{x}^p \,, \tag{3.24}$$

or again, according to the definition of the deformation tensor

$$\boldsymbol{\sigma}_{\text{M}} = \frac{1}{V(\omega)} \sum_{p=1}^{N_{\text{nd}}} \sum_{q=1}^{N_{\text{nd}}} \left(\boldsymbol{x}^p \otimes \boldsymbol{K}^{pq} \otimes \boldsymbol{x}^q\right) : \boldsymbol{\varepsilon}_{\text{M}} \,. \tag{3.25}$$

The apparent elasticity tensor $\mathbb{C}_{\text{M}}$ is then directly obtained as

$$\mathbb{C}_{\text{M}} = \frac{1}{V(\omega)} \sum_{p=1}^{N_{\text{nd}}} \sum_{q=1}^{N_{\text{nd}}} \boldsymbol{x}^p \otimes \boldsymbol{K}^{pq} \otimes \boldsymbol{x}^q \,. \tag{3.26}$$

As already introduced before, with a view to the generation of the material tensor random field, the fourth-order symmetric elasticity tensor $\mathbb{C}_{\text{M}}$ is represented using the Voigt or Kelvin notation. Out of the 81 components of the tensor $\mathbb{C}_{\text{M}}$, only 21 components are enough to fully characterised the elastic operator, which can be represented by a 6×6 symmetric elasticity matrix $\boldsymbol{C}_{\text{M}}$.

3.3 Extension to thermo-elasticity

The apparent –or homogenised– meso-scale material tensors in the thermo-elastic case can be estimated once again from the finite element resolution of a meso-scale boundary value problem. The problem of thermo-elasticity was formulated and discussed in [72, 91]. In the following we rewrite the thermo-elasticity scale transition equations, with a particular emphasis on the extraction of the material operators of the homogenised thermo-elastic properties using the multiple-constraint projection method described in [2].

3.3.1 Definition of scales transition

The homogenisation of thermo-elastic problems is summarised hereafter. First of all, in the homogenisation process of the thermo-mechanical problem, the two requirements which state the separation of the macro- and meso-scales and the thermal steady-state in the SVE read:

1. The SVE ω should be small enough for the time of the strain wave to propagate in the SVE to remain negligible, so that the equivalence of the

micro-strain to the macro-strain is instantaneous. This assumption allows writing

$$\boldsymbol{\nabla}_{\mathrm{m}} \cdot \boldsymbol{\sigma}_{\mathrm{m}} = \mathbf{0} \quad \text{in } \omega\,. \tag{3.27}$$

2. The SVE should be small enough for the time variation of heat storage to remain negligible. This assumption corresponds to the thermal steady-state of micro-scale, which is expressed as

$$\boldsymbol{\nabla}_{\mathrm{m}} \cdot \boldsymbol{q}_{\mathrm{m}} = 0 \quad \text{in } \omega\,. \tag{3.28}$$

In the application Chapter 5, we will verfiy that these steady state assumptions hold.

These two scale-separation requirements hold in the vibration problem of micro resonator as the SVEs are by definition of reduced sizes. Therefore, the finite element formulation of the meso-scale BVP is similar to Eq. (2.52), but stated in a steady state, and reads

$$\begin{bmatrix} \boldsymbol{K}_{uu} & \boldsymbol{K}_{u\vartheta} \\ \mathbf{0} & \boldsymbol{K}_{\vartheta\vartheta} \end{bmatrix} \begin{bmatrix} \mathbf{u} \\ \boldsymbol{\vartheta} \end{bmatrix} = \begin{bmatrix} \boldsymbol{f}_u \\ \boldsymbol{f}_\vartheta \end{bmatrix}\,. \tag{3.29}$$

Within a multi-scale framework, macro-scale values can be defined as the volume average of a micro-scale field on the meso-scale volume-element ω, following Eq. (3.2). The following homogenised values on the SVE need to be consistent with their micro values:

- The mass density:

$$\rho_{\mathrm{M}} = < \rho_{\mathrm{m}} > \,. \tag{3.30}$$

- The heat capacity at constant volume C_v, which has to satisfy the consistency of heat capacity at the different scales:

$$\rho_{\mathrm{M}} C_{v\mathrm{M}} = < \rho_{\mathrm{m}} C_{v\mathrm{m}} > \quad \text{and} \quad C_{v\mathrm{M}} = \frac{< \rho_{\mathrm{m}} C_{v\mathrm{m}} >}{< \rho_{\mathrm{m}} >}\,. \tag{3.31}$$

- The stress and strain tensors:

$$\begin{aligned} \boldsymbol{\sigma}_{\mathrm{M}} &= < \boldsymbol{\sigma}_{\mathrm{m}} > = < \mathbb{C}_{\mathrm{m}} : \boldsymbol{\varepsilon}_{\mathrm{m}} - \mathbb{C}_{\mathrm{m}} : \boldsymbol{\alpha}_{\mathrm{m}} \vartheta_{\mathrm{m}} > \\ &= \mathbb{C}_{\mathrm{M}} : \boldsymbol{\varepsilon}_{\mathrm{M}} - \mathbb{C}_{\mathrm{M}} : \boldsymbol{\alpha}_{\mathrm{M}} \vartheta_{\mathrm{M}}\,, \end{aligned} \tag{3.32}$$

  and

$$\boldsymbol{\varepsilon}_{\mathrm{M}} = \left(\frac{\boldsymbol{\nabla}_{\mathrm{M}} \otimes \boldsymbol{u}_{\mathrm{M}} + \left(\boldsymbol{\nabla}_{\mathrm{M}} \otimes \boldsymbol{u}_{\mathrm{M}}\right)^T}{2} \right) = < \boldsymbol{\varepsilon}_{\mathrm{m}} > \,. \tag{3.33}$$

- The heat flux and temperature gradient:

$$\boldsymbol{q}_{\mathrm{M}} = < \boldsymbol{q}_{\mathrm{m}} >\,, \tag{3.34}$$

  and

$$\boldsymbol{\nabla}_{\mathrm{M}} \vartheta_{\mathrm{M}} = < \boldsymbol{\nabla}_{\mathrm{m}} \vartheta_{\mathrm{m}} > \,. \tag{3.35}$$

According to the scale consistent conditions of stress (3.32) and heat flux (3.34), and using equilibrium equations (3.27) and (3.28) the macro-stress and heat flux can be written as

$$\boldsymbol{\sigma}_{\mathrm{M}} = \frac{1}{V(\omega)} \int_{\partial\omega} (\boldsymbol{\sigma}_{\mathrm{m}} \cdot \boldsymbol{n}_{\mathrm{m}}) \otimes \boldsymbol{x} dS \,, \tag{3.36}$$

and

$$\boldsymbol{q}_{\mathrm{M}} = \frac{1}{V(\omega)} \int_{\partial\omega} (\boldsymbol{q}_{\mathrm{m}} \cdot \boldsymbol{n}_{\mathrm{m}}) \otimes \boldsymbol{x} dS \,, \tag{3.37}$$

where $\boldsymbol{n}_{\mathrm{m}}$ is the normal of the boundary $\partial\omega$.

In order to respect the energy consistency at the different scales, the following conditions have also to be respected:

- The consistency of deformation energy at the different scales:

$$\begin{aligned} \boldsymbol{\sigma}_{\mathrm{M}} : \delta\boldsymbol{\varepsilon}_{\mathrm{M}} &= \delta\boldsymbol{\varepsilon}_{\mathrm{M}} : \mathbb{C}_{\mathrm{M}} : \boldsymbol{\varepsilon}_{\mathrm{M}} - \delta\boldsymbol{\varepsilon}_{\mathrm{M}} : \mathbb{C}_{\mathrm{M}} : \boldsymbol{\alpha}_{\mathrm{M}} \vartheta_{\mathrm{M}} \\ &= < \delta\boldsymbol{\varepsilon}_{\mathrm{m}} : \mathbb{C}_{\mathrm{m}} : \boldsymbol{\varepsilon}_{\mathrm{m}} - \delta\boldsymbol{\varepsilon}_{\mathrm{m}} \mathbb{C}_{\mathrm{m}} : \boldsymbol{\alpha}_{\mathrm{m}} \vartheta_{\mathrm{m}} > \,, \end{aligned} \tag{3.38}$$

  for any temperature ϑ_{M} or deformation field $\boldsymbol{\varepsilon}_{\mathrm{M}}$.

- The consistency of entropy change at the different scales is obtained for infinitesimal temperature changes[3]

$$\boldsymbol{q}_{\mathrm{M}} \cdot \boldsymbol{\nabla}_{\mathrm{M}} \delta\vartheta_{\mathrm{M}} =< \boldsymbol{q}_{\mathrm{m}} \cdot \boldsymbol{\nabla}_{\mathrm{m}} \delta\vartheta_{\mathrm{m}} > \,. \tag{3.39}$$

- The consistency of heat storage at the micro- and macro-scales:

$$\rho_{\mathrm{M}} C_{v\mathrm{M}} \vartheta_{\mathrm{M}} =< \rho_{\mathrm{m}} C_{v\mathrm{m}} \vartheta_{\mathrm{m}} > \,. \tag{3.40}$$

Considering a first order homogenisation process, the micro-scale fields are defined as

$$\begin{aligned} \boldsymbol{u}_{\mathrm{m}}(\boldsymbol{x}) &= (\boldsymbol{u}_{\mathrm{M}} \otimes \boldsymbol{\nabla}_{\mathrm{M}}) \cdot \boldsymbol{x} + \boldsymbol{u}'_{\mathrm{m}}(\boldsymbol{x}) \,, & (3.41) \\ \vartheta_{\mathrm{m}}(\boldsymbol{x}) &= \vartheta_{\mathrm{ref}} + \boldsymbol{\nabla}_{\mathrm{M}} \vartheta_{\mathrm{M}} \cdot \boldsymbol{x} + \vartheta'_{\mathrm{m}}(\boldsymbol{x}) \,, & (3.42) \end{aligned}$$

where $\boldsymbol{u}'$ and ϑ' are the perturbation fields. To satisfy Eqs. (3.33) and (3.35), the following respective conditions should be satisfied

$$\begin{aligned} 0 &= < \boldsymbol{\nabla}_m \boldsymbol{u}'(\boldsymbol{x}) >= \frac{1}{V(\omega)} \int_{\partial\omega} \boldsymbol{u}'_{\mathrm{m}} \otimes \boldsymbol{n}_{\mathrm{m}} dS \,, & (3.43) \\ 0 &= < \boldsymbol{\nabla}_m \vartheta'(\boldsymbol{x}) >= \frac{1}{V(\omega)} \int_{\partial\omega} \vartheta'_{\mathrm{m}} \boldsymbol{n}_{\mathrm{m}} dS \,. & (3.44) \end{aligned}$$

---

[3] for finite temperature changes, this last relation is an approximation of $\frac{\boldsymbol{q}_{\mathrm{M}} \cdot \boldsymbol{\nabla}_{\mathrm{M}} \delta\vartheta_{\mathrm{M}}}{T_{\mathrm{M}}} = \left\langle \frac{\boldsymbol{q}_{\mathrm{m}} \cdot \boldsymbol{\nabla}_{\mathrm{m}} \delta\vartheta_{\mathrm{m}}}{T_{\mathrm{m}}} \right\rangle$

Finally, in order to satisfy the energy and entropy change consistency conditions, using Eqs. (3.41) and (3.42) in respectively Eqs. (3.38) and (3.39), integrating by parts and using the equilibrium Eqs. (3.27) and (3.28), lead to

$$\boldsymbol{\sigma}_{\mathrm{M}} : \delta\boldsymbol{\varepsilon}_{\mathrm{M}} =< \boldsymbol{\sigma}_{\mathrm{m}} : \delta\boldsymbol{\varepsilon}_{\mathrm{m}} >= \boldsymbol{\sigma}_{\mathrm{M}} : \delta\boldsymbol{\varepsilon}_{\mathrm{M}} + \frac{1}{V(\omega)}\int_{\partial\omega} (\boldsymbol{\sigma}_{\mathrm{m}} \cdot \boldsymbol{n}_{\mathrm{m}}) \cdot \delta\boldsymbol{u}'_{\mathrm{m}} dS\,, \quad (3.45)$$

$$\begin{aligned} &\boldsymbol{q}_{\mathrm{M}} \cdot \boldsymbol{\nabla}_{\mathrm{M}}\delta\vartheta_{\mathrm{M}} =< \boldsymbol{q}_{\mathrm{m}} \cdot \boldsymbol{\nabla}_{\mathrm{m}}\delta\vartheta_{\mathrm{m}} >= \\ &\qquad \boldsymbol{q}_{\mathrm{M}} \cdot \boldsymbol{\nabla}_{\mathrm{M}}\delta\vartheta_{\mathrm{M}} + \frac{1}{V(\omega)}\int_{\partial\omega} (\boldsymbol{q}_{\mathrm{m}} \cdot \boldsymbol{n}_{\mathrm{m}})\, \delta\vartheta'_{\mathrm{m}} dS\,, \end{aligned} \quad (3.46)$$

or again

$$0 = \int_{\partial\omega} (\boldsymbol{\sigma}_{\mathrm{m}} \cdot \boldsymbol{n}) \cdot \delta\boldsymbol{u}'_{\mathrm{m}} dS\,, \quad (3.47)$$

$$0 = \int_{\partial\omega} (\boldsymbol{q}_{\mathrm{m}} \cdot \boldsymbol{n})\, \delta\vartheta'_{\mathrm{m}} dS\,, \quad (3.48)$$

which is similar to the conditions for the mechanical problems defined in Section 3.2 with the addition of the thermal aspect.

Under the conditions (3.43-3.44) and (3.47-3.48), the homogenised elastic tensor $\mathbb{C}_{\mathrm{M}}$, the thermal conductivity tensor $\boldsymbol{\kappa}_{\mathrm{M}}$ and the thermal expansion tensor $\boldsymbol{\alpha}_{\mathrm{M}}$ of the SVE need to be evaluated by solving the BVP (3.29) on SVE ω.

3.3.2 Definition of the constrained micro-scale finite element problem

The constrained micro-scale problem is obtained by applying appropriate boundary condition over the volume element. In this thermo-elastic problem, KUBC, PBC or SUBC can be applied [4], see Section 3.2.1. The periodic boundary condition is now detailed as an example. The Periodic Boundary Conditions (PBCs) of the displacement $\boldsymbol{u}_{\mathrm{m}}$ and the temperature ϑ_{m} reads

$$\begin{aligned} &\boldsymbol{u}_{\mathrm{m}}(\boldsymbol{x}^+) - \boldsymbol{u}_{\mathrm{m}}(\boldsymbol{x}^-) = (\boldsymbol{u}_{\mathrm{M}} \otimes \boldsymbol{\nabla}_M) \cdot (\boldsymbol{x}^+ - \boldsymbol{x}^-)\,, \\ &\vartheta_{\mathrm{m}}(\boldsymbol{x}^+) - \vartheta_{\mathrm{m}}(\boldsymbol{x}^-) = \boldsymbol{\nabla}_{\mathrm{M}}\vartheta_{\mathrm{M}} \cdot (\boldsymbol{x}^+ - \boldsymbol{x}^-)\,, \\ &\forall \boldsymbol{x}^+ \in \partial\omega^+ \text{ and corresponding } \boldsymbol{x}^- \in \partial\omega^-\,, \end{aligned} \quad (3.49)$$

where the parallelepiped SVE faces have been separated in opposite surfaces $\partial\omega^-$ and $\partial\omega^+$. The values at the corners are obtained from $\boldsymbol{u}_{\mathrm{m}}(\boldsymbol{x}) = (\boldsymbol{u}_{\mathrm{M}} \otimes \boldsymbol{\nabla}_{\mathrm{M}}) \cdot \boldsymbol{x}$ and $\vartheta_{\mathrm{m}}(\boldsymbol{x}) = \vartheta_{\mathrm{ref}} + \nabla_{\mathrm{M}}\vartheta_{\mathrm{M}} \cdot \boldsymbol{x}$. These PBCs result in the anti-periodic traction and normal flux boundary conditions, which read

$$\begin{aligned} &\boldsymbol{\sigma}_{\mathrm{m}}(\boldsymbol{x}^+) \cdot \boldsymbol{n}^+_{\mathrm{m}} = -\boldsymbol{\sigma}_{\mathrm{m}}(\boldsymbol{x}^-) \cdot \boldsymbol{n}^-_{\mathrm{m}}\,, \\ &\boldsymbol{q}_{\mathrm{m}}(\boldsymbol{x}^+) \cdot \boldsymbol{n}^+_{\mathrm{m}} = -\boldsymbol{q}_{\mathrm{m}}(\boldsymbol{x}^-) \cdot \boldsymbol{n}^-_{\mathrm{m}}\,, \\ &\forall \boldsymbol{x}^+ \in \partial\omega^+ \text{ and corresponding } \boldsymbol{x}^- \in \partial\omega^-\,. \end{aligned} \quad (3.50)$$

---

[4] MBC cannot be applied for the thermal part

These boundary conditions are completed by the consistency condition (3.40). Such a condition was not present for the mechanical problem.

The kinematics constraints are defined by $\boldsymbol{\epsilon}_{\mathrm{M}} = \boldsymbol{u}_{\mathrm{M}} \otimes \boldsymbol{\nabla}_{\mathrm{M}}$ the macroscopic displacement gradient, with $\boldsymbol{F}_{\mathrm{M}}$ the nine components of $\boldsymbol{u}_{\mathrm{M}} \otimes \boldsymbol{\nabla}_{\mathrm{M}}$ written under a vectorial form, by $\boldsymbol{\nabla}_{\mathrm{M}}\vartheta_{\mathrm{M}}$ the macroscopic temperature gradient, and by ϑ_{M} the macroscopic temperature. These kinematics constraints can be grouped under the vector $\boldsymbol{K}_{\mathrm{M}}^T = \left[\begin{array}{ccc} \boldsymbol{F}_{\mathrm{M}}^T & \boldsymbol{\nabla}_{\mathrm{M}}\vartheta_M^T & \vartheta_{\mathrm{M}} \end{array} \right]$.

Dropping the subscript 'm' for simplicity, the degrees of freedom (dofs) are separated in constrained dofs, such as the nodal displacements $\mathbf{u}_c$ at the corner nodes, in dependent dofs, which relates to the periodic boundary conditions (3.49) and to the heat consistency (3.40), such as the nodal displacements $\mathbf{u}_b$ at the boundary, the nodal temperatures $\boldsymbol{\vartheta}_c$ at the corners, $\boldsymbol{\vartheta}_b$ at the boundary, and $\boldsymbol{\vartheta}_i$ inside the volume element, and in independent dofs as the nodal displacements u_i inside the volume element, see Appendix B.3. Therefore, on the one hand, the micro-structural problem (3.29) is organised in terms of the nodal unknowns

$$\boldsymbol{\varphi} = \left[\begin{array}{ccc} \mathbf{u}_c^T & \boldsymbol{\varphi}_b^T & \mathbf{u}_i^T \end{array} \right]^T , \tag{3.51}$$

with $\boldsymbol{\varphi}_b^T = \left[\mathbf{u}_b^T \boldsymbol{\vartheta}_c^T \boldsymbol{\vartheta}_b^T \boldsymbol{\vartheta}_i^T\right]$, of the nodal forces

$$\boldsymbol{f} = \left[\begin{array}{ccc} \boldsymbol{f}_{u_c}^T & \boldsymbol{f}_{\varphi_b}^T & \boldsymbol{f}_{u_i}^T \end{array} \right]^T , \tag{3.52}$$

and of the stiffness matrix

$$\boldsymbol{K} = \left[\begin{array}{ccc} \boldsymbol{K}_{u_c u_c} & \boldsymbol{K}_{u_c \varphi_b} & \boldsymbol{K}_{u_c u_i} \\ \boldsymbol{K}_{\varphi_b u_c} & \boldsymbol{K}_{\varphi_b \varphi_b} & \boldsymbol{K}_{\varphi_b u_i} \\ \boldsymbol{K}_{u_i u_c} & \boldsymbol{K}_{u_i \varphi_b} & \boldsymbol{K}_{u_i u_i} \end{array} \right] . \tag{3.53}$$

On the other hand, the boundary conditions (3.49) and the heat consistency (3.40) are expressed as

$$0 = \mathbf{u}_c - \boldsymbol{S}_{\varphi_c}\boldsymbol{K}_{\mathrm{M}} , \tag{3.54}$$

$$0 = \boldsymbol{C}_{\varphi_c}\mathbf{u}_c + \boldsymbol{C}_{\varphi_b}\boldsymbol{\varphi}_b - \boldsymbol{S}_{\varphi_b}\boldsymbol{K}_{\mathrm{M}} , \tag{3.55}$$

where the constraints matrices $\boldsymbol{C}$ and $\boldsymbol{S}$ are detailed in Appendix B.3. Note that these expressions remain valid for non-periodic meshes when using the interpolant method developed by [66].

3.3.3 Resolution of the constrained micro-scale finite element problem

The resolution of the constrained micro-scale BVP follows the multiple-constraint projection method described by [2] and the condensation method developed by [59]. The functional related to the constrained micro-scale problem (3.29) completed by the conditions (3.54-3.55) reads

$$\Psi = \frac{1}{2}\boldsymbol{\varphi}^T\boldsymbol{K}\boldsymbol{\varphi} - \left[\mathbf{u}_c - \boldsymbol{S}_{\varphi_c}\boldsymbol{K}_{\mathrm{M}}\right]^T \boldsymbol{\lambda}_{u_c} - \left[\boldsymbol{C}_{\varphi_c}\mathbf{u}_c + \boldsymbol{C}_{\varphi_b}\boldsymbol{\varphi}_b - \boldsymbol{S}_{\varphi_b}\boldsymbol{K}_{\mathrm{M}}\right]^T \boldsymbol{\lambda}_{\varphi_b} , \tag{3.56}$$

where the Lagrange multipliers $\boldsymbol{\lambda}_{u_c}$ and $\boldsymbol{\lambda}_{\varphi_b}$ are respectively related to the corner displacement constraints (3.54) and to the dependent unknowns constraints (3.55).

The solution of the problem corresponds to the stationary point of Eq. (3.56) with respect to the nodal unknowns, which results into

$$\boldsymbol{\lambda}_{\varphi_b} = \boldsymbol{R}^T_{\varphi_b} \boldsymbol{f}_{\varphi_b} \, , \tag{3.57}$$

$$\boldsymbol{\lambda}_{u_c} = \boldsymbol{F}_{u_c} - \boldsymbol{C}^T_{\varphi_c} \boldsymbol{R}^T_{\varphi_b} \boldsymbol{f}_{\varphi_b} \, , \tag{3.58}$$

with $\boldsymbol{R}^T_{\varphi_b} = \left(\boldsymbol{C}_{\varphi_b} \boldsymbol{C}^T_{\varphi_b} \right)^{-1} \boldsymbol{C}_{\varphi_b}$, see Appendix B.3.2.

The homogenised stress tensor (3.32) and the homogenised thermal flux vector (3.34) can then be evaluated in the vectorial form as

$$\boldsymbol{\Sigma}_{\mathrm{M}} = \frac{1}{V(\omega)} \left(\frac{\partial \Psi}{\partial \boldsymbol{F}_{\mathrm{M}}} \right) = \frac{1}{V(\omega)} \left[\begin{array}{ccc} \boldsymbol{I}_{9\times 9} & \mathbf{0}_{9\times 3} & \mathbf{0}_{9\times 1} \end{array} \right] \left\{ \boldsymbol{S}^T_{\varphi_c} \boldsymbol{\lambda}_{u_c} + \boldsymbol{S}^T_{\varphi_b} \boldsymbol{\lambda}_{\varphi_b} \right\} \, , \tag{3.59}$$

$$\boldsymbol{q}_{\mathrm{M}} = \frac{1}{V(\omega)} \left(\frac{\partial \Psi}{\partial \boldsymbol{\nabla}_{\mathrm{M}} \vartheta_{\mathrm{M}}} \right) = \frac{1}{V(\omega)} \left[\begin{array}{ccc} \mathbf{0}_{3\times 9} & \boldsymbol{I}_{3\times 3} & \mathbf{0}_{3\times 1} \end{array} \right] \left\{ \boldsymbol{S}^T_{\varphi_c} \boldsymbol{\lambda}_{u_c} + \boldsymbol{S}^T_{\varphi_b} \boldsymbol{\lambda}_{\varphi_b} \right\} \, , \tag{3.60}$$

respectively, see Appendix B.3.3 for details.

To compute the material operators, the stationary point of (3.56) is linearised with respect to the kinematics constraints $\boldsymbol{K}_{\mathrm{M}}$. The independent dofs $\boldsymbol{u}_i$ can be eliminated by computing the reduced stiffness, yielding

$$\left[\begin{array}{cc} \tilde{\boldsymbol{K}}_{u_c u_c} & \tilde{\boldsymbol{K}}_{u_c \varphi_b} \\ \tilde{\boldsymbol{K}}_{\varphi_b u_c} & \tilde{\boldsymbol{K}}_{\varphi_b \varphi_b} \end{array} \right] \left[\begin{array}{c} \delta \mathbf{u}_c \\ \delta \boldsymbol{\varphi}_b \end{array} \right] = \left[\begin{array}{cc} \boldsymbol{I} & \boldsymbol{C}^T_{\varphi_c} \\ \mathbf{0} & \boldsymbol{C}^T_{\varphi_b} \end{array} \right] \left[\begin{array}{c} \delta \boldsymbol{\lambda}_{u_c} \\ \delta \boldsymbol{\lambda}_{\varphi_b} \end{array} \right] \, , \tag{3.61}$$

where

$$\tilde{\boldsymbol{K}}_{u_c u_c} = \left(\boldsymbol{K}_{u_c u_c} - \boldsymbol{K}_{u_c u_i} \boldsymbol{K}^{-1}_{u_i u_i} \boldsymbol{K}_{u_i u_c} \right) \, , \tag{3.62}$$

$$\tilde{\boldsymbol{K}}_{u_c \varphi_b} = \left(\boldsymbol{K}_{u_c \varphi_b} - \boldsymbol{K}_{u_c u_i} \boldsymbol{K}^{-1}_{u_i u_i} \boldsymbol{K}_{u_i \varphi_b} \right) \, , \tag{3.63}$$

$$\tilde{\boldsymbol{K}}_{\varphi_b u_c} = \left(\boldsymbol{K}_{\varphi_b u_c} - \boldsymbol{K}_{\varphi_b u_i} \boldsymbol{K}^{-1}_{u_i u_i} \boldsymbol{K}_{u_i u_c} \right) \, , \text{ and} \tag{3.64}$$

$$\tilde{\boldsymbol{K}}_{\varphi_b \varphi_b} = \left(\boldsymbol{K}_{\varphi_b \varphi_b} - \boldsymbol{K}_{\varphi_b u_i} \boldsymbol{K}^{-1}_{u_i u_i} \boldsymbol{K}_{u_i \varphi_b} \right) \, . \tag{3.65}$$

In order to extract the dependency on the kinematics constraints $\boldsymbol{K}_{\mathrm{M}}$, Eqs. (3.54-3.55) are linearised as

$$\delta \mathbf{u}_c = \boldsymbol{S}_{\varphi_c} \delta \boldsymbol{K}_{\mathrm{M}} \, , \tag{3.66}$$

$$\boldsymbol{C}_{\varphi_c} \delta \mathbf{u}_c + \boldsymbol{C}_{\varphi_b} \delta \boldsymbol{\varphi}_b = \boldsymbol{S}_{\varphi_b} \delta \boldsymbol{K}_{\mathrm{M}} \, . \tag{3.67}$$

Combining these two equations with the system (3.61), yields the expressions

$$\begin{aligned}
\delta\boldsymbol{\lambda}_{\varphi_b} &= -\tilde{\tilde{\boldsymbol{S}}}^{-1}_{\varphi_b\varphi_b}\tilde{\tilde{\boldsymbol{S}}}_{\varphi_b\varphi_c}\delta\boldsymbol{K}_{\mathrm{M}}\,, && (3.68)\\
\delta\boldsymbol{\lambda}_{u_c} &= \left[\tilde{\boldsymbol{K}}_{u_cu_c}-\tilde{\boldsymbol{K}}_{u_c\varphi_b}\tilde{\boldsymbol{K}}^{-1}_{\varphi_b\varphi_b}\tilde{\boldsymbol{K}}_{\varphi_bu_c}\right]\boldsymbol{S}_{\varphi_c}\delta\boldsymbol{K}_{\mathrm{M}}+ \\
&\quad\left[\boldsymbol{C}^T_{\varphi_c}-\tilde{\boldsymbol{K}}_{u_c\varphi_b}\tilde{\boldsymbol{K}}^{-1}_{\varphi_b\varphi_b}\boldsymbol{C}^T_{\varphi_b}\right]\tilde{\tilde{\boldsymbol{S}}}^{-1}_{\varphi_b\varphi_b}\tilde{\tilde{\boldsymbol{S}}}_{\varphi_b\varphi_c}\delta\boldsymbol{K}_{\mathrm{M}}\,, && (3.69)
\end{aligned}$$

with

$$\begin{aligned}
\tilde{\tilde{\boldsymbol{S}}}_{\varphi_b\varphi_b} &= -\boldsymbol{C}_{\varphi_b}\tilde{\boldsymbol{K}}^{-1}_{\varphi_b\varphi_b}\boldsymbol{C}^T_{\varphi_b}\,, && (3.70)\\
\tilde{\tilde{\boldsymbol{S}}}_{\varphi_b\varphi_c} &= \boldsymbol{S}_{\varphi_b}-\left(\boldsymbol{C}_{\varphi_c}-\boldsymbol{C}_{\varphi_b}\tilde{\boldsymbol{K}}^{-1}_{\varphi_b\varphi_b}\tilde{\boldsymbol{K}}_{\varphi_bu_c}\right)\boldsymbol{S}_{\varphi_c}\,, && (3.71)\\
\tilde{\tilde{\boldsymbol{S}}}_{\varphi_c\varphi_c} &= \boldsymbol{S}^T_{\varphi_c}\left[\tilde{\boldsymbol{K}}_{u_cu_c}-\tilde{\boldsymbol{K}}_{u_c\varphi_b}\tilde{\boldsymbol{K}}^{-1}_{\varphi_b\varphi_b}\tilde{\boldsymbol{K}}_{\varphi_bu_c}\right]\boldsymbol{S}_{\varphi_c}\,,\ \text{and} && (3.72)\\
\tilde{\tilde{\boldsymbol{S}}}_{\varphi_c\varphi_b} &= \boldsymbol{S}^T_{\varphi_b}-\boldsymbol{S}^T_{\varphi_c}\left[\boldsymbol{C}^T_{\varphi_c}-\tilde{\boldsymbol{K}}_{u_c\varphi_b}\tilde{\boldsymbol{K}}^{-1}_{\varphi_b\varphi_b}\boldsymbol{C}^T_{\varphi_b}\right]\,, && (3.73)
\end{aligned}$$

see Appendix B.3.4 for details.

The variation of the homogenised stress (3.59) yields the apparent elasticity tensor $\boldsymbol{C}_{\mathrm{M}}=\frac{\partial\boldsymbol{\Sigma}_{\mathrm{M}}}{\partial\boldsymbol{F}_{\mathrm{M}}}$ in the matrix form following

$$\begin{aligned}
\boldsymbol{C}_{\mathrm{M}} &= \frac{1}{V(\omega)}\left[\begin{array}{ccc}\boldsymbol{I}_{9\times9} & \boldsymbol{0}_{9\times3} & \boldsymbol{0}_{9\times1}\end{array}\right]\left\{\boldsymbol{S}^T_{\varphi_c}\frac{\partial\boldsymbol{\lambda}_{u_c}}{\partial\boldsymbol{K}_{\mathrm{M}}}+\boldsymbol{S}^T_{\varphi_b}\frac{\partial\boldsymbol{\lambda}_{\varphi_b}}{\partial\boldsymbol{K}_{\mathrm{M}}}\right\}\left[\begin{array}{c}\boldsymbol{I}_{9\times9}\\ \boldsymbol{0}_{3\times9}\\ \boldsymbol{0}_{1\times9}\end{array}\right],\\
&= \frac{1}{V(\omega)}\left[\begin{array}{ccc}\boldsymbol{I}_{9\times9} & \boldsymbol{0}_{9\times3} & \boldsymbol{0}_{9\times1}\end{array}\right]\left\{\tilde{\tilde{\boldsymbol{S}}}_{\varphi_c\varphi_c}-\tilde{\tilde{\boldsymbol{S}}}_{\varphi_c\varphi_b}\tilde{\tilde{\boldsymbol{S}}}^{-1}_{\varphi_b\varphi_b}\tilde{\tilde{\boldsymbol{S}}}_{\varphi_b\varphi_c}\right\}\left[\begin{array}{c}\boldsymbol{I}_{9\times9}\\ \boldsymbol{0}_{3\times9}\\ \boldsymbol{0}_{1\times9}\end{array}\right].
\end{aligned}\tag{3.74}$$

The homogenised conductivity tensor $\boldsymbol{\kappa}_{\mathrm{M}}=-\frac{\partial\boldsymbol{q}_{\mathrm{M}}}{\partial\nabla_M\vartheta_{\mathrm{M}}}$ is directly obtained following

$$\begin{aligned}
&\boldsymbol{\kappa}_{\mathrm{M}}=\\
&-\frac{1}{V(\omega)}\left[\begin{array}{ccc}\boldsymbol{0}_{3\times9} & \boldsymbol{I}_{3\times3} & \boldsymbol{0}_{3\times1}\end{array}\right]\left\{\tilde{\tilde{\boldsymbol{S}}}_{\varphi_c\varphi_c}-\tilde{\tilde{\boldsymbol{S}}}_{\varphi_c\varphi_b}\tilde{\tilde{\boldsymbol{S}}}^{-1}_{\varphi_b\varphi_b}\tilde{\tilde{\boldsymbol{S}}}_{\varphi_b\varphi_c}\right\}\left[\begin{array}{c}\boldsymbol{0}_{9\times3}\\ \boldsymbol{I}_{3\times3}\\ \boldsymbol{0}_{1\times3}\end{array}\right],
\end{aligned}\tag{3.75}$$

The apparent thermal expansion tensor $\boldsymbol{\alpha}_{\mathrm{M}}$ can be extracted in the vector form using $-\boldsymbol{C}_{\mathrm{M}}\boldsymbol{A}_{\mathrm{M}}=\frac{\partial\boldsymbol{\Sigma}_{\mathrm{M}}}{\partial\vartheta_{\mathrm{M}}}$ following

$$\begin{aligned}
&-\boldsymbol{C}_{\mathrm{M}}\boldsymbol{A}_{\mathrm{M}}=\\
&\frac{1}{V(\omega)}\left[\begin{array}{ccc}\boldsymbol{I}_{9\times9} & \boldsymbol{0}_{9\times3} & \boldsymbol{0}_{9\times1}\end{array}\right]\left\{\tilde{\tilde{\boldsymbol{S}}}_{\varphi_c\varphi_c}-\tilde{\tilde{\boldsymbol{S}}}_{\varphi_c\varphi_b}\tilde{\tilde{\boldsymbol{S}}}^{-1}_{\varphi_b\varphi_b}\tilde{\tilde{\boldsymbol{S}}}_{\varphi_b\varphi_c}\right\}\left[\begin{array}{c}\boldsymbol{0}_{9\times1}\\ \boldsymbol{0}_{3\times1}\\ \boldsymbol{I}_{1\times1}\end{array}\right].
\end{aligned}\tag{3.76}$$

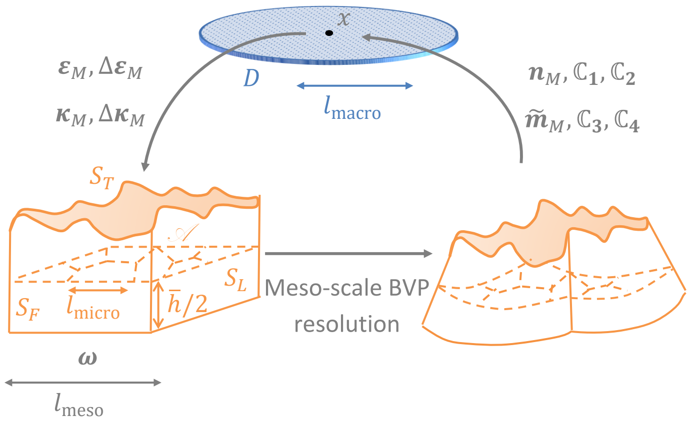

Figure 3.3: Homogenisation-based multi-scale method with 2^{nd}-order homogenisation for macro-scale Kirchhoff-Love plates.

3.4 Second-order homogenisation to account for surface roughness

The third problem considered in this work deals with thin plates which can be subjected to surface roughness, see Section 2.5. Now, the meso-scale material properties $\boldsymbol{U}(\boldsymbol{x}, \boldsymbol{\theta})$, see Eq. (2.80), which corresponds to the 4 resultant material tensors $\mathbb{C}_1^* - \mathbb{C}_4^*$ (plate formalism) written under the matrix form, are extracted from the meso-scale volume element BVP resolution. The volume elements can now be subjected to roughness. The meso-scale (R)SVE ω is almost a parallelepiped, with 5 flat surfaces and 1 rough surface when roughness is considered, see Fig. 3.3. Each surface is referred to as either S_F, S_{BA}, S_L, S_R, S_T, or S_{BO} respectively for the forward, backward, left, right, top and bottom surfaces, the top surface being the one which might be rough. The average plane of the rough surface defines the thickness $\bar{h}$ of the (R)SVE.

If the volume element ω is small enough, the dynamic behaviour behind strain waves can be neglected and the equilibrium equation is written as:

$$\boldsymbol{\nabla}_{\text{m}} \cdot \boldsymbol{\sigma}_{\text{m}} = \boldsymbol{0} \tag{3.77}$$

In terms of displacement, the problem to be solved based on a finite element formulation is the following:

$$\boldsymbol{K}\mathbf{u} = \boldsymbol{f} \tag{3.78}$$

In the first part of this section, generalities about computational second-order homogenisation are recalled. In particular, the second-order homogenisation process for thin structure is described. Afterwards, consistent boundary conditions on rough volume elements are defined. Finally, from the homogenisation process, the matrix $\boldsymbol{U}$ is extracted in order to contain all the information required for the macro-scale plate elements resolution under the Kirchhoff-Love assumption, *i.e.* the resultant material tensors $\mathbb{C}_1^* - \mathbb{C}_4^*$.

3.4.1 Definition of scales transition

In the context of a first-order computational homogenisation, the only kinematic constraint is first order [21], see Section 3.2. Assuming small deformations, the symmetric macro-scale Cauchy strain tensor $\boldsymbol{\varepsilon}_{\mathrm{M}}$ thus drives the problem while $\boldsymbol{u}_{\mathrm{M}}$ is the displacement at macro-scale. Under the infinitesimal strain assumption, the Cauchy strain is linked to the displacement by:

$$\boldsymbol{\varepsilon}_{\mathrm{M}} = \frac{1}{2}\left(\boldsymbol{\nabla}_{\mathrm{M}} \otimes \boldsymbol{u}_{\mathrm{M}} + \left(\boldsymbol{\nabla}_{\mathrm{M}} \otimes \boldsymbol{u}_{\mathrm{M}}\right)^T\right) . \tag{3.79}$$

Besides, the asymmetric strain $\boldsymbol{\epsilon}_{\mathrm{M}}$, which possibly includes the rotation of the volume element, is defined by

$$\boldsymbol{\epsilon}_{\mathrm{M}} = \boldsymbol{u}_{\mathrm{M}} \otimes \boldsymbol{\nabla}_{\mathrm{M}} . \tag{3.80}$$

In the case of second-order homogenisation, described in [45] for large deformation and in [37] for small strains, the gradient of the deformation gradient is also introduced. It is denoted $\boldsymbol{\eta}_{\mathrm{M}}$ and reads

$$\boldsymbol{\eta}_{\mathrm{M}} = \boldsymbol{u}_{\mathrm{M}} \otimes \boldsymbol{\nabla}_{\mathrm{M}} \otimes \boldsymbol{\nabla}_{\mathrm{M}} . \tag{3.81}$$

In a deformation driven macro-scale procedure, the different stress components are computed from the macro-scale deformation state characterised by $\boldsymbol{\epsilon}_{\mathrm{M}}$ and $\boldsymbol{\eta}_{\mathrm{M}}$, see Fig. 3.3. The idea behind multi-scale computation is to link stress and strain through the resolution of a meso-scale boundary value problem. This meso-scale BVP is described once again by a micro-scale displacements $\boldsymbol{u}_{\mathrm{m}}$. From a second order Taylor expansion applied on the macro-scale displacement, one can define the micro-scale displacement as

$$\boldsymbol{u}_{\mathrm{m}} = \boldsymbol{\epsilon}_{\mathrm{M}} \cdot \boldsymbol{x} + \frac{1}{2}\boldsymbol{\eta}_{\mathrm{M}} : (\boldsymbol{x} \otimes \boldsymbol{x}) + \boldsymbol{u}'_{\mathrm{m}} , \tag{3.82}$$

where $\boldsymbol{u}'_{\mathrm{m}}$ is the micro-scale fluctuation field. The micro-scale Cauchy strain tensor is defined as the gradient of the micro-scale displacement, with

$$\boldsymbol{\epsilon}_{\mathrm{m}} = \boldsymbol{u}_{\mathrm{m}} \otimes \boldsymbol{\nabla}_{\mathrm{m}} = \boldsymbol{\epsilon}_{\mathrm{M}} + \boldsymbol{\eta}_{\mathrm{M}} \cdot \boldsymbol{x} + \boldsymbol{u}'_{\mathrm{m}} \otimes \boldsymbol{\nabla}_{\mathrm{m}} . \tag{3.83}$$

Ensuring the strain scale-transition during the down-scaling process follows from

$$\boldsymbol{\epsilon}_{\mathrm{M}} = \frac{1}{V}\int_{\omega} \boldsymbol{\epsilon}_{\mathrm{m}} dV . \tag{3.84}$$

This scale transition is satisfied if the following two conditions, based on the definition of the micro-scale strain in Eq. (3.83), are respected:

$$\begin{aligned} \int_\omega \boldsymbol{x} dV &= 0\,, \text{ and} && (3.85)\\ \int_\omega \boldsymbol{u}'_{\mathrm{m}} \otimes \boldsymbol{\nabla}_{\mathrm{m}} dV &= 0\,. && (3.86) \end{aligned}$$

Equation (3.85) is always satisfied if the volume element is centred at its centroid. This implies that if Eq. (3.84) has to be satisfied, the boundary conditions should be defined according to Eq. (3.86) which, using the divergence theorem, can be rewritten in terms of the surface integral as

$$\int_{\partial\omega} \boldsymbol{n}_{\mathrm{m}} \otimes \boldsymbol{u}'_{\mathrm{m}} dS = 0\,, \tag{3.87}$$

where $\boldsymbol{n}_{\mathrm{m}}$ is the unit vector normal to the surface $\partial\omega$ of the volume element.

Let us note that, once again, besides down-scaling the strain tensor, the higher-order strain tensor ensures a correct constraint of the high-order deformation modes. To define this down-scaling, Eq. (3.83) is first multiplied by the position

$$\boldsymbol{\epsilon}_{\mathrm{m}} \otimes \boldsymbol{x} = (\boldsymbol{u}_{\mathrm{m}} \otimes \boldsymbol{\nabla}_{\mathrm{m}}) \otimes \boldsymbol{x} = \boldsymbol{\epsilon}_{\mathrm{M}} \otimes \boldsymbol{x} + \boldsymbol{\eta}_{\mathrm{M}} \cdot (\boldsymbol{x} \otimes \boldsymbol{x}) + (\boldsymbol{u}'_{\mathrm{m}} \otimes \boldsymbol{\nabla}_{\mathrm{m}}) \otimes \boldsymbol{x}\,. \tag{3.88}$$

Integrating this last equation on the volume, using Eq. (3.85), defining the inertia $\boldsymbol{J} = \frac{1}{V}\int_\omega \boldsymbol{x}\otimes\boldsymbol{x} dV$, and integrating by parts the displacement and fluctuation related terms lead to

$$\begin{aligned} &\frac{1}{V}\int_{\partial\omega} \boldsymbol{u}_{\mathrm{m}} \otimes \boldsymbol{n}_{\mathrm{m}} \otimes \boldsymbol{x} dS - \frac{1}{V}\int_\omega \boldsymbol{u}_{\mathrm{m}} dV \otimes \boldsymbol{I} = \\ &\qquad \boldsymbol{\eta}_{\mathrm{M}} \cdot \boldsymbol{J} - \frac{1}{V}\int_\omega \boldsymbol{u}'_{\mathrm{m}} dV \otimes \boldsymbol{I} + \frac{1}{V}\int_{\partial\omega} \boldsymbol{u}'_{\mathrm{m}} \otimes \boldsymbol{n}_{\mathrm{m}} \otimes \boldsymbol{x} dS\,, \qquad (3.89) \end{aligned}$$

where $\boldsymbol{I}$ is the identity tensor. Substituting Eq. (3.82) in the second term of the left hand side of Eq. (3.89) and using Eq. (3.85) result into

$$\frac{1}{V}\int_{\partial\omega} \boldsymbol{u}_{\mathrm{m}} \otimes \boldsymbol{n}_{\mathrm{m}} \otimes \boldsymbol{x} dS - \frac{1}{2}\boldsymbol{\eta}_{\mathrm{M}} : \boldsymbol{J} \otimes \boldsymbol{I} = \boldsymbol{\eta}_{\mathrm{M}} \cdot \boldsymbol{J} + \frac{1}{V}\int_{\partial\omega} \boldsymbol{u}'_{\mathrm{m}} \otimes \boldsymbol{n}_{\mathrm{m}} \otimes \boldsymbol{x} dS\,. \tag{3.90}$$

From this equation, in order for the high-order strain down-scaling to be independent on the fluctuation field, the following condition should be satisfied

$$\int_{\partial\omega} \boldsymbol{u}'_{\mathrm{m}} \otimes \boldsymbol{n}_{\mathrm{m}} \otimes \boldsymbol{x} dS = 0\,. \tag{3.91}$$

Both micro-scale and macro-scale problems are now defined as well as the kinematic scale transition. However, a multi-scale approach only provides a relevant solution when the transition between the micro- and the macro-scales is energetically consistent. This consistency is achieved by appropriate choices of the boundary conditions. Energetically consistent boundary conditions are obtained if the Hill-Mandel condition, which states the conservation of energy variation between the micro-scale and the macro-scale problems, is satisfied. From the micro-scale energy per unit area S of the Cosserat plane, one can obtain[5]:

$$\begin{aligned} \frac{1}{S}\int_{\omega} \boldsymbol{\sigma}_{\mathrm{m}} : \delta\boldsymbol{\epsilon}_{\mathrm{m}} dV &= \frac{1}{S}\int_{\omega} \boldsymbol{\sigma}_{\mathrm{m}} : \left(\delta\boldsymbol{\epsilon}_{\mathrm{M}} + \delta\boldsymbol{\eta}_{\mathrm{M}}\cdot\boldsymbol{x} + \delta\boldsymbol{u}'_{\mathrm{m}}\otimes\boldsymbol{\nabla}_{\mathrm{m}}\right) dV \\ &= \boldsymbol{n}_{\mathrm{M}} : \delta\boldsymbol{\epsilon}_{\mathrm{M}} + \tilde{\boldsymbol{m}}_{\mathrm{M}} \vdots \delta\boldsymbol{\eta}_{\mathrm{M}} + \frac{1}{S}\int_{\omega} \boldsymbol{\sigma}_{\mathrm{m}} : \left(\delta\boldsymbol{u}'_{\mathrm{m}}\otimes\boldsymbol{\nabla}_{\mathrm{m}}\right) dV\,, \end{aligned} \tag{3.92}$$

with the force and moment per unit width

$$\boldsymbol{n}_{\mathrm{M}} = \frac{1}{S}\int_{\omega} \boldsymbol{\sigma}_{\mathrm{m}} dV\,, \text{ and} \tag{3.93}$$

$$\tilde{\boldsymbol{m}}_{\mathrm{M}} = \frac{1}{S}\int_{\omega} \frac{\boldsymbol{\sigma}_{\mathrm{m}}\otimes\boldsymbol{x} + \left(\boldsymbol{\sigma}_{\mathrm{m}}\otimes\boldsymbol{x}\right)^{rc}}{2} dV\,, \tag{3.94}$$

$$\tag{3.95}$$

where the superscript "rc" means right transposed, *i.e.* $\left(\boldsymbol{A}^{rc}\right)_{ijk} = \boldsymbol{A}_{ikj}$.

Equation (3.92) implies that the Hill-Mandel condition is fulfilled if

$$\frac{1}{S}\int_{\omega} \boldsymbol{\sigma}_{\mathrm{m}} : \left(\delta\boldsymbol{u}'_{\mathrm{m}}\otimes\boldsymbol{\nabla}_{\mathrm{m}}\right) dV = 0\,, \tag{3.96}$$

or again, using the divergence theorem, if

$$\frac{1}{S}\int_{\partial\omega} \boldsymbol{t}_{\mathrm{m}}\cdot\delta\boldsymbol{u}'_{\mathrm{m}} dS = 0\,, \tag{3.97}$$

where $\boldsymbol{t}_{\mathrm{m}} = \boldsymbol{n}_{\mathrm{m}}\cdot\boldsymbol{\sigma}_{\mathrm{m}}$ and $\boldsymbol{n}_{\mathrm{m}}$ is the unit outward vector normal to the surface $\partial\omega$ (the surface of the meso-scale volume element ω, which is not equal to S the area of the Cosserat plane).

3.4.2 Definition of the constrained micro-scale finite element problem

Equation (3.97) defines the boundary conditions of the meso-scale BVP required to satisfy the Hill-Mandel condition. Equations (3.87) and (3.91) ensure the correct down-scaling of the strain tensors.

Due to the rough top surface, the boundary condition on the (R)SVE must be applied carefully. As proposed in [10], thin structures can be considered for which the plane-stress state is assumed. The top and bottom surfaces are then stress-free with

$$\boldsymbol{t}_{m}\left(\boldsymbol{x}\right) = \boldsymbol{0} \qquad \forall \boldsymbol{x}\in S_T\cup S_{BO}, \tag{3.98}$$

---

[5] as $\boldsymbol{\sigma}$ is symmetric, $\boldsymbol{\sigma} : \delta\boldsymbol{\epsilon} = \boldsymbol{\sigma} : \delta\boldsymbol{\varepsilon}$

which satisfies (3.97) on the $S_T \cup S_{BO}$ part of $\partial\omega$. The conditions (3.87) and (3.91) are not constrained on those faces, and as a result some macro-strain and higher-order macro-strain modes cannot be down-scaled on the SVE. However, this is in agreement with the plate kinematics as it will be discussed in Section 3.4.3.

The fluctuation field is constrained on the other four flat surfaces. Note that Eq. (3.87) is automatically satisfied with Kinematic Uniform Boundary Conditions (KUBCs) –$\boldsymbol{u}'_{\mathrm{m}} = 0$– and static Uniform Boundary Conditions (SUBCs) –as constraining a uniform surface traction corresponds to enforcing Eq. (3.87) [59]– while Eq. (3.91) is automatically satisfied for KUBCs and also for Periodic Boundary Conditions (PBCs) if (3.87) is enforced simultaneously.

In this paper we choose to apply Mixed Uniform Boundary Conditions (MUBCs). Although periodic boundary conditions could also be considered, as the geometry is not periodic MUBCs are a simpler alternative. Moreover it will been shown in Section 5.2.1 that the effect of the grain uncertainties is more important than the effect of the boundary conditions. In order to apply MUBCs, on the one hand, Kinematic Uniform Boundary Conditions (KUBCs) are considered in the plate in-plane directions:

$$\boldsymbol{u}'_{\mathrm{m}_x}(\boldsymbol{x}) = \boldsymbol{u}'_{\mathrm{m}_y}(\boldsymbol{x}) = 0 \qquad \forall \boldsymbol{x} \in S_F \cup S_{BA}, \text{ and } \forall \boldsymbol{x} \in S_L \cup S_R, \tag{3.99}$$

where the x-direction is the direction normal to the surfaces S_F and S_{BA}, and the y-direction is the direction normal to the surfaces S_L and S_R. On the other hand, Static Uniform Boundary Conditions (SUBCs) are considered in the plate out-of-plane direction, with

$$\boldsymbol{t}^z_{\mathrm{m}} = \boldsymbol{n}_{\mathrm{m}_k} \boldsymbol{\sigma}^{kz}_{\mathrm{M}} \quad \forall \boldsymbol{x} \in S_F \cup S_{BA}, \text{ and } \forall \boldsymbol{x} \in S_L \cup S_R. \tag{3.100}$$

Combining Eqs. (3.99) and (3.100), as S_F and S_{BA} are opposite flat surfaces, the Hill-Mandel condition can be verified for the forward and backward surfaces part of $\partial\omega$ as

$$\int_{S_F \cup S_{BA}} \boldsymbol{t}_{\mathrm{m}_i} \boldsymbol{u}'_{\mathrm{m}_i} dS \;=\; \int_{S_F \cup S_{BA}} \boldsymbol{t}^z_{\mathrm{m}} \boldsymbol{u}'_{\mathrm{m}_z} dS = \boldsymbol{\sigma}^{kz}_{\mathrm{M}} \int_{S_F \cup S_{BA}} \boldsymbol{n}_{\mathrm{m}_k} \boldsymbol{u}'_{\mathrm{m}_z} dS. \tag{3.101}$$

This last term vanishes providing the boundary condition (3.87) has been enforced on the two surfaces. The same applies for the last two surfaces S_L and S_R, satisfying the Hill-Mandel condition.

For these last four side surfaces, although the condition (3.91) is automatically satisfied for the x- and y-components of the displacement field due to the use of KUBCs, we do not constraint it along the z-component of the displacement field to reduce the number of constraints in the system. Indeed, not enforcing this condition corresponds to the impossibility to constrain high-order deformation modes which are not down-scaled from the Kirchhoff-Love plate kinematics as it will be discussed in Section 3.4.3, and has thus no effect on the homogenisation result.

3.4.3 Resolution of the constrained micro-scale finite element problem and extraction of the resultant material tensor $\boldsymbol{U}$

In the context of the meso-scale BVP resolution, the tangent matrix of the second-order multi-scale process can be extracted by condensing the micro-scale stiffness matrix using the boundary condition constraints. To this end, the process described in Section 3.3.3 is applied by considering the kinematic constraint $\boldsymbol{K}_{\mathrm{M}}$ from the vector forms of $\boldsymbol{\epsilon}_M$ and $\boldsymbol{\eta}_M$. Details can be found in [44, 67]. In case of linear elasticity, this tangent matrix corresponds to the homogenised material operators, yielding

$$\boldsymbol{n}_{\mathrm{M}} = \mathbb{C}_1 : \boldsymbol{\epsilon}_{\mathrm{M}} + \mathbb{C}_2 \vdots \boldsymbol{\eta}_{\mathrm{M}}\,, \tag{3.102}$$

$$\tilde{\boldsymbol{m}}_{\mathrm{M}} = \mathbb{C}_3 : \boldsymbol{\epsilon}_{\mathrm{M}} + \mathbb{C}_4 \vdots \boldsymbol{\eta}_{\mathrm{M}}\,, \tag{3.103}$$

where $\mathbb{C}_1$, $\mathbb{C}_2$, $\mathbb{C}_3$, and $\mathbb{C}_4$ are respectively a fourth order tensor, two fifth order tensors, and one sixth order tensor.

However, in the context of plates at the macro-scale, the relevant material tensors are the resultant material tensors $\mathbb{C}_1^*$, $\mathbb{C}_2^*$, $\mathbb{C}_3^*$, and $\mathbb{C}_4^*$ defined in Eqs. (2.78-2.79), or in the matrix form, the resultant tensor $\boldsymbol{U}$ defined in Eq. (2.80). We thus need to extract the resultant tensors from the homogenised tensors $\mathbb{C}_1$, $\mathbb{C}_2$, $\mathbb{C}_3$, and $\mathbb{C}_4$. To this end, the kinematic constraints and the homogenised properties resulting from the meso-scale BVP resolution, see Fig. 3.3, can be written in terms of their components.

The homogenised symmetric first-order stress tensor has 6 independent components and is expressed as:

$$\boldsymbol{n}_{\mathrm{M}} = \tilde{\boldsymbol{n}}^{*\,\alpha\beta}\boldsymbol{E}_\alpha \otimes \boldsymbol{E}_\beta + \tilde{\boldsymbol{q}}^{*\,\alpha}\left(\boldsymbol{E}_\alpha \otimes \boldsymbol{E}_z + \boldsymbol{E}_z \otimes \boldsymbol{E}_\alpha\right) + \tilde{\boldsymbol{n}}^{zz}\boldsymbol{E}_z \otimes \boldsymbol{E}_z\,, \tag{3.104}$$

where due to the plane-stress state, $\tilde{\boldsymbol{n}}_{zz} = 0$ is naturally enforced during the meso-scale BVP resolution as the top and bottom surfaces are stress-free surfaces, see Section 3.4.2. In this section, we drop the subscript M on the resultant stress component for conciseness. The homogenised second-order stress tensor has 18 independent components. Considering the symmetric 2×2 matrix $\tilde{\boldsymbol{m}}^{*\,\alpha\beta}$, the component $\tilde{\boldsymbol{m}}^{\mathrm{skew}\,xy} = -\tilde{\boldsymbol{m}}^{\mathrm{skew}\,yx}$ related to the lack of major symmetry in $\tilde{\boldsymbol{m}}_M$, the 2×2 symmetric matrix $\boldsymbol{p}^{1^{\alpha\beta}}$, the 2-component vectors $\boldsymbol{p}^{2^{\alpha}}$ and $\boldsymbol{p}^{3^{\alpha}}$, and the component $\tilde{\boldsymbol{m}}^{zz}$, the homogenised second-order stress tensor reads

$$\begin{aligned}
\tilde{\boldsymbol{m}}_{\mathrm{M}} &= \left(\tilde{\boldsymbol{m}}^{*\,\alpha\beta} + \tilde{\boldsymbol{m}}^{\mathrm{skew}\,\alpha\beta}\right)\left(\boldsymbol{E}_\alpha \otimes \boldsymbol{E}_\beta \otimes \boldsymbol{E}_z + \boldsymbol{E}_\alpha \otimes \boldsymbol{E}_z \otimes \boldsymbol{E}_\beta\right)\\
&+ \boldsymbol{p}^{1^{\alpha\beta}}\left(\boldsymbol{E}_z \otimes \boldsymbol{E}_\alpha \otimes \boldsymbol{E}_\beta\right) + \boldsymbol{p}^{2^{\alpha}}\left(\boldsymbol{E}_z \otimes \boldsymbol{E}_z \otimes \boldsymbol{E}_\alpha + \boldsymbol{E}_z \otimes \boldsymbol{E}_\alpha \otimes \boldsymbol{E}_z\right)\\
&+ \boldsymbol{p}^{3^{\alpha}}\left(\boldsymbol{E}_\alpha \otimes \boldsymbol{E}_z \otimes \boldsymbol{E}_z\right) + \tilde{\boldsymbol{m}}^{zz}\boldsymbol{E}_z \otimes \boldsymbol{E}_z \otimes \boldsymbol{E}_z + \hat{\tilde{\boldsymbol{m}}}_M,
\end{aligned} \tag{3.105}$$

where $\hat{\tilde{\boldsymbol{m}}}_{\mathrm{M}}$ represents the contribution of the 6 remaining independent components along $\boldsymbol{E}_\alpha \otimes \boldsymbol{E}_\beta \otimes \boldsymbol{E}_\gamma$. Owing to the plane-stress state, $\tilde{\boldsymbol{m}}^{zz} = 0$ is naturally enforced during the meso-scale BVP resolution. Similarly $\boldsymbol{p}^{1^{xy}} = \boldsymbol{p}^{1^{yx}} = 0$, and $\boldsymbol{p}^{2^{\alpha}} = 0$ are also verified because of the plane-stress state.

The symmetric first-order kinematic constraint $\boldsymbol{\varepsilon}_{\mathrm{M}}$ possesses 6 independent components and can be written as

$$\boldsymbol{\varepsilon}_{\mathrm{M}} = \boldsymbol{\varepsilon}^{*}_{\alpha\beta} \boldsymbol{E}_{\alpha} \otimes \boldsymbol{E}_{\beta} + \boldsymbol{\gamma}^{*}_{\alpha} \left(\boldsymbol{E}_{\alpha} \otimes \boldsymbol{E}_{z} + \boldsymbol{E}_{z} \otimes \boldsymbol{E}_{\alpha} \right) + \boldsymbol{\varepsilon}^{*}_{zz} \boldsymbol{E}_{z} \otimes \boldsymbol{E}_{z}, \tag{3.106}$$

where $\boldsymbol{\varepsilon}^{*}_{\alpha\beta}$ is a 2×2 symmetric matrix defining the membrane deformation. In this expression, the out-of-plane strain $\boldsymbol{\varepsilon}^{*}_{zz}$ is an unknown not necessarily defined in the macro-scale plate problem, and is not down-scaled during the multi-scale process as its value results from the plane-stress state. The second-order kinematic constraint is written as:

$$\begin{aligned} \boldsymbol{\eta}_{\mathrm{M}} &= \left(\boldsymbol{\kappa}^{*}_{\alpha\beta} + \boldsymbol{\kappa}^{\mathrm{skew}}_{\alpha\beta} \right) \left(\boldsymbol{E}_{\alpha} \otimes \boldsymbol{E}_{\beta} \otimes \boldsymbol{E}_{z} + \boldsymbol{E}_{\alpha} \otimes \boldsymbol{E}_{z} \otimes \boldsymbol{E}_{\beta} \right) \\ &+ \boldsymbol{b}^{1}_{\alpha\beta} \left(\boldsymbol{E}_{z} \otimes \boldsymbol{E}_{\alpha} \otimes \boldsymbol{E}_{\beta} \right) + \boldsymbol{b}^{2}_{\alpha} \left(\boldsymbol{E}_{z} \otimes \boldsymbol{E}_{z} \otimes \boldsymbol{E}_{\alpha} + \boldsymbol{E}_{z} \otimes \boldsymbol{E}_{\alpha} \otimes \boldsymbol{E}_{z} \right) \\ &+ \boldsymbol{b}^{3}_{\alpha} \left(\boldsymbol{E}_{\alpha} \otimes \boldsymbol{E}_{z} \otimes \boldsymbol{E}_{z} \right) + \boldsymbol{b}_{zz} \boldsymbol{E}_{z} \otimes \boldsymbol{E}_{z} \otimes \boldsymbol{E}_{z} + \hat{\boldsymbol{\eta}}_{M}, \end{aligned} \tag{3.107}$$

where $\boldsymbol{\kappa}^{*}_{\alpha\beta}$ is a 2×2 symmetric matrix containing the bending curvatures so that $\boldsymbol{\kappa}^{*}_{\alpha\beta} = \frac{\boldsymbol{\eta}_{\mathrm{M}\,\alpha\beta z} + \boldsymbol{\eta}_{\mathrm{M}\,\beta\alpha z}}{2}$, $\boldsymbol{\kappa}^{\mathrm{skew}}_{xy} = -\boldsymbol{\kappa}^{\mathrm{skew}}_{yx}$ is the skewness, $\boldsymbol{b}^{1}_{\alpha\beta}$ is a 2×2 symmetric matrix, $\boldsymbol{b}^{2}_{\alpha}$ and $\boldsymbol{b}^{3}_{\alpha}$ are 2-component vectors, $\boldsymbol{b}_{zz}$ is a scalar, and where $\hat{\boldsymbol{\eta}}_{\mathrm{M}}$ represents the contribution of the 6 remaining independent components along $\boldsymbol{E}_{\alpha} \otimes \boldsymbol{E}_{\beta} \otimes \boldsymbol{E}_{\gamma}$. In the frame of plate elements, the higher-order strain components $\boldsymbol{b}^{1}_{xy} = \boldsymbol{b}^{1}_{yx}$, $\boldsymbol{b}^{2}_{\alpha}$, and $\boldsymbol{b}_{zz}$ are four components that are not down-scaled from the macro-scale as their values result from the plane-stress state.

Five equations linking the homogenised stresses ($\tilde{\boldsymbol{n}}_{zz} = 0$, $\boldsymbol{p}^{1^{xy}} = \boldsymbol{p}^{1^{yx}} = 0$, $\boldsymbol{p}^{2^{\alpha}} = 0$, and $\tilde{\boldsymbol{m}}^{zz} = 0$[6]) to the kinematic constraints can thus be directly removed from the system (3.102-3.103) as five kinematic constraints ($\boldsymbol{\varepsilon}^{*}_{zz}$, $\boldsymbol{b}^{1}_{xy} = \boldsymbol{b}^{1}_{yx}$, $\boldsymbol{b}^{2}_{\alpha}$, and $\boldsymbol{b}_{zz}$) result from the boundary conditions constraining the plane-stress state.

Moreover, as the plate elements at the macro-scale follow the Kirchhoff-Love assumption and as this hypothesis is not applied on the RSVE itself during the computational homogenisation, the contribution of some stresses is explicitly enforced to zero to recover the behaviour associated to this assumption. Therefore the remaining system of 19 equations linking 19 homogenised stress components to 19 kinematic constraints components can be reduced. The out-of-plane shear $\tilde{\boldsymbol{q}}^{*\,\alpha}$ is enforced to be zero. Similarly, the influence of the out-of-plane shear on the higher-order stress, obtained through $\boldsymbol{p}^{1^{\alpha\alpha}}$ (no sum on α meant), $\boldsymbol{p}^{3^{\alpha}}$, and through the skew-symmetric matrix $\tilde{\boldsymbol{m}}^{\mathrm{skew}\;xy}$, are enforced to zero. As the elements of $\hat{\tilde{\boldsymbol{m}}}_{\mathrm{M}}$ cannot be up-scaled to the plate problem, they are also enforced to zero. We thus gather those stress contributions to be enforced to zero in the 13-component vector (no sum on α meant)

$$\boldsymbol{\psi}_{0} = \left[\boldsymbol{q}^{*\alpha}, \tilde{\boldsymbol{m}}^{\mathrm{skew}\,xy}, \boldsymbol{p}^{1^{\alpha\alpha}}, \boldsymbol{p}^{3^{\alpha}}, \hat{\tilde{\boldsymbol{m}}}_{\mathrm{M}}{}^{\alpha\beta\gamma} \right]. \tag{3.108}$$

---

[6] For ease of implementation, the RSVE centroïd is defined as the centre of the parallelepiped defined using the average plane of the rough-surface and is thus not exactly the RSVE centroïd, so these terms are several orders of magnitude lower than the other but not strictly zero as Eq. (3.85) is not exactly satisfied.

The corresponding strain components, which are not down-scaled from the macro-scale plate model, are gathered in the 13-component vector (no sum on α meant)

$$\boldsymbol{\chi}_u = \left[\boldsymbol{\gamma}^*_\alpha, \boldsymbol{\kappa}^{\text{skew}}_{xy}, \boldsymbol{b}^1_{\alpha\alpha}, \boldsymbol{b}^3_\alpha, \hat{\boldsymbol{\eta}}_{\text{M}\,\alpha\beta\gamma}\right] . \tag{3.109}$$

Once the plane-stress state and the Kirchhoff-Love assumption being considered, the remaining stresses are the resultant (symmetric) membrane stress $\tilde{\boldsymbol{n}}^*$ and the resultant (symmetric) bending stress $\tilde{\boldsymbol{m}}^*$. These symmetric matrices can be written in terms of the 6-component vector

$$\boldsymbol{\psi}^\star_\sigma = \left[\tilde{\boldsymbol{n}}^{*\ \alpha\beta}, \tilde{\boldsymbol{m}}^{*\ \alpha\beta}\right] . \tag{3.110}$$

Similarly, the relevant 6 independent strains are the elements of the (symmetric) membrane strains $\boldsymbol{\varepsilon}^*$ and the (symmetric) curvatures $\boldsymbol{\kappa}^*$, which can be written in terms of the 6-component vector

$$\boldsymbol{\chi}^\star_\epsilon = \left[\boldsymbol{\varepsilon}^*_{\alpha\beta}, \boldsymbol{\kappa}^*_{\alpha\beta}\right] . \tag{3.111}$$

Therefore, the linear system (3.102-3.103) is reorganised into the system

$$\begin{pmatrix} \boldsymbol{\psi}^\star_\sigma \\ \boldsymbol{\psi}_0 \end{pmatrix} = \begin{pmatrix} \mathbf{C}_{\epsilon\epsilon} & \mathbf{C}_{\epsilon u} \\ \mathbf{C}_{u\epsilon} & \mathbf{C}_{uu} \end{pmatrix} \begin{pmatrix} \boldsymbol{\chi}^\star_\epsilon \\ \boldsymbol{\chi}_u \end{pmatrix} , \tag{3.112}$$

where the $\mathbf{C}_{ik}$ elements are matrices obtained from the different tangents $\mathbb{C}_i$. As $\boldsymbol{\psi}_0 = \mathbf{0}$ is enforced, this system reduces to

$$\boldsymbol{\psi}^\star_\sigma = \left(\mathbf{C}_{\epsilon\epsilon} + \mathbf{C}_{\epsilon u}\mathbf{C}^{-1}_{uu}\mathbf{C}_{u\epsilon}\right)\boldsymbol{\chi}^\star_\epsilon . \tag{3.113}$$

Finally, the resultant material tensor $\boldsymbol{U}_\text{M}$ (2.80), a 6 × 6 matrix already introduced in Section 2.5, is retrieved as the linear operator between $\boldsymbol{\psi}^\star_\sigma$ and $\boldsymbol{\chi}^\star_\epsilon$:

$$\boldsymbol{U}_\text{M} = \left(\mathbf{C}_{\epsilon\epsilon} + \mathbf{C}_{\epsilon u}\mathbf{C}^{-1}_{uu}\mathbf{C}_{u\epsilon}\right) . \tag{3.114}$$

3.5 Assessing the stochastic behaviour: stochastic homogenisation and meso-scale random fields

For generalisation purposes, let us first define a random vector field $\mathcal{U}\left(\boldsymbol{x}, \boldsymbol{\theta}\right) : \boldsymbol{D} \times \boldsymbol{\Omega} \to \boldsymbol{W}$ where $\boldsymbol{W}$ is the output space. At each spatial position $\boldsymbol{x}$ and for each randomness state $\boldsymbol{\theta}$, a random vector $\mathcal{U}$ of size n defined over $\boldsymbol{W}$ is assigned. The components of the vector $\mathcal{U}$ can be the components of the elasticity tensor $\boldsymbol{C}_\text{M}$, which means that $\mathcal{U}^{(1)}, ..., \mathcal{U}^{(21)}$ are the 21 independent components of $\boldsymbol{C}_\text{M}$. Additional information, if available and required, can be appended to the vector by taking the independent components of, *e.g.*, the different thermo-mechanics fields $\boldsymbol{\kappa}_\text{M}$, and $\boldsymbol{\alpha}_\text{M}$. Different problems can also be solved. In the case of thin plates, the vector field $\mathcal{U}$ is made of the independent components of the generalised tangent $\boldsymbol{U}_{\mathrm{M}}$, and of $\bar{\rho}_{\mathrm{M}}$ (the uncertainty effect in the cross section inertia I_p is approximated as $I_p = \frac{\bar{\rho}^3}{12\rho^2}$). In other words, the vector field $\mathcal{U}$ is made of all the components of the properties of interest.

Assessing the stochastic behaviour of a multidimensional random field involves the evaluation of three types of information:

- the probability of each element of $\mathcal{U}$ itself through the marginal probability density function,
- the spatial correlation, and
- the stochastic dependence between the different elements of $\mathcal{U}$ which can be computed with the cross-correlation.

This information can be estimated thanks to measurements, when it is available for the application of interest, or with simulations, which is the case in this work. The recourse to homogenisation techniques described in the previous sections enables the assessment of the random field $\mathcal{U}$.

The homogenisation computes, from a (R)SVE sample, a homogenised property. Therefore, from samples of (R)SVEs, samples of the homogenised properties (and thus samples of $\mathcal{U}$) can be computed and the marginal probability density function of its elements can be obtained with the help of kernel density estimation or, if a particular PDF shape is assumed, with the estimation of the moments. The results are meaningful only when enough samples are available and the convergence is observed (law of large numbers). Thus the probability distribution of each element of $\mathcal{U}$ is known.

However, the spatial correlation cannot be obtained from (R)SVE samples directly. A windowing technique must be used [5]. Taking the 3D case as an example, to obtain one random field realisation, a volume which contains the information of the micro structure is first created. This volume should be large enough in order to be able to capture a complete spatial correlation, *i.e.* enough for all the spatial correlations to reach zero. Then, from this volume, a complete series of SVEs, which are indexed by the coordinates (x_1, x_2, x_3) of their centres, is extracted, see Fig. 3.4(a). After evaluating the apparent meso-scale material properties on these SVEs, together with the spatial relation (the central coordinates) of these SVEs, a realisation of the required random field is obtained. We need to note that the distance between the neighbouring SVEs, which is defined by the distance between their centres, needs to be small enough to obtain the behaviour of the decline process of the spatial correlation functions.

In this work, the random field is assumed to be homogeneous. With a sufficient number of random field realisations, the spatial cross-correlation matrix $\underline{\boldsymbol{R}}_{\mathcal{U}}(\boldsymbol{\tau})$ of the assumed homogeneous vector field $\mathcal{U}$, underlying the spatial correlation information, is evaluated as follows

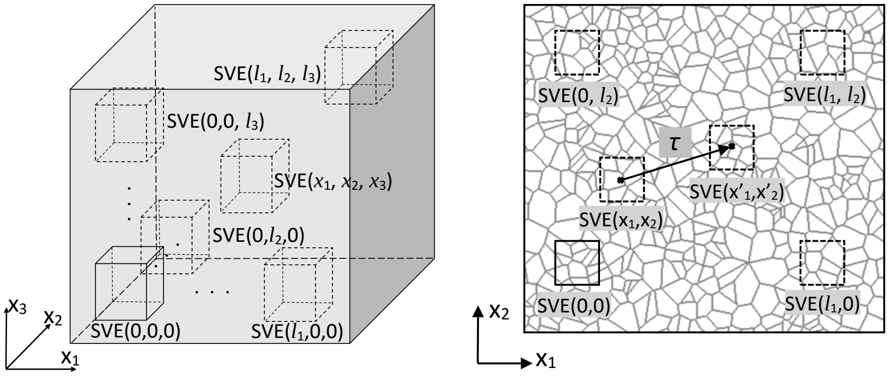

(a) 3-Dimensional case

(b) 2-Dimensional case (Poisson-Voronoï tessellation)

Figure 3.4: Extraction of a series of SVEs

$$\underline{\boldsymbol{R}}_{\mathcal{U}}^{(rs)}(\boldsymbol{\tau}) = \frac{\mathbb{E}\left[\left(\mathcal{U}^{(r)}(\boldsymbol{x}) - \mathbb{E}\left[\mathcal{U}^{(r)}\right]\right)\left(\mathcal{U}^{(s)}(\boldsymbol{x}+\boldsymbol{\tau}) - \mathbb{E}\left[\mathcal{U}^{(s)}\right]\right)\right]}{\sigma_{\mathcal{U}^{(r)}}\sigma_{\mathcal{U}^{(s)}}} \qquad \forall\, r,\, s = 1,\, ...,\, n\,, \tag{3.115}$$

where $\boldsymbol{\tau}$ is a spatial vector between the centres of two SVEs, see Fig. 3.4(b), and where $\mathcal{U}^{(r)}$ is the r^{th} entry of $\mathcal{U}$. The requirement of a large enough volume can be expressed as $\underline{\boldsymbol{R}}_{\mathcal{U}}^{(rs)}(\boldsymbol{l}) = 0, \forall\, r,\, s = 1,\, ...,\, n$, see Fig.3.4. The cross-correlation are included in Eq. (3.115), thus the stochastic information can be computed.

3.6 Conclusion

Throughout this chapter, we have extracted the uncertain material behaviour at a meso-scale by recourse to stochastic homogenisation performed on volume elements. Three different cases were considered. First, the mechanical behaviour of the SVE was investigated with a first-order computational homogenisation. Afterwards, the procedure was extended for a thermo-mechanical analysis. Finally, the case of rough SVEs was investigated with the recourse to second-order homogenisation. Stochastic homogenisation thus allows the elaboration of a meso-scale random field which can be used in the frame of a SFEM procedure as described in Chapter 2. However, performing a homogenisation analysis at each spatial position of interest and for each desired random case is too expensive. Therefore we need a stochastic model: it is the focus of Chapter 4.

Chapter 4

Stochastic model of the meso-scale properties

Following the procedure described in Chapter 3, the stochastic behaviour of the properties of interest can be assessed. The purpose of Chapter 4 is to use this information in a stochastic model.

First the modelling of a spatially correlated vector field is considered. Then the particular case of the generation of a positive-definite matrix is looked into. The actual method considered in this work, the spectral approach, is described in details. It aims at taking into account the spatial correlation, the cross-correlation and the positive-definiteness of concerned matrices. Finally the extension to non-Gaussian fields and considerations about implementation are investigated.

Throughout this chapter, different vector fields are considered. The following notations are used. Random vector fields are represented by calligraphic letters. When a method is described for a general n sized vector field, it is referred to as $\mathcal{V}$. Another field already introduced in the previous chapter is $\mathcal{U}$. Its components are the independent components of the homogenised properties computed in Chapter 3. To ease its stochastic modelling, it is mapped to a new vector field also denoted $\mathcal{V}$. This is described in Section 4.2.2. The r^{th} component of the vector field $\mathcal{V}$ is referred to as $\mathcal{V}^{(r)}$. The mean and the fluctuation of $\mathcal{V}$ are referred to respectively as $\bar{\mathcal{V}}$ and $\mathcal{V}'$ so that $\mathcal{V} = \bar{\mathcal{V}} + \mathcal{V}'$. The stochastic model is built based on initial samples of the vector field. These initial samples are referred to with the subscript $''0''$. The stochastic model will be used to generate samples of the vector field. The subscript $''\text{gen}''$ is used to refer to these new samples. Therefore, the initial and generated samples of $\mathcal{V}$ are referred to respectively as $\mathcal{V}_0$ and $\mathcal{V}_{\text{gen}}$.

4.1 Random fields

As already described in Section 2.1, a random field is a collection of possibly correlated random variables, each of them being associated to a spatial position in our case. In the following sections, we only consider the case of homogeneous random fields. Two methods are often encountered in the literature and can be used to model and generate spatially correlated vector fields: the Karhunen-Loève expansion (KL) and the spectral methods. Both will now be described.

4.1.1 Karhunen-Loève

A random field can be represented with the Karhunen-Loève expansion [88, 24, 47], which basically consists of an orthogonal series expansion based on a covariance decomposition of the random field. The orthogonal basis used for the series expansion consists in the eigenfunctions and eigenvalues of the covariance function obtained with the solution of the Fredholm equation of the second kind:

$$\int_{\boldsymbol{D}} R\left(\boldsymbol{x}, \boldsymbol{x}'\right) u_i\left(\boldsymbol{x}'\right) d\boldsymbol{x}' = \lambda_i u_i\left(\boldsymbol{x}'\right) \ , \tag{4.1}$$

where R is the uni-variate covariance function, $u_i(\boldsymbol{x})$ is the i^{th} eigenfunction and λ_i is the i^{th} eigenvalue.

Samples $\mathcal{V}_{\text{gen}}$ for the field $\mathcal{V}$ are obtained following:

$$\mathcal{V}_{\text{gen}}\left(\boldsymbol{x}, \boldsymbol{\theta}\right) = \bar{\mathcal{V}} + \sum_{i=1}^{\infty} \sqrt{\lambda_i} u_i\left(\boldsymbol{x}\right) \xi_i\left(\boldsymbol{\theta}\right) \ . \tag{4.2}$$

In this equation, $\bar{\mathcal{V}}$ is the mean of $\mathcal{V}$ and ξ_i are zero-mean unit variance uncorrelated random variables. From the central limit theorem, if the ξ_i variables are independent, then $\mathcal{V}$ follows a Gaussian distribution.

Without loss of generality, the eigenvalues can be arranged in decreasing order. Thus arises an interesting property of Karhunen-Loève fields: a truncated KL expansion is optimal in the mean square sense. In other words, the approximated field $\tilde{\mathcal{V}}$ which includes a finite number N of eigenvalues and eigenfunctions minimises the mean square error that can be obtained with an expansion truncated after N terms.

The main problem with the KL expansion is solving the Fredholm equation (4.1). Some analytical solution exists: it is the case for the exponential correlation and the solution can be found in [47]. If the solution is not a priori known, it can be costly to compute it. The problem can also be solved in a discrete case, thus involving a matrix subspace, eigenvalues, and eigenvectors. This allows for a straightforward extension to multi-variate Karhunen-Loève fields in 3D space: the covariance matrix is built based on the cross-covariance between each element of the random vector field at each discrete distance of interest.

4.1.2 Spectral methods

A common way to represent a random field is with the spectral representation method. It is briefly described in this section and more details can be found in Section 4.3. Once again, the stochastic field is expanded over a set of orthogonal basis functions. In the spectral representation method, trigonometric functions are used. First, the spectral density S of the random field must be computed. The spectral density is the covariance expressed in the frequency space (Wiener-Khinchin theorem). By computing the Fast Fourier Transform of the covariance function, the spectral density S is known. Once it is computed, the stochastic field in 1D can be expanded as:

$$\mathcal{V}_{\text{gen}}\left(x,\boldsymbol{\theta}\right) = \bar{\mathcal{V}} + \sum_{i=1}^{N} \sqrt{\left(2S\left(k_i\right)\Delta k\right)}\,\eta_i\left(\boldsymbol{\theta}\right)\cos\left[k_i x + \phi_i\left(\boldsymbol{\theta}\right)\right] \ , \tag{4.3}$$

where N is the number of retained frequency k_i, Δk is the frequency increment defined so that $\Delta k = \frac{k_u}{N}$, k_u is a cut-off frequency bounding the frequency space, ϕ_i represents a random phase uniformly distributed in the range $[0, 2\pi]$, and the η_i variables add randomness to the amplitude if needed. The resulting field $\mathcal{V}_{\text{gen}}$ is asymptotically Gaussian due to the central limit theorem.

As it is described in [25, 88], adding randomness in the amplitude has advantages and drawbacks. When only the phase angle is random, the stochastic field is Gaussian for $N \to \infty$, while it is Gaussian for any value of N with a random amplitude randomness η_i. However, adding randomness to the amplitude weakens the ergodic properties of the field [25].

The extension of the method for random vectors in a 3D space is considered in Section 4.3.

4.2 Positive-definite matrix generation: different approaches

When random fields involve small matrices with no particular constraints, it is straightforward to use Karhunen-Loève expansions or the spectral representation method to generate a vector field containing all the elements of the matrices of interest. However, when big matrices are involved, modelling the cross-correlation between each combination of elements might not be mandatory for some applications. Furthermore, by generating directly the elements of the matrices, some properties might be lost such as bounds or positive-definiteness. In [86], matrices with a known trace are studied. This can be useful when treating uncertainties over the mass matrix of a dynamical system when the total mass is known (and therefore the trace of the matrix) but not its spatial distribution.

In this work, most matrices of interest are bounded positive-definite matrices: the elasticity tensor in Voigt notations $\boldsymbol{C}$, the generalised tangent $\boldsymbol{U}$, ... We focus on the generation of such matrices. To remain general in this section, we consider the random field of the symmetric positive-definite matrix $\boldsymbol{B}$ of size n with a lower bound $\boldsymbol{B}_L$ [1] and a mean $\bar{\boldsymbol{B}}$.

4.2.1 Maximum entropy based approach

The entropy, as defined by Shannon [82] in the frame of information theory, can be considered as a measure of the amount of information. In probability theory, it can be seen as a measure through a scalar value of the amount of uncertainty. To illustrate this notion of entropy, let us consider the case of a discrete random variable with a finite set of possible realisations. If the probability of one event is 1 and the probability of the other events is 0, the random variable is certain and the entropy is minimum. However, if the probabilities of all realisations are equal, then the uncertainty, and therefore the entropy is maximum.

If the probability density function of the random matrix $\boldsymbol{B}$ is noted $p\left(\boldsymbol{B}\right)$, then the entropy associated to this PDF, noted $s\left(p\right) \in \mathbb{R}$ is defined with an integration with respect to measure $d\boldsymbol{B}$ [86]:

$$s\left(p\right) = -\int_{\boldsymbol{M}_n^+\left(\mathbb{R}\right)} p\left(\boldsymbol{B}\right) \log\left(p\left(\boldsymbol{B}\right)\right) d\boldsymbol{B}\,. \tag{4.4}$$

The notion of entropy can be used to define a probability density function. Assuming some information concerning a random quantity, the maximum entropy principle, stated by Jaynes [36] and also described in [41], can be used to define a probability density function corresponding to the randomness. The uncertainty refers to the modelled variability of the randomness while unknown information corresponds to a lack of information concerning this randomness. To avoid including unknown information in the model, the maximum entropy principle maximises the entropy $s(p)$ and therefore the overall uncertainty of the system under a set of constraints encompassing the available information. In other words, what is unknown is uncertain.

A common example used to described the maximum entropy principle is the following [3]. The mean and the variance of a continuous random variable u defined over $\mathbb{R}$ are the only known information about this random variable (e.g. due to limited experimental data). The maximum entropy principle can be used with 3 constraints. One constraint normalises the probability density function: $\int_{\mathbb{R}} p\left(u\right) du = 1$. The other constraints enforce respectively the mean and the variance of u. Solving the maximisation problem under the set of constraint, for example with the Lagrange multiplier method, gives the Gaussian distribution for u. The Gaussian distribution in this case is a guess based on the maximum entropy principle which considers unknown information to be uncertain. If more information about the random variable is known, such as a lower bound, another distribution may become a more appropriate guess.

The method can be applied to obtain the probability density function of positive-definite matrices [86]. First, the mean matrix $\bar{\boldsymbol{B}}$ can be removed of

---

[1] Based on the Loewner ordering, $\boldsymbol{A} > \boldsymbol{B}$ if $\boldsymbol{A} - \boldsymbol{B}$ is positive definite and $\boldsymbol{A} \geq \boldsymbol{B}$ if $\boldsymbol{A} - \boldsymbol{B}$ is positive semi-definite

the problem without loss of generality. As $\bar{\boldsymbol{B}}$ is positive-definite, it possesses a Cholesky decomposition:

$$\bar{\boldsymbol{B}} = \bar{L}^T \bar{L}\,, \tag{4.5}$$

where $\bar{L}$ is an upper triangular matrix. The maximum entropy principle is used to generate the matrix $\boldsymbol{G}$ defined so that:

$$\boldsymbol{B} = \bar{L}^T \boldsymbol{G} \bar{L}\,, \tag{4.6}$$

and $\mathbb{E}\left[\boldsymbol{G}\right] = \boldsymbol{I}_n$ where $\boldsymbol{I}_n$ is the $n \times n$ identity matrix.

The following optimisation problem has to be solved:

$$p\left(\boldsymbol{G}\right) = \underset{p(\boldsymbol{G'}) \in C_{ad}}{\arg\max} \left[- \int_{\boldsymbol{M}_n^+(\mathbb{R})} p\left(\boldsymbol{G'}\right) \log\left(p\left(\boldsymbol{G'}\right)\right) d\boldsymbol{G'} \right] , \tag{4.7}$$

where

$$C_{ad} = \left\{ p\left(\boldsymbol{G'}\right) = 0 \text{ if } G' \notin \boldsymbol{M}_n^+\left(\mathbb{R}\right) \right\} , \tag{4.8}$$

under the set of constraints:

$$\int_{\boldsymbol{M}_n^+(\mathbb{R})} p\left(\boldsymbol{G}\right) d\boldsymbol{G} = 1\,, \tag{4.9}$$

$$\mathbb{E}\left[\boldsymbol{G}\right] = \boldsymbol{I}_n\,, \tag{4.10}$$

$$\mathbb{E}\left[\ln(\det(\boldsymbol{G}))\right] = v\ ,\ |v| < +\infty\,. \tag{4.11}$$

The positive-definiteness of $\boldsymbol{G}$ is enforced by the set C_{ad}. The first constraint, Eq. (4.9), enforces the normalisation of the PDF. The second constraint, Eq. (4.10), enforces the mean of the matrix. The last constraint, Eq. (4.11), ensures mean-square convergence of the invertibility of $\boldsymbol{G}$[86] which is represented by the property (4.12):

$$\mathbb{E}\left[||\boldsymbol{G}^{-1}||_F^2\right] < +\infty\,, \tag{4.12}$$

where the operator $|| \bullet ||_F$ stands for the Frobenius norm[2].

As one can see, the variability of the matrix is not assessed yet. This is done in [86] through the dispersion parameter $\delta_{\boldsymbol{G}}$ defined as:

$$\delta_{\boldsymbol{G}}^2 = \frac{\mathbb{E}\left[||\boldsymbol{G} - \bar{\boldsymbol{G}}||_F^2\right]}{||\bar{\boldsymbol{G}}||_F^2}\,, \tag{4.13}$$

where $\bar{\boldsymbol{G}} = \mathbb{E}\left[G\right]$.

It is not required to add a constraint in the system on the value of the dispersion parameter. The optimisation problem defined with Eqs. (4.7-4.11) can be

---

[2] $|| \bullet ||_F = \sqrt{\sum_i \sum_j | \bullet^{(ij)} |^2}$

solved with the Lagrange multiplier method and the Lagrange multiplier corresponding to constraint (4.11) is used to enforce the dispersion parameter of the generated matrices. For the property (4.12) to hold, the dispersion parameter must be in the range [86]:

$$0 < \delta < \sqrt{(n+1)\,(n+5)^{-1}}\,. \tag{4.14}$$

From *a priori* known samples of $\boldsymbol{G}$, new samples can be generated according to the following procedure [26, 86]. First, the dispersion parameter has to be estimated from the samples using Eq. (4.13). Then an upper triangular matrix $\boldsymbol{P}$ can be generated according to:

$$\boldsymbol{P}_{ii} = \frac{\delta_{\boldsymbol{G}}}{\sqrt{n+1}}\sqrt{2h_{a_i}\left(\xi_{ii}\right)}\ \text{, and} \tag{4.15}$$

$$\boldsymbol{P}_{ij} = \frac{\delta_{\boldsymbol{G}}}{\sqrt{n+1}}\xi_{ij}\ \text{, for } i < j\,, \tag{4.16}$$

where $a_i = (n+1)/(2\delta_{\boldsymbol{G}}^2) + (1-i)/2$ and h_{a_i} defines a mapping from Gaussian random variables towards Gamma random variables with shape parameter a_i and rate parameter 1. The ξ_{ij} random variables are independent centred Gaussian random variables.

Finally, a sample of $\boldsymbol{G}$ can be obtained according to:

$$\boldsymbol{G} = \boldsymbol{P}^T\boldsymbol{P}\,, \tag{4.17}$$

as the triangular matrix $\boldsymbol{P}$ is the Cholesky decomposition of $\boldsymbol{G}$. Let us note that spatial correlation is added to the system in [26] through the random variables ξ_{ij}. The latter variables follow a parametric correlation based on the correlation length.

To conclude this section, the problem of bounded matrices is studied. Introducing a lower bound is straightforward as a linear change of variables can be done:

$$\boldsymbol{B} = \boldsymbol{B}_L + \Delta\boldsymbol{B}\,, \tag{4.18}$$

where the positive-definite matrix $\Delta\boldsymbol{B}$ can be generated according to the procedure defined in Section 4.2.1.

Let us now describe two ways to introduce both a lower and an upper bound $\boldsymbol{B}_L$ and $\boldsymbol{B}_U$. First, a non-linear change of variable can be made:

$$\boldsymbol{N} = \left(\boldsymbol{B} - \boldsymbol{B}_L\right)^{-1} - \left(\boldsymbol{B}_U - \boldsymbol{B}_L\right)^{-1}\,. \tag{4.19}$$

A positive-definite matrix $\boldsymbol{N}$ corresponds to a matrix $\boldsymbol{B}$ bounded by its lower and upper bound. The positive-definite matrix $\boldsymbol{N}$ can be generated according to the maximum entropy principle applied on positive-definite matrices. This procedure allows for a convenient stochastic model. However, the recourse to non-linear change of variables must be investigated with care as, while the generated samples of $\boldsymbol{N}$ follow the appropriate PDF, the corresponding $\boldsymbol{B}$ matrices might show a much different stochastic behaviour than the samples of $\boldsymbol{B}$. As an example, the mean of $\boldsymbol{B}$ cannot be enforced directly. This approach was used in [26, 69].

A second way to introduce both a lower and an upper bounds is the following. The maximum entropy principle is used along with a different set of constraints enforcing both the lower bound and the upper bound:

$$\boldsymbol{B} \in \boldsymbol{M}_n^+(\mathbb{R}) \text{ a.s.}\,, \tag{4.20}$$

$$\mathbb{E}\left[\boldsymbol{B}\right] = \bar{\boldsymbol{B}}\,, \tag{4.21}$$

$$\mathbb{E}\left[\ln(\det(\boldsymbol{B} - \boldsymbol{B}_L))\right] = v_l \ , \ |v_l| < +\infty\,, \tag{4.22}$$

$$\mathbb{E}\left[\ln(\det(\boldsymbol{B}_U - \boldsymbol{B}))\right] = v_u \ , \ |v_u| < +\infty\,, \tag{4.23}$$

where a.s. stands for almost sure[3].

Maximising entropy leads to the generalised matrix variate Kummer-Beta distribution [12], [26]. More flexibility, when compared to the non-linear change of variable (4.19), can be used to fix the behaviour of $\boldsymbol{B}$ as one more parameter is available, *i.e.* the Lagrange multiplier of the additional constraint. Let us note however that, as stated in [26], the generation of $\boldsymbol{B}$ according to this new set of constraints is not as straightforward as generating the positive-definite matrix $\boldsymbol{N}$: Markov Chain Monte-Carlo procedures or the slice sampling technique are required [26]. If the constraint (4.21) is dropped, the matrix-variate beta type I distribution is obtained [12]. The maximum entropy principle was also applied in [60]. In the latter, the variance of a set of eigenvalues are also enforced.

4.2.2 High number of parameters approach

In the case of a positive-definite matrix $\boldsymbol{B}$, possibly bounded, the following simple approach to build a stochastic model and to generate samples can be considered. Once again, the Cholesky decomposition is useful. Enforcing a lower bound $\boldsymbol{B}_L$ is important to satisfy the invertibility condition defined in [87]. As one can read in [86, 87], the existence of the expectation of the norm of the generated elasticity tensor inverse is a fundamental property of the matrix random field. This existence can be proven owing to the lower bound of the elasticity tensor.

Indeed, this fundamental property is written as [87]:

$$\mathbb{E}\left[\left(\sup_{\boldsymbol{x}\in\Omega}\left\|(\boldsymbol{B}(\boldsymbol{x},\boldsymbol{\theta}))^{-1}\right\|\right)^2\right] = c^2 < +\infty\,, \tag{4.24}$$

---

[3] A condition is almost sure if there is a subset of probability 0 where it is not respected. For example, for an infinite flip of coins, there is a subset where each flip results in the same result but its probability tends to zero when the number of flips tends to infinity (see `https://en.wikipedia.org/wiki/Almost_surely`)

where “sup” is the supremum and c is a finite positive constant. The norm operator used in Eq. (4.24) is defined as (for a square matrix) $\|\boldsymbol{A}\| = \left|\lambda_{\max}^{A}\right|$, where $\left|\lambda_{\max}^{A}\right|$ is the largest modulus of the eigenvalues of $\boldsymbol{A}$ [87].

Using the inverse of the lower bound $\boldsymbol{S}_{\mathrm{L}}$, the inverse of $\boldsymbol{B}$ noted $\boldsymbol{S}$, and the property $\boldsymbol{S}_{\mathrm{L}} - \boldsymbol{S}(\boldsymbol{x},\boldsymbol{\theta}) \geq 0$, from the definition of a positive semi-definite matrix, one has:

$$\boldsymbol{z}^T \boldsymbol{S}_{\mathrm{L}} \boldsymbol{z} - \boldsymbol{z}^T \boldsymbol{S}(\boldsymbol{x},\boldsymbol{\theta}) \boldsymbol{z} \geq 0 \quad \forall \boldsymbol{z} \in \mathbb{R}^n \,. \tag{4.25}$$

As this equation holds for every $\boldsymbol{z}$, it is also satisfied for the (normalised) eigenvector $\boldsymbol{z}_{\max}^{S}(\boldsymbol{x})$ of $\boldsymbol{S}(\boldsymbol{x},\boldsymbol{\theta})$, which corresponds to the maximum eigenvalue $\lambda_{\max}^{S}$, yielding

$$\left(\boldsymbol{z}_{\max}^{S}(\boldsymbol{x})\right)^T \boldsymbol{S}_{\mathrm{L}} \boldsymbol{z}_{\max}^{S}(\boldsymbol{x}) - \left(\boldsymbol{z}_{\max}^{S}(\boldsymbol{x})\right)^T \boldsymbol{S}(\boldsymbol{x},\boldsymbol{\theta}) \boldsymbol{z}_{\max}^{S}(\boldsymbol{x}) \geq 0 \,. \tag{4.26}$$

Using the definition of the maximum eigenvalue of a positive definite real symmetric matrix, one also has

$$\boldsymbol{z}^T \boldsymbol{S}_{\mathrm{L}} \boldsymbol{z} \leq \lambda_{\max}^{S_{\mathrm{L}}} ||\boldsymbol{z}||_2^2 \quad \forall \boldsymbol{z} \in \mathbb{R}^n \,, \tag{4.27}$$

Including (4.27) in (4.26) results in, as $\boldsymbol{z}_{\max}^{S}$ is normalised,

$$\lambda_{\max}^{S_{\mathrm{L}}} \geq \lambda_{\max}^{S} \,, \tag{4.28}$$

which demonstrates the property (4.24).

Based on the lower bound $\boldsymbol{B}_L$, a semi-positive definite symmetric increment $\Delta\boldsymbol{B}$ is defined such that

$$\boldsymbol{B} = \boldsymbol{B}_L + \Delta\boldsymbol{B} \,, \tag{4.29}$$

is always a positive definite matrix, bounded by $\boldsymbol{B}_L$. To generate such a positive semi-definite matrix $\Delta\boldsymbol{B}$, one can use the Cholesky decomposition as described in [86], which reads

$$\Delta\boldsymbol{B} = \boldsymbol{L}\boldsymbol{L}^T \,. \tag{4.30}$$

In this equation, the matrix $\boldsymbol{L}$ is a lower triangular matrix and the superscript “T” refers to the transposed matrix. The matrix $\boldsymbol{L}$ is made of $n(n+1)/2$ entries, which form $n(n+1)/2$ entries of the random vector field $\mathcal{V}$. No requirements are put on the elements of the random vector $\mathcal{V}$. Indeed, the non-negativity condition on the diagonal elements of $\boldsymbol{L}$ enforced in [26, 69, 86], ensures the uniqueness of the Cholesky decomposition as the samples of $\mathcal{V}$ are generated through the Cholesky decomposition, which leads to the non-negative diagonal elements of the samples. However, it is not required in our sampling process. If it is not respected, the generated sample $\Delta\boldsymbol{B}$ are still ensured to be positive-definite which is our main concern. The modelling of the $\mathcal{V}$ vector field can be done with the spectral approach, the Karhunen-Loève expansion, ...

This approach, involving an high number of parameters, can be applied in the frame of the stochastic multi-scale procedure. Towards this end, two random fields at meso-scale are defined. The samples of the meso-scale property of interest, such as the elasticity tensor, are gathered in the first random field $\mathcal{U}$.

However, some constraint on the values of $\mathcal{U}$ must be respected. In the case of the elasticity tensor, it must be positive-definite. To enforce the constraints, the field $\mathcal{U}$ is mapped to a new field, $\mathcal{V}$, as is described in this section. Samples of this new field, without constraints, are computed following the spectral approach described in the next section. Finally, these samples are mapped back to obtain samples of $\mathcal{U}$. The mapping is chosen so that the constraints on $\mathcal{U}$ are respected.

4.3 Generation of the random field with the spectral approach

The positive-definite matrices present in this work are generated using a high number of parameters approach. The first reason is that the variability of each element of the matrix should be accounted for. This is important as one element of the matrix can be the main source of variability for the response of the structure which is the case for a cantilever beam for which the young's modulus in one direction drives the resonance frequency, as was described in section 2.3. The second reason is that, with such an approach, accounting for other random variables correlated with the matrix can easily be done.

Elements can be added to the random vector field $\mathcal{V}$. As an example, let us add the mass per membrane area $\bar{\rho}\left(\boldsymbol{x},\boldsymbol{\theta}\right)$ in the random field, as it was introduced in section 2.5. When we consider the propagation of the roughness uncertainties, two correlated random fields are to be generated. The first one corresponds to the generalised tangent $\boldsymbol{U}$. The method described in Section 4.2.2 is used, thus defining the first 21 elements of the random vector $\mathcal{V}$. The second random field is $\bar{\rho}\left(\boldsymbol{x},\boldsymbol{\theta}\right) : \mathcal{A} \times \boldsymbol{\Omega} \rightarrow R^{+}$. The lower bound of the mass per membrane area is enforced according to:

$$\bar{\rho} = \bar{\rho}_L + \Delta\bar{\rho}\,, \tag{4.31}$$

where $\bar{\rho}_L$ is the lower bound and $\Delta\bar{\rho}$ is a positive value. The positiveness of $\Delta\bar{\rho}$ is enforced by a logarithmic mapping. Thus one element is added to the random vector field $\mathcal{V}$: $\log\left(\Delta\bar{\rho}\right)$. Finally, the random vector field $\mathcal{V}$ contains all the random elements that must be generated. The spectral representation can be used to model and generate samples of $\mathcal{V}$.

The random vector field is thus modelled based on the spectral representation method. As no assumptions are made on the correlation function, using a continuous random field based on the Karhunen-Loève extension is complicated as the Fredholm equation of the second kind must be solved. A discrete KL field can be considered. However, the matrices involved are very large when 3D vector fields are of interest. Furthermore, as the discretization is made in the spatial space, the spatial position must be known *a priori* and if they change, the eigenvalues and eigenfunctions must be computed again. With spectral methods, this is not the case as the discretisation is propagated to the frequency space. Values of the field can be obtained for any bounded spatial positions. Let us also note that Fast Fourier Transforms (FFT) can further help to fasten the computation. This however has a cost: the random field is evaluated on an *a priori* known grid and results for any $\boldsymbol{x}$ spatial position can be retrieved with the help of an interpolation procedure.

In this section we detail the spectral representation method [85], which is applied to generate a random vector field $\mathcal{V}\left(\boldsymbol{x},\, \boldsymbol{\theta}\right)$ of dimension n. We assume in this work that the random field $\mathcal{V}(\boldsymbol{x},\, \boldsymbol{\theta})$ is homogeneous. First let us consider, without loss of generality, the centred normalised field of the fluctuation $\mathcal{V}'(\boldsymbol{x}, \boldsymbol{\theta})$ so that:

$$\mathcal{V}^{(r)}(\boldsymbol{x}, \boldsymbol{\theta}) = \bar{\mathcal{V}}^{(r)} + \sigma_{\mathcal{V}^{(r)}} \mathcal{V}'^{(r)}(\boldsymbol{x}, \boldsymbol{\theta}) \quad \text{for} \quad r = 1, .., n \;, \tag{4.32}$$

where $\mathcal{V}^{(r)}$ is the r^{th} entry in the vector $\mathcal{V}$, $\bar{\mathcal{V}}^{(r)}$ is its mean and $\sigma_{\mathcal{V}^{(r)}}$ is its standard deviation. The fluctuation is normalised with the standard deviation so that, even though some elements in $\mathcal{V}$ are different within a few orders of magnitude, they can all be treated equivalently by the spectral representation.

The cross-covariance matrix $\boldsymbol{R}_{\mathcal{V}'}(\boldsymbol{\tau})$ has been obtained through Eq. (3.115) using the random field $\mathcal{V}_0$ obtained from the stochastic homogenisation described in Chapter 3 on which we have applied Eq. (4.32) to obtain $\mathcal{V}'_0$. It can be computed directly or the Fourier transforms can be used to compute the covariance functions.

In order to use the Discrete Fourier Transform (DFT), the cross-covariance has to be defined in a discrete way. On the one hand, when something is defined with respect to a continuous variable, parenthesis are used. On the other hand, if it is defined with respect to discrete variables, rectangular brackets are used. Thus the discrete covariance of an homogeneous field at distance $\boldsymbol{\tau_n}$ is defined such that:

$$\boldsymbol{R}^{(rs)}[\boldsymbol{\tau_n}] = \boldsymbol{R}^{(rs)}_{\mathcal{V}'}(\boldsymbol{\tau_n})\,, \tag{4.33}$$

where we drop the subscript $\mathcal{V}'$ for conciseness.

Considering the general 3D case, the set of discrete positions $\boldsymbol{\tau_n}$ is defined by its vector components $\boldsymbol{\tau_n}^{(n_x n_y n_z)} = [n_x \Delta\tau_x,\, n_y \Delta\tau_y,\, n_z \Delta\tau_z]$, where $\Delta\tau_i$, for $i = x,\, y,\, z$, is the spatial increment in each dimension i and where $n_i = 0,\, 1,\, 2,\, ...,\, N_i - 1$, for $i = x,\, y,\, z$, with N_i the total number of discrete points in each dimension i. Depending on the spatial size, $[l_x,\, l_y,\, l_z]$, of the required random field, we need to make sure that $N_i \Delta\tau_i \geq l_i$ (no sum on i). This is achieved herein by considering a zero-padding once $\boldsymbol{R}_{\mathcal{V}'}(\boldsymbol{\tau})$ reaches zero, allowing to increase the number of points N_i as much as required. We now need to periodise $\boldsymbol{R}[\boldsymbol{\tau_n}]$ by adding extra discrete points at its end in order to satisfy

$$\begin{aligned}
&\boldsymbol{R}[((N_x - 1) + j)\Delta\tau_x, ((N_y - 1) + k)\Delta\tau_y, ((N_z - 1) + p)\Delta\tau_z] = \\
&\quad \boldsymbol{R}[(N_x - j)\Delta\tau_x, (N_y - k)\Delta\tau_y, (N_z - p)\Delta\tau_z] \\
&\qquad \text{for} \quad j = 1,\, 2,\, ...,\, N_x - 1;\; k = 1,\, 2,\, ...,\, N_y - 1;\; p = 1,\, 2,\, ...,\, N_z - 1\,.
\end{aligned} \tag{4.34}$$

Thus we have $2N_i - 1$ discrete points in each dimension.

The spectral density matrix $\boldsymbol{S}[\boldsymbol{\kappa_m}]$ of the cross-covariance $\boldsymbol{R}[\boldsymbol{\tau_n}]$ can now be computed using the DFT method as

$$S^{(rs)}[\boldsymbol{\kappa_m}] = \\ \sum_{n_x=0}^{2N_x-2} \sum_{n_y=0}^{2N_y-2} \sum_{n_z=0}^{2N_z-2} \boldsymbol{R}^{(rs)}[\boldsymbol{\tau_n}^{(n_x n_y n_z)}] e^{-2\pi i (\frac{m_x n_x}{2N_x-1} + \frac{m_y n_y}{2N_y-1} + \frac{m_z n_z}{2N_z-1})} \,, \tag{4.35}$$

where the matrix $\boldsymbol{m}$ is defined by $\boldsymbol{m}^{(m_x m_y m_z)} = [m_x,\, m_y,\, m_z]$ with $m_i = 0,\, 1,\, ...,\, 2N_i - 2$ for $i = x,\, y,\, z$. The frequency space is defined based on the increment in frequency $\Delta\kappa_i$, computed in each direction following

$$\Delta\kappa_i = \frac{1}{(2N_i - 2)\Delta\tau_i}, \quad i = x,\, y,\, z \,, \tag{4.36}$$

and the matrix $\boldsymbol{\kappa_m}$ is defined by $\boldsymbol{\kappa_m} = [\kappa_{\boldsymbol{m}}^{(x)},\, \kappa_{\boldsymbol{m}}^{(y)},\, \kappa_{\boldsymbol{m}}^{(z)}]$ is defined from (no sum on $i = x,\, y,\, z$)

$$\kappa_{\boldsymbol{m}}^{(i)} = \begin{cases} m_i \Delta\kappa_i & \text{if} \quad m_i < (2N_i - 1)/2; \\ [m_i - (2N_i - 1)]\Delta\kappa_i & \text{if} \quad m_i > (2N_i - 1)/2; \end{cases} \tag{4.37}$$

to avoid the failure of power and logarithm identities.

The spectral density $\boldsymbol{S}[\boldsymbol{\kappa_m}]$ is an Hermitian matrix, which can be expressed as

$$\boldsymbol{S}[\boldsymbol{\kappa_m}] = \quad \boldsymbol{H}[\boldsymbol{\kappa_m}]\boldsymbol{H}^*[\boldsymbol{\kappa_m}] \,, \tag{4.38}$$

with $\boldsymbol{H}^*[\boldsymbol{\kappa_m}]$ the conjugate transpose of the matrix $\boldsymbol{H}[\boldsymbol{\kappa_m}]$.

Finally, the n components of the random field $\mathcal{V}'$ are generated using

$$\mathcal{V'}_{\text{gen}}^{(r)}(\boldsymbol{x},\, \boldsymbol{\theta}) = \sqrt{2\boldsymbol{\Delta}}\Re \left\{ \sum_{s=1}^{21} \sum_{m_x=0}^{2N_x-2} \sum_{m_y=0}^{2N_y-2} \sum_{m_z=0}^{2N_z-2} \boldsymbol{H}^{(rs)}[\boldsymbol{\kappa_m}] \right. \\ \left. \eta^{(s,\, m_x,\, m_y,\, m_z)} e^{2\pi i \left(\boldsymbol{x}\cdot\boldsymbol{\kappa_m} + \theta^{(s,\, m_x,\, m_y,\, m_z)}\right)} \right\} \,, \tag{4.39}$$

where $\boldsymbol{\Delta} = \Delta\kappa_x \Delta\kappa_y \Delta\kappa_z$, $\theta^{(s,\, m_x,\, m_y,\, m_z)}$ is an independent random variable (for each s, m_x, m_y, m_z) uniformly distributed on $[0, 1]$, and where $\eta^{(s,\, m_x,\, m_y,\, m_z)}$ can be defined in the two following ways

$$\eta^{(s,\, m_x,\, m_y,\, m_z)} = \begin{cases} 1 & \text{yields a Gaussian field only when} \\ & N_x,\, N_y,\, N_z \to \infty; \\ \sqrt{-\log\varphi^{(s,\, m_x,\, m_y,\, m_z)}} & \text{yields a Gaussian field when} \\ & \varphi^{(s,\, m_x,\, m_y,\, m_z)} \text{ is uniformly} \\ & \text{distributed on } [0,\, 1]. \end{cases} \tag{4.40}$$

In this work, the first case is considered.

When the required samples of the vector field include many spatial positions[4], it may be interesting to compute the samples following Eq. (4.39) with Fast Fourier Transforms. Towards this end, an intermediate matrix $\boldsymbol{P}^{(rs)}[\boldsymbol{\kappa_m}]$ can be defined as:

$$\boldsymbol{P}^{(rs)}[\boldsymbol{\kappa_m}] = \boldsymbol{H}^{(rs)}[\boldsymbol{\kappa_m}]\eta^{(s,\, m_x,\, m_y,\, m_z)} e^{2\pi i \theta^{(s,\, m_x,\, m_y,\, m_z)}} . \tag{4.41}$$

Following Eq. (4.39), samples of the field $\mathcal{V}'^{(r)}_{\text{gen}}$ can be obtained by computing the inverse FFTs of $\boldsymbol{P}^{(rs)}[\boldsymbol{\kappa_m}]$ for $s = 1, ..., n$.

The main drawback when using FFTs is that the samples are obtained for an *a priori* fixed spatial grid corresponding to the previously computed sampling points. Samples for any spatial position $\boldsymbol{x}$ can be obtained through an interpolation procedure.

4.4 Extension to non-Gaussian

As discussed in Section 2.1, the Gaussian distribution naturally arises from the central limit theorem and the maximum entropy principle. However, many engineering problems involve non-Gaussian quantities such as material properties, wind or soil properties. To solve our problems, the recourse to non-Gaussian methods can be useful. The marginal distribution of some meso-scale homogenised properties tends to be highly skewed, thus justifying the recourse to non-Gaussian approaches.

As it is described in [88], the simulation of non-Gaussian fields can be classified in 2 main categories. The first one, referred in this work as the parametrised approach, try to fit the distribution and correlation of the samples to prescribed distribution and correlation based on the statistical moments of the samples (mainly mean, variance, skewness, kurtosis). Such an approach provides good results when an appropriate parametrised distribution exists. However, different distributions can correspond to the same statistical moments, the distribution is not unique. Therefore, as only the lower-order moments are considered, the tail of the distribution is usually not properly simulated. This can be a problem when the tail is of major importance which is the case when computing the soil liquefaction from non-Gaussian soil properties [76].

The second approach tries to generate samples depicting the complete probabilistic information. These methods are more challenging as both the marginal density functions and the spectral densities are taken into account. The main methods to perform such non-Gaussian simulations are the correlation distortion methods. One of them will be explained in the following.

The spectral representation method developed in [85] is not directly applicable to generate non-Gaussian fields, and an iterative mapping process is thus required as suggested in [99, 75, 13]. In this iterative mapping process,

---

[4] In our 3-scale procedure, the spatial position corresponds to the macro-scale integration points. Thus for large scale problems, many spatial positions are required.

the target spectrum $\boldsymbol{S}^{(rs)}_{\mathrm{Target}}(\boldsymbol{\kappa})$ is obtained through the Fourier transform of the auto/cross-covariance $\boldsymbol{R}^{(rs)}_{\mathcal{V}'}(\boldsymbol{\tau})$, where r, s = 1, 2, ..., n are the index of the entries in the random vector $\mathcal{V}'$, according to Wiener-Khintchine relationship. A Gaussian stochastic vector field is first generated using the spectral representation method [85] and then mapped to a non-Gaussian field. Afterwards, the spectrum of the resulting non-Gaussian field $\boldsymbol{S}^{(rs)}_{\mathrm{NG}}(\boldsymbol{\kappa})$ is calculated and compared with the target spectrum $\boldsymbol{S}^{(rs)}_{\mathrm{Target}}(\boldsymbol{\kappa})$; if they are different, a updated spectrum will be used in the next iteration to generate a new Gaussian field. Iterations are performed until $\boldsymbol{S}^{(rs)}_{\mathrm{NG}}(\boldsymbol{\kappa}) \approx \boldsymbol{S}^{(rs)}_{\mathrm{Target}}(\boldsymbol{\kappa})$. The flow chart of this method is shown in Fig. 4.1, and each step of the procedure can now be described[5]:

Step 1. Set the random variables in the spectral representation formula for the generation of Gaussian field, and set $\boldsymbol{S}^{(rs)}_{\mathrm{G}(0)}(\boldsymbol{\kappa}) = \boldsymbol{S}^{(rs)}_{\mathrm{Target}}(\boldsymbol{\kappa})$; Iteration index is initiated at $i = 0$;

Step 2. Generate the Gaussian field $\mathcal{V}'_{\mathrm{G}}(\boldsymbol{x})$ with $\boldsymbol{S}^{(rs)}_{\mathrm{G}(i)}(\boldsymbol{\kappa})$, following the process detailed in Section 4.3;

Step 3. Compute the variance σ_r of each component $\mathcal{V}'^{(r)}_{\mathrm{G}}(\boldsymbol{x})$, and map the Gaussian field to a non-Gaussian field by [13]

$$\mathcal{V}'^{(r)}_{\mathrm{NG}}(\boldsymbol{x}) = {F^{\mathrm{NG}}_{\mathcal{V}'^{(r)}}}^{-1}\left[F^{\mathrm{G}}_{\mathcal{V}'^{(r)}}(\mathcal{V}'^{(r)}_{\mathrm{G}}(\boldsymbol{x}))\right]\,, \tag{4.42}$$

where $F^{\mathrm{G}}_{\mathcal{V}'^{(r)}}$ is a Gaussian distribution function with zero mean and variance σ_r, and ${F^{\mathrm{NG}}_{\mathcal{V}'^{(r)}}}^{-1}$ is the inverse of the marginal distribution function of random variable $\mathcal{V}'^{(r)}$ which is obtained from the micro-sampling of SVEs;

Step 4. Compute the Fourier transform of $\mathcal{V}'^{(r)}_{\mathrm{NG}}(\boldsymbol{x})$ by

$$\hat{\mathcal{V}}'^{(r)}_{\mathrm{NG}}(\boldsymbol{\kappa}) = \sum_{\boldsymbol{x}=\boldsymbol{0}}^{\boldsymbol{l}} \mathcal{V}'^{(r)}_{\mathrm{NG}}(\boldsymbol{x})e^{-2\pi i\boldsymbol{x}\cdot\boldsymbol{\kappa}}\,; \tag{4.43}$$

and evaluate the spectrum of $\mathcal{V}'_{\mathrm{NG}}(\boldsymbol{x})$ by

$$\boldsymbol{S}^{(rs)}_{\mathrm{NG}}(\boldsymbol{\kappa}) = \frac{1}{N}\bar{\hat{\mathcal{V}}}'^{(r)}_{\mathrm{NG}}(\boldsymbol{\kappa})\hat{\mathcal{V}}'^{(s)}_{\mathrm{NG}}(\boldsymbol{\kappa})\,, \tag{4.44}$$

where N is the total number of discrete points of the generated field, and $\bar{\hat{\mathcal{V}}}'^{(r)}_{\mathrm{NG}}(\boldsymbol{\kappa})$ is the conjugate of $\hat{\mathcal{V}}'^{(r)}_{\mathrm{NG}}(\boldsymbol{\kappa})$;

---

[5] The subscript "gen" is removed for $\mathcal{V}'$ in this section for simplicity

Step 5. Compare $\boldsymbol{S}_{\mathrm{NG}}^{(rs)}(\boldsymbol{\kappa})$ with $\boldsymbol{S}_{\mathrm{Target}}^{(rs)}(\boldsymbol{\kappa})$, the error being calculated by [75]

$$err = \frac{\int_{\Omega_\kappa} \left| \boldsymbol{S}_{\mathrm{NG}}^{(rr)}(\boldsymbol{\kappa}) - \boldsymbol{S}_{\mathrm{Target}}^{(rr)}(\boldsymbol{\kappa}) \right| \mathrm{d}\boldsymbol{\kappa}}{\int_{\Omega_\kappa} \left| \boldsymbol{S}_{\mathrm{Target}}^{(rr)}(\boldsymbol{\kappa}) \right| \mathrm{d}\boldsymbol{\kappa}}\,, \tag{4.45}$$

where Ω_κ refers to the frequency domain;

Step 6. If the error is lower than the given tolerance, $err < Tol$, stop the iteration and $\mathcal{V}'_{\mathrm{NG}}(\boldsymbol{x})$ is the required random field; Else, if $err > Tol$, update the spectrum by

$$\begin{aligned} \boldsymbol{S}_{\mathrm{G}(i+1)}^{(rr)}(\boldsymbol{\kappa}) &= \boldsymbol{S}_{\mathrm{G}(i)}^{(rr)}(\boldsymbol{\kappa}) \frac{\boldsymbol{S}_{\mathrm{Target}}^{(rr)}(\boldsymbol{\kappa})}{\boldsymbol{S}_{\mathrm{NG}}^{(rr)}(\boldsymbol{\kappa})}\,, & (4.46) \\ \boldsymbol{S}_{\mathrm{G}(i+1)}^{(rs)}(\boldsymbol{\kappa}) &= \boldsymbol{S}_{\mathrm{G}(i)}^{(rs)}(\boldsymbol{\kappa}) \left(\frac{\boldsymbol{S}_{\mathrm{Target}}^{(rr)}(\boldsymbol{\kappa}) \boldsymbol{S}_{\mathrm{Target}}^{(ss)}(\boldsymbol{\kappa})}{\boldsymbol{S}_{\mathrm{NG}}^{(rr)}(\boldsymbol{\kappa}) \boldsymbol{S}_{\mathrm{NG}}^{(ss)}(\boldsymbol{\kappa})} \right)^{\frac{1}{2}}\,; & (4.47) \end{aligned}$$

set $i = i + 1$; and go back to step 2.

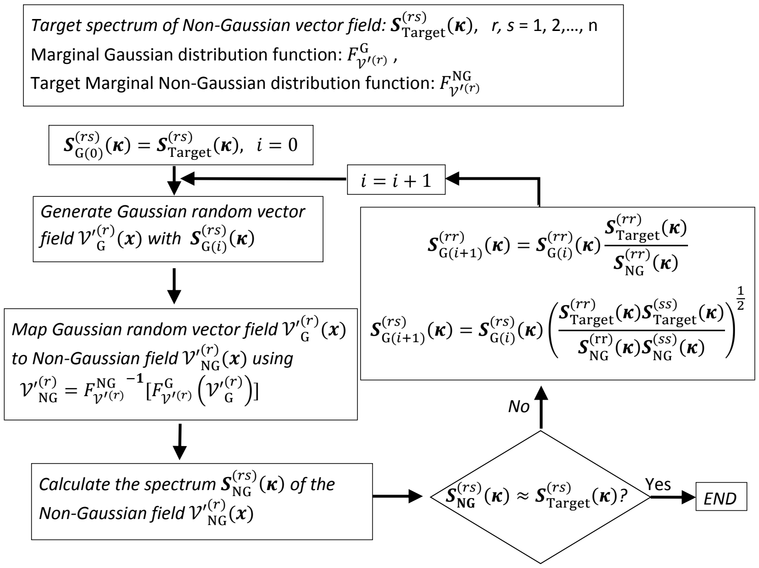

Figure 4.1: Flow chart of the non-Gaussian stochastic vector field generation

In our applications, because the sample points of each random field are not enough to calculate the converged spectrum $\boldsymbol{S}_{\mathrm{NG}}^{(rs)}(\boldsymbol{\kappa})$, thousands of random fields are generated at once to calculate the converged spectrum $\boldsymbol{S}_{\mathrm{NG}}^{(rs)}(\boldsymbol{\kappa})$. After iterations, the final spectrum $\boldsymbol{S}_{\mathrm{G}}^{(rs)}(\boldsymbol{\kappa})$ is obtained. In the real applications, the obtained final spectrum $\boldsymbol{S}_{\mathrm{G}}^{(rs)}(\boldsymbol{\kappa})$ is used to generate the Gaussian random vector fields which will be mapped to the required non-Gaussian vector field following the process described in Step 3.

4.5 Implementation considerations

The random field generator described in this chapter involves many different steps. To summarise the procedure, we introduce the main blocks that one could identify in an implementation of the generator. The different blocks are shown in Fig. 4.2. Let us recall that the stochastic model is used in the frame of a SFEM analysis. Therefore, samples of the macro-scale structure are required to estimate the uncertainty of the response of the structure. A macro-scale sample is thus a sample of the meso-scale random field over the structure. At each integration point of the SFEM approach, the meso-scale property at the current spatial position is retrieved from the random field. This involves the following steps.

At first, before samples can be generated, the random field has to be initialised. The initialisation refers to the computation of the spectral density. This can be done in 3 different ways. Either it can be directly computed with the help of the Gaussian assumption; this requires no iteration and was described in Section 4.3. Or the spectral density for the non-Gaussian case can be computed as described in Section 4.4, thus requiring a costly iterative procedure. Once a spectral density is computed, it can be saved. It is particularly useful when dealing with non-Gaussian distributions as the iterative procedure can once be done *a priori*. Let us note that, to save computational resources, the matrix $\boldsymbol{H}$ (defined according to Eq. (4.38)) can be computed and saved.

Secondly, before the analysis of one sample of the macro-scale structure, the randomisation step has to be done. This can be done directly or with a Fast-Fourier approach. The first one allows for the computation of the random field at each integration point without the recourse to an interpolation procedure. The randomness over the whole field as to be computed and saved through the matrix $\boldsymbol{P}^{(rs)}[\boldsymbol{\kappa_m}]$ which includes the randomness $\theta^{(s,\,m_x,\,m_y,\,m_z)}$ and $\eta^{(s,\,m_x,\,m_y,\,m_z)}$ and the spectral information $\boldsymbol{H}$. However, it can be computationally expensive when large fields are of interest. The Fast-Fourier approach allows for faster computation but the values are only computed at an a priori known grid. During the randomisation step, the whole field over the spatial grid can be computed by recourse to FFTs and saved.

The last step of the procedure consists in computing a sample for each spatial position $\boldsymbol{x}$. When FFT are not considered, samples can be retrieved based on Eq (4.39). If the FFT approach is considered, an interpolation approach is then required to generate values for any spatial position. Let us note that a non-Gaussian mapping is required when the spectral density corresponding to a non-Gaussian stochastic model is used.

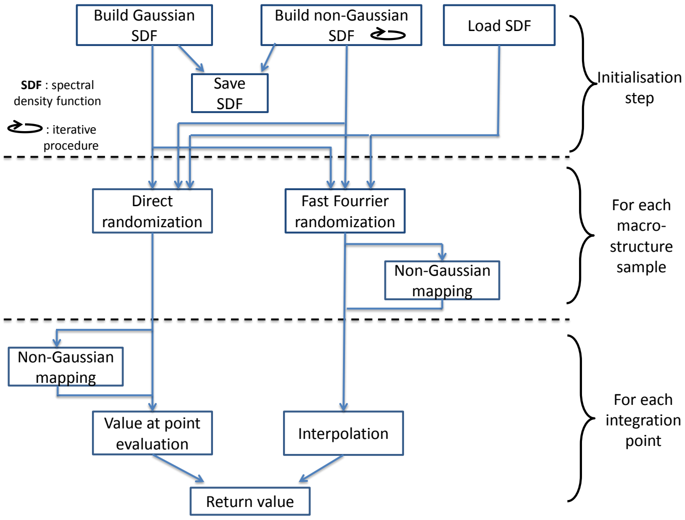

Figure 4.2: Implementation of the random field generator

4.6 Conclusion

Throughout this chapter, the stochastic modelling of the different meso-scale random fields was investigated. First, different approaches were described. Then the spectral approach was described, in particular when positive-definite matrices must be modelled. The extension to non-Gaussian fields was briefly discussed. Finally the implementation of a random field generator was considered.

The stochastic model defined in this chapter can be used to model the meso-scale random field assessed in Chapter 3. This random field, with its stochastic model, can thus be used at an affordable cost as an input for the SFEM approach described in Chapter 2. Therefore, the whole 3-scale uncertainty propagation can be performed. Such a stochastic multi-scale approach will now be applied on MEMS micro-beams in the next chapter.

Chapter 5

Application to MEMS

In this chapter, the 3-scale procedure is applied on 3 case studies: the 1D beam in linear elasticity for verification, the extension to thermo-elastic 3D beams, and the rough thin plates. At first, the uncertainty of the micro structure needs to be defined (from measurements if available) so that volume elements can be generated. Then the meso-scale homogenised properties are used as input of the generator. The generated random fields can be compared to the initial samples. The meso-scale uncertainties can thus be propagated up to the macro-scale. Finally the effects of different uncertainty sources (grain orientation, anchor, roughness, MEMS design, ...) are discussed on MEMS resonators.

5.1 Uncertainty characterisation

5.1.1 Micro-scale measurements

As the main objective of this work is to represent the uncertainties related to actual MEMS, we have recourse to measurements performed on samples of the micro-structures. The micro-beams discussed in this section were fabricated by the IMT institute in Bucharest. The IMT institute also provided us with the actual measurements.

The thin structures are made of poly-silicon, one of the most common material present in MEMS using low pressure chemical vapour deposition (LPCVD) technique. From the $< 100 >$ orientation silicon wafer of p-type, a silicon dioxide layer was grown by thermal technique at 1000 °C. Columnar[1] poly-crystalline poly-silicon was thus deposited on this silicon dioxide layer. The properties of the micro structure, such as grain orientation and size, varies with the deposition temperature and time. Samples obtained for the successive temperatures

---

[1] Structures obtained by the Low Pressure Chemical Vapor Deposition (LPCVD) process are not strictly columnar as the lower side of the deposition is made of smaller grains, the size of the grains gradually increasing toward the top surface. However, as an important part of the MEMS thickness is made of the last grains layer, we assume in this work that a columnar structure characterized by the upper grains represents the MEMS behavior.

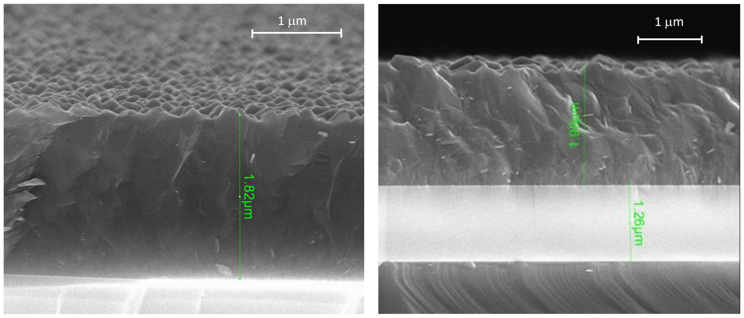

(a) 580 °C (b) 610 °C

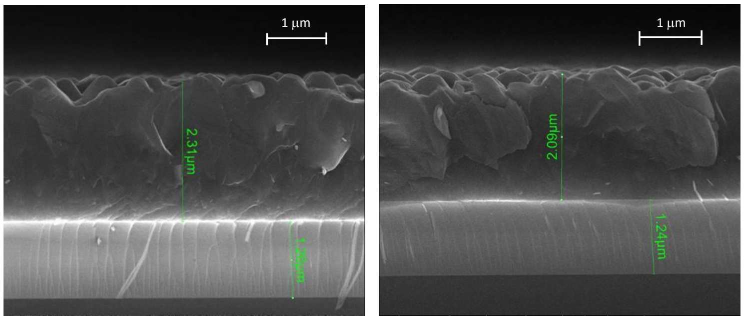

(c) 630 °C (d) 650 °C

Figure 5.1: Cross-section SEM images for different temperatures of the fabrication process

of 580 °C, 610 °C, 630 °C, and 650 °C, were manufactured at pressure of 0.267 mbar and with a Silane flow of respectively 15, 15, 20, and 25 sccm. The thickness of the samples, which influences the grains size, is about 2 μm, respectively 1.82 μm, 1.98 μm, 2.31 μm, and 2.09 μm for the four temperatures, as illustrated in the cross-section views in Fig. 5.1.

The measurements are the starting point for the definition of the (R)SVEs. Three types of measurements are available for the poly-silicon layers obtained at the different deposition temperatures.

- Scanning Electron Microscope (SEM) images for the grain size analyses;
- X-Ray Diffraction (XRD) measurements for the grain orientation distribution analyses;
- Atomic-force microscopy (AFM) measurements for the top surface roughness (the bottom surface roughness being of several orders lower).

First, top views of the films obtained from SEM images are shown for the different deposition temperatures in Fig. 5.2, *i.e.* for temperatures of 580 °C, 610 °C, 630 °C, and 650 °C. Processing the images allows obtaining the grain size distributions for the different temperature cases. The average grain diameters, for the different temperatures of the fabrication process, are reported in Table 5.1, where it can be seen that the grain size strongly depends on the temperature of the fabrication process.

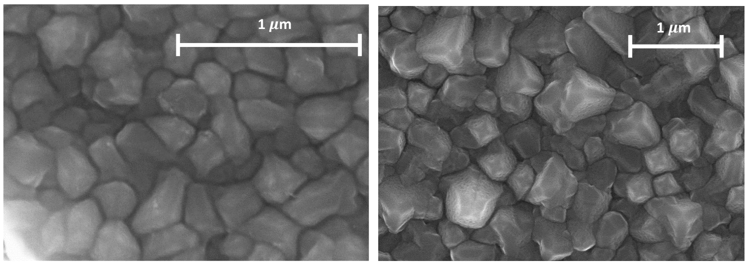

(a) 580 °C (b) 610 °C

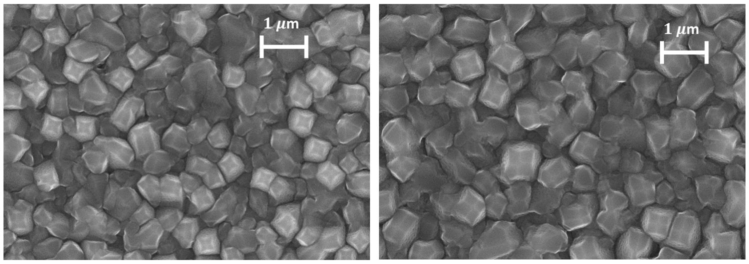

(c) 630 °C (d) 650 °C

Figure 5.2: SEM images (top view) for the different temperatures of the fabrication process

Table 5.1: Average grain diameter for the different temperatures of the fabrication process

Temperature [°C]	580	610	630	650
Average grain diameter [μm]	0.21	0.447	0.7195	0.83

The XRD results are reported in Fig. 5.3 for the different deposition temperatures. From the XRD measurements, the crystallinity is always higher than 97.48%. Therefore no amorphous phase is considered in this work. The XRD-measurements also provide information about the relative weight fraction for the different orientations.

With high quality data, we can determine how much of each phase is present. The ratio of peak intensity I varies linearly as a function of weight fractions for any two phases in a mixture. Here the two phases refer to poly-silicon grains with two different orientations (α and β) towards the surface of the measured sample. Assuming that their weight fraction are X_α and X_β, respectively, we have

$$\frac{I_\alpha}{I_\beta} = \frac{I_\alpha^0 (I/I_{\mathrm{cor}})_\beta X_\alpha}{I_\beta^0 (I/I_{\mathrm{cor}})_\alpha X_\beta}\,, \tag{5.1}$$

where

$$\frac{I}{I_{\mathrm{cor}}} = \frac{\text{Intensity of sample' s 100\% peak}}{\text{Intensity of Corundum' s 100\% peak}}\,, \tag{5.2}$$

and where I_*^0 is the reference relative intensity. For silicon we have

$$\frac{I}{I_{\mathrm{cor}}} = 4.7 \quad \text{and} \quad I(111) = 100\%\,, \tag{5.3}$$

and the reference relative intensities ($I_*^0 = I_*/I(111)$ according to powder XRD measurements) are reported in Table 5.2.

Table 5.2: Reference relative intensity with respect to the direction < 111 > for silicon [63]

Orientation	< 111 >	< 220 >	< 311 >	< 400 >	< 331 >	< 422 >
$\mathbf{I_*^0}$ [%]	100	55	30	6	11	12

Applying these formula on the XRD measurements reported in Fig. 5.3 yields the results in terms of weight fractions, with a crystallinity of 100% considered, as reported in Table 5.3.

Table 5.3: Percentage of the different grain orientations based on XRD measurements for the different temperatures of the fabrication process

Temperature [°C]	580	610	630	650
< **111** >	12.57	19.96	12.88	11.72
< **220** >	7.19	13.67	7.96	7.59
< **311** >	42.83	28.83	39.08	38.47
< **400** >	4.28	5.54	3.13	3.93
< **331** >	17.97	18.14	21.32	20.45
< **422** >	15.15	13.86	15.63	17.84

The influence of the XRD-based orientation on the Young's modulus distribution for a single crystal is investigated in Fig. 5.4, in which two different cases are considered: in Fig. 5.4(a), the grain orientation is uniformly distributed and

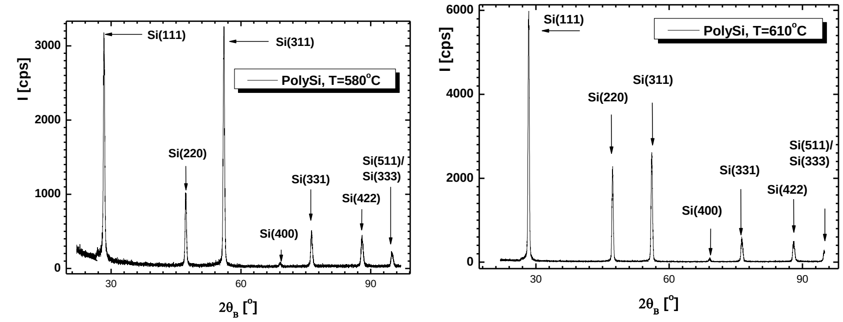

(a) 580 °C (b) 610 °C

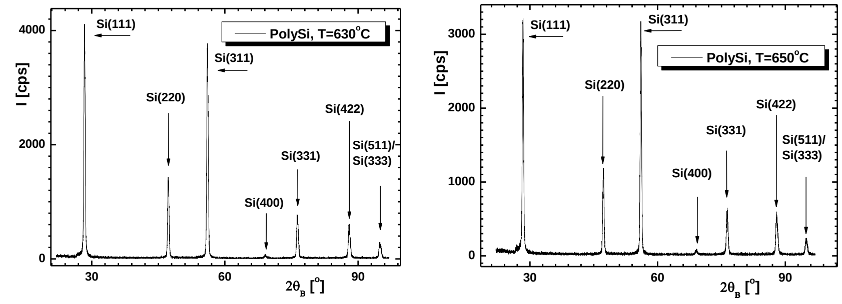

(c) 630 °C (d) 650 °C

Figure 5.3: XRD measurements for different temperatures of the fabrication process. The intensity of each peak, associated to one orientation, is given in counts per seconds. The relative intensity of the peaks provides, through a linear relationship, the relative weight fraction for the different orientations.

in Fig. 5.4(b) the grain orientation is based on the XRD-measurements for polysilicon deposited at 610 °C as reported in Table 5.3. Compared to the preferred orientation case, the uniform distribution gives a more uniform modulus distribution, although there is an increase in density around 170 GPa and a small decrease around 180 GPa. When the preferred orientation defined from the XRD measurements are taken into account, the histogram is drastically different as some orientations are preferred. Although the whole spectrum is spanned (from 130 GPa to 188 GPa), very few samples are obtained in some regions and most of the samples are obtained either in a close vicinity of $\approx$ 150 GPa or above $\approx$ 162 GPa. In terms of statistical moments, the means of the Young's modulus are respectively 159 GPa and 161.09 GPa for the uniform distribution and the preferred orientation cases. The standard deviations are respectively 15.76 GPa

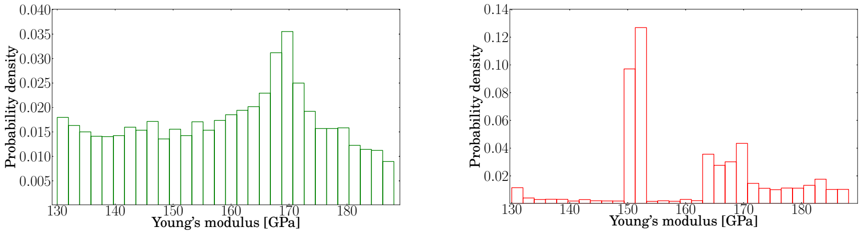

(a) Uniform distribution (b) Preferred orientation

Figure 5.4: Young's modulus for a silicon crystal whose orientation is (a) uniformly distributed, (b) preferentially distributed following Table 5.3 at 610 °C

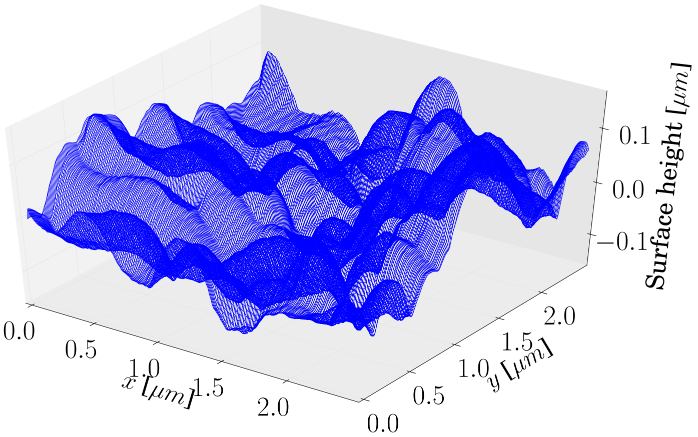

Figure 5.5: Sample of a rough surface obtained with AFM measurements

and 12.98 GPa for the uniform distribution and the preferred orientation cases. Therefore, although the two PDFs are drastically different, the first and second moments of their statistical behaviour are similar.

The AFM measurements reported in Fig. 5.5 correspond to the sample processed with the deposition temperature of 610 °C. Five sets of AFM measurements are available; each with 1024 × 1024 sampling points of the surface height and with a spatial step along both x and y directions of 4.883 μm. The height distribution shows a standard deviation of 60.3 nm for the deposition temperature of 610 °C, see Table 5.4.

Moreover, although the experimental measurements were obtained for a poly-silicon thickness of 2 μm, in order to study the effect of the roughness for different MEMS thicknesses, we will consider that the AFM measurements

Table 5.4: Standard deviation of the asperities height from AFM images and for the different temperatures of the fabrication process

Temperature [°C]	**Standard deviation of the asperities height** [nm]
580	35.6
610	60.3
630	90.7
650	88.3

remain valid for other thicknesses[2].

5.1.2 The elementary volume elements

Mechanical properties

With a view toward the study of a MEMS resonator, we consider micro-size volume elements made of silicon organised in a poly-crystalline structure. The material uncertainties are coming from two sources: the grain size/geometry and the grain orientations.

The first one is captured by the Voronoï tessellation whose main parameter is the grain size, which depend on the typical fabrication process. Arbitrarily small grain sizes are first considered for some SVE sets in this work to verify numerically the results with direct MC simulations. Afterwards, the grain size are obtained from SEM images, as described in Section 5.1.1.

The Poisson-Voronoï tessellations are generated as detailed in Appendix D. Random seeds are uniformly distributed over a 2D grid based on the desired grain size and a Voronoï tessellation can be generated from these seeds. The tessellations must be large enough so that the spatial stochastic behaviour of the properties of interest can be captured, as described in Section 3.5. One tessellation is illustrated in Fig. 5.6. Several SVEs are extracted from the tessellations to study its meso-scale material properties. One SVE is illustrated in Fig. 5.7. Moreover, since the considered MEMS structures are fabricated through LPCVD, similar micro material structures (at the grain scale) will be obtained on the whole MEMS-structure, which justifies the use of the homogeneous random field.

The second source of uncertainty is represented by assigning random orientations to the grains. Indeed, silicon material is anisotropic, with a cubic symmetry, and the properties of a silicon grain depend on its orientation with respect to the crystal lattice. The material properties of a silicon crystal are studied in [33]. Its Young's modulus can range from 130 GPa up to 188 GPa and

---

[2] Measurements actually performed on 1 μm-thick poly-silicon films confirm that the main driving parameter is the deposition temperature. The main difference lies in the roughness. For example at a deposition temperature of 610 °C, the standard deviation of the height distribution decreases from 60.3 nm to 54.3 nm when the poly-silicon film thickness decreases from 2 to 1 μm, while for a deposition temperature of 580 °C, the standard deviation of the height distribution is around 35 nm.

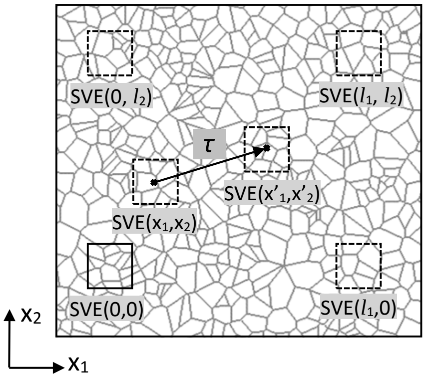

Figure 5.6: SVEs generation strategy. The average grain size is ≈ 4.4 μm.

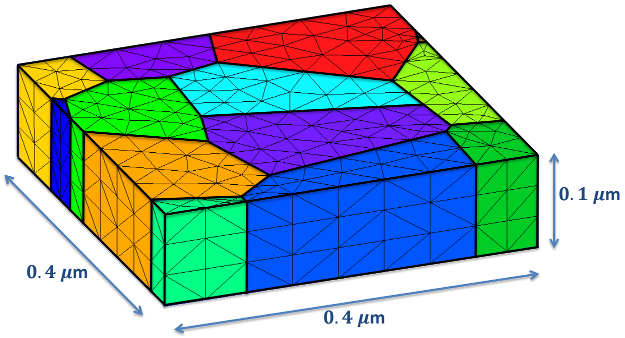

Figure 5.7: A sample of the meso-scale volume element ω. One colour is associated to each grain.

its Poisson ratio can range from 0.048 up to 0.4. For the silicon crystal oriented with [100], [010] and [001] along the Cartesian coordinates, the crystal elasticity tensor $\boldsymbol{C}_{\mathrm{S}}$ –where the subscript S indicates the properties for the single crystal–reads, in GPa,

$$\boldsymbol{C}_{\mathrm{S}} = \begin{bmatrix} 165.7 & 63.9 & 63.9 & 0 & 0 & 0 \\ 63.9 & 165.7 & 63.9 & 0 & 0 & 0 \\ 63.9 & 63.9 & 165.7 & 0 & 0 & 0 \\ 0 & 0 & 0 & 79.6 & 0 & 0 \\ 0 & 0 & 0 & 0 & 79.6 & 0 \\ 0 & 0 & 0 & 0 & 0 & 79.6 \end{bmatrix} . \tag{5.4}$$

Two cases of orientation distribution are considered in this work. One considers uniformly distributed orientations. The second case considers a preferred orientation based on experimental measurements described in Section 5.1.1.

Thermal properties

Two thermal properties have to be defined for thermo-mechanical analyses: the thermal conductivity and the thermal expansion.

The thermal conductivities for thin films of poly-silicon are substantially different from those of the bulk silicon. Depending on the applications of MEMS, different deposition and doping techniques, which affect the micro structure of poly-silicon, will be adopted and different thermal conductivities of the resulting materials are observed. The thermal conductivities of poly-silicon layers depend on the grain size and shape, and the concentration and type of dopant atoms as shown in [58].

In dielectric materials, heat transport in both amorphous and crystalline solids occurs by elastic vibrations of the lattice; phonons are the energy quanta of lattice vibration waves and are the main energy carriers. This transport mode is limited by the elastic scattering of phonons due to the lattice defects. The effect of boundary scattering of phonons on thermal conductivities in single-crystal silicon layers has been previously investigated in [4], and the thermal conductivities of poly-silicon are found to be lower than those of single-crystal silicon layers due to phonon scattering at the grain boundaries. For doped silicon layers, such as phosphorus and boron-doped silicon layers, with impurity concentrations, the impurity scattering causes a further reduction in the thermal conductivity as compared to pure silicon layers. Because of the difficulties in the modeling of phonon scattering at grain boundaries, the theoretical prediction of the thermal conductivity for a given impurity concentration and micro structure is still not possible [58].

Based on theoretical models and the experimental measurements, the thermal conductivity of poly-silicon layer was given in a simplified closed-form expression in [58]. This closed-form expression which relates the room-temperature thermal conductivity to the grain size and to the impurity concentration and type, reads

$$\kappa(\bar{d}, c_{\mathrm{i}}) = \frac{1}{3} C_{\mathrm{S}} v_{\mathrm{s}} \left(\frac{A_1}{\bar{d}} + A_2 c_{\mathrm{i}} \right)^{-1} , \tag{5.5}$$

in which the obtained thermal conductivity has the unit of $\mathrm{W}/(\mathrm{m} \cdot \mathrm{K})$, $\bar{d}$ is the average grain size in unit of nm, c_{i} is the impurity concentration in unit of cm^{-3}, $v_{\mathrm{s}} = 6166$ m/s is the averaged phonon group velocity in silicon, and $C_{\mathrm{S}} = 1.654 \times 10^6\ \mathrm{J/m^3K}$ is the phonon specific heat at 300K in silicon. The constants A_1 and A_2 depend on the dopant atoms, which are known from the fabrication process. In this work, we assume that the poly-silicon is boron-doped, which gives $A_1 = 2.887 \times 10^{10}$ and $A_2 = 3.200 \times 10^{-13}\ \mathrm{m}^2$, and a measured impurity concentration $c_{\mathrm{i}} = 1.6 \times 10^{19}\ \mathrm{cm}^{-3}$ is chosen for our applications.

The conductivities obtained from Eq. (5.5) are related to the average grain size and take into account the grain boundaries present along the 3 directions (in-plane and out-of-plane directions of the poly-silicon layer). As using these results in the meso-scale (SVEs) simulations, in which only few grains exist in each SVE, is not feasible, we assume that Eq. (5.5) also holds for only one grain with the effect of its boundaries included. Hence, because of the cubic symmetric of silicon crystal, a thermal conductivity and an isotropic thermal conductivity tensor are computed for this grain, depending on the size of a grain, which results in

$$\boldsymbol{\kappa}_{ij}(\bar{d}) = \delta_{ij} \kappa(\bar{d}) , \tag{5.6}$$

where δ_{ij} is the Kronecker symbol. We need to note that it would also be possible to define an anisotropic thermal conductivity tensor according to the grain geometry which includes the information of the grain shape and boundaries. However, in this work, we consider an isotropic thermal conductivity tensor for each grain to keep the problem simple.

The thermal expansion tensor is a structure sensitive property and reflects any change in the micro structure. For crystalline materials, the number of independent thermal expansion components varies with the type of crystal system [15]. The tensor for poly-crystalline materials is more complicated and has a wide divergence. However the thermal expansion tensors of different grains differ only by their orientation.

For cubic symmetric crystal systems, the thermal expansion tensor has a simple form as $\boldsymbol{\alpha}_{ij} = \delta_{ij} \alpha_T$, where the linear thermal expansion coefficient, α_T, at temperature T expressed in K, can be calculated from an empirical equation. Around 273 K and above, this empirical equation for a wide range of temperatures is given by

$$\alpha_T = A + B(T - T_0) + C(T - T_0)^2 , \tag{5.7}$$

in terms of the coefficients A, B, and C, respectively expressed in K^{-1}, K^{-2}, and K^{-3}.

For silicon crystal, at $T_0 = 273$ K the different factors are identified as $A = 3.084$ ($T:\ 293 \sim 970$ K) and $A = 2.327$ ($T:\ 298 \sim 314$ K) according to different references, $B = 1.957$ and $C = 0$ [15]. The value of $A = 3.084 \times 10^{-6}/\mathrm{K}$ is adopted in this work.

Although in all generalities, the apparent thermal expansion tensor $\boldsymbol{\alpha}_{\mathrm{M}}$ of an SVE can be computed through equation (3.76) following the homogenisation process described in Section 3.3, because of the cubic symmetry of the silicon crystal, the poly-silicon SVEs all have the same isotropic thermal expansion tensor

$$\boldsymbol{\alpha}_{\mathrm{Mij}} = \delta_{ij}\alpha_{\mathrm{m}} \,, \tag{5.8}$$

where $\alpha_{\mathrm{m}} = 3.084 \times 10^{-6} + 1.957 \times 10^{-9}(T - T_0)$ in K^{-1}. In the conducted modal analyses, the equations are linearised and the material parameters are considered as constant with respect to the temperature.

5.1.3 Extension to rough volume elements based on AFM measurements

Two sources of material uncertainties are already considered on the meso-scale volume elements: the grain size/distribution and the grain orientation. We also introduce geometrical uncertainties resulting from the surface roughness. In order to illustrate the procedure, we consider, as an example, the case of poly-silicon deposited at 610 °C.

As the grain distribution and the asperities are correlated, as shown in [105], both AFM and SEM measurements are used to generate samples of the RSVE structures. Indeed, as the asperities are normally formed on the top grains, the valleys of the surface topology thus being located at grain boundaries, both grain generation and roughness generation should be closely linked. This can be achieved in 2 ways: either the grains are generated first and the surface is defined with respect to the grains or the surface is generated first and the grains are defined with respect to the surface. With the former procedure, the grain centres define the position of the asperities but a lot of degrees of freedom still need to be fixed (valley depth, peak high, ...) while respecting the surface properties (mean plane, RMS value, ...). The latter procedure is much easier to implement as follows. Once a correlation structure for the surface is defined (based on AFM measurements, grain size...), samples of the surface can be generated. The tips of the asperities for each surface can be detected and their positions used as seeds of a Voronoï tessellation to define the grains. The different steps of the meso-scale volume element generation, for both rough and flat SVEs, are discussed in the following paragraph.

Asperities detection

The first step of the RSVE generation is to define an asperities detection process from the AFM images. In other words, from a sample surface based on the AFM measurements, the position of the local maxima must be found. The procedure defined is this work is a very simple one which requires smooth surfaces to

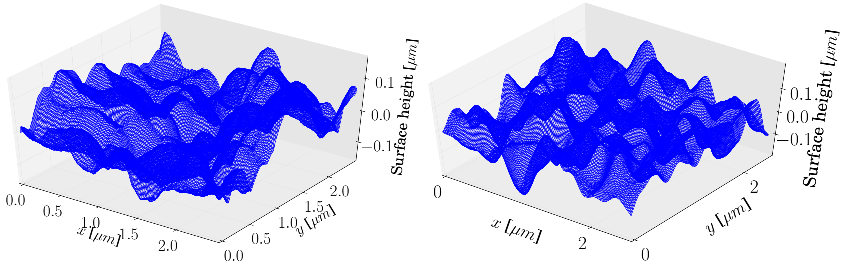

(a) AFM measurements (b) Generated surface

Figure 5.8: Sample of rough surfaces obtained with (a) AFM measurements on the poly-silicon deposited at 610 °C, and (b) generated surface

provide relevant results. Each sample point of the surface of interest is analysed. A point is considered to be the tip of one asperity if the following two conditions are respected simultaneously:

1. It is the maximum value over its neighbors located in a square of corner length L^1_{lim};
2. There is no other asperity nearby located in a square of corner length L^2_{lim}.

To illustrate the process, we consider the AFM measurements reported in Fig. 5.8(a), which correspond to the deposition temperature of 610 °C. The values of L^1_{lim} and L^2_{lim} are chosen to be $0.6\,\mu$m, as for the given smooth surfaces analysed, these values provide relevant asperities. Applying the simple asperity detection method on these AFM measurements gives us an estimate of the grain size as each asperity is assimilated to one grain and as the area of each grain is $\pi\left(\frac{d}{2}\right)^2$, d being the grain size. A computed grain size of $\approx 0.57\,\mu$m is obtained. There is a difference between this value and the grain size $\approx 0.447\,\mu$m computed with the help of the SEM images, see Table 5.1. The grain size resulting from the SEM images of $0.447\,\mu$m is thus enforced when generating the RSVEs in the following sections.

Correlation structure of the rough surfaces

To generate the rough stochastic volume elements, the first thing that is created is their top rough surface. This is achieved using the spectral methods [83]. A scalar value h', the variation between the mean thickness and the local thickness, is generated over a 2D space. This process requires a 2D spatial covariance function $R_{h'}(\boldsymbol{\tau})$ of h', where $\boldsymbol{\tau}$ is the in-plane spatial distance between two points of interest. From the covariance function $R_{h'}(\boldsymbol{\tau})$, h' is generated as a stationary Gaussian random field using the theory reported in Chapter 4, but for a single variable h'.

As smooth surfaces must be considered for the asperity detection process, a Gaussian covariance function is assumed (and will be assessed by comparison with the experimental measurements) with

$$R_{h'}(\tau) = \sigma_{h'}^2 \exp^{-\frac{\tau^2\pi}{l_{h'}^2}} . \tag{5.9}$$

This Gaussian covariance structure has two degrees of freedom: the standard deviation $\sigma_{h'}$ and the correlation length $l_{h'}$. The former value corresponds to the measured standard deviation obtained from the AFM measurements (and thus from the surface topology), and is evaluated as $\sigma_{h'} = 60.3\,\text{nm}$.

The correlation length remains to be defined as it drives the distance between the asperities of the random field, thus enforcing the grain size. The grain size is a parameter of prime importance, not only concerning the roughness but also concerning the material property. The bigger the grain size, the higher the uncertainties at the meso-scale, as will be shown in Section 5.2.1. The correlation length of $R_{h'}(\tau)$ is computed so that the generated RSVEs possess an average grain size similar as the estimation of the SEM images, *i.e.* at a deposition temperature of 610°C an average grain size of $0.447\,\mu$m. This is achieved by defining an optimization procedure. From a first guess of the correlation length (based on the AFM measurements), surfaces can be generated and the corresponding grain size can be estimated. The correlation length is updated until the appropriate grain size is obtained. After computation, a value of $\frac{l_{h'}}{\sqrt{\pi}} = 0.03125\,\mu$m was obtained.

The resulting Gaussian covariance is depicted in Fig. 5.9(a), and is compared to the data computed from the AFM measurements reported in Fig. 5.9(b). Let us note that the correlation is the covariance scaled with respect to the variance. As one can see in the picture, the experimental results do not converge for long distance as there were not enough sampling points. This justifies the use of a Gaussian correlation instead of the direct use of the AFM measurements. The standard deviation of the surface is obtained from the AFM measurements while the grain size is fixed with the SEM measurements. Let us note that keeping a spacing δx of 4.883 nm, which is the spacing of the AFM measurements, is computationally expensive when volume elements of sizes around 1μm must be generated. The Gaussian correlation assumption allows us to choose the spatial spacing and therefore a larger spacing of $10^{-2}\mu$m is used.

Once the covariance structure is known, samples of the rough surfaces can be generated, and a sample of the surface is illustrated in Fig. 5.8(b).

From the asperities to the RSVE meshes

From a sample of the rough surface, its corresponding asperities can be identified following the procedure depicted above. As the rough surface and the grain structure are correlated, the Voronoï tessellation is generated based on the asperities information. The seeds of the tessellation corresponds to the asperities of the surface. Based on the sample surface of Fig. 5.8(b), the corresponding Voronoï tesselation and its seeds are depicted in Fig. 5.10(a). A columnar finite

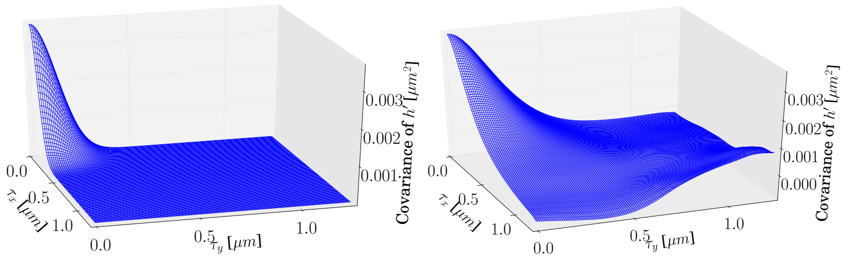

(a) Gaussian covariance

(b) Covariance from AFM measurements

Figure 5.9: The covariance $R_{h'}(\tau)\sigma_{h'}$ of the surface height (a) Gaussian covariance, and (b) from AFM measurements

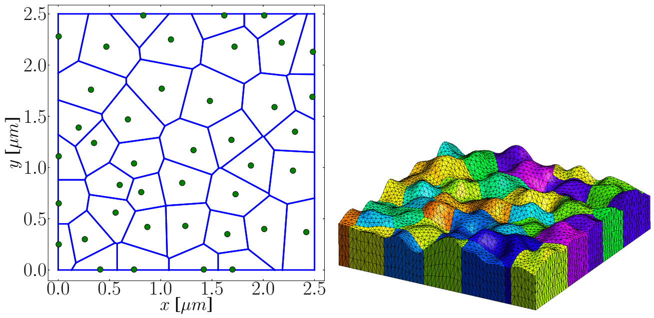

(a) The Voronoï tessellation and its seeds

(b) The finite element mesh

Figure 5.10: One sample of large Voronoï tessellation-based micro-structure, (a) the basis tessellation, and (b) the extruded finite element mesh

element mesh can then be extruded with the help of *gmsh* [23], and the position of each vertex of the mesh is then modified so that the top surface matches the rough surface illustrated in Fig. 5.8(b), leading to the finite element mesh reported in Fig. 5.10(b).

At this point the poly-crystalline material with its correlated roughness is then defined. As required for the computation of the homogenised material operators of the (R)SVEs, the desired outputs must be computed at different x and y locations of the micro-structure reported in Fig. 5.10(b), so that the spatial correlation can be captured using the window technique detailed in [52]. A set of RSVEs is then extracted from the micro-structure illustrated in Fig. 5.10, and one sample is reported in Fig. 5.11.

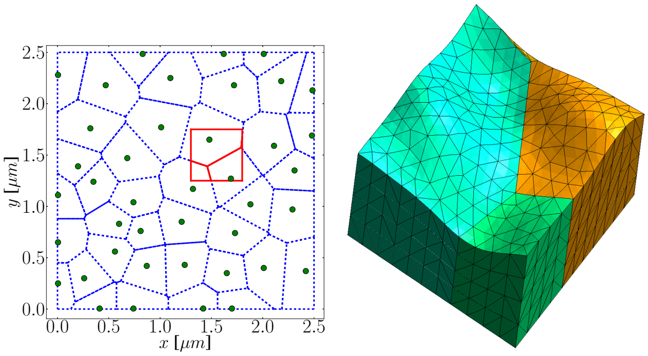

(a) A window in the tessellation (b) The RSVE mesh

Figure 5.11: One sample of an RSVE obtained from (a) one moving window of the tessellation, and (b) the corresponding RSVE finite element mesh

5.2 Numerical verification of the 3-scale procedure

The 3-scale procedure is now applied on MEMS. First the stochastic 3-scale method is verified with direct numerical simulations on a simple case: the uncertainty characterisation of the resonance frequency of micro-beams modelled with 1D beams elements. 3D thermo-elastic problems and rough thin plates are considered respectively in Section 5.3 and Section 5.4.

The 3-scale approach and its implementation are briefly described in Fig. 5.12. The left dashed box deals with the stochastic homogenisation. Samples of SVEs are obtained based on Section 5.1. The stochastic homogenisation process is based on the procedure developed in Chapter 3. The information of interest at the meso-scale in this case is the elasticity tensor. For each SVE sample, one homogenised elasticity tensor is extracted. The results are shown in Section 5.2.1. Once enough samples of the elasticity tensor are obtained so that convergence is observed, the samples of the elasticity tensor are used as input for the macro-scale SFEM (the right dashed box in Fig. 5.12). First, the random field must be defined and the spectral density of the field is computed, according to Chapter 4. If required, zero-padding is performed: a zero correlation is appended to the spatial correlation so that bigger fields can be generated. The behaviour of the stochastic model is investigated in Section 5.2.2. Finally, samples of the meso-scale random field are generated using the stochastic model, and are used in the frame of a SFEM approach following Chapter 2. Samples of quantities of interest are obtained, such as the resonance frequencies, and thus the variability of the response of the structure is assessed as shown in Section 5.2.3. The accuracy and efficiency of the resulting 3-scale stochastic method is ascertained by comparing the predictions with the results obtained from direct MC simulations on a full discretization of the structure, *i.e.* for which the grains are meshed individually.

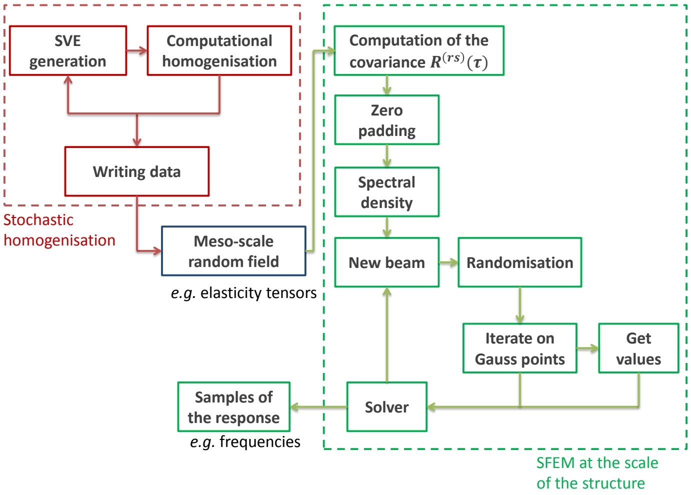

Figure 5.12: The implementation of the 3-scale procedure

As an illustration example we consider the problem of micro-beam resonators made of poly-silicon. In particular we study the distributions of its first three resonance frequencies[3]. The modes of interest will be respectively seen in Figures 5.22(a), 5.23(a), and 5.24(a).

5.2.1 Homogenised properties over basic SVEs

In this simplified model used for verification purposes, basic SVEs are considered. The basic SVEs considers only the grain size (whose average is assumed to be 200 nm) and the orientation (uniform) as uncertainties. Roughness is not considered in this case and the material properties are constant along the thickness (columnar micro-structure). Only the homogenised elasticity tensor is of interest. Thus the first order homogenisation is considered for a linear elastic problem.

From the procedure defined in Section 3.2, we can study 3D SVEs representing the poly-silicon structure. The resulting uncertainties are meant to be propagated to the macro-scale following the procedure described in Section 2.3 using beam SFEM. Indeed the width (thickness) of the macro-scale beam is

---

[3] The homogenisation process described in Chapter 3 does not account for the dynamic effects. This assumption is valid as the time-scales separation of the problem exists. Indeed the characteristic time of the dynamic problem t_{macro} depends on the first resonance frequency which is approximately 13 MHz as it will be shown. Therefore $t_{\text{macro}} \approx 7 \cdot 10^{-8}\,\text{s}$. As the speed of sound in silicon is about $8433\,\text{ms}^{-1}$ and as the size of the largest SVE is $0.6\,\mu\text{m}$, the characteristic time of the micro problem is $t_{\text{micro}} \approx 7 \cdot 10^{-11}\,\text{s}$. As there are several orders of magnitude between the time-scales, one can neglect the stress wave problem within an SVE.

small compared to its length, 1D-finite elements will be considered at the macro-scale and the SVE width (thickness) considered is the one of the macro-beam. Therefore both the width and the thickness (properties constant over the thickness) of the macro-beam are implicitly considered in the 3D homogenisation and, in turn, in the beam discretization.

SVE definition

The only relevant geometric parameter to study the size effect of the SVE is thus its length. This also means that the spatial correlation is only required in one direction. We consider four different SVE lengths, l_{SVE}, successively equal to $0.1\,\mu$m, $0.2\,\mu$m, $0.4\,\mu$m, and $0.6\,\mu$m. The width and height of the SVEs are respectively $0.5\,\mu$m and $0.1\,\mu$m. Let us note that if the SVE size is too small, the SVEs are only small parts of unique grains and thus the meso-scale random field becomes a noise field [5], leading to a non-smooth meso-scale random field.

Homogenisation

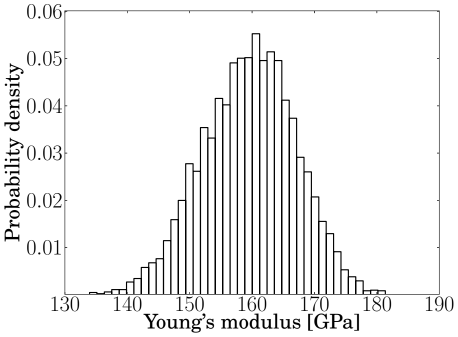

Figure 5.13: Samples of Young's modulus obtained for an SVE length of $0.2\,\mu$m

Applying the described homogenisation methodology, the meso-scale mechanical properties distribution can be obtained through the evaluation of the material tensor $\boldsymbol{C}_{\mathrm{M}}$ using Eq. (3.26) for the different SVE realisations. The number of tessellations generated are 1084, 855, 312, and 117 for respectively an SVE length l_{SVE} of 0.1, 0.2, 0.4, and $0.6\,\mu$m. The distance between the centres of the successive SVEs extracted from the tessellation is $0.5\times l_{\mathrm{SVE}}$ for a l_{SVE} of 0.1 and $0.2\,\mu$m and $0.25\times l_{\mathrm{SVE}}$ for the 2 remaining SVE lengths. As an example the resulting histogram of the Young's modulus E_x[4] along the x-direction (x is along the SVE length, y along the width, and z along its height) is illustrated in Fig. 5.13 for an SVE of length $l_{\mathrm{SVE}} = 0.2\,\mu$m. The effect of the SVE length on the meso-scale properties is depicted in Fig. 5.14. Fig. 5.14(a) represents the evolution of the distribution of the Young's modulus for different

---

[4] For conciseness, in what follows we drop the subscript M which refers to the homogenised meso-scale properties.

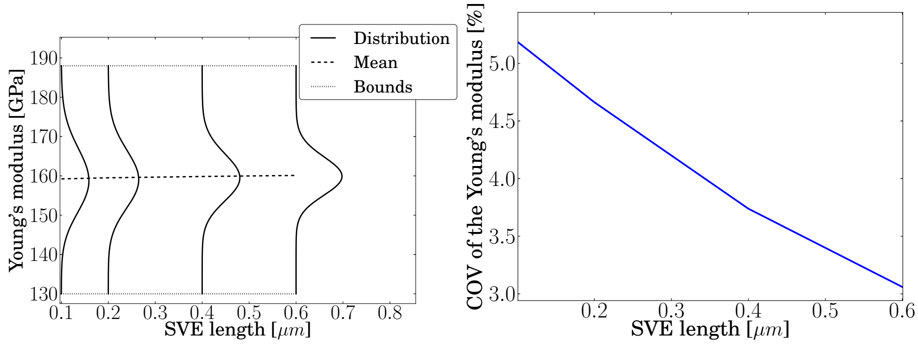

(a) Evolution of the Young's modulus

(b) Evolution of the variance

Figure 5.14: Meso-scale Young's modulus E_x distribution for different SVE lengths (x is along the SVE length)

SVE lengths l_{SVE}. The silicon bounds are also reported on that figure. One can see in the figure that a larger SVE involves a more peaky distribution. The mean Young's modulus is found to be around 160 GPa, roughly in between the two bounds obtained for Silicon crystals in [33]. The evolution of the Coefficient of Variation (COV) of the meso-scale Young's modulus with respect to the SVE length is reported in Fig. 5.14(b). As expected based on [5], the coefficient of variation decreases with the SVE length.

The auto-correlation of the Young's modulus E_x and the cross-correlations of the Young's modulus E_x, with other material properties extracted from the elasticity tensor, are computed for an SVE length of $l_{\text{SVE}} = 0.1\,\mu$m using Eq. (3.115) and are reported in Fig. 5.15(a) for different values of the distance τ –along x. Such an analysis was previously achieved in [80] in the case of a Bernoulli lattice. The evolution with the distance τ –along x– of the auto-correlation of the Young's modulus E_x is also evaluated using Eq. (3.115) and is illustrated in Fig. 5.15(b) for the four considered SVE lengths.

The following conclusions can be drawn from Fig. 5.15:

- As expected for $\tau = 0$, the auto-correlation is equal to the unity and the cross-correlations are always < 1 and > -1;
- The correlations obtained for $\tau = l_{\text{SVE}}$, *i.e.* when the two SVEs are adjacent, are low but do not vanish as two adjacent SVEs share some common grains; This effect decreases with the increase of the SVE length, as the proportion of shared grains also decreases; As an example, the auto-correlation obtained for $\tau = l_{\text{SVE}}$ is ≈ 0.6 for an SVE length of $0.1\,\mu$m and is ≈ 0.17 for an SVE of $0.4\,\mu$m, see Fig. 5.15(b);
- For longer meso-scale volume elements, sharing of common grains takes place at longer distances between SVEs and the correlation lengths defined by Eq. (2.11) of the Young's modulus for the different SVE lengths increases, see Table 5.5;

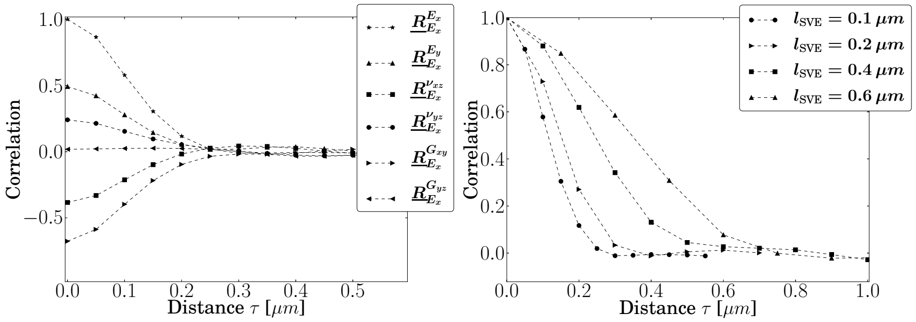

(a) Cross-correlations of E_x

(b) Auto-correlation of E_x

Figure 5.15: Two-points statistics for different values of the distance τ along x between the centres of the SVEs. (a) Auto- and cross-correlations of the Young's modulus in the x direction with respect to different material properties for an SVE length $l_{\mathrm{SVE}} = 0.1\,\mu$m ($x$ is along the SVE length, y along the width, and z along its height). (b) The auto-correlation of the Young's modulus for different SVE lengths.

Table 5.5: Correlation length l_{E_x} of the Young's modulus E_x for different SVE lengths

SVE length [μm]	**Correlation Length** [μm]
0.1	0.233
0.2	0.307
0.4	0.504
0.6	0.693

- When τ increases the auto- and cross-correlations decrease to 0 as does the probability to share some grains;
- The cross-correlation between E_x and E_y is positive while the cross-correlation between E_x and the Poisson ratio ν_{xz} and the in-plane shear modulus G_{xy} is negative because of the cubic symmetry of the silicon crystal; Indeed the silicon crystal has a minimum Young's modulus along the directions [1 0 0], [0 1 0], and [0 0 1];
- The cross-correlation between E_x and the out-of-plane shear modulus is almost zero.

Finally, the effect of the applied BCs on the SVE homogenisation results is investigated. The standard deviations of the Young's modulus along x obtained for KUBCs, OUMBCs, and SUBCs are reported in Table 5.6. Three different SVE lengths are successively considered: $0.1\,\mu$m, $0.2\,\mu$m, and $0.4\,\mu$m. The difference in the standard deviation obtained with the OUMBCs distribution is found to be lower than 2% as compared with the other BCs, justifying the use of the sole OUMBCs.

Table 5.6: Standard deviation of the Young's modulus E_x obtained with different boundary conditions and SVE lengths

SVE lengths [μm]	**KUBC**	**OUMBC**	**SUBC**
0.1	$\sigma_{E_x} = 8.33$ GPa	$\sigma_{E_x} = 8.43$ GPa	$\sigma_{E_x} = 8.43$ GPa
0.2	$\sigma_{E_x} = 7.22$ GPa	$\sigma_{E_x} = 7.31$ GPa	$\sigma_{E_x} = 7.31$ GPa
0.4	$\sigma_{E_x} = 6.02$ GPa	$\sigma_{E_x} = 6.11$ GPa	$\sigma_{E_x} = 6.13$ GPa

5.2.2 Stochastic model behaviour

The stochastic model of the random field of the elasticity tensor is now characterised. First, the lower bound is defined as was required to build the stochastic model in Chapter 4 in Section 5.2.2. Afterwards, statistical properties of the generated samples of the elasticity tensor are compared to the ones of the initial samples extracted in Section 5.2.2.

Lower bound of the elasticity tensor

Although only the lower bound $\boldsymbol{C}_{\text{L}}$ of the elasticity tensor $\boldsymbol{C}$ is enforced when generating the random field, both the lower and upper bounds for the elasticity tensor are discussed hereafter for the sake of generality.

As discussed in Section 3.2.1, for heterogeneous materials made of different material phases, there are two absolute bounds which are used to define the variation range of the elasticity tensor on a representative volume element (RVE): the upper bound –or Voigt bound– $\overline{\boldsymbol{C}}_{\text{M}}$ and the lower bound –or Reuss bound– $\underline{\boldsymbol{C}}_{\text{M}}$. In the case of a multi-phase material, these bounds read

$$\begin{aligned} \overline{\boldsymbol{C}}_{\text{M}} &= \langle \boldsymbol{C}_{\text{m}} \rangle = \sum_{i=1}^{n} \beta_i \boldsymbol{C}_i && (5.10) \\ \underline{\boldsymbol{C}}_{\text{M}} &= \left(\langle \boldsymbol{C}_{\text{m}}^{-1} \rangle \right)^{-1} = (\sum_{i=1}^{n} \beta_i \boldsymbol{C}_i^{-1})^{-1} \,, && (5.11) \end{aligned}$$

respectively, where $\boldsymbol{C}_i$ $(i = 1, 2, ..., n)$ is the elasticity tensor of phase i and β_i the volume fraction of phase i, which satisfies $\sum_{i=1}^{n} \beta_i = 1$.

However, when considering different SVEs, the bounds (5.10-5.11) cannot be determined anymore, as the volume fractions β_i of each phase is different for each SVE. Moreover, in the problem of a poly-crystalline material, which is an aggregate of grains based on the same crystal but with random orientations, as the same anisotropic material is considered in each grain, of random shape and orientation, it is not possible to define $\boldsymbol{C}_i$ and β_i, as the different elasticity tensors $\boldsymbol{C}_i$ are expressions of the same tensor in different coordinates systems.

For the same reasons, it is not possible to defined bounds, which satisfy $\boldsymbol{C}_{\mathrm{L}} \leqslant \boldsymbol{C}_{\mathrm{M}} \leqslant \boldsymbol{C}_{\mathrm{U}}$ [5], directly from the grains material tensors $\boldsymbol{C}_i$ as

$$\begin{aligned}\boldsymbol{C}_{\mathrm{U}} &= \max\{\boldsymbol{C}_i | i = 1, 2, ..., n\} \\ \boldsymbol{C}_{\mathrm{L}} &= \min\{\boldsymbol{C}_i | i = 1, 2, ..., n\}\,. \end{aligned} \tag{5.12}$$

Indeed, as all the grains are associated to elasticity tensors $\boldsymbol{C}_i$ $(i = 1, 2, ..., n)$ which are the same tensors in different coordinates, they have the same eigenvalues.

In this work we propose an efficient method to define the lower bound $\boldsymbol{C}_{\mathrm{L}}$ and the upper bound $\boldsymbol{C}_{\mathrm{U}}$ of a poly-crystalline material, for any size of the SVEs. As we have described previously, $\boldsymbol{C}_i$ $(i = 1, 2, ..., n)$ are the expressions of the same elasticity tensor in different coordinates. Let $\boldsymbol{C}_{\mathrm{S}}$ be the elasticity tensor of a single crystal. To define the two bounds $\boldsymbol{C}_{\mathrm{L}}$ and $\boldsymbol{C}_{\mathrm{U}}$, we need to guaranty that $\boldsymbol{C}_{\mathrm{L}} \leqslant \boldsymbol{C}_{\mathrm{S}} \leqslant \boldsymbol{C}_{\mathrm{U}}$ for any orientation of the crystal, and thus for any rotation of $\boldsymbol{C}_{\mathrm{S}}$. By satisfying this relation, $\boldsymbol{C}_{\mathrm{L}}$ and $\boldsymbol{C}_{\mathrm{U}}$ are bounds for the poly-crystalline material and for the single crystal. Moreover, as the grains can have any orientation, the bounds are defined as isotropic tensors and are thus characterized by two material parameters only. They can thus be expressed as

$$\boldsymbol{C}^{\mathrm{iso}} = \begin{bmatrix} 2G+\lambda & \lambda & \lambda & 0 & 0 & 0 \\ \lambda & 2G+\lambda & \lambda & 0 & 0 & 0 \\ \lambda & \lambda & 2G+\lambda & 0 & 0 & 0 \\ 0 & 0 & 0 & G & 0 & 0 \\ 0 & 0 & 0 & 0 & G & 0 \\ 0 & 0 & 0 & 0 & 0 & G \end{bmatrix}, \tag{5.13}$$

for example in terms of the shear modulus $G = \frac{E}{2(1+\nu)}$ and Lamé constant $\lambda = \frac{E\nu}{(1+\nu)(1-2\nu)}$, with Young's modulus E and Poisson ratio ν.

The two isotropic bounds $\boldsymbol{C}^{\mathrm{iso}}_{\mathrm{L}}$ and $\boldsymbol{C}^{\mathrm{iso}}_{\mathrm{U}}$ can thus be obtained by solving two optimization problems, respectively,

$$\min_{G,\,\lambda \in R^{+}} \|\boldsymbol{C}^{\mathrm{iso}} - \boldsymbol{C}_{\mathrm{S}}\|_F \quad \text{subject to} \quad \boldsymbol{C}^{\mathrm{iso}} \leqslant \boldsymbol{C}_{\mathrm{S}} \quad \text{and} \tag{5.14}$$

$$\min_{G,\,\lambda \in R^{+}} \|\boldsymbol{C}^{\mathrm{iso}} - \boldsymbol{C}_{\mathrm{S}}\|_F \quad \text{subject to} \quad \boldsymbol{C}^{\mathrm{iso}} \geqslant \boldsymbol{C}_{\mathrm{S}}\,. \tag{5.15}$$

According to Eq. (5.12), the resulting tensors $\boldsymbol{C}^{\mathrm{iso}}_{\mathrm{L}}$ and $\boldsymbol{C}^{\mathrm{iso}}_{\mathrm{U}}$ can be used as bounds of the elasticity tensor for a poly-crystalline material.

For the silicon crystal oriented with [100], [010] and [001] along the Cartesian coordinates, the crystal elasticity tensor $\boldsymbol{C}_{\mathrm{S}}$ is given in Eq. (5.4). The lower and upper bounds, respectively obtained from Eqs. (5.14) and (5.15), can be expressed in terms of their corresponding Young's modulus E and Poisson ratio ν as $\boldsymbol{C}^{\mathrm{iso}}(E,\,\nu)$ following Eq. (5.13). After solving the optimization problem, the bounds are found to be $\boldsymbol{C}^{\mathrm{iso}}_{\mathrm{L}}(E = 130.0\text{ GPa}, \nu = 0.278)$ and $\boldsymbol{C}^{\mathrm{iso}}_{\mathrm{U}}(E =$

---

[5] Based on the Loewner ordering, $\boldsymbol{A} > \boldsymbol{B}$ if $\boldsymbol{A} - \boldsymbol{B}$ is positive definite and $\boldsymbol{A} \geq \boldsymbol{B}$ if $\boldsymbol{A} - \boldsymbol{B}$ is positive semi-definite

187.9 GPa, $\nu = 0.181$). These two values of the Young's modulus, *i.e.* 130.0 GPa and 187.9 GPa, correspond to the lowest and highest values of Young's moduli that a single silicon crystal can reach.

Stochastic model

The input of the SFEM approach developed in Section 2.3 is the meso-scale random field of the elasticity tensor $\boldsymbol{C}_{\mathrm{M}}(x, \boldsymbol{\theta})$. First, a semi-positive definite symmetric increment $\Delta \boldsymbol{C}$ is defined such that

$$\boldsymbol{C}_{\mathrm{M}} = \boldsymbol{C}_{L} + \Delta \boldsymbol{C}\,, \tag{5.16}$$

is always a symmetric positive definite matrix, bounded by $\boldsymbol{C}_{L}$. To generate such a semi-positive-definite matrix, one can use the Cholesky decomposition as described in [86], which reads

$$\Delta \boldsymbol{C} = \boldsymbol{L}\boldsymbol{L}^{\mathrm{T}}\,. \tag{5.17}$$

In this equation, the matrix $\boldsymbol{L}$ is a lower triangular matrix. The matrix $\boldsymbol{L}$ is made of 21 independent entries, which form a random vector field.

In this work a vector field $\mathcal{V}$ of 21 elements is considered: the 21 elements of $\boldsymbol{L}$. Let $\bar{\mathcal{V}}$, $\sigma_{\mathcal{V}}$ and $\mathcal{V}'$ be respectively the mean, the standard deviation, and the normalized fluctuation of the elements of $\mathcal{V}$ so that the random vector field reads

$$\mathcal{V}^{(r)} = \bar{\mathcal{V}}^{(r)} + \mathcal{V}'^{(r)}\sigma_{\mathcal{V}^{(r)}}\,. \tag{5.18}$$

The random field $\mathcal{V}'(x, \boldsymbol{\theta})$ can be generated following the spectral approach described in Section 4.3. From samples of $\mathcal{V}'(x, \boldsymbol{\theta})$, samples of the elasticity tensor can be retrieved owing to Eqs (5.16-5.18).

Stochastic behaviour of generated samples

Table 5.7: Errors in the material properties mean values and standard deviations obtained with the spectral generator as compared to the values obtained directly from the SVE realisations, for an SVE length of 0.4 μm

Material property	**Error in the mean**	**Error in the standard deviation**
Young's modulus E_x	0.026 %	0.97 %
Poisson ratio ν_{yx}	0.043 %	1.48 %
Shear modulus G_{xz}	0.072 %	10.09 %

We now generate the meso-scale random field of the elasticity tensor using the stochastic model described in Section 4.3. The Non-Gaussian mapping is not considered. The input of this stochastic model are the homogenised material tensor realisation obtained in Section 5.2.1. The distribution of the generated

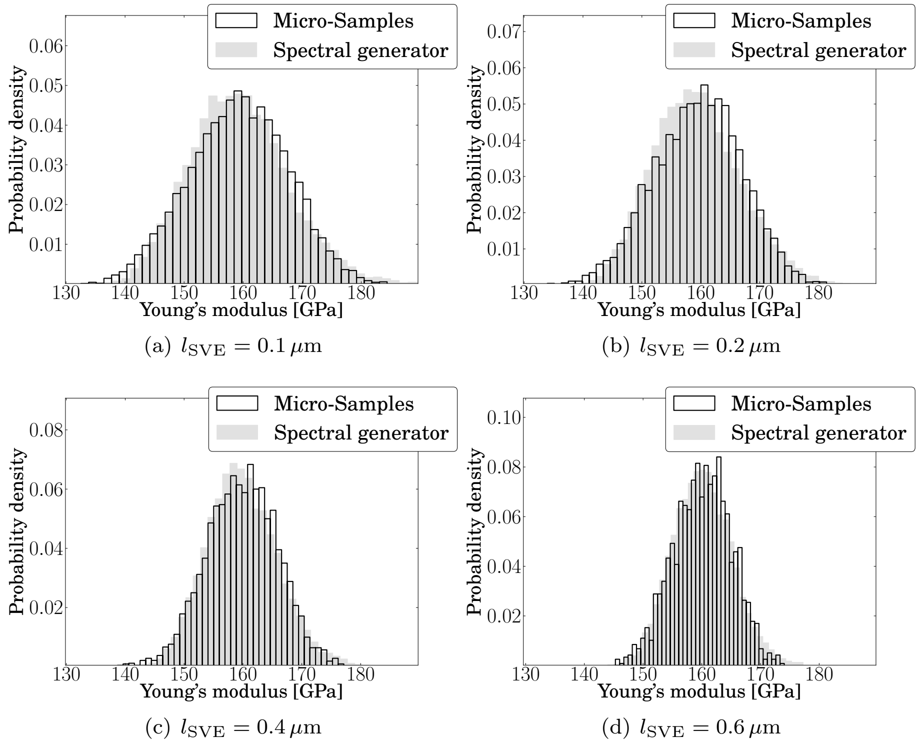

(a) $l_{\mathrm{SVE}} = 0.1\,\mu$m (b) $l_{\mathrm{SVE}} = 0.2\,\mu$m

(c) $l_{\mathrm{SVE}} = 0.4\,\mu$m (d) $l_{\mathrm{SVE}} = 0.6\,\mu$m

Figure 5.16: Comparison of the Young's modulus E_x histograms obtained directly from the SVE realisations and with the spectral generator for different SVE lengths (x is along the SVE length)

random field is compared with the distribution directly obtained from the sample realisations.

In Fig. 5.16, the histograms of E_x, the Young's modulus along the SVE length direction, extracted from the elasticity tensor $\boldsymbol{C}_{\mathrm{M}}$ are compared for different SVE lengths. The distributions obtained with the generator are qualitatively in good agreements with the ones obtained from the SVE realizations. The same conclusion holds for the histograms of the Poisson ratio and of the shear modulus respectively shown in Figs. 5.17(a) and 5.17(b). The errors on the mean and the standard deviation of the material distribution resulting from the generator are reported in Table 5.7 for an SVE length of $0.4\,\mu$m. While good agreements are obtained for the Young's modulus and the Poisson ratio, a higher difference is obtained for the shear modulus. As, in our case, the Young's modulus is the main parameter governing the structural problem, the accuracy of the random generator is satisfying for our application as it will be shown when verifying the prediction with the direct Monte-Carlo results. The skewness of the Young's modulus distribution, $\gamma_{1_{E_x}} = \frac{\mathbb{E}\left[(E_x-\mathbb{E}[E_x])^3\right]}{\sigma^3_{E_x}}$, obtained from

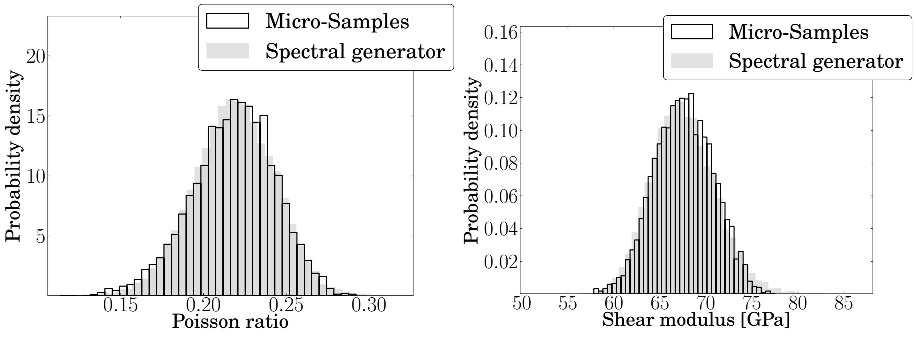

(a) Poisson ratio in the yx-direction (b) Shear modulus in the xz-direction

Figure 5.17: Comparison of the material properties histograms obtained directly from the SVE realisations and with the spectral generator for an SVE length of $0.4\,\mu$m: (a) yx-Poisson ratio, and (b) xz-shear modulus (x is along the SVE length, y along the width, and z along its height)

the micro-samples and from the generator is -0.11 and 0.26, respectively. Both characterize a distribution close to symmetry, although the use of a lower bound for the generator induces a positive value. The peak intensity of the Young's modulus distribution is characterized by the kurtosis, $\beta_{2E_x} = \frac{\mathbb{E}\left[(E_x - \mathbb{E}[E_x])^4\right]}{\sigma^4_{E_x}}$ and is found to be 2.93 and 3.02, for the distribution obtained from the micro-samples and from the generator, respectively. The kurtosis is thus found to be in good agreement justifying the use of the developed generator. To improve the prediction of the shear modulus, non-Gaussian mapping can be considered. Non-Gaussian mapping is considered for the thermo-mechanical and the rough thin plates problems in the following Sections.

Finally, Figs. 5.18(a) and 5.18(b) respectively compare the 1D-spatial auto-correlation of the Young's modulus and of the shear modulus obtained directly from the SVE computations (with the zero-padding) and with the generator for an SVE length of $0.4\,\mu$m. The two curves are almost identical. Fig. 5.18(c) compares the different cross-correlations, already studied in Fig. 5.15(a), obtained with both the micro-samples (with the zero-padding) and with the generator for an SVE length of $0.1\,\mu$m. The behaviours obtained with the generator is in good agreement with the original distribution.

Once the generator has been numerically verified for the different SVE lengths l_{SVE}, it can be used to provide several meso-scale random field realisations at a lower cost than solving the SVEs at each sampling point. As a way of illustration, Figs. 5.19(a) and (b) represent five realisations of the Young's modulus meso-scale random field along a distance of $1\,\mu$m obtained using the generator based on SVE lengths $l_{\text{SVE}} = 0.1\,\mu$m and $l_{\text{SVE}} = 0.4\,\mu$m, respectively. The x-evolution of the Young's modulus is compared to $\mathbb{E}\left[E_x\right]$ its average meso-scale value and to σ_{E_x}, its standard deviation. The effect of the SVE length when propagating the meso-scale uncertainties to the macro-scale will be stud-

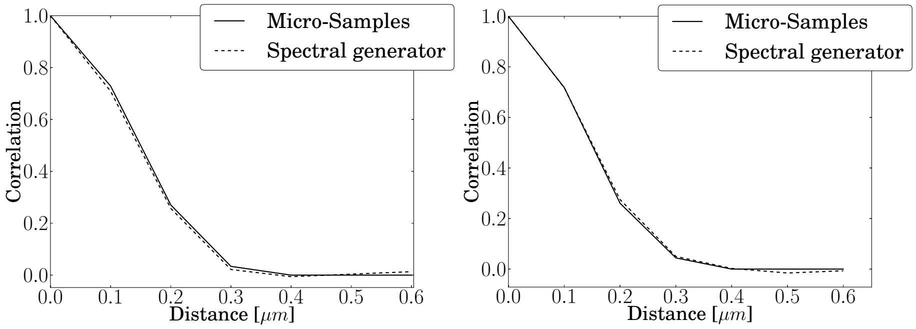

(a) Young's modulus along the x direction (b) Shear modulus in the xz-direction

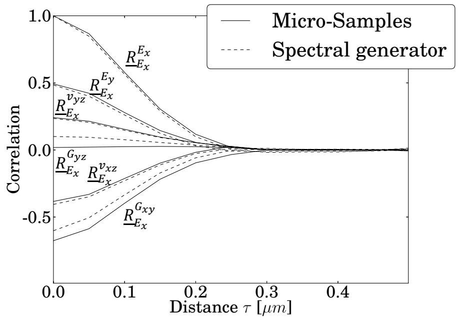

(c) Cross-correlation

Figure 5.18: Comparison of the 1D spatial correlations obtained directly from the SVE realisations and with the spectral generator: (a) Auto-correlation of the Young's modulus along the x-direction for an SVE length of $0.4\,\mu$m, (b) auto-correlation of the xz-shear modulus for an SVE length of $0.4\,\mu$m (x is along the SVE length, y along the width, and z along its height), and (c) Cross-correlations of the the Young's modulus along the x-direction with other material constants, for an SVE length of $0.1\,\mu$m.

ied in the next section, in which the results are shown to converge with the macro-scale finite element mesh size (for all l_{SVE}).

5.2.3 Macro-scale results of the 1D beam problem and numerical verification

We first consider micro-beams of dimensions $3.2\,\mu\text{m} \times 0.5\,\mu\text{m} \times 0.1\,\mu\text{m}$. The structural-scale has the size of the first mode shape, which is four times the size of the beam: $l_{\text{macro}} = 12.8\,\mu$m. As the largest SVE length considered is $0.6\,\mu$m, we satisfy the length scale separation $l_{\text{meso}} << l_{\text{macro}}$ in this application. A short length of the beam is chosen in order to be able to obtain a reference solution of the problem by direct MC simulations of the poly-crystalline structure in a reasonable time. The Monte-Carlo simulations are thus applied on a finite-

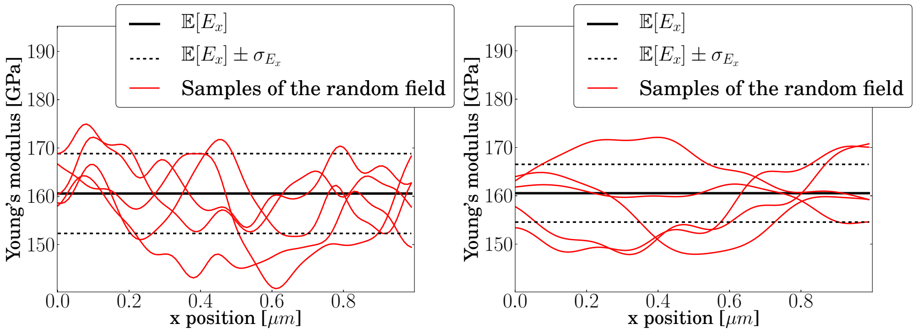

(a) $l_{\text{SVE}} = 0.1\,\mu$m (b) $l_{\text{SVE}} = 0.4\,\mu$m

Figure 5.19: Five realisations of the meso-scale random field obtained with (a) an SVE length $l_{\text{SVE}} = 0.1\,\mu$m and (b) an SVE length $l_{\text{SVE}} = 0.4\,\mu$m: meso-scale x-evolution of the Young's modulus. The bold line correspond to $\mathbb{E}\left[E_x\right]$, the average meso-scale value of the Young's modulus, and the dotted lines include σ_{E_x}, its standard deviation.

element model of about $\approx 20\,000$ quadratic tetrahedral finite elements.

To apply the stochastic 3-scale method, the micro-beam is discretized using Timoshenko beam finite elements as described in Section 2.3.2.

In the context of the point discretization method, the Young's and shear moduli of an element are obtained from the generated meso-scale random elasticity tensor evaluated at the element centre point. The equations of the stochastic finite element problem (2.27), with $\boldsymbol{f} = 0$ for the free vibration problem, can then be directly obtained and solved for each realisation $\boldsymbol{\theta}$. A Monte-Carlo analysis is then applied to compute the distribution of the micro-beam resonance frequencies.

In order to evaluate the existing bias from the deterministic FE models, *i.e.* by using 1D-beam and 3D finite elements, the beam is studied using an isotropic material (Young's modulus of 160 GPa and shear modulus of 68 GPa). The number of elements for both models is enough to ensure the convergence of (at least) the first three eigen-frequencies with respect to the element-size to reach an accuracy better than 0.5 %. With the 1D-beam finite elements the first resonance frequency is found to be 13.068 MHz while it is found to be 13.106 MHz with the 3D finite elements. This difference of 0.29 % is lower than the uncertainties resulting from the poly-crystalline material organization.

Finally, all the MC simulations results are presented for a sufficiently high number of generated samples, *i.e.* respectively at least 5000 and 3500 for the 3-scale and the direct procedures, to ensure the convergence of the average resonance frequencies and of their standard deviations. As an example, in the particular case which will be study hereafter (3.2 μm-long beam; $l_{\text{SVE}} = 0.4\,\mu$m and a macro mesh size of 0.25 μm for the 3-scale simulations), Figs. 5.20(a)

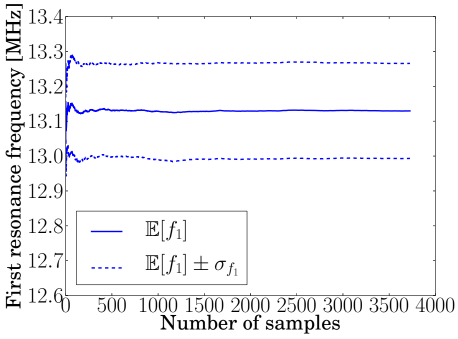

(a) Direct finite elements

(b) 3-scale approach

Figure 5.20: Convergence study of the MC simulations of the 3.2 μm-long beam for both (a) the direct finite element approach and (b) the 3-scale approach ($l_{\text{SVE}} = 0.4\,\mu$m and a macro-mesh size of 0.25 μm)

and (b) report, for respectively the direct finite element simulations and the 3-scale approach, the convergence of these values with respect to the number of samples. It can be seen that, beyond 1500 samples, the MC simulations have converged.

Effects of the SVE and structural mesh sizes

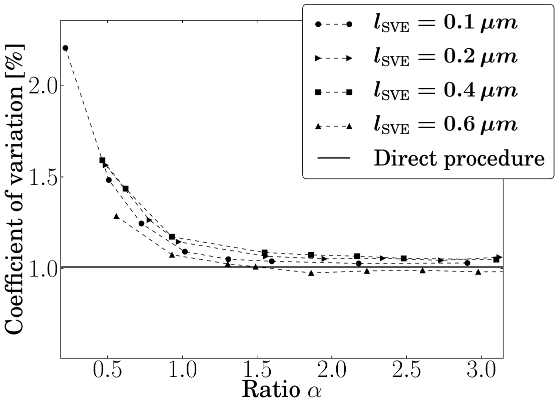

Figure 5.21: The COV of the first resonance frequency for a 3.2 μm-long beam for different SVE lengths and finite element mesh sizes in terms of $\alpha = \frac{l_{E_x}}{l_{\text{mesh}}}$, the ratio between the correlation length of the Young's modulus, l_{E_x}, and the mesh size, l_{mesh}

The developed 3-scale stochastic method is applied for different finite element discretizations (mesh sizes l_{mesh}) and SVE lengths (l_{SVE}) .

In order to illustrate the effect of the mesh size, the evolution of the predicted first resonance frequency COV is reported in Fig. 5.21 in terms of the ratio $\alpha = \frac{l_{E_x}}{l_{\text{mesh}}}$ between the correlation length of the Young's modulus, l_{E_x}, see Table 5.13, and the mesh size, l_{mesh}. In the cases of $\alpha < 1$, the mesh size is larger than the correlation length, and the stochastic finite element method suffers from a lack of accuracy [28, 84]. Indeed, the predicted COV is found to depend on the mesh-size –and thus on SVE length through the correlation length l_{E_x}– and to be higher than the reference solution. This is physically explained by the fact that, in this case, the finite element size is larger than its associated SVE and the amount of grains associated to each finite element is underestimated, leading to an over-prediction of the uncertainties. When refining the finite element mesh, *i.e.* for α larger than one, the 3-scale predictions are found to converge toward the reference solution as expected with the use of the SFEM. In these cases, the SVEs are of size comparable to or larger than the finite-element sizes and the existing spatial correlation between the SVEs defined on the finite elements accounts for the change of meso-scale distribution arising with a change of SVE length. As we are using the centre point method to discretize the random field, the 3-scale method converges by overestimating the uncertainties, in agreement with the literature [14].

Table 5.8: Comparison of the first three mean resonance frequencies obtained with the 3-scale stochastic method and with the direct MC simulations

Mode	**3-scale approach**	**Direct procedure**	**Relative difference**
1	13.055 MHz	13.129 MHz	0.57 %
2	64.448 MHz	64.115 MHz	0.51 %
3	81.554 MHz	81.896 MHz	0.42 %

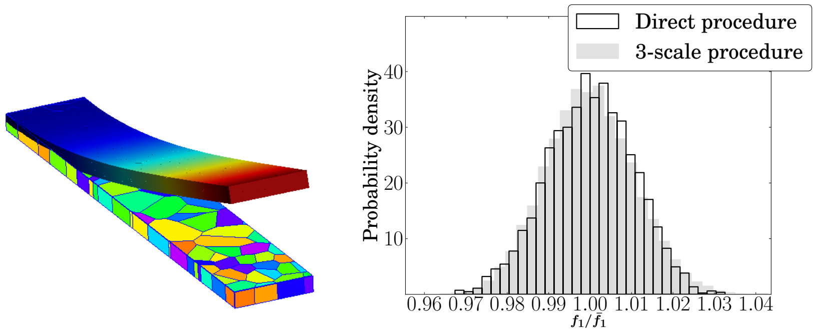

(a) Direct finite element sample

(b) Resonance frequency histograms

Figure 5.22: Comparison of the first resonance frequency histograms obtained with the 3-scale stochastic method and with the direct MC simulations. (a) Example of a direct finite element simulation. (b) Resonance frequency histograms.

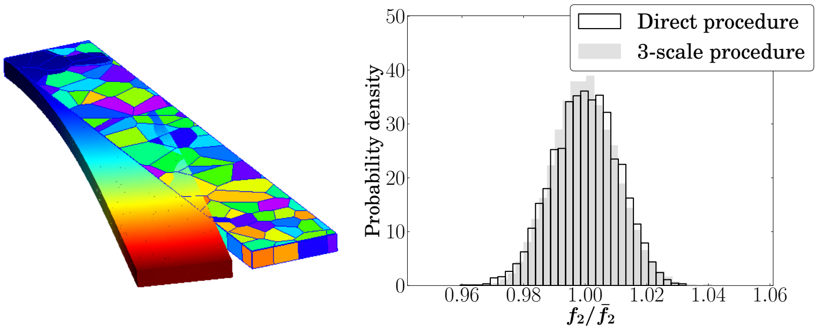

(a) Direct finite element sample (b) Resonance frequency histograms

Figure 5.23: Comparison of the second resonance frequency histograms obtained with the 3-scale stochastic method and with the direct MC simulations. (a) Example of a direct finite element simulation. (b) Resonance frequency histograms.

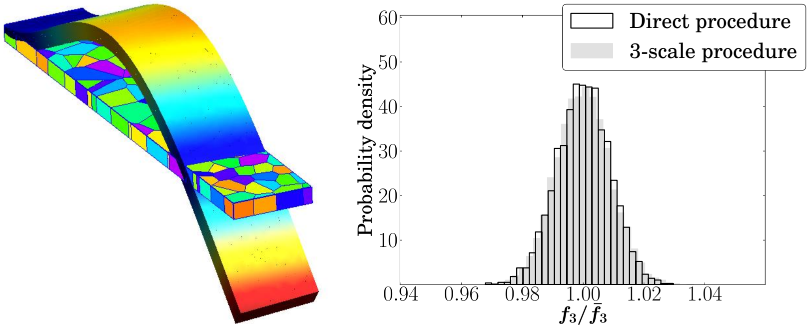

(a) Direct finite element sample (b) Resonance frequency histograms

Figure 5.24: Comparison of the third resonance frequency histograms obtained with the 3-scale stochastic method and with the direct MC simulations. (a) Example of a direct finite element simulation. (b) Resonance frequency histograms.

The first three resonance frequencies histograms obtained with the 3-scale stochastic method and with the direct MC simulations are reported in Figs. 5.22 - 5.24 along with the illustration of the resonance modes. For the 3-scale model, the considered SVE length and mesh size are respectively $0.4\,\mu$m and $0.27\,\mu$m. The resonance frequencies obtained with both procedures are normalised with their corresponding mean reported in Table 5.8. The histograms obtained by the stochastic 3-scale method are in good agreement with the reference results obtained by the direct MC simulations. The difference in the mean frequency mainly results from the bias between the models based on 3D finite elements and the 1D-beam finite elements (based on the results obtained with an isotropic material). For the second resonance frequency, the resonance-mode is out of plane and as the grains are not columnar, the Young's modulus is not uniform along the vibrating direction either. The second-order homogenisation developed in Section 3.4 should thus ideally be used for that bending mode.

When comparing the computation times, the resolution of the full model represents a computational cost around nine hours per sample on a $3.4\,GHz$ CPU to be compared to a few milliseconds per sample for the 3-scale procedure with the mesh size equal to $0.2\,\mu$m. However in order to define the generator, SVE homogenisation had to be computed, which is also time consuming. The extraction of the homogenised material tensor of a sample for a $0.2\,\mu$m-long SVE requires about 97 seconds. Approximately 50 hours are thus required to define the meso-scale random field. This remains much shorter than the time required to compute samples with the direct procedure. Moreover, the computed SVE information can be used for different meso-to-macro scale problems. If the size of the structural problem were to be increased, the interest of the proposed stochastic 3-scale process would become higher as direct MC simulations would become unreachable. Noticeably, the probabilistic distributions obtained with the 3-scale approach converge to the same ones as with the direct MC simulation, there is thus no loss of accuracy. Finally, using a smaller SVE reduces the homogenisation computational time, but requires a finer mesh size at the structural scale, or an increase in the number of integration points.

Effect of the micro-beam length

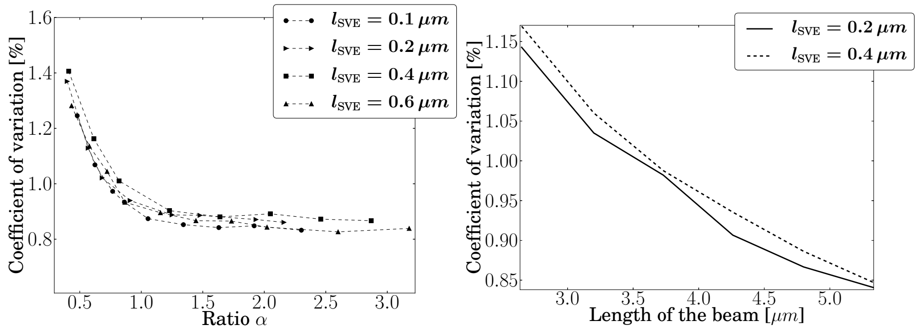

(a) $4.8\,\mu$m-long beam

(b) Influence of the beam length

Figure 5.25: Results for different beam lengths. (a) The COV of the first resonance frequency for a $4.8\,\mu$m-long beam for different SVE lengths and finite element mesh sizes in terms of $\alpha = \frac{l_{E_x}}{l_{\text{mesh}}}$, the ratio between the correlation length of the Young's modulus, l_{E_x}, and the mesh size, l_{mesh}. (b) Evolution of the first resonance frequency COV with respect to the beam length for different SVE lengths.

Results were also computed for different lengths of the micro-beam. Fig. 5.25(a) illustrates the evolution with α of the coefficient of variation obtained with different SVE lengths for a 4.8 μm-long micro-beam. It can be seen that the uncertainty is smaller than for the 3.2 μm beam. The coefficient of variation for the first mode frequency is COV $\approx$ 1% for the 3.2 μm beam while it is COV $\approx$ 0.9% for the 4.8 μm beam. The beam is made of more grains and thus, due to an averaging process, uncertainties are lower. This was also seen for the Young's modulus of the meso-scale SVEs and it is also discussed in [5]. The influence of the beam length is depicted in Fig. 5.25(b) for two SVE lengths: 0.2 and 0.4 μm. The finite element mesh is such that a constant ratio α is obtained (respectively, $\alpha = 2.3$ and $\alpha = 1.9$). As expected, the coefficient of variation of the first resonance frequency decreases with an increase of the length of the beam.

5.3 Extension to thermo-elastic problems over 3D structures

This section aims at estimating the uncertainty in terms of quality factor of micro-beams modelled in 3D. Therefore, the thermo-elastic homogenisation process[6] is used to estimate the meso-scale random fields. The combination of the spectral generator with the non-Gaussian mapping is considered to build the stochastic model and generate the meso-scale random field. The samples of the random field are then used as an input for the thermo-elastic SFEM approach described in Section 2.4. Modelling the beam in 3D allows the anchor types to be considered in macro-scale analyses.

5.3.1 Stochastic model behaviour of the homogenised properties

This section illustrates the meso-scale random field obtained from the stochastic homogenisation and its corresponding stochastic modelling with the spectral approach.

Lower bound for the thermal conductivity tensor

As lower bounds are required, the lower bound for the thermal conductivity tensor is discussed in the next section. The lower bound for the elasticity tensor was investigated in Section 5.2.2. Since the apparent thermal conductivity tensors of SVEs are combined results of a few grains, it is possible to define a low/high bound from Eq. (5.5) by using a grain size much smaller/higher than the generated grain size of the considered poly-silicon SVEs. For example, when

---

[6] The homogenisation process described in Chapter 3 does not account for the dynamic effects. This assumption was already validated in the previous application for the mechanical problem. It is also valid for the thermal problem due to the time-scales separation. The characteristic time of the macro-scale dynamic problem t_{macro} is based on the first mode resonance frequency and is $\approx 8 \cdot 10^{-8}$s for a $15 \times 3 \times 2\,\mu$m micro-beam. The relaxation time of the thermal problem over an SVE is $\approx 8 \cdot 10^{-10}$s.

we consider the poly-silicon layer deposited at the temperature of 610°C, the average grain size $d = 210$ nm at the deposition temperature of 580°, see Table 5.1, can be used to define a low bound for the thermal conductivities of SVEs, and one has

$$\kappa_{\text{SVE}} > \kappa_{\text{L}}, \quad \text{and} \quad \kappa_{\text{L}} = \kappa(210 \text{ nm})\,. \tag{5.19}$$

Stochastic model

By introducing the lower bounds $\boldsymbol{C}_{\text{L}}$ and $\boldsymbol{\kappa}_{\text{L}}$, the realisations of the random elasticity tensor and thermal conductivity tensor can be rewritten as

$$\boldsymbol{C}_{\text{M}} = \boldsymbol{C}_{\text{L}} + \Delta\boldsymbol{C}\,, \tag{5.20}$$

$$\boldsymbol{\kappa}_{\text{M}} = \boldsymbol{\kappa}_{\text{L}} + \Delta\boldsymbol{\kappa}\,, \tag{5.21}$$

where $\Delta\boldsymbol{C}$ and $\Delta\boldsymbol{\kappa}$ are positive definite matrices. The Cholesky decomposition algorithm [97] can be used directly to obtain the positive definite matrices, which are expressed as

$$\Delta\boldsymbol{C} = \boldsymbol{L}_{\boldsymbol{C}}\boldsymbol{L}_{\boldsymbol{C}}{}^{\text{T}}\,, \tag{5.22}$$

$$\Delta\boldsymbol{\kappa} = \boldsymbol{L}_{\boldsymbol{\kappa}}\boldsymbol{L}_{\boldsymbol{\kappa}}{}^{\text{T}}\,, \tag{5.23}$$

where $\boldsymbol{L}_{\boldsymbol{C}}$ and $\boldsymbol{L}_{\boldsymbol{\kappa}}$ are 6×6 and 3×3 lower triangular matrices, respectively, and the subscript T refers to their transpose.

For each large micro structure realization, we write the 21 entries of $\boldsymbol{L}_{\boldsymbol{C}}$ and 6 entries of $\boldsymbol{L}_{\boldsymbol{\kappa}}$ of each SVE into a vector $\mathcal{V}$ to obtain the realizations of the random vector field $\mathcal{V}(\boldsymbol{x}, \boldsymbol{\theta})$. Once again, $\bar{\mathcal{V}}$ and $\mathcal{V}'$ are respectively the mean and fluctuation of the random vector field, with $\mathcal{V} = \bar{\mathcal{V}} + \mathcal{V}'$. We assume that the random vector field $\mathcal{V}$ can be described as a homogeneous random field. Therefore $\bar{\mathcal{V}}$ is constant with respect to $\boldsymbol{x}$ and $\mathcal{V}'$ is a homogeneous zero-mean random field. This required random field $\mathcal{V}'(\boldsymbol{x}, \boldsymbol{\theta})$ can be generated through the spectral representation method based on the known cross-covariance matrix $\boldsymbol{R}_{\mathcal{V}'}(\boldsymbol{\tau})$, see Section 4.3. From samples of the random field $\mathcal{V}(\boldsymbol{x}, \boldsymbol{\theta})$, samples of the random fields $\boldsymbol{L}_{\boldsymbol{C}}(\boldsymbol{x}, \boldsymbol{\theta})$ and $\boldsymbol{L}_{\boldsymbol{\kappa}}(\boldsymbol{x}, \boldsymbol{\theta})$ can be retrieved. Finally, samples of meso-scale material properties can be obtained from Eqs. (5.20-5.23) as

$$\boldsymbol{C}_{\text{M}}(\boldsymbol{x},\boldsymbol{\theta}) = \boldsymbol{C}_{\text{L}} + \left(\boldsymbol{L}_{\boldsymbol{C}}(\boldsymbol{x}, \boldsymbol{\theta})\right)\left(\boldsymbol{L}_{\boldsymbol{C}}(\boldsymbol{x}, \boldsymbol{\theta})\right)^{T}\,, \tag{5.24}$$

$$\boldsymbol{\kappa}_{\text{M}}(\boldsymbol{x},\boldsymbol{\theta}) = \boldsymbol{\kappa}_{\text{L}} + \left(\boldsymbol{L}_{\boldsymbol{\kappa}}(\boldsymbol{x}, \boldsymbol{\theta})\right)\left(\boldsymbol{L}_{\boldsymbol{\kappa}}(\boldsymbol{x}, \boldsymbol{\theta})\right)^{T}\,, \tag{5.25}$$

Stochastic behaviour of generated macro-scale samples

In this section, the meso-scale properties of the thermo-elastic properties are illustrated as well as the behaviour of the random field generator, described in Section 4.3 and considering the Non-Gaussian mapping described in Section 4.4. Let us note that the first 21 values of $\mathcal{V}'$ are used to build the elasticity tensor following Eq. (5.24) and the last 3 values of $\mathcal{V}'$ are used to build the conductivity tensor as the obtained thermal conductivity tensor with the homogenised results has 3 different non-zero entries.

For the stochastic homogenisation of the thermo-elastic problem, we chose the SVE sizes of 0.5 μm and 0.8 μm for the poly-silicon layers deposited at 610°C and 630°C, respectively. In order to build the meso-scale random fields using the window technique as illustrated in Fig. 5.6, 200 (140) large Voronoï tessellations are built for the poly-silicon layers deposited at 610°C (630°C, respectively), from which 100 SVEs are extracted per tessellation by progressing by a distance of 0.25 μm (0.4 μm, respectively). The resulting number of SVEs, 20 000 (14 000) SVEs for the poly-silicon layers deposited at 610°C (630°C, respectively), ensures the convergence of the extracted meso-scale random fields.

First, we study the behaviour of the random field $\mathcal{V}'$. Because a mapping process is used in the non-Gaussian generator, the distributions of the generated $\mathcal{V}'^{(r)}$, $(r = 1, 2, ..., 24)$ recover the exact distributions of the micro-samples, which are obtained from the homogenization on SVE realisations. In Fig. 5.26, the histograms obtained by micro-sampling and by the generator are compared for $\mathcal{V}'^{(6)}$ and $\mathcal{V}'^{(9)}$, which have a highly skewed distributions. The generated random variables represent well their distributions obtained from the homogenization on SVEs.

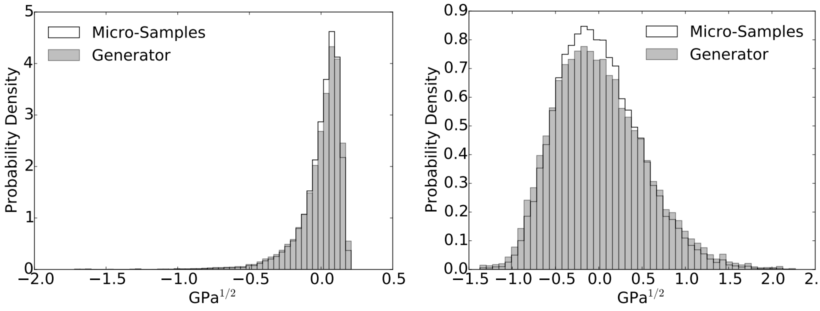

(a) Histogram of $\mathcal{V}'^{(6)}$

(b) Histogram of $\mathcal{V}'^{(9)}$

Figure 5.26: Comparison of histograms of $\mathcal{V}'^{(r)}$ between the micro-samples and the generated samples

Auto-correlation functions $\underline{\boldsymbol{R}}_{\mathcal{V}'}^{(r,r)}$ $(r = 1, 2, ..., 24)$ are also well recovered by the non-Gaussian random vector generator, as illustrated by Fig. 5.27, which depicts the 3D-view of the normalized auto-correlation function $\underline{\boldsymbol{R}}_{\mathcal{V}'}^{(1,1)}$. Since the 2-dimensional correlation functions are symmetric with respect to the planes $x = 0$ and $y = 0$, only one quarter of the function is displayed. More comparisons of auto-correlation curves, in the $y = 0$-plane, are presented in Fig. 5.28, for which the entries of $\mathcal{V}'$ are picked randomly from those related to the material tensor, Figs. 5.28(a)-5.28(c), and to the thermal conductivity tensor, Fig. 5.28(d).

For the cross-correlation functions, their trends are well preserved by the random field generator, as demonstrated by Fig. 5.29, which shows the 3D-view of the normalised cross-correlation function $\underline{\boldsymbol{R}}_{\mathcal{V}'}^{(1,\,2)}$. More cross correlations are

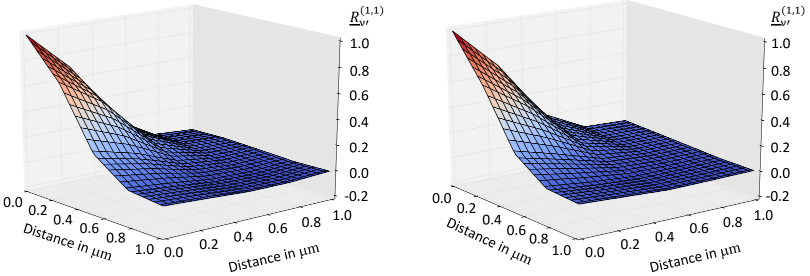

(a) Micro-samples (b) Generator

Figure 5.27: Comparison of a normalized auto-correlation function between the micro-samples and the generated samples of ${\mathcal{V}'}^{(1)}$ (3D-view)

compared in Fig. 5.30. On the one hand, when the two random variables are not correlated, the cross-correlation $\underline{\boldsymbol{R}}_{\mathcal{V}'}^{(r,\,s)} = 0$ is obtained for both micro-samples and generated samples, see Fig. 5.30(a) and Fig. 5.30(b) for the comparison of cross-correlation curves in the $y = 0$-plane. On the other hand, when the two variables are highly correlated, the cross-correlations are accurately recovered by the non-Gaussian random vector field generator, see Fig. 5.30(c). However, when the two random variables are moderately correlated, the cross-correlations obtained by the generator are less accurate and only their trends are preserved, see Fig. 5.30(d).

The histograms of some entries of $\boldsymbol{C}_{\mathrm{M}}$ and $\boldsymbol{\kappa}_{\mathrm{M}}$, which are obtained from the generated $\mathcal{V}'$, are presented in Fig. 5.31, in which the results from the micro-samples are also presented for comparison purpose. When using Eqs. (5.20-5.25) to compute $\boldsymbol{C}_{\mathrm{M}}$, for different ${\boldsymbol{C}_{\mathrm{M}}}^{(ij)}$, ($i$, j = 1, 2, ..., 6), different numbers of entries of $\mathcal{V}'$ will be used: for $\boldsymbol{C}_{\mathrm{M}}^{(11)}$ only ${\mathcal{V}'}^{(1)}$ is used, but for $\boldsymbol{C}_{\mathrm{M}}^{(66)}$, the entries from ${\mathcal{V}'}^{(16)}$ to ${\mathcal{V}'}^{(21)}$ are required. As expected, for the components of $\boldsymbol{C}_{\mathrm{M}}$ and $\boldsymbol{\kappa}_{\mathrm{M}}$ computed using only one entry of $\mathcal{V}'$, their distributions are well recovered by the generator, see Figs. 5.31(a) and 5.31(d). However, for the components of $\boldsymbol{C}_{\mathrm{M}}$ using more entries from $\mathcal{V}'$, the distributions of their generated samples have more discrepancy with the distributions of their micro-samples, see Fig. 5.31(b). The worst case is found for $\boldsymbol{C}_{\mathrm{M}}^{(66)}$, Fig. 5.31(c), in which the maximum number of entries ${\mathcal{V}'}^{(r)}$ is involved. This problem can be explained by the reduced accuracy of the cross-correlation obtained by the non-Gaussian generator: when more random variables ${\mathcal{V}'}^{(r)}$ are used to compute a component of $\boldsymbol{C}_{\mathrm{M}}$, the effect of a loss of accuracy in the cross-correlation becomes more obvious.

Although the non-Gaussian random field generator gives less accurate distributions for a few entries in $\boldsymbol{C}_{\mathrm{M}}$, those entries are related to the shearing behaviour of the material, which is not an important property in our applica-

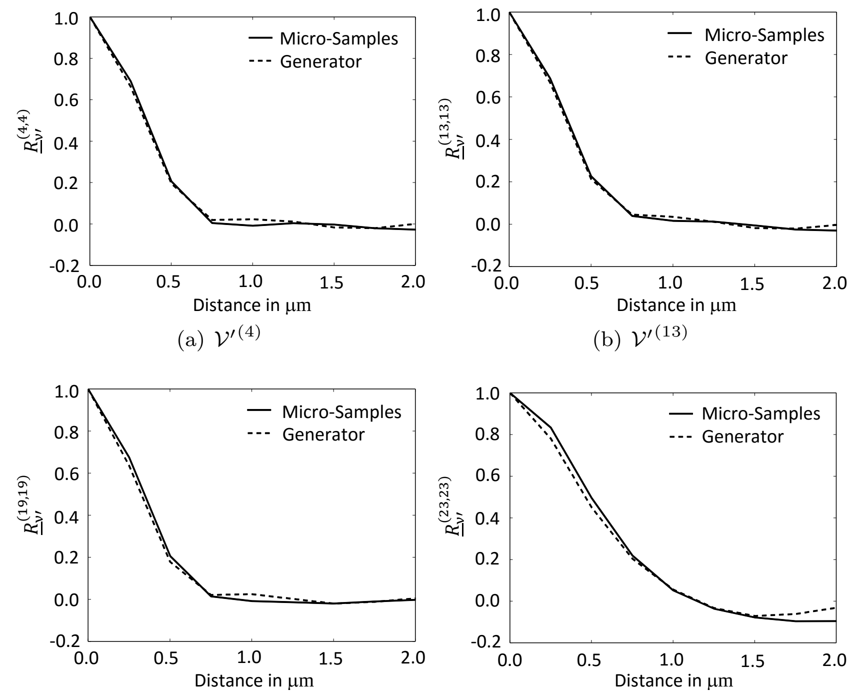

(a) $\mathcal{V}'^{(4)}$ (b) $\mathcal{V}'^{(13)}$

(c) $\mathcal{V}'^{(19)}$ (d) $\mathcal{V}'^{(23)}$

Figure 5.28: Comparison of normalized auto-correlation functions between micro-sampling and generated samples in the $y = 0$-plane (2D-view)

tion, while the material properties related to the tension and compression, which are the most important properties to estimate the thermo-mechanical damping are accurately represented. However, this inaccuracy can lead to some physically unreasonable values for those entries. In order to keep all the entries in a physically admissible range, an extra mapping process can be applied on the entries with inaccurate distribution, following

$$\boldsymbol{C}_{\mathrm{M},C}^{(ij)} = F_{ij}^{MS^{-1}}(F_{ij}^{\mathrm{N}}(\boldsymbol{C}_{\mathrm{M}}^{(ij)}))\,, \tag{5.26}$$

where $\boldsymbol{C}_{\mathrm{M}}^{(ij)}$ and $\boldsymbol{C}_{\mathrm{M},C}^{(ij)}$ are the generated components respectively without and with the mapping correction, $F_{ij}^{MS^{-1}}$ is the inverse marginal distribution function of the component $\boldsymbol{C}_{\mathrm{M}}^{(ij)}$ obtained from micro-samples and F_{ij}^{N} the marginal distribution function of the component $\boldsymbol{C}_{\mathrm{M}}^{(ij)}$ obtained from the non-Gaussian generator. In Fig. 5.32, the marginal distributions of $\boldsymbol{C}_{\mathrm{M}}^{(55)}$ obtained from the generated samples are presented before (Fig. 5.32(a)) and after (Fig. 5.32(b)) the mapping correction. However, the proper solution to address the inaccurate shearing properties is to use a more accurate non-Gaussian vector field

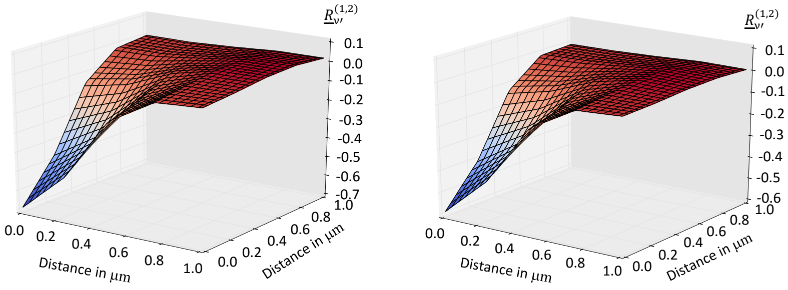

(a) Micro-Samples (b) Generator

Figure 5.29: Comparison of a normalized cross-correlation function between micro-samples and generated samples for $\mathcal{V}'^{(1)}$ and $\mathcal{V}'^{(2)}$ (3D-view)

generator.

Finally, some realisations of the random field are presented in Fig. 5.33 for the components picked as examples. For both the 2D view, Fig. 5.33(a) and Fig. 5.33(b), and the 3D view, Fig. 5.33(c) and Fig. 5.33(d), of the random field, a similar correlation of the material properties among the neighboring material points can be seen between the micro-samples and the generated ones.

5.3.2 Macro-scale results

In this section, we study the thermo-elastic quality factor of micro-resonators which are fabricated at two different temperatures, 610°C and 630°C, respectively. The thermo-mechanical finite element analysis which is presented in Section 2.4 is applied on the micro-resonator. At each integration point of the procedure, the random field defined in Chapter 4 is used to obtain the thermo-mechanical behaviour of the micro-beam. However care must be taken of two aspects.

1. First, when generating the random field, one approximation results from the bi-linear interpolation used to retrieve the values at a desired $\boldsymbol{x}$ position (positions of the integration points defined by the macro-scale SFEM) from the values generated at *a priori* $\boldsymbol{x}'$ position obtained using the FFT approach (regular spacing).
2. Second, the boundary effect, which is now described.

The boundary effect

A boundary effect exists when an integration point is located at the vicinity of the boundary of the structure: the heterogeneities number can then be overestimated as the centered (R)SVE has part of its domain outside the macro-scale

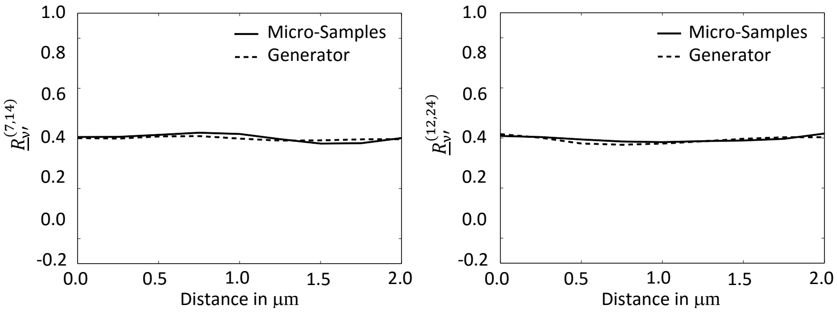

(a) $\mathcal{V}'^{(7)}$ and $\mathcal{V}'^{(14)}$ (b) $\mathcal{V}'^{(12)}$ and $\mathcal{V}'^{(24)}$

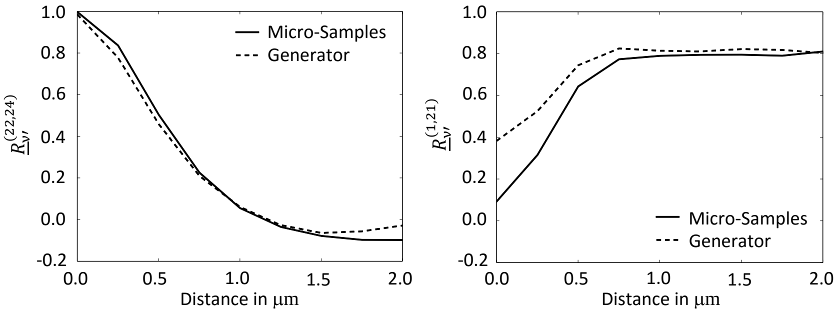

(c) $\mathcal{V}'^{(22)}$ and $\mathcal{V}'^{(24)}$ (d) $\mathcal{V}'^{(1)}$ and $\mathcal{V}'^{(21)}$

Figure 5.30: Comparison of normalized cross-correlation functions between micro-samples and generated samples in plane $y = 0$ (2D-view)

mesh as illustrated in Fig. 5.34. In other words, if the integration point is close to the cantilever surface, the effect of grains which are implicitly included in the SVEs and lying outside of the structure geometry are taken into account and should be avoided. To circumvent this issue, the associated (R)SVE centre is moved inward the plate to capture the right amount of heterogeneities as described in Fig. 5.34. Other discretization methods of the random fields could also be applied to avoid the boundary effect.

The boundary effect was not important for the 1D beam discussed previously as the SVE width and the macro-beam width were the same, and as the beam inertia uncertainty is directly linked to the width and thickness. For the 3D case and for the thin plates, it is not the case and thus the boundary effect will be considered.

Results with perfect clamping

The micro-resonator is now simplified as a micro-cantilever beam with the dimension of $L \times w \times t$, see Fig. 5.35. The material properties at each integration

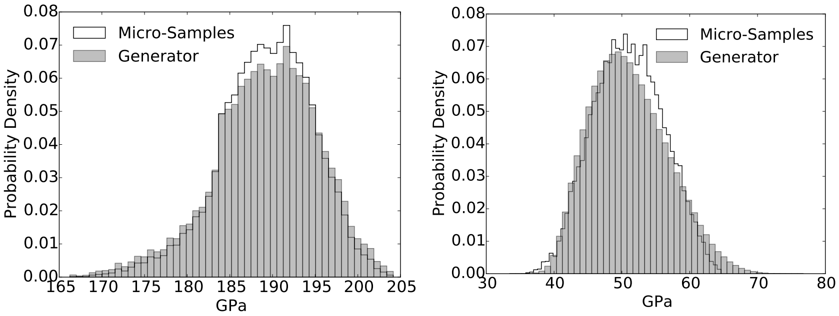

(a) $\boldsymbol{C}_{\mathrm{M}}^{(11)}$ (b) $\boldsymbol{C}_{\mathrm{M}}^{(23)}$

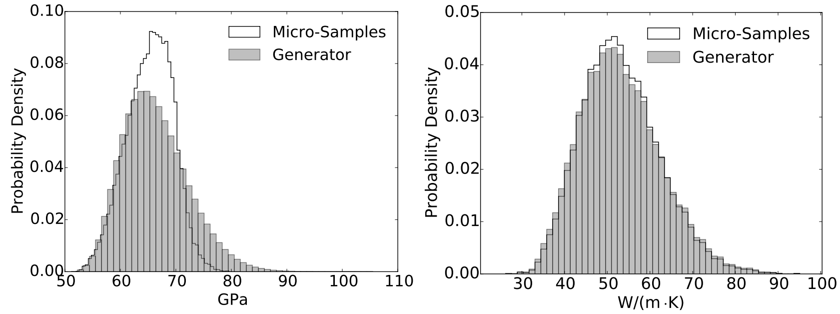

(c) $\boldsymbol{C}_{\mathrm{M}}^{(66)}$ (d) $\boldsymbol{\kappa}_{\mathrm{M}}^{(33)}$

Figure 5.31: Comparison of the histograms of $\boldsymbol{C}_{\mathrm{M}}^{(ij)}$ and $\boldsymbol{\kappa}_{\mathrm{M}}^{(ll)}$ (no sum on l) between micro-samples and generated samples

point are given by the random field generator as described in Chapter 4, which is based on the stochastic homogenisation of meso-scale SVEs presented in Section 3.3, see the results reported in Section 5.3.1. The discretization of the random field is in agreement with the finite element discretization. However in order to obtain a converged stochastic finite element analysis, the spacing of the discretized random field, *i.e.* the spacing between the integration points, must be lower than the correlation length $l_{\mathbf{C}}$ of the random field, as this has been demonstrated by the convergence study performed in Section 5.2. According to the homogenised results at the meso-scale, the correlation length of the random field of the material properties $\boldsymbol{C}_{\mathrm{M}}(\boldsymbol{x},\boldsymbol{\theta})$ and $\boldsymbol{\kappa}_{\mathrm{M}}(\boldsymbol{x},\boldsymbol{\theta})$ can be calculated by equation (2.11) and corresponds to $l_{\mathbf{C}}^{610} \approx 0.73\ \mu$m for the poly-silicon layer deposited at 610°C and with the SVE size of 0.5 μm, and to $l_{\mathbf{C}}^{630} \approx 1.23\ \mu$m for the poly-silicon layer deposited at 630°C and with the SVE size of 0.8 μm. In the conducted Finite Element analyses, we use quadratic elements with $3\times3\times3$ Gauss integration points. The largest finite elements that are considered in this section are of size $1\times1\times1\mu\mathrm{m}^3$, leading to a maximum distance between the integration points of $\approx 0.387\,\mu$m, which is smaller than the correlation length of

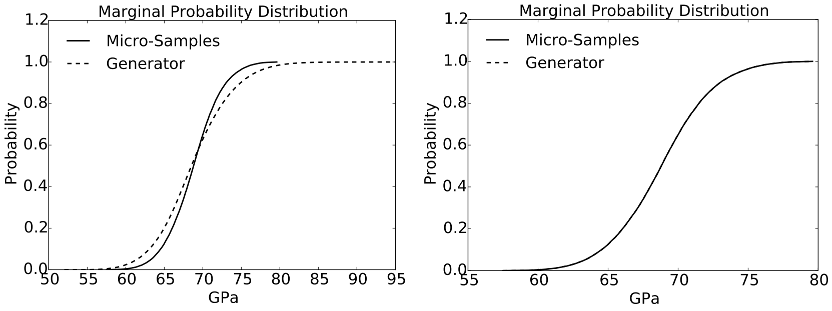

(a) Without mapping correction (b) With mapping correction

Figure 5.32: Comparison of marginal distributions of $\boldsymbol{C}_{\mathrm{M}}^{(55)}$ between micro-samples and generated samples

the meso-scale random fields.

Besides the random fields considered for the material properties $\boldsymbol{C}_{\mathrm{M}}(\boldsymbol{x},\boldsymbol{\theta})$ and $\boldsymbol{\kappa}_{\mathrm{M}}(\boldsymbol{x},\boldsymbol{\theta})$, the necessary deterministic properties for the analyses are the density ρ_{M}, the thermal expansion coefficient α_{M}, and the heat capacity per unit mass at constant volume $C_{v\mathrm{M}}$ for poly-silicon. The adopted values in this work are

$$\rho_{\mathrm{M}} = 2330\,\mathrm{Kg/m^3}, \quad \alpha_{\mathrm{M}} = 3.084^{-6}/\mathrm{K} \quad \text{and} \quad C_{v\mathrm{M}} = 712\,\mathrm{J/(Kg\cdot K)}\,. \tag{5.27}$$

Table 5.9: Statistical moments of the first resonance frequency f_1 for the different cases

	$\mathbb{E}[f_1]$ [MHz]	$\boldsymbol{\sigma}_{f_1}$ [MHz]	COV$_{f_1}$ [%]
15×3×2, 610°C	11.91	0.051	0.43
10×3×2, 610°C	26.47	0.136	0.512
15×3×1, 610°C	6.02	0.026	0.437
15×3×2, 630°C	11.89	0.068	0.575
15×3×2, 610°C, anchor	10.63	0.037	0.349

First a clamped cantilever beam is studied following the schematics of Fig. 5.35(a). At clamp, the boundary conditions read

$$\boldsymbol{u} = 0 \quad \text{and } T = T_0\,. \tag{5.28}$$

The following cases are compared

- **Case 15×3×2, 610°C**: this consists of a beam geometry of 15×3×2μm^3 deposited at 610°C and studied at room temperature. The finite element mesh consists of 1×1×1μm^3 quadratic bricks with 27 Gauss integration points. The SVE length considered is 0.5 μm.

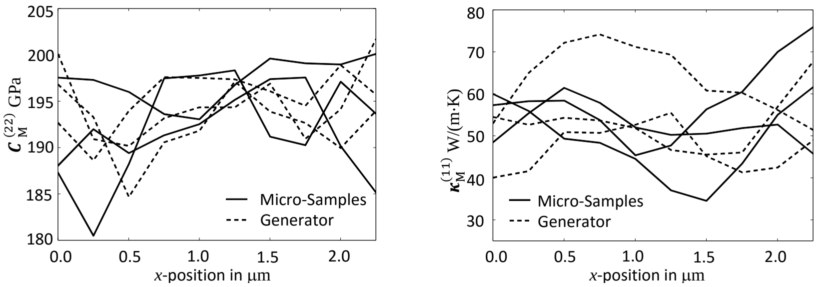

(a) Realizations of $\boldsymbol{C}_{\mathrm{M}}^{(22)}$ at constant y-position

(b) Realizations of $\boldsymbol{\kappa}_{\mathrm{M}}^{(11)}$ at constant y-position

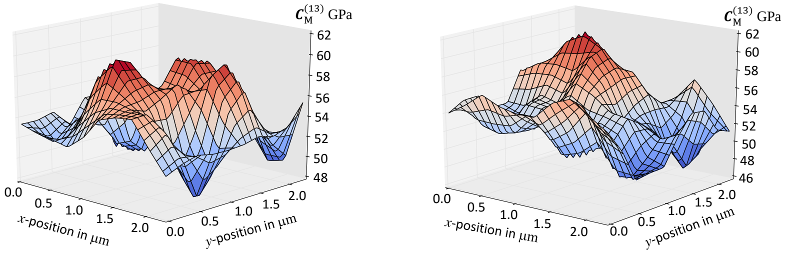

(c) Realizations of $\boldsymbol{C}_{\mathrm{M}}^{(13)}$ from micro-samples

(d) Realizations of $\boldsymbol{C}_{\mathrm{M}}^{(13)}$ from generator

Figure 5.33: Comparison of realisations of the random field between micro-samples and generated samples

Table 5.10: Statistical moments of the quality factor Q for the different cases

	$\mathbb{E}[Q]$	$\boldsymbol{\sigma}_Q$	COV_Q [%]
15×3×2, 610°C	7771	82.95	1.067
10×3×2, 610°C	8634	93.35	1.081
15×3×1, 610°C	31855	481.9	1.513
15×3×2, 630°C	9074	153.71	1.694
15×3×2, 610°C, anchor	7164	57.47	0.802

- **Case 10×3×2, 610°C**: this consists of a beam geometry of $10\times3\times2\mu\mathrm{m}^3$ deposited at 610°C and studied at room temperature. The finite element mesh consists of $1\times1\times1\mu\mathrm{m}^3$ quadratic bricks with 27 Gauss integration points. The SVE length considered is 0.5 μm.
- **Case 15×3×1, 610°C**: this consists of a beam geometry of $15\times3\times1\mu\mathrm{m}^3$ deposited at 610°C and studied at room temperature. The finite element mesh consists of $1\times1\times0.5\mu\mathrm{m}^3$ quadratic bricks with 27 Gauss integration points. The SVE length considered is 0.5 μm.

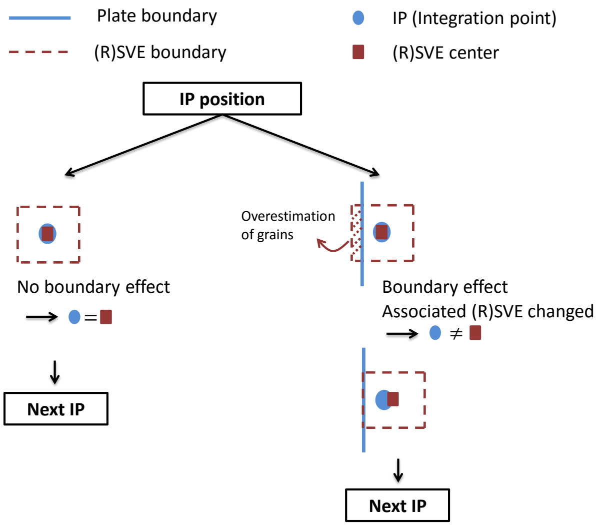

Figure 5.34: The boundary effect and its avoidance

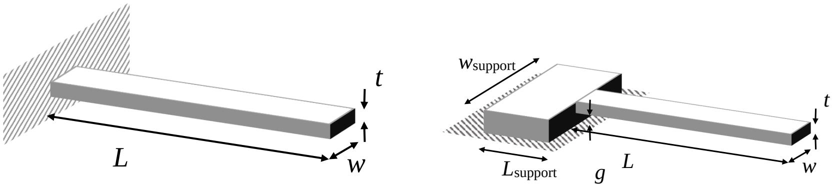

(a) Perfect clamp (b) Realistic clamp

Figure 5.35: Schematics of the studied cantilevers (a) with a perfect clamp, (b) with a more realistic anchor

- **Case 15×3×2, 630°C**: this consists of a beam geometry of $15{\times}3{\times}2\mu\mathrm{m}^3$ deposited at 630°C and studied at room temperature. The finite element mesh consists of $1{\times}1{\times}1\mu\mathrm{m}^3$ quadratic bricks with 27 Gauss integration points. The SVE length considered is 0.8 μm.

More than 10 000 samples have been computed for each case.

The resulting distributions of the first resonance frequency and of the quality factor are reported in Fig. 5.36 and the statistical moments in Table 5.9 and Table 5.10. As predicted by other theories, the effect of the thickness on the quality factor is the most important geometrical one. When comparing the effect of the deposition temperature during the manufacturing process, the distribution of the eigen-frequency f_1 for a deposition temperature of 610°C, Fig.

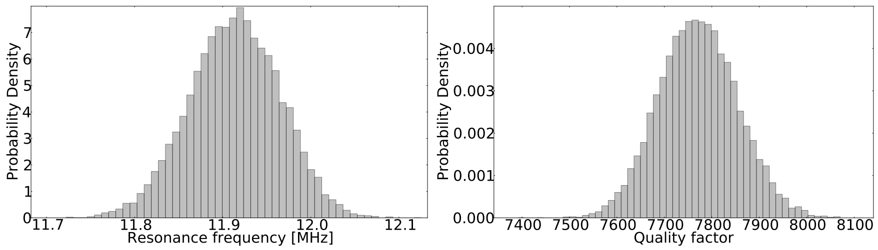

(a) f_1 for the 15×3×2, 610°C case (b) Q for the 15×3×2, 610°C case

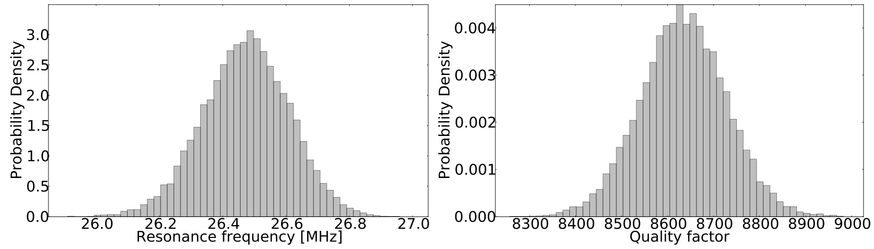

(c) f_1 for the 10×3×2, 610°C case (d) Q for the 10×3×2, 610°C case

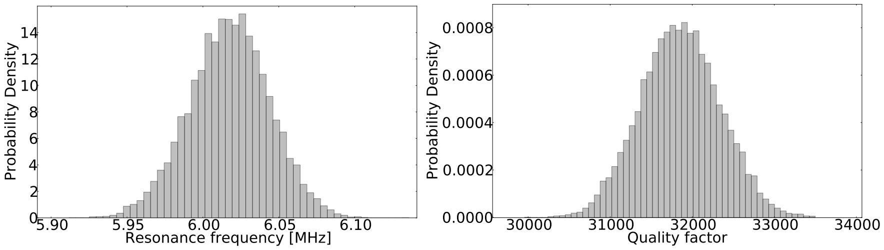

(e) f_1 for the 15×3×1, 610°C case (f) Q for the 15×3×1, 610°C case

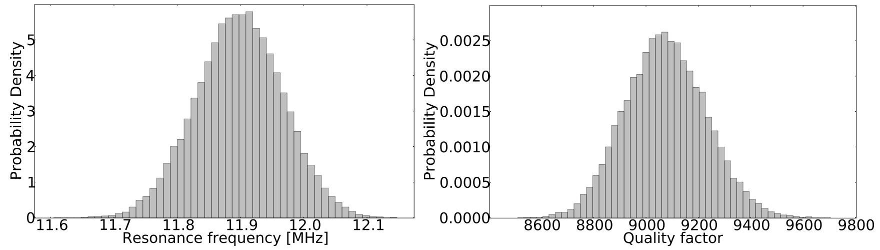

(g) f_1 for the 13×3×2, 630°C case (h) Q for the 13×3×2, 630°C case

Figure 5.36: Histograms of the resonance frequency (left column) and of the quality factor (right) column of the perfectly clamped micro-resonator: (a) and (b) for the 15×3×2, 610°C case, (c) and (d) 10×3×2, 610°C case, (e) and (f) 5×3×1, 610°C case, and (g) and (h) 15×3×2, 630°C case

5.36(a) is similar to the distribution of the eigen-frequency f_1 for a deposition temperature of 630°C, Fig. 5.36(g). However, its effect on the quality factor Q is more sensitive as its mean value increases with the deposition temperature, see Figs. 5.36(b) and 5.36(h). This is mainly due to the effect of the grain size on the thermal conductivity.

Results with anchor

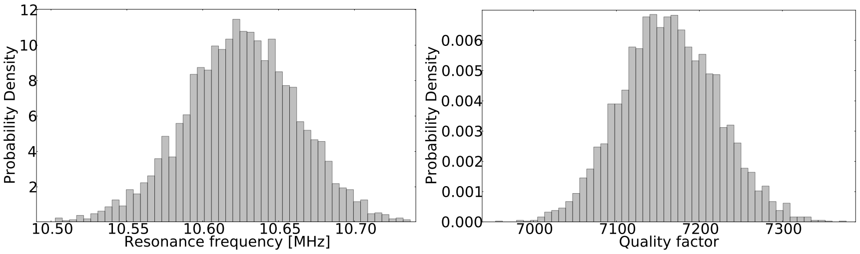

(a) f_1 for the 15×3×2, 610°C, anchor, case

(b) Q for the 15×3×2, 610°C, anchor, case

Figure 5.37: Histograms of the (a) resonance frequency and of (b) the quality factor of the micro-resonator with the idealised anchor (15×3×2, 610°C, anchor, case)

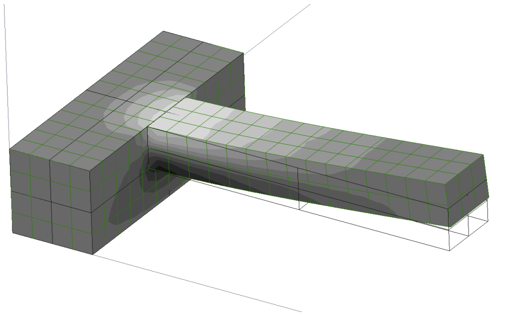

Figure 5.38: Illustration of the first vibrating mode with the temperature distribution (at a multiplicative constant) of the 15 X 3 X 2, 610°C, anchor case

To account for the effect of the boundary condition, we also consider a geometry with the anchor as displayed in Fig. 5.35(b). The boundary condition at the anchor clamp corresponds to Eq. (5.28). The following geometry is considered

- **Case 15×3×2, 610°C, anchor**: this consists of a beam geometry of $15\times3\times2\mu\text{m}^3$ with an anchor geometry of $4\times12\times4\mu\text{m}^3$ deposited at 610°C and studied at room temperature. The finite element mesh consists of $1\times1\times1\mu\text{m}^3$ quadratic bricks with 27 Gauss integration points. The SVE length considered is 0.5 μm.

More than 2 000 samples have been computed for this case.

The resulting distributions of the first resonance frequency and of the quality factor are reported in Fig. 5.37 and the statistical moments in Table 5.9. As compared to the perfect clamping condition, Figs. 5.36(a) and 5.36(b), it can be seen that both the eigen-frequency and quality factor means are lower when considering the anchor. Moreover, the COV of the statistical distributions are lower with the anchor directly modeled, see Table 5.9. An illustration of the first vibration mode, with a temperature distribution is reported in Fig. 5.38.

5.4 Influence of different uncertainty sources for vibrating thin micro-beams modelled with KL plates

This section discusses the effect of the roughness on the macro-scale predictions. First, the grain size and the grain orientation follow the measurements, see Section 5.1.1. Second, rough surfaces and thus RSVEs can be generated (based on AFM measurements), see Section 5.1.3. The meso-scale behaviour can be computed with the second-order stochastic homogenisation, see Section 3.4, so that the influence of the roughness on the bending behaviour of the volume element can be captured.

Thus the probabilistic material behaviour at the meso-scale can be extracted from the (R)SVEs information, and because of the window technique, the spatial correlation is captured as well. In terms of (R)SVE shape, only squared-shaped (R)SVEs are generated. Using the stochastic model described in Section 4.3 and considering the Non-Gaussian mapping discussed in Section 4.4, a stochastic model of the meso-scale properties can be built, and meso-scale random fields can be generated as input for the SFEM. Using the KL plate SFEM reported in Section 2.5, the uncertainties in terms of resonance frequency can be estimated.

5.4.1 Homogenised properties based on measurements

The (R)SVE length ranges between $0.5\,\mu$m to $1.5\,\mu$m and the thickness between $0.5\,\mu$m to $2\,\mu$m. Although the poly-silicon film statistical properties (grain size, roughness) can change with the deposition thickness, in order to separate and compare the different effects (material, surface roughness, and the MEMS thickness), we will assume identical statistical properties for the different MEMS thicknesses. The deposition temperature is 610 °C.

The effects of different sources of uncertainties are investigated in this section. The name of the different uncertainty cases respects the following notation:

1. The first letter, 'F' or 'R', refers to flat –*i.e.* without profile uncertainties– or rough SVEs;
2. Then the type of material is given, 'Si' referring to the anisotropic silicon and 'Iso' to a pseudo isotropic material;
3. Finally, two cases of grain orientation are considered: either uniform orientation distribution (subscript 'uni') or preferred XRD-based orientation (subscript 'pref').

The different cases are thus denoted by

1. **Case $\mathbf{F}-\mathbf{Si}_{\mathbf{uni}}$**: Flat SVEs made of silicon with a uniform grain orientation distribution;
2. **Case $\mathbf{F}-\mathbf{Si}_{\mathbf{pref}}$**: Flat SVEs made of silicon whose grain orientation distribution is based on the XRD measurements;
3. **Case $\mathbf{R}-\mathbf{Iso}$**: RSVEs made of a pseudo isotropic material (160 GPa);
4. **Case $\mathbf{R}-\mathbf{Si}_{\mathbf{uni}}$**: RSVEs made of silicon with a uniform grain orientation distribution;
5. **Case $\mathbf{R}-\mathbf{Si}_{\mathbf{pref}}$**: RSVEs made of silicon whose grain orientation distribution is based on the XRD measurements.

Effect of the preferred grain orientation

The influence of the orientation is studied in Fig. 5.39, where the distribution of the homogenised meso-scale Young's modulus E_x, the Young's modulus along the x direction, is reported for $0.5 \times 0.5 \times 0.5\,\mu\text{m}^3$ flat SVEs. 122 and 116 Voronoï tessellations were constructed respectively for the uniform grain orientation distribution and for the preferred grain orientation distribution, and 100 SVEs were extracted in each Voronoï tessellation. The average number of grains per SVE is ≈ 5.4.

In terms of statistical moments, the means of the Young's modulus are respectively 161.87 GPa and 162.09 GPa for the uniform orientation distribution and for the preferred orientation distribution, while their standard deviations are respectively 9.45 GPa and 8.01 GPa. Compared to the single crystal case, see Fig. 5.4, the mean value remains similar but the variance decreases after homogenisation as expected. As it was already observed for the single crystal cases, the variance of E_x decreases when the preferred orientation distribution is considered, although the PDFs are much more similar, and closer to a Gaussian distribution, than for the single crystal case.

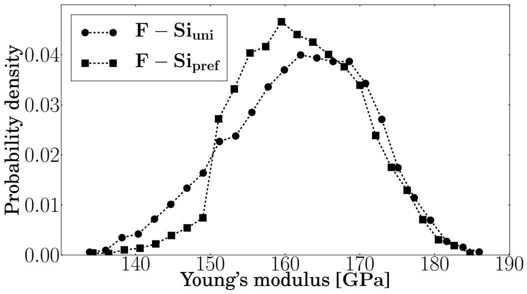

Figure 5.39: Distribution of the meso-scale Young 's modulus along the x-direction with and without preferred grain orientation for $0.5 \times 0.5 \times 0.5\,\mu\mathrm{m}^3$ SVEs

Effect of the surface topology

The effects of the roughness on the meso-scale mass per membrane unit area $\bar{\rho}$ and on the meso-scale material tensor $\boldsymbol{U}$ are now investigated. As in this case the quantity of interest at the macro-scale is the beam resonance frequency, the element $\boldsymbol{U}^{(44)}$ of the meso-scale material tensor is the main focus as it links the bending stress and strain.

At first, the probability density function of the mass per unit area $\bar{\rho}$ is illustrated in Fig. 5.40 where 52 900 RSVEs samples of size $0.5 \times 0.5 \times 0.5\,\mu\mathrm{m}^3$ were considered.

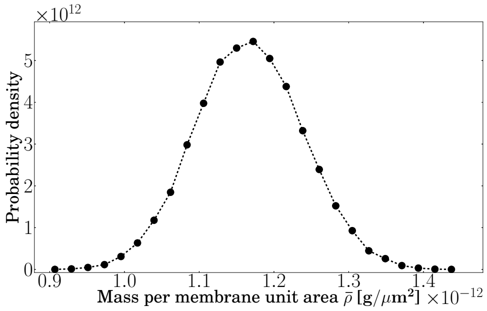

Figure 5.40: Distribution of the meso-scale mass per unit area $\bar{\rho}$ for $0.5 \times 0.5 \times 0.5\,\mu\mathrm{m}^3$ RSVEs

The distribution of $\boldsymbol{U}^{(44)}$ is illustrated in Fig. 5.41 for a (R)SVE of size $0.5 \times 0.5 \times 0.5 \mu m^3$[7]. The different SVE cases are compared and it can be seen

---

[7] In the case of RSVEs, the thickness size is actually the mean thickness $\bar{h}$ of the Voronoï

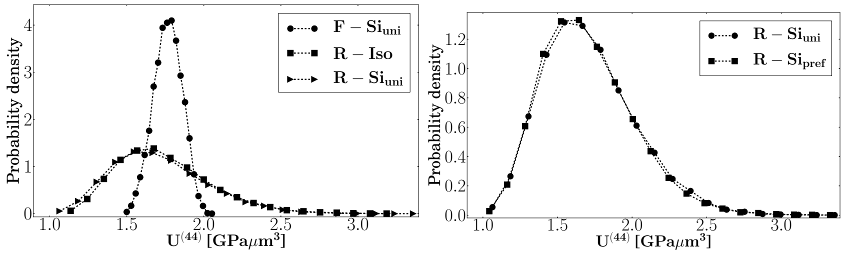

(a) Rough vs. flat SVEs (b) Grain orientation distribution effect

Figure 5.41: Distributions of the meso-scale $\boldsymbol{U}^{(44)}$ for different uncertainty cases with $0.5 \times 0.5 \times 0.5\mu\mathrm{m}^3$ (R)SVEs

that the roughness is the main source of uncertainty. Indeed, while the PDFs when considering the rough SVEs are similar for the uniform grain orientation distribution and for the preferred grain orientation distribution, they are drastically different to the one obtained with flat SVEs. The statistical moments for the different cases are reported in Table 5.11. Finally, one can note that the distributions are not Gaussian thus showing the need for non-Gaussian stochastic models.

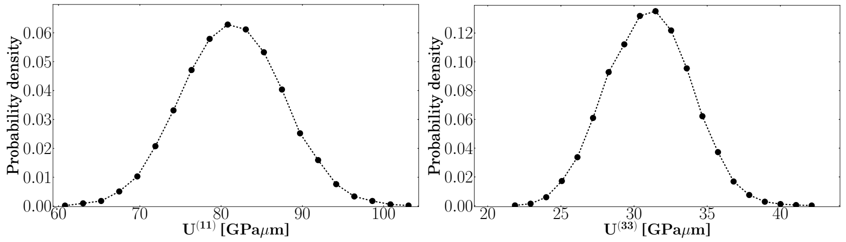

(a) $\boldsymbol{U}^{(11)}$ (b) $\boldsymbol{U}^{(33)}$

Figure 5.42: Distributions of the meso-scale (a) $\boldsymbol{U}^{(11)}$ and (b) $\boldsymbol{U}^{(33)}$ obtained for the particular $\mathrm{R}-\mathrm{Si}_{\mathrm{pref}}$ case with RSVEs of dimension $0.5 \times 0.5 \times 0.5\mu\mathrm{m}^3$

Besides the bending properties, for completness the distribution of $\boldsymbol{U}^{(11)}$, which links the in-plane tension stress $\tilde{\boldsymbol{n}}_{xx}$ and strain $\boldsymbol{\epsilon}_{xx}$ can be seen in Fig. 5.42(a) for the particular $\mathrm{R}-\mathrm{Si}_{\mathrm{pref}}$ case. Moreover the distribution of $\boldsymbol{U}^{(33)}$, characterising the response of the (R)SVEs to in-plane shearing, is illustrated in Fig. 5.42(b).

The effect of the importance of the roughness on the uncertainties tends to decrease when we consider thicker SVEs. This is expected as the roughness is

---

tessellation

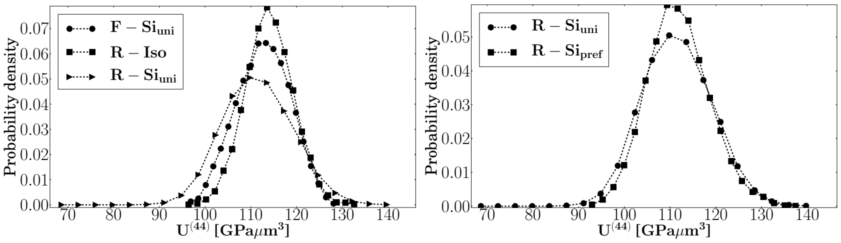

(a) Rough *vs.* flat SVEs (b) Grain orientation distribution effect

Figure 5.43: Distributions of the meso-scale $\boldsymbol{U}^{(44)}$ for different uncertainty cases with $0.5 \times 0.5 \times 2\mu\text{m}^3$ (R)SVEs

the same in all cases. When the ratio between the roughness and the thickness is lower, the roughness induces less uncertainty. In Figs. 5.43(a) and 5.43(b), in which the RSVEs mean thickness is $\bar{h} = 2\,\mu\text{m}$, the material uncertainty, which comes from the effect of the grain orientation distribution, becomes comparable to the roughness effect.

Table 5.11: Statistical moments of $\boldsymbol{U}^{(44)}$ for the different meso-scale uncertainties cases. $N_{\text{Voronoï}}$ corresponds to the number of Voronoï tessellations generated. N_{window} corresponds to the number of windows considered for each Voronoï tessellation to generate the $0.5 \times 0.5 \times 0.5\mu\text{m}^3$ (R)SVEs

Cases	$\mathbb{E}[\boldsymbol{U}^{(44)}]$ [GPa $\cdot\,\mu$m^3]	$\sigma_{\boldsymbol{U}^{(44)}}$ [GPa $\cdot\,\mu$m^3]	$N_{\text{Voronoï}}$	N_{window}
$\mathbf{F - Si_{uni}}$	1.77	0.092	149	100
$\mathbf{F - Si_{pref}}$	1.78	0.068	162	100
$\mathbf{R - Iso}$	1.74	0.306	136	100
$\mathbf{R - Si_{uni}}$	1.71	0.312	201	100
$\mathbf{R - Si_{pref}}$	1.70	0.306	258	100

Effect of the RSVE length

The effect of the RSVE length on the meso-scale $\boldsymbol{U}^{(44)}$ is illustrated in Fig. 5.44. Square-shaped RSVEs of successive lengths 0.5, 1., and 1.5 μm are considered.

The computed PDFs of $\boldsymbol{U}^{(44)}$ are shown in Fig. 5.44(a) for an RSVE thickness $0.5\,\mu$m, and the computed mean $\mathbb{E}[\boldsymbol{U}^{(44)}]$ and standard deviation $\sigma_{\boldsymbol{U}^{(44)}}$ are reported in Table 5.12. As expected, uncertainties decrease with the RSVE sizes. This can also be seen in Fig. 5.44(b) where the coefficient of variation of $\boldsymbol{U}^{(44)}$, $\text{COV}_{\boldsymbol{U}^{(44)}} = \frac{\sigma_{\boldsymbol{U}^{(44)}}}{\mathbb{E}[\boldsymbol{U}^{(44)}]} \times 100\%$, is shown for different RSVE sizes and thicknesses.

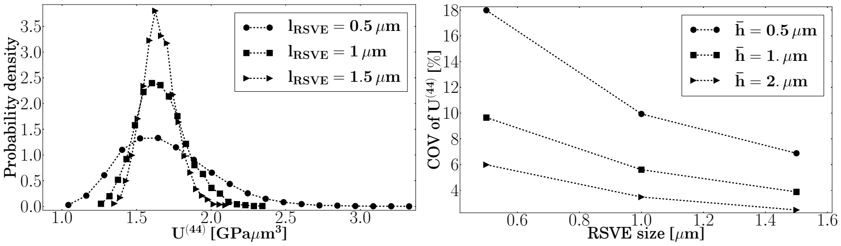

(a) Length effect (b) Length and thickness effects

Figure 5.44: Distributions properties of the meso-scale $\boldsymbol{U}^{(44)}$ for different RSVE sizes and for the particular $\mathrm{R-Si_{pref}}$ case (a) PDFs for RSVEs of lengths 0.5, 1. and 1.5 μm, and of thickness 0.5 μm and (b) coefficient of variations for different RSVEs lengths and thicknesses

Table 5.12: Statistical moments of $\boldsymbol{U}^{(44)}$ for the different RSVE lengths, for an RSVE thickness of 0.5 μm, and for the particular $\mathrm{R-Si_{pref}}$ case. $N_{\text{Voronoï}}$ corresponds to the number of Voronoï tessellations generated. N_{window} corresponds to the number of windows considered for each Voronoï tessellation

l_{RSVE} [μm]	$\mathbb{E}[\boldsymbol{U}^{(44)}]$ [GPa $\cdot\,\mu$m^3]	$\sigma_{\boldsymbol{U}^{(44)}}$ [GPa $\cdot\,\mu$m^3]	$N_{\text{Voronoï}}$	N_{window}
0.5	1.70	0.312	258	100
1.	1.67	0.165	202	36
1.5	1.65	0.114	191	25

Spatial correlation

With the window technique used when extracting the RSVEs from the large Voronoï tesselations [52], the in-plane spatial (auto)-correlation $\underline{R}_{\boldsymbol{U}^{(44)}}(\boldsymbol{\tau})$ of $\boldsymbol{U}^{(44)}$ is directly available following Eq. (2.10).

The 2D in-plane spatial correlation is illustrated in Fig. 5.45(a) for an RSVE length of 0.5 μm, an RSVE mean thickness $\bar{h} = 0.5\,\mu m$, and for the particular $\mathrm{R-Si_{pref}}$ case. Ten windows per direction (and per Voronoï tesselation) are considered, with a spacing along both x and y directions of 0.125 μm. The spatial correlation along the x-direction is illustrated in Fig. 5.45(b) for different RSVE lengths. These figures show that the correlation becomes close to zero for RSVE distances getting close to the RSVE length, as the windows are not overlapping each other anymore and thus share a reduced amount of grains. The computed correlation lengths $l_{\boldsymbol{U}^{(44)}}$, based on Eq. (2.11), are reported in Table 5.13.

Finally the cross-correlations, following Eq. (2.8), between different elements of the tangent $\boldsymbol{U}$ and $\bar{\rho}$ are shown in Fig. 5.46 for a distance $\boldsymbol{\tau} = \mathbf{0}$. In particular it can be seen that the meso-scale mass per unit area (which depends on the average thickness over the RSVE) is strongly correlated to the entry of the meso-scale material tensor corresponding to the bending behaviour as $\underline{R}^{\bar{\rho}}_{\boldsymbol{U}^{(44)}}$ is

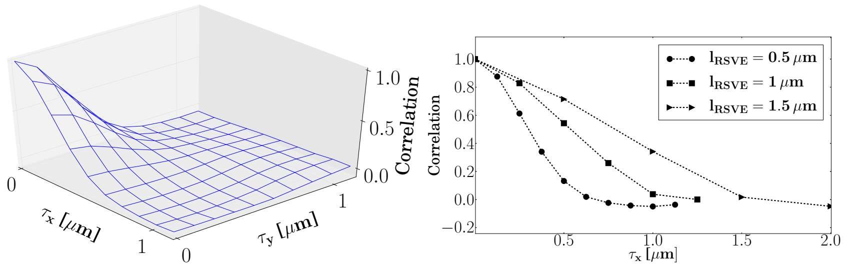

(a) 2D-spatial correlation

(b) 1D-spatial correlation for different RSVE sizes

Figure 5.45: The spatial correlation of $\boldsymbol{U}^{(44)}$ for the particular $\mathrm{R}-\mathrm{Si}_{\mathrm{pref}}$ case (a) 2D-spatial correlation for RSVEs of size $0.5 \times 0.5 \times 0.5\,\mu\mathrm{m}^3$ and (b) spatial correlation along the x-direction for different RSVE lengths and for an RSVE thickness of 0.5μm

Table 5.13: Correlation length $l_{\boldsymbol{U}^{(44)}}$ of $\boldsymbol{U}^{(44)}$ for different RSVE lengths for the particular $\mathrm{R}-\mathrm{Si}_{\mathrm{pref}}$ case and for an RSVE thickness of 0.5μm

l_{RSVE} [μm]	**Correlation Length** [μm]
0.5	0.59
1.	1.09
1.5	1.55

higher than 0.8.

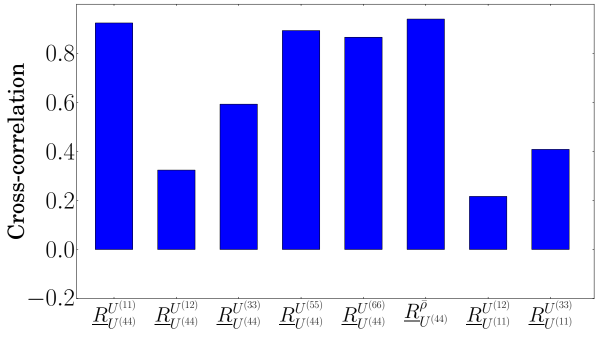

Figure 5.46: Cross-correlation between different elements of $\boldsymbol{U}$ and $\bar{\rho}$ for RSVEs of size $0.5 \times 0.5 \times 0.5\,\mu\mathrm{m}^3$ and for the particular $\mathrm{R}-\mathrm{Si}_{\mathrm{pref}}$ case

5.4.2 Stochastic model behaviour of the homogenised properties

The meso-scale fields for the thin plate problem are now generated using the framework of Section 4.3 and Section 4.4.

Lower bound for the generalised tangent $\boldsymbol{U}$

The lower bound of the generalised tangent $\boldsymbol{U}_L$ is based on the available samples of $\boldsymbol{U}$, as was already done in [26] for the generation of elasticity tensors. All the available samples, computed with the stochastic homogenisation, are gathered in a set Υ.

The lower bound $\boldsymbol{U}_L$ is assumed to have the following configuration:

$$\boldsymbol{U}_L = \lambda_L \boldsymbol{I}_6 \,, \tag{5.29}$$

where λ_L is $\lambda_L = \iota_\lambda \lambda_{\min}$, with ι_λ a tolerance parameter arbitrarily fixed to 0.95 and $\lambda_{\min}$ the smallest eigenvalue of all the computed samples of $\boldsymbol{U}$ (the tolerance should be strictly lower than one to be able to recover the minimal values during the generation).

Therefore, the increment matrix $\Delta\boldsymbol{U}$ defined as $\boldsymbol{U} = \Delta\boldsymbol{U} + \boldsymbol{U}_L$ is positive-definite as its eigenvalues $\lambda_i^{\Delta\boldsymbol{U}}$ are:

$$\lambda_i^{\Delta\boldsymbol{U}} = \lambda_i^{\boldsymbol{U}} - \lambda_L \,, \quad i = 1, ..., 6 \quad \text{and} \quad \forall \boldsymbol{U} \in \Upsilon \,. \tag{5.30}$$

Lower bound for the mass per membrane unit area ρ

As the mass matrix should be strictly positive as it has to be inverted in an eigen-frequency analysis, a lower bound $\bar{\rho}_L$ is defined for the mass per unit membrane area $\bar{\rho}$:

$$\bar{\rho}_L = \iota_\rho \bar{\rho}_{\min} \,, \tag{5.31}$$

where ι_ρ is once again a tolerance parameter arbitrary fixed to 0.95 and $\bar{\rho}_{\min}$ is is the smallest mass per unit area of all computed samples.

Stochastic model

The input of the SFEM approach developed in Section 2.5 is the correlated meso-scale random fields of the generalised tangent $\boldsymbol{U}(\boldsymbol{x}, \boldsymbol{\theta})$ and of the mass density per membrane unit area $\bar{\rho}(\boldsymbol{x}, \boldsymbol{\theta})$. First, a semi-positive definite symmetric increment $\Delta\boldsymbol{U}$ is defined such that

$$\boldsymbol{U} = \boldsymbol{U}_L + \Delta\boldsymbol{U} \,, \tag{5.32}$$

is always a symmetric positive definite matrix, bounded by $\boldsymbol{U}_L$. To generate such a semi-positive-definite matrix, one can use the Cholesky decomposition as described in [86], which reads

$$\Delta\boldsymbol{U} = \boldsymbol{L}\boldsymbol{L}^{\mathrm{T}} \,. \tag{5.33}$$

In this equation, the matrix $\boldsymbol{L}$ is a lower triangular matrix. The matrix $\boldsymbol{L}$ is made of 21 independent entries, which form a random vector field. The lower bound of the mass densities per membrane unit area $\bar{\rho}$ is enforced by defining

$$\bar{\rho} = \bar{\rho}_L + \Delta\bar{\rho}\,, \tag{5.34}$$

where $\Delta\bar{\rho}$ has to be enforced to be positive.

In this work a vector field $\mathcal{V}$ of 22 elements is considered: the 21 elements of $\boldsymbol{L}$ as well as the logarithmic mapping $\mathcal{V}^{(22)} = \log(\Delta\bar{\rho})$, which enforces the positive nature of $\Delta\bar{\rho}$. The random vector field reads

$$\mathcal{V}^{(r)} = \bar{\mathcal{V}}^{(r)} + \mathcal{V}'^{(r)}\sigma_{\mathcal{V}^{(r)}}\,. \tag{5.35}$$

The zero-mean fluctuations $\mathcal{V}'^{(r)}$ are normalized with their standard deviation in order to be able to generate values for the different entries of $\mathcal{V}$ which are different by several orders of magnitude. Let us note that the uncertainty in the mass inertia per width is approximated as it is defined from the mass per membrane unit area: $I_p = \frac{\bar{\rho}^3}{12\rho^2}$.

Stochastic behaviour of generated macro-scale samples

The random field generator described in Section 4.3 is now applied to generate correlated fields for $\boldsymbol{U}$ and $\bar{\rho}$ based on the meso-scale properties computed in Section 5.4.1.

At first, the zero-mean and unit variance variables $\mathcal{V}'$, which are actually considered by the stochastic model, are looked upon. The third and fourth order statistical moments, respectively $\gamma_{1\bullet} = \frac{\mathbb{E}\left[(\bullet-\mathbb{E}[\bullet])^3\right]}{\sigma_\bullet^3}$ and $\beta_{2\bullet} = \frac{\mathbb{E}\left[(\bullet-\mathbb{E}[\bullet])^4\right]}{\sigma_\bullet^4}$, of the those variables obtained from the (R)SVE resolutions are also studied and are found to be not always close to Gaussianity. For example, for RSVE dimensions of $0.5 \times 0.5 \times 0.5\mu\text{m}^3$ and for the particular R - Si$_{\text{uni}}$ case, out of the 22 variables, the furthest skewness from Gaussianity is -1.172, corresponding to the entry $\mathcal{V}'^{(8)}$ (a Gaussian variable being symmetric, its skewness is 0), and the furthest Kurtosis from Gaussianity is 5.104, also corresponding to the entry $\mathcal{V}'^{(8)}$ (a Gaussian variable possessing a Kurtosis of 3). The distribution of $\mathcal{V}'^{(8)}$, obtained from the RSVE homogenisation process, obtained using the Gaussian spectral generator and the non-Gaussian mapping, can be seen in Fig. 5.47. The Gaussian spectral generator does not converge towards the micro-samples distribution, due to the higher moments of the distribution. This motivates the recourse to the non-Gaussian generator, as described in Section 4.4, whose results depicted in Fig. 5.47 are closer in terms of probability distribution to the micro-samples distribution than the Gaussian distribution. Indeed the non-Gaussian generated mapping $\mathcal{V}'^{(8)}$ skewness is $\gamma_{1\mathcal{V}'^{(8)}} = -1.197$ and its Kurtosis is $\beta_{2\mathcal{V}'^{(8)}} = 5.205$, in good agreement with the original inputs of the random field generator.

The accuracy of the non-Gaussian generator is now assessed by comparing the generated values of interest $\boldsymbol{U}$ and $\bar{\rho}$ to the ones resulting from the RSVEs

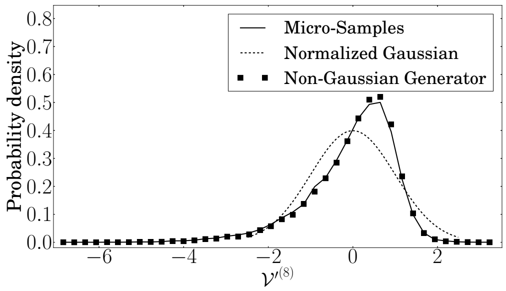

Figure 5.47: Computed and generated values of $\mathcal{V}'^{(8)}$ for RSVE dimensions of $0.5 \times 0.5 \times 0.5\mu\text{m}^3$ and for the particular R - Si_{uni} case (Continuous curve: distribution obtained from the RSVE homogenisation process; Dashed curve: normalised Gaussian distribution; Squares: non-Gaussian mapping)

Table 5.14: Mean values of the PDFs obtained from the micro-samples and from the generated random fields (non-Gaussian) for RSVE dimensions of $0.5 \times 0.5 \times 0.5\mu\text{m}^3$ and for the particular R - Si_{pref} case

	Micro-Samples	**NG-Generator**
$\mathbb{E}\left[\boldsymbol{U}^{(11)}\right]$ [GPaμm]	81.41	81.38
$\mathbb{E}\left[\boldsymbol{U}^{(12)}\right]$ [GPaμm]	16.85	16.84
$\mathbb{E}\left[\boldsymbol{U}^{(33)}\right]$ [GPaμm]	31.02	30.97
$\mathbb{E}\left[\boldsymbol{U}^{(44)}\right]$ [GPaμm^3]	1.70	1.69
$\mathbb{E}\left[\boldsymbol{U}^{(53)}\right]$ [GPaμm^2]	-0.025	-0.026
$\mathbb{E}\left[\bar{\rho}\right]$ [g/μm^2]	$1.1635\,10^{-12}$	$1.1624\,10^{-12}$

Table 5.15: Standard deviation values of the PDFs obtained from the micro-samples and from the generated random fields (non-Gaussian) for RSVE dimensions of $0.5 \times 0.5 \times 0.5\mu\text{m}^3$ and for the particular R - Si_{pref} case

	Micro-Samples	**NG-Generator**
$\sigma_{\boldsymbol{U}^{(11)}}$ [GPaμm]	6.18	5.92
$\sigma_{\boldsymbol{U}^{(12)}}$ [GPaμm]	2.86	2.68
$\sigma_{\boldsymbol{U}^{(33)}}$ [GPaμm]	2.83	2.66
$\sigma_{\boldsymbol{U}^{(44)}}$ [GPaμm^3]	0.31	0.29
$\sigma_{\boldsymbol{U}^{(53)}}$ [GPaμm^2]	0.12	0.12
$\sigma_{\bar{\rho}}$ [g/μm^2]	$7.16\,10^{-14}$	$6.81\,10^{-14}$

homogenisation process. RSVE dimensions of $0.5 \times 0.5 \times 0.5\mu\text{m}^3$ and for the particular R - Si_{pref} case are considered. The probability distribution functions obtained directly from the RSVEs homogenisation are compared to the non-

Table 5.16: Skewness values of the PDFs obtained from the micro-samples and from the generated random fields (non-Gaussian) for RSVE dimensions of $0.5 \times 0.5 \times 0.5\mu\text{m}^3$ and for the particular R - Si_{pref} case

	Micro-Samples	**NG-Generator**
$\gamma_{1\boldsymbol{U}^{(11)}}$	0.042	0.046
$\gamma_{1\boldsymbol{U}^{(12)}}$	-0.27	-0.24
$\gamma_{1\boldsymbol{U}^{(33)}}$	0.05	0.11
$\gamma_{1\boldsymbol{U}^{(44)}}$	0.73	0.62
$\gamma_{1\boldsymbol{U}^{(53)}}$	0.015	-0.002
$\gamma_{1\bar{\rho}}$	0.032	0.046

Table 5.17: Kurtosis values of the PDFs obtained from the micro-samples and from the generated random fields (non-Gaussian) with (R)SVE dimensions of $0.5 \times 0.5 \times 0.5\mu\text{m}^3$ for RSVE dimensions of $0.5 \times 0.5 \times 0.5\mu\text{m}^3$ and for the particular R - Si_{pref} case

	Micro-Samples	**NG-Generator**
$\beta_{2\boldsymbol{U}^{(11)}}$	2.97	2.97
$\beta_{2\boldsymbol{U}^{(12)}}$	3.08	3.07
$\beta_{2\boldsymbol{U}^{(33)}}$	2.83	2.91
$\beta_{2\boldsymbol{U}^{(44)}}$	3.80	3.55
$\beta_{2\boldsymbol{U}^{(53)}}$	3.86	3.73
$\beta_{2\bar{\rho}}$	2.97	2.92

Gaussian generated fields in Fig 5.48 for different entries of $\boldsymbol{U}$ and $\bar{\rho}$. The generated field distributions are in good agreement with the distributions directly obtained from the micro-samples, although the spectral density of entries $\boldsymbol{U}$ obtained from the non-Gaussian generator slightly differs from the orignal one, as $\boldsymbol{U}$ results from several entries of $\mathcal{V}'$ which are the originally treated values. However the accuracy of the non-Gaussian generator is confirmed by comparing the mean, standard deviation, skewness, and kurtosis, of the distributions obtained from the micro-samples and the non-Gaussian (NG) generator, which are respectively reported in Tables 5.14, 5.15, 5.16, and 5.17.

The last properties whose accuracy has to be assessed are the spatial correlation and cross-correlation for $\boldsymbol{U}$ and $\bar{\rho}$. The 2D in-plane (auto)-correlation of $\boldsymbol{U}^{(44)}$ resulting from the random field generated by the stochastic model is compared to the spatial distribution obtained after performing the homogeneization process on the RSVEs in Fig. 5.49. Similarly, the 1D spatial correlation along the RSVE length for $\boldsymbol{U}^{(44)}$ and $\boldsymbol{U}^{(11)}$, obtained from the micro-samples and from the random field generator, are respectively illustrated in Figs. 5.50(a) and 5.50(b). It appears that the spatial auto-correlation is reproduced with accuracy by the generator. Finally, the cross-correlations resulting from the homogenisation process and from the generated random field for different entries of $\boldsymbol{U}$ and $\bar{\rho}$ are compared in Fig. 5.51. Although some differences can be

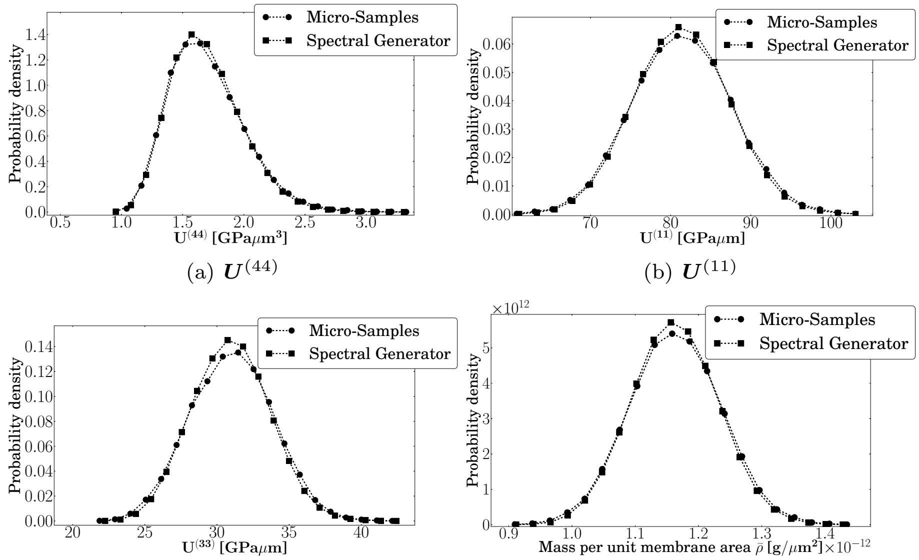

(a) $\boldsymbol{U}^{(44)}$ (b) $\boldsymbol{U}^{(11)}$

(c) $\boldsymbol{U}^{(33)}$ (d) $\bar{\rho}$

Figure 5.48: Comparison of different computed and generated meso-scale PDFs obtained for RSVE dimensions of $0.5 \times 0.5 \times 0.5 \mu\text{m}^3$ and for the particular R - Si$_{\text{pref}}$ case

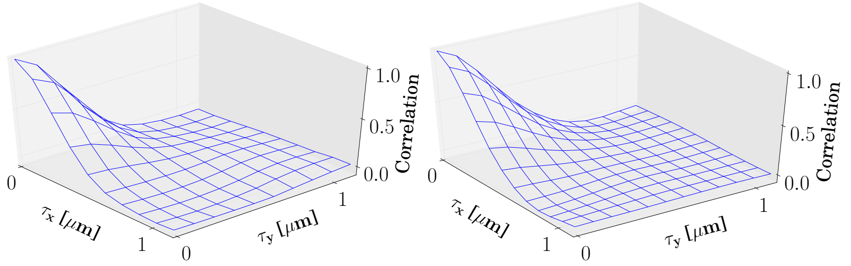

(a) Micro-Samples (b) Spectral Generator

Figure 5.49: Comparison of the 2D spatial (auto-)correlations of $\boldsymbol{U}^{(44)}$ obtained from the RSVE homogenisation and from the generator (non-Gaussian mapping) for RSVE dimensions of $0.5 \times 0.5 \times 0.5 \mu\text{m}^3$ and for the particular R - Si$_{\text{pref}}$ case

seen in the cross-correlation, the accuracy remains satisfying to generate results at the macro-scale. Noticeably, the generator did not require the definition of parameters at the exception of the minimal bounds.

As a way of illustration, one realisation of the random field entry $\boldsymbol{U}^{(44)}$ can be seen in Fig. 5.52.

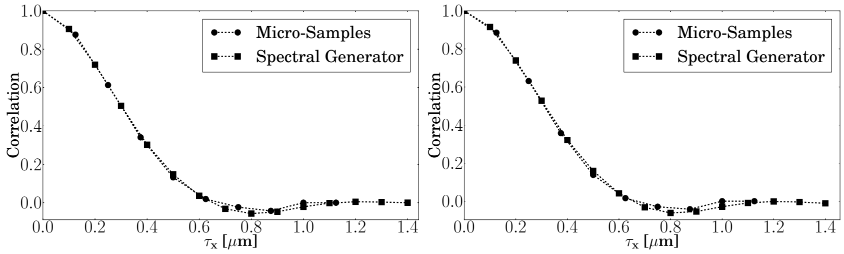

(a) $\boldsymbol{U}^{(44)}$ (b) $\boldsymbol{U}^{(11)}$

Figure 5.50: Comparison of the 1D spatial (auto-)correlations of (a) $\boldsymbol{U}^{(44)}$ and (b) $\boldsymbol{U}^{(11)}$ obtained from the RSVE homogenisation and from the generator (non-Gaussian mapping) for RSVE dimensions of $0.5 \times 0.5 \times 0.5 \mu\text{m}^3$ and for the particular R - Si_{pref} case

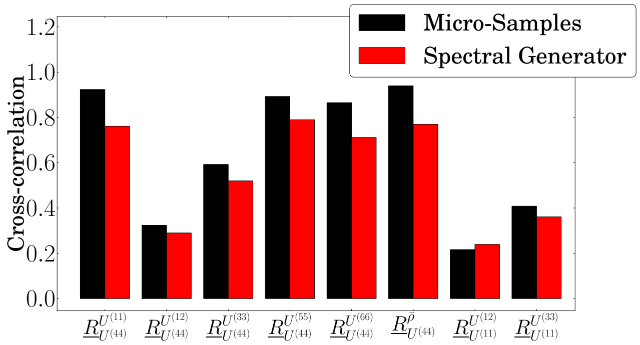

Figure 5.51: Comparison of the cross-correlations between different elements of $\boldsymbol{U}$ and $\bar{\rho}$ obtained from the RSVE homogenisation and from the generator (non-Gaussian mapping) for RSVE dimensions of $0.5 \times 0.5 \times 0.5 \mu\text{m}^3$ and for the particular R - Si_{pref} case

5.4.3 Macro-scale results

Using the random fields assessed in Section 5.4.1 (and based on the measurements as discussed in Section 5.1.1), macro-scale stochastic plate finite element as defined in Section 2.5 are used on the basis of a Monte-Carlo procedure. At each spatial position $\boldsymbol{x}$, the spectral generator defined in Chapter 4 is used to obtain realisations of the resultant meso-scale material tensor $\boldsymbol{U}(\boldsymbol{x}, \boldsymbol{\theta})$ and of the meso-scale mass per membrane unit area $\bar{\rho}(\boldsymbol{x}, \boldsymbol{\theta})$ (and thus of the mass inertia per unit width $I_p(\boldsymbol{x}, \boldsymbol{\theta})$).

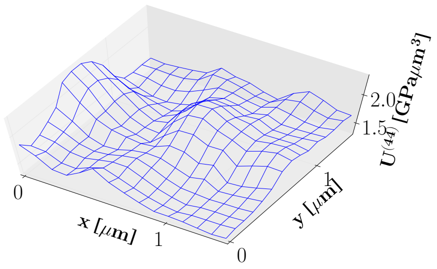

Figure 5.52: A sample of the generated field $\boldsymbol{U}^{(44)}$ for RSVE dimensions of $0.5 \times 0.5 \times 0.5\mu\text{m}^3$ and for the particular $R - Si_{\text{pref}}$ case

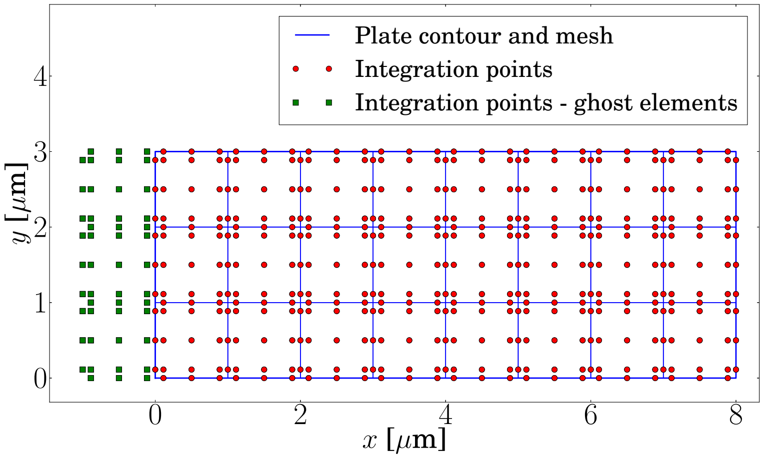

Figure 5.53: One macro-scale mesh with the corresponding integration points for a plate of dimension $8 \times 3\,\mu\text{m}^2$

The spatial positions $\boldsymbol{x}$ of interest are defined based on the macro-scale mesh of the plate. Such a mesh, made of quadrangle plate elements, is depicted in Fig. 5.53 along with the corresponding integration points. Because of the use of the Continuous/Discontinuous Galerkin method, interface elements, with their integration points, are also required to integrate the interface contributions. The ghost elements, located outside the plate, are required to model the clamping of the plate, by enforcing weakly a zero out-of-plane displacement derivative. Bi-quadratic shape functions are considered for plate elements and quadratic shape functions are considered at the interfaces to enforce weakly the continuity of the out-of-plane displacement derivative.

Once again, the boundary effect described in Section 5.3.2 is taken into

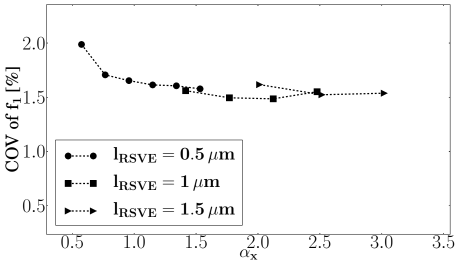

Figure 5.54: COV for different mesh sizes and RSVE lengths of the first mode frequency for a $16 \times 2 \times 0.5\,\mu\mathrm{m}^3$ rectangular plate considering RSVE dimensions of $0.5 \times 0.5 \times 0.5\mu\mathrm{m}^3$ and the R - $\mathrm{Si}_{\mathrm{pref}}$ case

account. As it was numerically verified by direct numerical simulations with a discretization of the micro-structure of MEMS resonator in Section 5.2, the stochastic multi-scale approach provides relevant results if the maximum distance $l_{\mathrm{IP}}^{\max}$ between the Integration Gauss Points (IP) of the macro-scale mesh is smaller than the correlation length $l_{\boldsymbol{U}\,\bar{\rho}}$ (2.11) of the meso-scale random fields, which in turn depends on the (R)SVE size. The ratio α_i is thus defined, along the direction i, as:

$$\alpha_i = \frac{l_{\boldsymbol{U}\,\bar{\rho}\,i}}{l_{\mathrm{IP}\ \ i}^{\max}}\,. \tag{5.36}$$

If the ratio α is smaller than 1, the uncertainty effects are overestimated as not enough heterogeneities are considered per integration point. Relevant results can only be obtained if $\alpha_i > 1$ for each direction i. As the problem is herein mainly governed by $\boldsymbol{U}^{(44)}$, we define $\alpha_i > 1$ using the correlation length $l_{\boldsymbol{U}^{(44)}}$.

The convergence of the method with respect to α_x is shown in Fig. 5.54, for a $16 \times 2 \times 0.5\,\mu\mathrm{m}^3$ rectangular plate, with the $\mathrm{R} - \mathrm{Si}_{\mathrm{pref}}$ case. The three different RSVE sizes studied at the meso-scale in Section 5.4.1 are considered: 0.5, 1 and $1.5\,\mu$m. Furthermore, different macro-scale mesh discretizations are considered. As the main direction of interest for this case of application is the plate length, the number of mesh elements along the x-direction is not constant, but the the mesh size along the y-direction does not change accordingly. The corresponding α_y parameters for each SVE size, 0.5, 1, and $1.5\,\mu$m, are respectively 2.3, 4.25, and 6.04, except for the two finest meshes of the 0.5μm SVEs for which we have added a last finite element along the y-direction. As it can be seen on Fig. 5.54, the results converge toward a COV of about 1.5% for $\alpha_x > 1$. The difference of convergence point between the curves results, on the one hand from the constant and different values of α_y, which cannot evolve with α_x because of mesh discretization constraints, and on the other hand from the boundary effect correction.

Once the macro-scale plate finite element problem has been defined, in order to conduct the probabilistic study, the number of realisations that has to solved

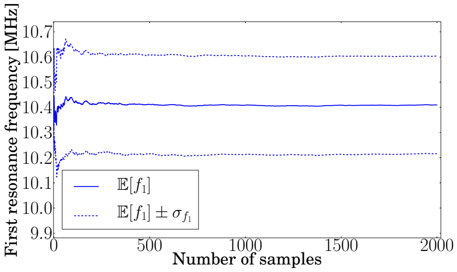

Figure 5.55: Convergence of the first mode frequency distribution for a $8 \times 3 \times 0.5\,\mu\mathrm{m}^3$ rectangular plate considering RSVE dimensions of $0.5 \times 0.5 \times 0.5\mu\mathrm{m}^3$ and the $\mathrm{R} - \mathrm{Si}_{\mathrm{pref}}$ case

should be defined. As the Monte Carlo simulation method is considered, for each macro-scale plate finite element realisation, one random field is generated. Because of the existence of the random field generator and because of the reduced cost of the plate finite element model, the Monte Carlo simulation method is actually an efficient tool. To define the number of realisations, the convergence of the distribution of the first bending mode frequency f_1 is studied in Fig. 5.55 for a $8 \times 3 \times 0.5\,\mu\mathrm{m}^3$ rectangular plate. The uncertainty case involved is the $\mathrm{R} - \mathrm{Si}_{\mathrm{pref}}$ case, and the RSVE dimensions are $0.5 \times 0.5 \times 0.5\mu\mathrm{m}^3$. The results have converged for 2000 samples, which is the number of realizations that will be considered in this section.

The macro-scale effect of the different sources of uncertainties

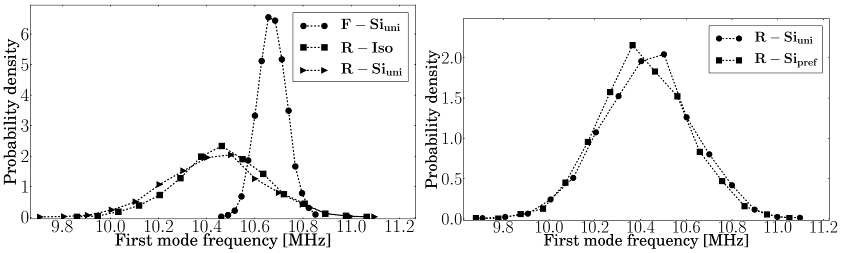

(a) Uncertainty cases (b) Influence of orientation

Figure 5.56: The distribution of the resonance frequency of $8 \times 3 \times 0.5\,\mu\mathrm{m}^3$ plates for different uncertainty cases

The method is now used to study the effect of the different uncertainty cases, described in Section 5.4.1, on the plate behaviour. In particular the

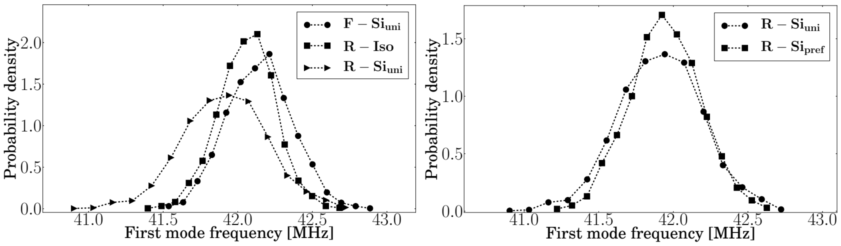

(a) Uncertainty cases (b) Influence of orientation

Figure 5.57: The distribution of the resonance frequency of $8 \times 3 \times 2\,\mu\text{m}^3$ plates for different uncertainty cases

first resonance frequency of $8 \times 3\,\mu\text{m}^2$ rectangular plates subjected to different cases of uncertainty is studied for two different thicknesses of $0.5\,\mu$m and $2\,\mu$m. The RSVE length is 0.5μm. The estimated probability density functions are depicted in Fig. 5.56 and in Fig. 5.57 for the respective average plate thicknesses $\bar{h} = 0.5\,\mu$m and $\bar{h} = 2\,\mu$m. The corresponding mean and standard deviation are given in Table 5.18. In agreement with the results provided in Section 5.4.1, Table 5.18 and Figs. 5.56 and 5.57 show that the main source of uncertainty changes with the thickness of the plate. For a $0.5\,\mu$m-thick plate, the main source of uncertainty is due to the roughness, while for $2\,\mu$m-thick plate, the two sources of uncertainty (material and roughness) become of comparable effects.

Table 5.18: Statistical moments of the first resonance frequency of $8 \times 3\,\mu\text{m}^2$ rectangular plates for the different meso-scale uncertainties cases

Cases	$\bar{\mathbf{h}} = \mathbf{0.5}\,\boldsymbol{\mu}\mathbf{m}$		$\bar{\mathbf{h}} = \mathbf{2}\,\boldsymbol{\mu}\mathbf{m}$	
	$\mathbb{E}[f_1]$ [MHz]	$\boldsymbol{\sigma}_{f_1}$ [MHz]	$\mathbb{E}[f_1]$ [MHz]	$\boldsymbol{\sigma}_{f_1}$ [MHz]
$\mathbf{F - Si_{uni}}$	10.67	0.060	42.15	0.215
$\mathbf{F - Si_{pref}}$	10.70	0.045	42.26	0.162
$\mathbf{R - Iso}$	10.46	0.181	42.06	0.187
$\mathbf{R - Si_{uni}}$	10.43	0.199	41.91	0.278
$\mathbf{R - Si_{pref}}$	10.41	0.194	41.94	0.236

The effect of the plate dimensions

The effect of the plate dimension is studied for the R − Si$_{\text{pref}}$ uncertainty case and for 0.5 μm-long RSVEs in Fig. 5.58. Results obtained for different plate thicknesses are shown in Fig. 5.58(a). As expected, uncertainties decrease with the increase of the thickness of the plate as the roughness effect becomes less important. Changing the width has a large impact on the uncertainty as shown in Fig. 5.58(b): the larger the plate, the lower the uncertainties as the heterogeneities have less effects. Finally, results obtained for different lengths

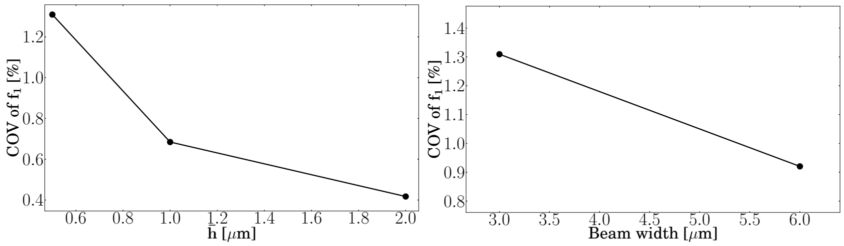

(a) Effect of the thickness (b) Effect of the width

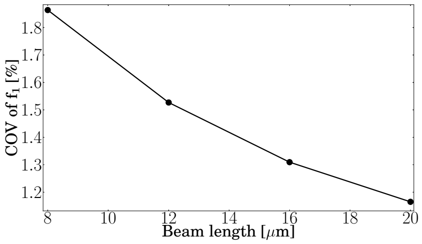

(c) Effect of the length

Figure 5.58: The effect of the plate dimensions on the first resonance frequency distribution for the $\mathrm{R}-\mathrm{Si}_{\mathrm{pref}}$ case and (a) for a $16\,\mu$m-long, $3\,\mu$m-wide plate and for different thicknesses, (b) for a $16\,\mu$m-long, $0.5\,\mu$m-thick plate and for different widths, and (c) for a $3\,\mu$m-wide, $0.5\,\mu$m-thick plate and for different lengths

of the plate are shown in Fig. 5.58(c), where it can be seen that the uncertainty of the resonance frequency decreases with the length of the plate. However, considering a more realistic anchor of the MEMS than a perfect clamp, as done in Section 5.3.2 could change this conclusion.

Finally, the first two statistical moments obtained for different plate dimensions are gathered in Table 5.19.

Table 5.19: Statistical moments of the plate first resonance frequency for the different plate dimensions for the $\mathrm{R}-\mathrm{Si}_{\mathrm{pref}}$ case

Membrane geometry	$\mathbb{E}[f_1]$ [MHz]		
	$\mathbf{h}=\mathbf{0.5}\,\mu\mathbf{m}$	$\mathbf{h}=\mathbf{1}\,\mu\mathbf{m}$	$\mathbf{h}=\mathbf{2}\,\mu\mathbf{m}$
$\mathbf{8}\times\mathbf{3}\,\mu\mathbf{m}$	10.41	20.98	41.94
$\mathbf{8}\times\mathbf{6}\,\mu\mathbf{m}$	10.46	21.06	42.11
$\mathbf{16}\times\mathbf{3}\,\mu\mathbf{m}$	2.58	5.22	10.50
$\mathbf{16}\times\mathbf{6}\,\mu\mathbf{m}$	2.59	5.24	10.54

Membrane geometry	σ_{f_1} [MHz]		
	$\mathbf{h}=\mathbf{0.5}\,\mu\mathbf{m}$	$\mathbf{h}=\mathbf{1}\,\mu\mathbf{m}$	$\mathbf{h}=\mathbf{2}\,\mu\mathbf{m}$
$\mathbf{8}\times\mathbf{3}\,\mu\mathbf{m}$	0.194	0.205	0.236
$\mathbf{8}\times\mathbf{6}\,\mu\mathbf{m}$	0.134	0.139	0.166
$\mathbf{16}\times\mathbf{3}\,\mu\mathbf{m}$	0.0338	0.0357	0.0438
$\mathbf{16}\times\mathbf{6}\,\mu\mathbf{m}$	0.0239	0.0252	0.0297

Chapter 6

Conclusions and perspectives

Deterministic numerical approaches are widespread tools to study the response of structures. Quantifying the uncertainty of this response can also be a valuable resource and it can nowadays be done in many ways. However, for structures made of heterogeneous materials, estimating the scatter of the response of the structure can be unaffordable with a direct Monte-Carlo simulation. Indeed it would require a model of the structure which encompasses each heterogeneity. Therefore an affordable alternative procedure is of interest. The purpose of this thesis dissertation was to investigate the recourse to multi-scale approaches so that uncertainties are propagated throughout the different scales of the problem.

The starting point of this 3-scale approach is the stochastic finite element method, as described in Chapter 2. The problem at the scale of the structure is defined and the variability of the response can be computed using a Monte-Carlo analysis. This method requires a random field as input, which represents the uncertainties at the lower scale. Without recourse to the 3-scale approach, such a random field would possess a small correlation length and thus involve high computational cost. The cornerstone of the approach is to consider a random field based on homogenised properties. Such a random field possesses a larger correlation length and thus a computationally efficient procedure is defined.

The meso-scale random fields, based on homogenised properties, were assessed in Chapter 3. Computational homogenisation is used to homogenised meso-scale properties such as the elasticity tensor or the thermal conductivity tensor. Owing to a window technique, spatial correlation can be captured and the meso-scale random field can be defined.

Using this random field in the frame of the SFEM method is time consuming as, at each macro-scale point of interest, a volume element must be homogenised. Therefore, a stochastic model of the meso-scale random field is defined. Assuming enough samples of the meso-scale random field are available, new samples can be generated and used in the SFEM approach. This was the focus of Chapter 4.

The 3-scale approach was then used in the frame of MEMS micro-beams in Chapter 5. The micro-scale uncertainties are modelled based on experimental measurements provided by the IMT institute in Bucharest. These uncertainties are then propagated for 3 different problems. The first problem consists of a simple case: 1D beams in linear elasticity. It is used to verify the procedure with respect to a fully modelled beam. The verification shows that accurate results are obtained as soon as the macro-scale finite element mesh is small enough compared to the correlation length of the meso-scale random field. Afterwards, the method is applied for 3D beams in thermo-elasticity. This allows the study of the uncertainties in terms of quality factor. The modelling of the anchor could also be performed. The last problem aimed at propagating the uncertainty in terms of roughness up to the macro-scale resonance frequency of MEMS thin plates.

The propagation of uncertainties throughout the different scales was verified and its application on different problems underline its versatility. Nevertheless, there is still a lot of room for future works.

First, the method was verified but not validated. MEMS micro-beams can be produced and their corresponding resonance frequencies or quality factors (in vaccum or with air damping) can be measured owing to a vibrometer. This however requires the accurate manufacturing of micro-beams in order to study the uncertainties of interest. Once enough micro-beams samples with the same design process are manufactured, the validation of the 3-scale approach could be envisioned.

Second, the variability calculation was performed, both in the stochastic homogenisation and in the SFEM analysis, with a Monte-Carlo procedure. Other procedures can be investigated, such as the spectral stochastic finite elements approach.

Third, the 3-scale approach was studied on 3 different problems. It can be used on other problems. Different sources of uncertainty can be studied such as the crystallinity of the poly-crystalline structure or due to an uncertain clamp geometry. The latter can be studied by considering a random geometry of the macro-scale structure. The problem can be extended to problems with a different physic, to propagate uncertainties for electro-mechanical problems for example.

All these macro-scale uncertainties are already relevant information. However, the 3-scale approach can be used in the frame of an optimisation procedure so that efficient design processes can be formulated. For example, if the quality factor of a resonant sensor is below a certain threshold, it is thrown away as they do not comply to the quality standard for the application. The 3-scale approach, along with an optimisation procedure, would help figure out a design process which would involve the lowest probability of waste.

Appendix A

The elementary stiffness and mass matrix for a Timoshenko beam element

The elementary stiffness matrix $\boldsymbol{K}_e^{ab}$ for a Timoshenko beam element between two nodes a and b considering the interdependent interpolation element is [79]:

$$\boldsymbol{K}_e^{ab} = \frac{2EI}{(1+12\Theta)\,l^3} \begin{pmatrix} 6 & -3l & -6 & -3l \\ -3l & 2l^2\,(1+3\Theta) & 3l & l^2\,(1-6\Theta) \\ -6 & 3l & 6 & 3l \\ -3l & l^2\,(1-6\Theta) & 3l & 2l^2\,(1+3\Theta) \end{pmatrix}, \tag{A.1}$$

where $\Theta = \frac{EI}{GAK_s l^2}$ and l is the element size. The elementary mass matrix $\boldsymbol{M}_e^{ab}$ is:

$$\boldsymbol{M}_e^{ab} = \rho A l \begin{pmatrix} \frac{13}{35} & \frac{-11}{210}l & \frac{9}{70} & \frac{13}{420}l \\ \frac{-11}{210}l & \frac{1}{105}l^2 & \frac{-13}{420}l & \frac{-1}{140}l^2 \\ \frac{9}{70} & \frac{-13}{420}l & \frac{13}{35} & \frac{11}{210}l \\ \frac{13}{420}l & \frac{-1}{140}l^2 & \frac{11}{210}l & \frac{1}{105}l^2 \end{pmatrix}, \tag{A.2}$$

Appendix B

Insight in the formulation of the thermo-elastic problem

B.1 Thermo-mechanical formulation

In the thermo-mechanics context, besides the linear momentum Eq. (2.30), the deformable solid behavior is governed by the (localized) energy balance per unit volume [57]

$$\rho \dot{e} - \rho s - \boldsymbol{\sigma} : \dot{\boldsymbol{\varepsilon}} + \boldsymbol{\nabla} \cdot \boldsymbol{q} = 0 \,, \tag{B.1}$$

where e is the internal energy per unit mass, $\boldsymbol{\sigma}$ is the Cauchy stress tensor, $\boldsymbol{\varepsilon}$ is the Cauchy strain tensor, T is the absolute temperature, s is the heat source per unit mass, and $\boldsymbol{q}$ is the thermal flux vector.

The (localized) Clausius-Duhem inequality reads

$$\rho \dot{\eta} + \boldsymbol{\nabla} \cdot \left(\frac{\boldsymbol{q}}{T} \right) - \frac{\rho s}{T} \geq 0 \,, \tag{B.2}$$

where η is the entropy per unit mass. This last relation can be rewritten as

$$\rho \dot{\eta} - \frac{1}{T} \left(\rho s - \boldsymbol{\nabla} \cdot \boldsymbol{q} \right) - \frac{1}{T^2} \boldsymbol{q} \cdot \boldsymbol{\nabla} T \geq 0 \,. \tag{B.3}$$

Multiplying this last equation by T and subtracting it from (B.1) yields

$$\rho \left(\dot{e} - T \dot{\eta} \right) - \boldsymbol{\sigma} : \dot{\boldsymbol{\varepsilon}} + \frac{1}{T} \left(\boldsymbol{q} \cdot \boldsymbol{\nabla} T \right) \leq 0 \,. \tag{B.4}$$

Defining the specific free energy $\phi = e - T\eta$ allows writing

$$\dot{\phi} = \dot{e} - T \dot{\eta} - \dot{T} \eta \,, \tag{B.5}$$

and Eq. (B.4) allows defining the dissipation per unit volume $\mathcal{D}$ as

$$-\mathcal{D} = \rho \left(\dot{\phi} + \dot{T} \eta \right) - \boldsymbol{\sigma} : \dot{\boldsymbol{\varepsilon}} + \frac{1}{T} \left(\boldsymbol{q} \cdot \boldsymbol{\nabla} T \right) \leq 0 \,. \tag{B.6}$$

The thermodynamics forces are set to be

$$\left(\frac{\partial\phi}{\partial T}\right)_{\boldsymbol{\varepsilon}} = -\eta \text{ and } \rho\left(\frac{\partial\phi}{\partial\boldsymbol{\varepsilon}}\right)_{T} = \boldsymbol{\sigma}\,, \tag{B.7}$$

and are completed by the condition $\boldsymbol{q}\cdot\boldsymbol{\nabla}T \leq 0$. By differentiation of the specific free energy one thus has

$$\rho\dot{\phi} = \boldsymbol{\sigma} : \dot{\boldsymbol{\varepsilon}} - \rho\eta\dot{T}\,, \tag{B.8}$$

which, combined to Eq. (B.5) leads to the so-called Gibbs relation

$$\rho\dot{e} = \boldsymbol{\sigma} : \dot{\boldsymbol{\varepsilon}} + \rho T\dot{\eta}. \tag{B.9}$$

Combining this relation to Eq. (B.1) leads to the expression of the entropy rate

$$\rho T\dot{\eta} = \rho\dot{e} - \boldsymbol{\sigma} : \dot{\boldsymbol{\varepsilon}} = \rho s - \boldsymbol{\nabla}\cdot\boldsymbol{q}\,. \tag{B.10}$$

Eventually, using Eqs. (B.5), the entropy relation (B.10), and the energy balance (B.1) in the dissipation expression (B.6) yields

$$\mathcal{D} = -\rho\dot{e} + \rho s - \boldsymbol{\nabla}\cdot\boldsymbol{q} + \boldsymbol{\sigma} : \dot{\boldsymbol{\varepsilon}} - \frac{1}{T}\left(\boldsymbol{q}\cdot\boldsymbol{\nabla}T\right) = -\frac{1}{T}\left(\boldsymbol{q}\cdot\boldsymbol{\nabla}T\right)\,. \tag{B.11}$$

Let us now consider thermo-elasticity with $\mathcal{S} = \rho\eta$ the entropy per unit volume, $\rho e = \rho C_v T$ with C_v the heat capacity per unit mass, and $\mathcal{F}\left(T, \boldsymbol{\varepsilon}\right) = \rho\phi = \rho C_v T - T\mathcal{S}$ the Helmholtz free energy defined in Eq. (2.33) for constant material parameters. The framework reported here above thus reduces to the set of equations reported in Section 2.4.2.

B.2 The definition of sub-matrices in finite element formula

The sub-matrices in Eq. (2.52) are defined by

$$\boldsymbol{M} = \int_{\Omega} \rho\boldsymbol{N}_u^{\mathrm{T}}\boldsymbol{N}_u \mathrm{d}\Omega\,, \tag{B.12a}$$

$$\boldsymbol{D}_{\vartheta u} = T_0\int_{\Omega} \boldsymbol{N}_{\vartheta}^{\mathrm{T}}\boldsymbol{\alpha}\boldsymbol{C}\boldsymbol{B}_u \mathrm{d}\Omega\,, \tag{B.12b}$$

$$\boldsymbol{D}_{\vartheta\vartheta} = \int_{\Omega} \rho C_v\boldsymbol{N}_{\vartheta}^{\mathrm{T}}\boldsymbol{N}_{\vartheta} \mathrm{d}\Omega\,, \tag{B.12c}$$

$$\boldsymbol{K}_{uu} = \int_{\Omega} \boldsymbol{B}_u^{\mathrm{T}}\boldsymbol{C}\boldsymbol{B}_u \mathrm{d}\Omega\,, \tag{B.12d}$$

$$\boldsymbol{K}_{u\vartheta} = -\int_{\Omega} \boldsymbol{B}_u^{\mathrm{T}}\boldsymbol{C}\boldsymbol{\alpha}\boldsymbol{N}_{\vartheta} \mathrm{d}\Omega\,, \text{ and} \tag{B.12e}$$

$$\boldsymbol{K}_{\vartheta\vartheta} = \int_{\Omega} \boldsymbol{B}_{\vartheta}^{\mathrm{T}}\boldsymbol{\kappa}\boldsymbol{B}_{\vartheta} \mathrm{d}\Omega\,. \tag{B.12f}$$

The external force vectors are easily obtained from

$$\boldsymbol{f}_u = \int_\Omega \boldsymbol{N}_u^{\mathrm{T}} \rho \boldsymbol{b} \mathrm{d}\Omega + \int_{\partial \boldsymbol{D}_{\mathcal{T}}} \boldsymbol{N}_u^{\mathrm{T}} \boldsymbol{\mathcal{T}} \mathrm{d}\partial \boldsymbol{D}\,, \tag{B.13a}$$

$$\boldsymbol{f}_\vartheta = - \int_{\partial \boldsymbol{D}_q^T} \boldsymbol{N}_\vartheta^{\mathrm{T}} \mathcal{Q} \mathrm{d}\partial \boldsymbol{D}^T\,. \tag{B.13b}$$

B.3 The constrained micro-scale finite element formulation

B.3.1 Definition of the constraints

The specified kinematic admissible boundary conditions applied on a finite element discretization (3.29) of the SVE in this work are the Periodic Boundary Conditions (PBCs) (3.49) of displacement $\boldsymbol{u}_{\mathrm{m}}$ and temperature ϑ_{m}, completed by the consistency condition (3.40).

The degrees of freedom of the micro-scale problem (we drop the subscript 'm' for conciseness) are organized in terms of $\mathbf{u}_c$, $\mathbf{u}_b$, and $\mathbf{u}_i$, respectively the corner nodal displacements, the boundary nodal displacements, and the internal nodal displacements, and in terms of $\boldsymbol{\vartheta}_c$, $\boldsymbol{\vartheta}_b$, and $\boldsymbol{\vartheta}_i$, respectively the corner nodal temperatures, the boundary nodal temperatures, and the internal nodal temperatures.

The kinematics constraints are defined by $\mathbb{F}_{\mathrm{M}} = \boldsymbol{u}_{\mathrm{M}} \otimes \boldsymbol{\nabla}_{\mathrm{M}}$ the macroscopic deformation gradient, with $\boldsymbol{F}_{\mathrm{M}}$ the nine components of $\mathbb{F}_{\mathrm{M}}$ written under a vectorial form, by $\boldsymbol{\nabla}_{\mathrm{M}} \vartheta_{\mathrm{M}}$ the macroscopic temperature gradient, and by ϑ_{M} the macroscopic temperature.

The periodic boundary conditions (3.49) are first used to define the constraints on the displacement field at the corner nodes p, leading to

$$\mathbf{u}_c^p = \begin{bmatrix} \boldsymbol{x}^{pT} & \mathbf{0}_{1\times 3} & \mathbf{0}_{1\times 3} \\ \mathbf{0}_{1\times 3} & \boldsymbol{x}^{pT} & \mathbf{0}_{1\times 3} \\ \mathbf{0}_{1\times 3} & \mathbf{0}_{1\times 3} & \boldsymbol{x}^{pT} \end{bmatrix} \boldsymbol{F}_{\mathrm{M}} = \boldsymbol{S}_{u_c}^p \boldsymbol{F}_{\mathrm{M}}\,, \tag{B.14}$$

or after assembly

$$\mathbf{u}_c - \boldsymbol{S}_{u_c} \boldsymbol{F}_{\mathrm{M}} = 0\,. \tag{B.15}$$

The periodic boundary conditions (3.49) are then used to define the constraints on the displacement field on two opposite boundary nodes p^+ and p^-, leading to

$$\boldsymbol{u}_b^{p^+} - \boldsymbol{u}_b^{p^-} = \begin{bmatrix} \boldsymbol{x}^{p^+T} - \boldsymbol{x}^{p^-T} & \mathbf{0}_{1\times 3} & \mathbf{0}_{1\times 3} \\ \mathbf{0}_{1\times 3} & \boldsymbol{x}^{p^+T} - \boldsymbol{x}^{p^-T} & \mathbf{0}_{1\times 3} \\ \mathbf{0}_{1\times 3} & \mathbf{0}_{1\times 3} & \boldsymbol{x}^{p^+T} - \boldsymbol{x}^{p^-T} \end{bmatrix} \boldsymbol{F}_{\mathrm{M}} = \boldsymbol{S}_{u_b}^p \boldsymbol{F}_{\mathrm{M}}\,, \tag{B.16}$$

or after assembly

$$\boldsymbol{C}_{u_b} \mathbf{u}_b - \boldsymbol{S}_{u_b} \boldsymbol{F}_{\mathrm{M}} = 0\,. \tag{B.17}$$

In case of a non-periodic mesh, the use of the interpolation method developed in [66] yields a similar relation which involves the corner nodes as well

$$\boldsymbol{C}_{u_c}\mathbf{u}_c + \boldsymbol{C}_{u_b}\mathbf{u}_b - \boldsymbol{S}_{u_b}\boldsymbol{F}_{\mathrm{M}} = 0\,. \tag{B.18}$$

Concerning the temperature field, the rigid mode is constrained by the condition (3.40), and not by a constraint similar to (B.15). The thermal part of the periodic boundary conditions (3.49) thus involves both corner and boundary nodal temperatures, which results in

$$\boldsymbol{\vartheta}^{p^+}_{b(c)} - \boldsymbol{\vartheta}^{p^-}_{b(c)} = \left[\boldsymbol{x}^{p^+T} - \boldsymbol{x}^{p^-T}\right]\boldsymbol{\nabla}\vartheta_{\mathrm{M}} = \boldsymbol{S}^{p}_{\vartheta_{b(c)}}\boldsymbol{\nabla}\vartheta_{\mathrm{M}}\,, \tag{B.19}$$

or after assembly

$$\boldsymbol{C}_{\vartheta_c}\boldsymbol{\vartheta}_c + \boldsymbol{C}_{\vartheta_b}\boldsymbol{\vartheta}_b - \boldsymbol{S}_{\vartheta_b}\boldsymbol{\nabla}\vartheta_{\mathrm{M}} = 0\,, \tag{B.20}$$

which remains valid in case of a non-periodic mesh when using the interpolation method. Finally, the last condition (3.40) is discretized by considering the corner, boundary, and internal nodal temperatures as

$$\frac{1}{V(\omega)}\int_{\omega}\rho_{\mathrm{m}}C_{v\mathrm{m}}\boldsymbol{N}^{p}_{\vartheta}dV\boldsymbol{\vartheta}^{p}_{(bci)} = \boldsymbol{C}^{p}_{\Theta_{(bci)}}\boldsymbol{\vartheta}^{p}_{(bci)} = \rho_{\mathrm{M}}C_{v\mathrm{M}}\vartheta_{\mathrm{M}} = S_{\Theta_b}\vartheta_{\mathrm{M}}\,, \tag{B.21}$$

or again

$$\boldsymbol{C}_{\Theta_c}\boldsymbol{\vartheta}_c + \boldsymbol{C}_{\Theta_b}\boldsymbol{\vartheta}_b + \boldsymbol{C}_{\Theta_i}\boldsymbol{\vartheta}_i - S_{\Theta_b}\vartheta_{\mathrm{M}} = 0\,. \tag{B.22}$$

As the constraints (B.18), (B.20), and (B.22), have the same structure, the related nodal fields are groups together into the vector $\boldsymbol{\varphi}_b^T = \left[\mathbf{u}_b^T\boldsymbol{\vartheta}_c^T\boldsymbol{\vartheta}_b^T\boldsymbol{\vartheta}_i^T\right]$, and the micro-structural problem (3.29) is thus organized in terms of the nodal unknowns

$$\boldsymbol{\varphi} = \begin{bmatrix} \mathbf{u}_c^T & \boldsymbol{\varphi}_b^T & \mathbf{u}_i^T \end{bmatrix}^T\,, \tag{B.23}$$

which are the constrained, dependent, and independent unknowns respectively, of the nodal forces

$$\boldsymbol{F} = \begin{bmatrix} \boldsymbol{f}_{u_c}^T & \boldsymbol{f}_{\varphi_b}^T & \boldsymbol{f}_{u_i}^T \end{bmatrix}^T\,, \tag{B.24}$$

and of the stiffness matrix

$$\boldsymbol{K} = \begin{bmatrix} \boldsymbol{K}_{u_c u_c} & \boldsymbol{K}_{u_c\varphi_b} & \boldsymbol{K}_{u_c u_i} \\ \boldsymbol{K}_{\varphi_b u_c} & \boldsymbol{K}_{\varphi_b\varphi_b} & \boldsymbol{K}_{\varphi_b u_i} \\ \boldsymbol{K}_{u_i u_c} & \boldsymbol{K}_{u_i\varphi_b} & \boldsymbol{K}_{u_i u_i} \end{bmatrix}\,. \tag{B.25}$$

The constraints (B.15), (B.18), (B.20), and (B.22) are reorganized, leading to

$$\begin{aligned} 0 &= \mathbf{u}_c - \boldsymbol{S}_{u_c}\boldsymbol{F}_{\mathrm{M}} = \mathbf{u}_c - \boldsymbol{S}_{\varphi_c}\boldsymbol{K}_{\mathrm{M}}\,, && \text{(B.26)} \\ 0 &= \boldsymbol{C}_{\varphi_c}\boldsymbol{u}_c + \boldsymbol{C}_{\varphi_b}\boldsymbol{\varphi}_b - \boldsymbol{S}_{\varphi_b}\boldsymbol{K}_{\mathrm{M}}\,, && \text{(B.27)} \end{aligned}$$

where

$$\boldsymbol{S}_{\varphi_b} = \begin{bmatrix} \boldsymbol{S}_{u_b} & \boldsymbol{0}_{\frac{N_{u_b}}{2}\times 3} & \boldsymbol{0}_{\frac{N_{u_b}}{2}\times 1} \\ \boldsymbol{0}_{\frac{N_{\vartheta_c}+N_{\vartheta_b}}{2}\times 9} & \boldsymbol{S}_{\vartheta_b} & \boldsymbol{0}_{\frac{N_{\vartheta_c}+N_{\vartheta_b}}{2}\times 1} \\ \boldsymbol{0}_{1\times 9} & \boldsymbol{0}_{1\times 3} & S_{\Theta_b} \end{bmatrix}\,,\quad \boldsymbol{S}^T_{\varphi_c} = \begin{bmatrix} \boldsymbol{S}^T_{u_c} \\ \boldsymbol{0}_{3\times N_{u_c}} \\ \boldsymbol{0}_{1\times N_{u_c}} \end{bmatrix}\,, \tag{B.28}$$

$$\boldsymbol{C}_{\varphi_b} = \left[\begin{array}{cccc} \boldsymbol{C}_{u_b} & \mathbf{0}_{\frac{N_{u_b}}{2} \times N_{\vartheta_c}} & \mathbf{0}_{\frac{N_{u_b}}{2} \times N_{\vartheta_b}} & \mathbf{0}_{\frac{N_{u_b}}{2} \times N_{\vartheta_i}} \\ \mathbf{0}_{\frac{N_{u_c}+N_{u_b}}{2} \times N_{u_b}} & \boldsymbol{C}_{\vartheta_c} & \boldsymbol{C}_{\vartheta_b} & \mathbf{0}_{\frac{N_{u_c}+N_{u_b}}{2} \times N_{\vartheta_i}} \\ \mathbf{0}_{1 \times N_{u_b}} & \boldsymbol{C}_{\Theta_c} & \boldsymbol{C}_{\Theta_b} & \boldsymbol{C}_{\Theta_i} \end{array} \right] , \tag{B.29}$$

$$\boldsymbol{C}_{\varphi_c} = \left[\begin{array}{c} \boldsymbol{C}_{u_c} \\ \mathbf{0}_{\frac{N_{u_c}+N_{u_b}}{2} \times N_{u_c}} \\ \mathbf{0}_{1 \times N_{u_c}} \end{array} \right] , \ \boldsymbol{K}_{\mathrm{M}} = \left[\begin{array}{c} \boldsymbol{F}_{\mathrm{M}} \\ \nabla_{\mathrm{M}} \vartheta_M \\ \vartheta_{\mathrm{M}} \end{array} \right] , \tag{B.30}$$

with N_{u_c} ... referring to the number of constraints per type (constrained or dependent degrees of freedom).

B.3.2 Resolution of the constrained micro-scale finite element problem

The resolution of the constrained micro-scale BVP follows the multiple-constraint projection method described in [2] and the condensation method developed in [59]. The functional related to the constrained micro-scale problem is defined, using the conditions (B.26-B.27), by

$$\Psi = \frac{1}{2} \boldsymbol{\varphi}^T \boldsymbol{K} \boldsymbol{\varphi} - \left[\mathbf{u}_c - \boldsymbol{S}_{\varphi_c} \boldsymbol{K}_{\mathrm{M}} \right]^T \boldsymbol{\lambda}_{u_c} - \left[\boldsymbol{C}_{\varphi_c} \mathbf{u}_c + \boldsymbol{C}_{\varphi_b} \boldsymbol{\varphi}_b - \boldsymbol{S}_{\varphi_b} \boldsymbol{K}_{\mathrm{M}} \right]^T \boldsymbol{\lambda}_{\varphi_b} , \tag{B.31}$$

with the Lagrange multipliers $\boldsymbol{\lambda}_{u_c}$ and $\boldsymbol{\lambda}_{\varphi_b}$ which are respectively related to the corner displacement constraints and to the dependent unknowns constraints. This last term can be rewritten

$$\boldsymbol{\lambda}_{\varphi_b}^T = \left[\begin{array}{ccc} \boldsymbol{\lambda}_{u_b}^T & \boldsymbol{\lambda}_{\vartheta}^T & \lambda_{\Theta} \end{array} \right] , \tag{B.32}$$

in terms of the Lagrange multipliers related to the boundary displacement constraints, boundary temperature constraints, and average temperature constraint. The resolution of the micro-scale finite element model is thus achieved by minimizing the functional.

First, the minimization of (B.31) with respect to the nodal unknowns yields

$$\begin{aligned} 0 &= \frac{\partial \Psi}{\partial \boldsymbol{u}_i} = \boldsymbol{f}_{u_i} , && \text{(B.33)} \\ 0 &= \frac{\partial \Psi}{\partial \boldsymbol{\varphi}_b} = \boldsymbol{f}_{\varphi_b} - \boldsymbol{C}_{\varphi_b}^T \boldsymbol{\lambda}_{\varphi_b} , && \text{(B.34)} \\ 0 &= \frac{\partial \Psi}{\partial \boldsymbol{u}_c} = \boldsymbol{f}_{u_c} - \boldsymbol{\lambda}_{u_c} - \boldsymbol{C}_{\varphi_c}^T \boldsymbol{\lambda}_{\varphi_b} . && \text{(B.35)} \end{aligned}$$

Defining $\boldsymbol{R}_{\varphi_b}^T = \left(\boldsymbol{C}_{\varphi_b} \boldsymbol{C}_{\varphi_b}^T \right)^{-1} \boldsymbol{C}_{\varphi_b}$, the solution of the system (B.33-B.35) reads

$$\begin{aligned} \boldsymbol{\lambda}_{\varphi_b} &= \boldsymbol{R}_{\varphi_b}^T \boldsymbol{f}_{\varphi_b} , && \text{(B.36)} \\ \boldsymbol{\lambda}_{u_c} &= \boldsymbol{f}_{u_c} - \boldsymbol{C}_{\varphi_c}^T \boldsymbol{R}_{\varphi_b}^T \boldsymbol{f}_{\varphi_b} . && \text{(B.37)} \end{aligned}$$

B.3.3 Homogenised stress and flux

The homogenised stress tensor (3.32) is evaluated in the matrix form as

$$\boldsymbol{\Sigma}_{\mathrm{M}} = \frac{1}{V(\omega)}\left(\frac{\partial \Psi}{\partial \boldsymbol{F}_{\mathrm{M}}}\right) = \frac{1}{V(\omega)}\left[\begin{array}{ccc} \boldsymbol{I}_{9\times 9} & \mathbf{0}_{9\times 3} & \mathbf{0}_{0\times 1} \end{array}\right]\left\{\boldsymbol{S}^T_{\varphi_c}\boldsymbol{\lambda}_{u_c} + \boldsymbol{S}^T_{\varphi_b}\boldsymbol{\lambda}_{\varphi_b}\right\}, \tag{B.38}$$

or using Eqs. (B.28)[1], (B.29), (B.30), (B.32), (B.36), and (B.37), as

$$\boldsymbol{\Sigma}_{\mathrm{M}} = \frac{1}{V(\omega)}\left\{\boldsymbol{S}^T_{u_c}\left(\boldsymbol{f}_{u_c} - \boldsymbol{C}^T_{u_c}\boldsymbol{R}^T_{u_b}\boldsymbol{f}_{u_b}\right) + \boldsymbol{S}^T_{u_b}\boldsymbol{R}^T_{u_b}\boldsymbol{f}_{u_b}\right\}, \tag{B.44}$$

where $\boldsymbol{f}_{u_b}$ is the boundary nodal displacement contribution to $\boldsymbol{f}_{\varphi_b}$.

Similarly, the homogenised thermal flux (3.34) is evaluated as

$$\boldsymbol{q}_{\mathrm{M}} = \frac{1}{V(\omega)}\left(\frac{\partial \Psi}{\partial \boldsymbol{\nabla}_{\mathrm{M}}\vartheta_{\mathrm{M}}}\right) = \frac{1}{V(\omega)}\left[\begin{array}{ccc} \mathbf{0}_{3\times 9} & \boldsymbol{I}_{3\times 3} & \mathbf{0}_{3\times 1} \end{array}\right]\left\{\boldsymbol{S}^T_{\varphi_c}\boldsymbol{\lambda}_{u_c} + \boldsymbol{S}^T_{\varphi_b}\boldsymbol{\lambda}_{\varphi_b}\right\}, \tag{B.45}$$

or using Eqs. (B.28), (B.29), (B.30), (B.32), and (B.36), as

$$\boldsymbol{q}_{\mathrm{M}} = \frac{1}{V(\omega)}\left[\begin{array}{cc} \boldsymbol{S}^T_{\vartheta_b} & \mathbf{0}_{3\times 1} \end{array}\right]\boldsymbol{R}^T_{\vartheta}\boldsymbol{F}_{\vartheta}, \tag{B.46}$$

where $\boldsymbol{f}_{\vartheta}$ is the thermal contribution to $\boldsymbol{f}_{\varphi_b}$.

B.3.4 Homogenised material properties

To compute the material operators, the stationary point of (B.31) is linearized with respect to the kinematics constraints $\boldsymbol{K}_{\mathrm{M}}$. Linearizing Eqs. (B.33-B.35)

---

[1] From the block diagonal structure of

$$\boldsymbol{C}_{\varphi_b} = \left[\begin{array}{cc} \boldsymbol{C}_{u_b} & \mathbf{0} \\ \mathbf{0} & \boldsymbol{C}_{\vartheta} \end{array}\right], \tag{B.39}$$

by defining $\boldsymbol{R}^T_{u_b} = \left(\boldsymbol{C}_{u_b}\boldsymbol{C}^T_{u_b}\right)^{-1}\boldsymbol{C}_{u_b}$ and $\boldsymbol{R}^T_{\vartheta} = \left(\boldsymbol{C}_{\vartheta}\boldsymbol{C}^T_{\vartheta}\right)^{-1}\boldsymbol{C}_{\vartheta}$, one has

$$\boldsymbol{R}^T_{\varphi_b} = \left[\begin{array}{cc} \boldsymbol{R}^T_{u_b} & \mathbf{0} \\ \mathbf{0} & \boldsymbol{R}^T_{\vartheta} \end{array}\right], \tag{B.40}$$

and Eq. (B.36) is rewritten

$$\boldsymbol{\lambda}_{\varphi_b} = \left[\begin{array}{c} \boldsymbol{\lambda}_{u_b} \\ \left[\begin{array}{c} \boldsymbol{\lambda}_{\vartheta} \\ \lambda_{\Theta} \end{array}\right] \end{array}\right] = \left[\begin{array}{cc} \boldsymbol{R}^T_{u_b} & \mathbf{0} \\ \mathbf{0} & \boldsymbol{R}^T_{\vartheta} \end{array}\right]\left[\begin{array}{c} \boldsymbol{f}_{u_b} \\ \boldsymbol{f}_{\vartheta} \end{array}\right], \tag{B.41}$$

or again

$$\boldsymbol{\lambda}_{u_b} = \boldsymbol{R}^T_{u_b}\boldsymbol{f}_{u_b}, \text{ and} \tag{B.42}$$

$$\left[\begin{array}{c} \boldsymbol{\lambda}_{\vartheta} \\ \lambda_{\Theta} \end{array}\right] = \boldsymbol{R}^T_{\vartheta}\boldsymbol{f}_{\vartheta}, \tag{B.43}$$

where $\boldsymbol{\lambda}_{\vartheta}$ relates to the periodic boundary conditions and λ_{Θ} to the energy consistency condition.

respectively yields

$$\begin{aligned}
\boldsymbol{K}_{u_i u_i}\delta\mathbf{u}_i + \boldsymbol{K}_{u_i u_c}\delta\mathbf{u}_c + \boldsymbol{K}_{u_i\varphi_b}\delta\boldsymbol{\varphi}_b &= 0\,, && \text{(B.47)}\\
\boldsymbol{K}_{\varphi_b u_i}\delta\mathbf{u}_i + \boldsymbol{K}_{\varphi_b u_c}\delta\mathbf{u}_c + \boldsymbol{K}_{\varphi_b\varphi_b}\delta\boldsymbol{\varphi}_b &= \boldsymbol{C}^T_{\varphi_b}\delta\boldsymbol{\lambda}_{\varphi_b}\,, && \text{(B.48)}\\
\boldsymbol{K}_{u_c u_i}\delta\mathbf{u}_i + \boldsymbol{K}_{u_c u_c}\delta\mathbf{u}_c + \boldsymbol{K}_{u_c\varphi_b}\delta\boldsymbol{\varphi}_b &= \delta\boldsymbol{\lambda}_{u_c} + \boldsymbol{C}^T_{\varphi_c}\delta\boldsymbol{\lambda}_{\varphi_b}\,. && \text{(B.49)}
\end{aligned}$$

As Eq. (B.47) implies

$$\delta\mathbf{u}_i = -\boldsymbol{K}^{-1}_{u_i u_i}\boldsymbol{K}_{u_i u_c}\delta\mathbf{u}_c - \boldsymbol{K}^{-1}_{u_i u_i}\boldsymbol{K}_{u_i\varphi_b}\delta\boldsymbol{\varphi}_b\,, \tag{B.50}$$

the two remaining equations (B.48-B.49) are rewritten as

$$\begin{aligned}
&\left(\boldsymbol{K}_{\varphi_b u_c} - \boldsymbol{K}_{\varphi_b u_i}\boldsymbol{K}^{-1}_{u_i u_i}\boldsymbol{K}_{u_i u_c}\right)\delta\mathbf{u}_c +\\
&\left(\boldsymbol{K}_{\varphi_b\varphi_b} - \boldsymbol{K}_{\varphi_b u_i}\boldsymbol{K}^{-1}_{u_i u_i}\boldsymbol{K}_{u_i\varphi_b}\right)\delta\boldsymbol{\varphi}_b = \boldsymbol{C}^T_{\varphi_b}\delta\boldsymbol{\lambda}_{\varphi_b}\,, && \text{(B.51)}\\
&\left(\boldsymbol{K}_{u_c u_c} - \boldsymbol{K}_{u_c u_i}\boldsymbol{K}^{-1}_{u_i u_i}\boldsymbol{K}_{u_i u_c}\right)\delta\mathbf{u}_c +\\
&\left(\boldsymbol{K}_{u_c\varphi_b} - \boldsymbol{K}_{u_c u_i}\boldsymbol{K}^{-1}_{u_i u_i}\boldsymbol{K}_{u_i\varphi_b}\right)\delta\boldsymbol{\varphi}_b = \delta\boldsymbol{\lambda}_{u_c} + \boldsymbol{C}^T_{\varphi_c}\delta\boldsymbol{\lambda}_{\varphi_b}\,. && \text{(B.52)}
\end{aligned}$$

This system can be written in the matrix form

$$\tilde{\boldsymbol{K}}\begin{bmatrix}\delta\mathbf{u}_c\\ \delta\boldsymbol{\varphi}_b\end{bmatrix} = \begin{bmatrix}\tilde{\boldsymbol{K}}_{u_c u_c} & \tilde{\boldsymbol{K}}_{u_c\varphi_b}\\ \tilde{\boldsymbol{K}}_{\varphi_b u_c} & \tilde{\boldsymbol{K}}_{\varphi_b\varphi_b}\end{bmatrix}\begin{bmatrix}\delta\mathbf{u}_c\\ \delta\boldsymbol{\varphi}_b\end{bmatrix} = \begin{bmatrix}\boldsymbol{I}_{N_{u_c}\times N_{u_c}} & \boldsymbol{C}^T_{\varphi_c}\\ \mathbf{0}_{N_{\varphi_b}\times N_{u_c}} & \boldsymbol{C}^T_{\varphi_b}\end{bmatrix}\begin{bmatrix}\delta\boldsymbol{\lambda}_{u_c}\\ \delta\boldsymbol{\lambda}_{\varphi_b}\end{bmatrix}, \tag{B.53}$$

and can be simplified by reducing its second equation, yielding

$$\begin{aligned}
\delta\boldsymbol{\varphi}_b &= \tilde{\boldsymbol{K}}^{-1}_{\varphi_b\varphi_b}\boldsymbol{C}^T_{\varphi_b}\delta\boldsymbol{\lambda}_{\varphi_b} - \tilde{\boldsymbol{K}}^{-1}_{\varphi_b\varphi_b}\tilde{\boldsymbol{K}}_{\varphi_b u_c}\delta\mathbf{u}_c\,, && \text{(B.54)}\\
\delta\boldsymbol{\lambda}_{u_c} &= \tilde{\tilde{\boldsymbol{K}}}_{u_c u_c}\delta\mathbf{u}_c - \left[\boldsymbol{C}^T_{\varphi_c} - \tilde{\boldsymbol{K}}_{u_c\varphi_b}\tilde{\boldsymbol{K}}^{-1}_{\varphi_b\varphi_b}\boldsymbol{C}^T_{\varphi_b}\right]\delta\boldsymbol{\lambda}_{\varphi_b} && \text{(B.55)}
\end{aligned}$$

with

$$\tilde{\tilde{\boldsymbol{K}}}_{u_c u_c} = \tilde{\boldsymbol{K}}_{u_c u_c} - \tilde{\boldsymbol{K}}_{u_c\varphi_b}\tilde{\boldsymbol{K}}^{-1}_{\varphi_b\varphi_b}\tilde{\boldsymbol{K}}_{\varphi_b u_c}\,. \tag{B.56}$$

In order to extract the dependency on the kinematics constraints $\boldsymbol{K}_{\mathrm{M}}$, Eqs. (B.26-B.27) are linearized as

$$\begin{aligned}
\delta\mathbf{u}_c = \boldsymbol{S}_{u_c}\delta\boldsymbol{F}_{\mathrm{M}} &= \boldsymbol{S}_{\varphi_c}\delta\boldsymbol{K}_{\mathrm{M}}\,, && \text{(B.57)}\\
\boldsymbol{C}_{\varphi_c}\delta\mathbf{u}_c + \boldsymbol{C}_{\varphi_b}\delta\boldsymbol{\varphi}_b &= \boldsymbol{S}_{\varphi_b}\delta\boldsymbol{K}_{\mathrm{M}}\,. && \text{(B.58)}
\end{aligned}$$

Using Eq. (B.54), this last result is rewritten as

$$\left(\boldsymbol{C}_{\varphi_c} - \boldsymbol{C}_{\varphi_b}\tilde{\boldsymbol{K}}^{-1}_{\varphi_b\varphi_b}\tilde{\boldsymbol{K}}_{\varphi_b u_c}\right)\delta\mathbf{u}_c + \boldsymbol{C}_{\varphi_b}\tilde{\boldsymbol{K}}^{-1}_{\varphi_b\varphi_b}\boldsymbol{C}^T_{\varphi_b}\delta\boldsymbol{\lambda}_{\varphi_b} = \boldsymbol{S}_{\varphi_b}\delta\boldsymbol{K}_{\mathrm{M}}\,, \tag{B.59}$$

which becomes with the help of Eq. (B.57)

$$\boldsymbol{C}_{\varphi_b}\tilde{\boldsymbol{K}}^{-1}_{\varphi_b\varphi_b}\boldsymbol{C}^T_{\varphi_b}\delta\boldsymbol{\lambda}_{\varphi_b} = \boldsymbol{S}_{\varphi_b}\delta\boldsymbol{K}_{\mathrm{M}} - \left(\boldsymbol{C}_{\varphi_c} - \boldsymbol{C}_{\varphi_b}\tilde{\boldsymbol{K}}^{-1}_{\varphi_b\varphi_b}\tilde{\boldsymbol{K}}_{\varphi_b u_c}\right)\boldsymbol{S}_{\varphi_c}\delta\boldsymbol{K}_{\mathrm{M}}\,, \tag{B.60}$$

or again, defining

$$\tilde{\tilde{\boldsymbol{S}}}_{\varphi_b\varphi_b} = -\boldsymbol{C}_{\varphi_b}\tilde{\boldsymbol{K}}^{-1}_{\varphi_b\varphi_b}\boldsymbol{C}^T_{\varphi_b}\,, \text{ and} \tag{B.61}$$

$$\tilde{\tilde{\boldsymbol{S}}}_{\varphi_b\varphi_c} = \boldsymbol{S}_{\varphi_b} - \left(\boldsymbol{C}_{\varphi_c} - \boldsymbol{C}_{\varphi_b}\tilde{\boldsymbol{K}}^{-1}_{\varphi_b\varphi_b}\tilde{\boldsymbol{K}}_{\varphi_b u_c}\right)\boldsymbol{S}_{\varphi_c}\,, \tag{B.62}$$

which becomes

$$\delta\boldsymbol{\lambda}_{\varphi_b} = -\tilde{\tilde{\boldsymbol{S}}}^{-1}_{\varphi_b\varphi_b}\tilde{\tilde{\boldsymbol{S}}}_{\varphi_b\varphi_c}\delta\boldsymbol{K}_{\mathrm{M}}\,. \tag{B.63}$$

Finally using this last result and Eq. (B.57) in Eq. (B.55) leads to

$$\delta\boldsymbol{\lambda}_{u_c} = \left[\tilde{\tilde{\boldsymbol{K}}}_{u_c u_c}\boldsymbol{S}_{\varphi_c} + \left[\boldsymbol{C}^T_{\varphi_c} - \tilde{\boldsymbol{K}}_{u_c\varphi_b}\tilde{\boldsymbol{K}}^{-1}_{\varphi_b\varphi_b}\boldsymbol{C}^T_{\varphi_b}\right]\tilde{\tilde{\boldsymbol{S}}}^{-1}_{\varphi_b\varphi_b}\tilde{\tilde{\boldsymbol{S}}}_{\varphi_b\varphi_c}\right]\delta\boldsymbol{K}_{\mathrm{M}}\,. \tag{B.64}$$

The variation of the homogenised stress (B.38) yields the apparent elasticity tensor $\boldsymbol{C}_{\mathrm{M}} = \frac{\partial\boldsymbol{\Sigma}_{\mathrm{M}}}{\partial\boldsymbol{F}_{\mathrm{M}}}$ in the matrix form following

$$\begin{aligned}\boldsymbol{C}_{\mathrm{M}} &= \frac{1}{V(\omega)}\left[\begin{array}{ccc}\boldsymbol{I}_{9\times9} & \boldsymbol{0}_{9\times3} & \boldsymbol{0}_{9\times1}\end{array}\right]\left\{\boldsymbol{S}^T_{\varphi_c}\frac{\partial\boldsymbol{\lambda}_{u_c}}{\partial\boldsymbol{K}_{\mathrm{M}}} + \boldsymbol{S}^T_{\varphi_b}\frac{\partial\boldsymbol{\lambda}_{\varphi_b}}{\partial\boldsymbol{K}_{\mathrm{M}}}\right\}\left[\begin{array}{c}\boldsymbol{I}_{9\times9}\\ \boldsymbol{0}_{3\times9}\\ \boldsymbol{0}_{1\times9}\end{array}\right]\,,\\ &= \frac{1}{V(\omega)}\left[\begin{array}{ccc}\boldsymbol{I}_{9\times9} & \boldsymbol{0}_{9\times3} & \boldsymbol{0}_{9\times1}\end{array}\right]\left\{\tilde{\tilde{\boldsymbol{S}}}_{\varphi_c\varphi_c} - \tilde{\tilde{\boldsymbol{S}}}_{\varphi_c\varphi_b}\tilde{\tilde{\boldsymbol{S}}}^{-1}_{\varphi_b\varphi_b}\tilde{\tilde{\boldsymbol{S}}}_{\varphi_b\varphi_c}\right\}\left[\begin{array}{c}\boldsymbol{I}_{9\times9}\\ \boldsymbol{0}_{3\times9}\\ \boldsymbol{0}_{1\times9}\end{array}\right]\,,\end{aligned} \tag{B.65}$$

with

$$\tilde{\tilde{\boldsymbol{S}}}_{\varphi_c\varphi_c} = \boldsymbol{S}^T_{\varphi_c}\tilde{\tilde{\boldsymbol{K}}}_{u_c u_c}\boldsymbol{S}_{\varphi_c}\,, \text{ and} \tag{B.66}$$

$$\tilde{\tilde{\boldsymbol{S}}}_{\varphi_c\varphi_b} = \boldsymbol{S}^T_{\varphi_b} - \boldsymbol{S}^T_{\varphi_c}\left[\boldsymbol{C}^T_{\varphi_c} - \tilde{\boldsymbol{K}}_{u_c\varphi_b}\tilde{\boldsymbol{K}}^{-1}_{\varphi_b\varphi_b}\boldsymbol{C}^T_{\varphi_b}\right]\,. \tag{B.67}$$

The homogenised conductivity tensor $\boldsymbol{\kappa}_{\mathrm{M}} = -\frac{\partial\boldsymbol{q}_{\mathrm{M}}}{\partial\boldsymbol{\nabla}_M\vartheta_{\mathrm{M}}}$ is directly obtained from Eq. (B.46) as

$$\boldsymbol{\kappa}_{\mathrm{M}} = -\frac{1}{V(\omega)}\left[\begin{array}{ccc}\boldsymbol{0}_{3\times9} & \boldsymbol{I}_{3\times3} & \boldsymbol{0}_{3\times1}\end{array}\right]\left\{\tilde{\tilde{\boldsymbol{S}}}_{\varphi_c\varphi_c} - \tilde{\tilde{\boldsymbol{S}}}_{\varphi_c\varphi_b}\tilde{\tilde{\boldsymbol{S}}}^{-1}_{\varphi_b\varphi_b}\tilde{\tilde{\boldsymbol{S}}}_{\varphi_b\varphi_c}\right\}\left[\begin{array}{c}\boldsymbol{0}_{9\times3}\\ \boldsymbol{I}_{3\times3}\\ \boldsymbol{0}_{1\times3}\end{array}\right]\,. \tag{B.68}$$

Finally, the apparent thermal expansion tensor $\boldsymbol{\alpha}_{\mathrm{M}}$ can be extracted in the vector form using $-\boldsymbol{C}_{\mathrm{M}}\boldsymbol{A}_{\mathrm{M}} = \frac{\partial\boldsymbol{\Sigma}_{\mathrm{M}}}{\partial\vartheta_{\mathrm{M}}}$. Using the variation of the homogenised stress (B.38) yields

$$-\boldsymbol{C}_{\mathrm{M}}\boldsymbol{A}_{\mathrm{M}} = \frac{1}{V(\omega)}\left[\begin{array}{ccc}\boldsymbol{I}_{9\times9} & \boldsymbol{0}_{9\times3} & \boldsymbol{0}_{9\times1}\end{array}\right]\left\{\tilde{\tilde{\boldsymbol{S}}}_{\varphi_c\varphi_c} - \tilde{\tilde{\boldsymbol{S}}}_{\varphi_c\varphi_b}\tilde{\tilde{\boldsymbol{S}}}^{-1}_{\varphi_b\varphi_b}\tilde{\tilde{\boldsymbol{S}}}_{\varphi_b\varphi_c}\right\}\left[\begin{array}{c}\boldsymbol{0}_{9\times1}\\ \boldsymbol{0}_{3\times1}\\ \boldsymbol{I}_{1\times1}\end{array}\right]\,. \tag{B.69}$$

Appendix C

Insight in the Continuous/Discontinuous Kirchhoff-Love plate formulation

C.1 Finite element matrices

The elementary matrices of the weak formulation (2.96-2.97) can be obtained using the discretization (2.98). For ease of reading, we report the weak form here below:

$$\sum_e \int_{\mathcal{A}^e} \bar{\rho} \ddot{\boldsymbol{u}}_\alpha \delta \boldsymbol{u}_\alpha d\mathcal{A}^e \quad + \quad \sum_e \int_{\mathcal{A}^e} \tilde{\boldsymbol{n}}^{*\,\alpha\beta} \delta \boldsymbol{u}_{\beta,\alpha} d\mathcal{A}^e \quad = \quad 0\,, \tag{C.1}$$

$$\begin{gathered}\sum_e \int_{\mathcal{A}^e} \bar{\rho} \ddot{\boldsymbol{u}}_z \delta \boldsymbol{u}_z d\mathcal{A}^e + \sum_e \int_{\mathcal{A}^e} I_p \ddot{\boldsymbol{u}}_{z,\alpha} \delta \boldsymbol{u}_{z,\alpha} d\mathcal{A}^e + \sum_e \int_{\mathcal{A}^e} \left(-\tilde{\boldsymbol{m}}^{*\,\alpha\beta} \delta \boldsymbol{u}_{z,\alpha\beta}\right) d\mathcal{A}^e + \\ \sum_s \int_{(\partial_I \mathcal{A})^s} \left\langle \tilde{\boldsymbol{m}}^{*\,\alpha\beta} \right\rangle [\![-\delta \boldsymbol{u}_{z,\beta} \boldsymbol{\nu}_\alpha]\!] \, d\partial\mathcal{A}^e + \\ \sum_s \int_{(\partial_I \mathcal{A})^s} \left\langle \mathbb{C}_3^{*\,\alpha\beta\gamma\delta} \delta \boldsymbol{\varepsilon}^*_{\gamma\delta} + \mathbb{C}_4^{*\,\alpha\beta\gamma\delta} \delta \boldsymbol{\kappa}^*_{\gamma\delta} \right\rangle [\![-\boldsymbol{u}_{z,\beta} \boldsymbol{\nu}_\alpha]\!] \, d\partial\mathcal{A}^e + \\ \sum_s \int_{(\partial_I \mathcal{A})^s} [\![-\delta \boldsymbol{u}_{z,\beta} \boldsymbol{\nu}_\alpha]\!] \left\langle \frac{\beta_s}{h_s} \mathbb{C}_4^{*\,\alpha\beta\gamma\delta} \right\rangle [\![-\boldsymbol{u}_{z,\gamma} \boldsymbol{\nu}_\delta]\!] \, d\partial\mathcal{A}^e = 0\,. \end{gathered} \tag{C.2}$$

The finite element discretization (2.98) is rewritten as

$$\mathbf{u} = N_u^a \boldsymbol{u}^a\,, \tag{C.3}$$

where the nodal shape functions N^a_u at node a are continuous across the element interfaces $(\partial_I\mathcal{A})^s$.

C.1.1 Mass matrix

Considering the elements $\mathcal{A}^e$, the mass matrix at nodes a and b reads

$$\boldsymbol{M}^{ab}_{\alpha\beta} = \sum_e \int_{\mathcal{A}^e} \bar{\rho} N^a_u N^b_u d\mathcal{A}^e \delta_{\alpha\beta}\,, \tag{C.4}$$

$$\boldsymbol{M}^{ab}_{zz} = \sum_e \int_{\mathcal{A}^e} \left(\bar{\rho} N^a_u N^b_u + I_p N^a_{u,\alpha} N^b_{u,\alpha}\right) d\mathcal{A}^e\,. \tag{C.5}$$

C.1.2 Bulk stiffness matrix

Considering the plate elements $\mathcal{A}^e$, their contribution to stiffness matrix at nodes a and b reads

$$\boldsymbol{K}^{ab}_{\mathrm{bulk}\alpha\beta} = \sum_e \int_{\mathcal{A}^e} N^a_{u,\gamma} \mathbb{C}^{*\,\alpha\gamma\beta\delta}_1 N^b_{u,\delta} d\mathcal{A}^e\,, \tag{C.6}$$

$$\boldsymbol{K}^{ab}_{\mathrm{bulk}\alpha z} = \sum_e \int_{\mathcal{A}^e} N^a_{u,\beta} \mathbb{C}^{*\,\alpha\gamma\beta\delta}_2 N^b_{u,\gamma\delta} d\mathcal{A}^e\,, \tag{C.7}$$

$$\boldsymbol{K}^{ab}_{\mathrm{bulk}z\beta} = \sum_e \int_{\mathcal{A}^e} N^a_{u,\alpha\gamma} \mathbb{C}^{*\,\alpha\gamma\beta\delta}_3 N^b_{u,\delta} d\mathcal{A}^e\,, \tag{C.8}$$

$$\boldsymbol{K}^{ab}_{\mathrm{bulk}zz} = \sum_e \int_{\mathcal{A}^e} N^a_{u,\alpha\gamma} \mathbb{C}^{*\,\alpha\gamma\beta\delta}_4 N^b_{u,\beta\delta} d\mathcal{A}^e\,. \tag{C.9}$$

C.1.3 Interface stiffness matrix

Considering the interface elements $(\partial_I\mathcal{A})^s$, their contribution to the stiffness matrix at nodes a and b reads

$$\boldsymbol{K}^{ab}_{\mathrm{interface}\alpha\beta} \quad = \quad 0\,, \tag{C.10}$$

$$\begin{aligned}\boldsymbol{K}^{ab}_{\mathrm{interface}\gamma z} \quad = \quad & -\frac{1}{2}\sum_s \int_{(\partial_I\mathcal{A})^s} \mathbb{C}^{*-\,\alpha\beta\gamma\delta}_3 \left(-N^{b\,-}_{u,\beta}\right)\left(N^{a-}_{u,\delta}\right) \boldsymbol{\nu}^-_\alpha d\partial\mathcal{A}^e + \\ & \frac{1}{2}\sum_s \int_{(\partial_I\mathcal{A})^s} \mathbb{C}^{*-\,\alpha\beta\gamma\delta}_3 \left(-N^{b+}_{u,\beta}\right)\left(N^{a-}_{u,\delta}\right) \boldsymbol{\nu}^-_\alpha d\partial\mathcal{A}^e - \\ & \frac{1}{2}\sum_s \int_{(\partial_I\mathcal{A})^s} \mathbb{C}^{*+\,\alpha\beta\gamma\delta}_3 \left(-N^{b-}_{u,\beta}\right)\left(N^{a+}_{u,\delta}\right) \boldsymbol{\nu}^-_\alpha d\partial\mathcal{A}^e + \\ & \frac{1}{2}\sum_s \int_{(\partial_I\mathcal{A})^s} \mathbb{C}^{*+\,\alpha\beta\gamma\delta}_3 \left(-N^{b+}_{u,\beta}\right)\left(N^{a+}_{u,\delta}\right) \boldsymbol{\nu}^-_\alpha d\partial\mathcal{A}^e\,,\end{aligned} \tag{C.11}$$

$$
\begin{aligned}
\boldsymbol{K}^{ab}_{\text{interface}\,z\gamma} \quad = \quad & -\frac{1}{2}\sum_s \int_{(\partial_I \mathcal{A})^s} \mathbb{C}_3^{*-\,\alpha\beta\gamma\delta} \left(-N^{a\,-}_{u,\beta}\right)\left(N^{b-}_{u,\delta}\right) \boldsymbol{\nu}^-_\alpha \, d\partial\mathcal{A}^e \, - \\
& \frac{1}{2}\sum_s \int_{(\partial_I \mathcal{A})^s} \mathbb{C}_3^{*+\,\alpha\beta\gamma\delta} \left(-N^{a-}_{u,\beta}\right)\left(N^{b+}_{u,\delta}\right) \boldsymbol{\nu}^-_\alpha \, d\partial\mathcal{A}^e \, + \\
& \frac{1}{2}\sum_s \int_{(\partial_I \mathcal{A})^s} \mathbb{C}_3^{*-\,\alpha\beta\gamma\delta} \left(-N^{a+}_{u,\beta}\right)\left(N^{b-}_{u,\delta}\right) \boldsymbol{\nu}^-_\alpha \, d\partial\mathcal{A}^e \, + \\
& \frac{1}{2}\sum_s \int_{(\partial_I \mathcal{A})^s} \mathbb{C}_3^{*+\,\alpha\beta\gamma\delta} \left(-N^{a+}_{u,\beta}\right)\left(N^{b+}_{u,\delta}\right) \boldsymbol{\nu}^-_\alpha \, d\partial\mathcal{A}^e \, , \qquad \text{(C.12)}
\end{aligned}
$$

$$
\begin{aligned}
\boldsymbol{K}^{ab}_{\text{interface}\,zz} \quad = \quad & -\frac{1}{2}\sum_s \int_{(\partial_I \mathcal{A})^s} \mathbb{C}_4^{*-\,\alpha\beta\gamma\delta} \left(-N^{a\,-}_{u,\beta}\right)\left(-N^{b-}_{u,\gamma\delta}\right) \boldsymbol{\nu}^-_\alpha \, d\partial\mathcal{A}^e \, - \\
& \frac{1}{2}\sum_s \int_{(\partial_I \mathcal{A})^s} \mathbb{C}_4^{*+\,\alpha\beta\gamma\delta} \left(-N^{a-}_{u,\beta}\right)\left(-N^{b+}_{u,\gamma\delta}\right) \boldsymbol{\nu}^-_\alpha \, d\partial\mathcal{A}^e \, + \\
& \frac{1}{2}\sum_s \int_{(\partial_I \mathcal{A})^s} \mathbb{C}_4^{*-\,\alpha\beta\gamma\delta} \left(-N^{a+}_{u,\beta}\right)\left(-N^{b-}_{u,\gamma\delta}\right) \boldsymbol{\nu}^-_\alpha \, d\partial\mathcal{A}^e \, + \\
& \frac{1}{2}\sum_s \int_{(\partial_I \mathcal{A})^s} \mathbb{C}_4^{*+\,\alpha\beta\gamma\delta} \left(-N^{a+}_{u,\beta}\right)\left(-N^{b+}_{u,\gamma\delta}\right) \boldsymbol{\nu}^-_\alpha \, d\partial\mathcal{A}^e \, - \\
& \frac{1}{2}\sum_s \int_{(\partial_I \mathcal{A})^s} \mathbb{C}_4^{*-\,\alpha\beta\gamma\delta} \left(-N^{b\,-}_{u,\beta}\right)\left(-N^{a-}_{u,\gamma\delta}\right) \boldsymbol{\nu}^-_\alpha \, d\partial\mathcal{A}^e \, + \\
& \frac{1}{2}\sum_s \int_{(\partial_I \mathcal{A})^s} \mathbb{C}_4^{*-\,\alpha\beta\gamma\delta} \left(-N^{b+}_{u,\beta}\right)\left(-N^{a-}_{u,\gamma\delta}\right) \boldsymbol{\nu}^-_\alpha \, d\partial\mathcal{A}^e \, - \\
& \frac{1}{2}\sum_s \int_{(\partial_I \mathcal{A})^s} \mathbb{C}_4^{*+\,\alpha\beta\gamma\delta} \left(-N^{b-}_{u,\beta}\right)\left(-N^{a+}_{u,\gamma\delta}\right) \boldsymbol{\nu}^-_\alpha \, d\partial\mathcal{A}^e \, + \\
& \frac{1}{2}\sum_s \int_{(\partial_I \mathcal{A})^s} \mathbb{C}_4^{*+\,\alpha\beta\gamma\delta} \left(-N^{b+}_{u,\beta}\right)\left(-N^{a+}_{u,\gamma\delta}\right) \boldsymbol{\nu}^-_\alpha \, d\partial\mathcal{A}^e \, + \\
& \sum_s \int_{(\partial_I \mathcal{A})^s} \frac{\beta_s}{h_s} \left\langle \mathbb{C}_4^{*\,\alpha\beta\gamma\delta} \right\rangle \left(-N^{a\,-}_{u,\beta}\right)\left(-N^{b-}_{u,\delta}\right) \boldsymbol{\nu}^-_\gamma \boldsymbol{\nu}^-_\alpha \, d\partial\mathcal{A}^e \, - \\
& \sum_s \int_{(\partial_I \mathcal{A})^s} \frac{\beta_s}{h_s} \left\langle \mathbb{C}_4^{*\,\alpha\beta\gamma\delta} \right\rangle \left(-N^{a\,-}_{u,\beta}\right)\left(-N^{b+}_{u,\delta}\right) \boldsymbol{\nu}^-_\gamma \boldsymbol{\nu}^-_\alpha \, d\partial\mathcal{A}^e \, - \\
& \sum_s \int_{(\partial_I \mathcal{A})^s} \frac{\beta_s}{h_s} \left\langle \mathbb{C}_4^{*\,\alpha\beta\gamma\delta} \right\rangle \left(-N^{a\,+}_{u,\beta}\right)\left(-N^{b-}_{u,\delta}\right) \boldsymbol{\nu}^-_\gamma \boldsymbol{\nu}^-_\alpha \, d\partial\mathcal{A}^e \, + \\
& \sum_s \int_{(\partial_I \mathcal{A})^s} \frac{\beta_s}{h_s} \left\langle \mathbb{C}_4^{*\,\alpha\beta\gamma\delta} \right\rangle \left(-N^{a\,+}_{u,\beta}\right)\left(-N^{b+}_{u,\delta}\right) \boldsymbol{\nu}^-_\gamma \boldsymbol{\nu}^-_\alpha \, d\partial\mathcal{A}^e \, .
\end{aligned}
$$

(C.13)

C.1.4 Finite element system

Assembling the different contributions (C.4-C.13), eventually leads to the system (2.99), which is also reported here below

$$\boldsymbol{M}\ddot{\mathbf{u}} + \boldsymbol{K}\mathbf{u} = 0\,. \tag{C.14}$$

Appendix D

Poisson-Voronoï tessellation and SVEs extraction

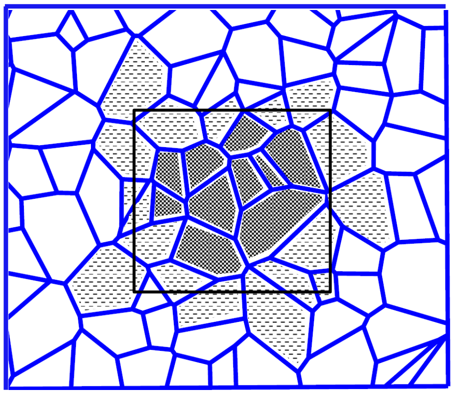

Figure D.1: Extraction of an SVE from a Poisson-Voronoï tessellation: the checked grains correspond to polygons not intersecting the SVE boundary and the dashed grains correspond to polygons intersecting the SVE boundary.

In this section we explain how to build the Poisson-Voronoï tessellation and how to construct the SVEs required for the moving window technique, see Chapter 5. A 2D Poisson-Voronoï tessellation can be generated using the “scipy.spatial” python library called “Voronoi” from random seeds which follow a uniform distribution. The resulting large Voronoï tessellation is described by the information of vertexes and lines of each polygon. One rectangular parallelepiped SVE can then be extracted from the large 2D Voronoï tessellation, see Fig. D.1, by going through the following steps:

- Looping on all the polygons of the large Voronoï tessellation, the polygons can be categorized into three groups: the polygons with all their vertexes inside the SVE –checked polygons in Fig. D.1, the polygons with a part of their vertexes inside the SVE –dashed polygons in Fig. D.1, and the polygons with none of their vertexes inside the SVE;

- For the first group of polygons, all the information (vertexes and lines) is kept for the SVE construction, while for the third group of polygons, all the information is discarded;

- For the polygons of the second group, their vertexes outside of the SVE are replaced by the intersection points of their lines with the boundaries of the SVE, their intersected lines are shortened, the lines outside of the SVE are discarded, and their lines are completed by the boundary parts of the SVE;

- A new set of polygons, with their associated vertexes and lines, is then defining the SVE; a 2D mesh conforming with these new polygons can then be generated using GMSH [23], and an extrusion follows to obtain a 3D columnar SVE meshed with quadratic tetraedra, see Fig. 5.7;

- Finally each extruded polygon is associated to a domain having its own anisotropic material law defined by its orientation angles, allowing the definition of grains with different orientations within the SVE.

Bibliography

[1] J. Aboudi. Micromechanical analysis of composites by the method of cells-update. *Applied Mechanics Reviews*, 49(10S):S83–S91, 1996.

[2] M. Ainsworth. Essential boundary conditions and multi-point constraints in finite element analysis. *Computer Methods in Applied Mechanics and Engineering*, 190(48):6323 – 6339, 2001.

[3] M. Arnst. Stochastic modelling in mechanics, 2013. Lecture notes.

[4] M. Asheghi, Y. K. Leung, S. S. Wong, and K. E. Goodson. Phonon-boundary scattering in thin silicon layers. *Applied Physics Letters*, 71(13):1798–1800, 1997.

[5] S. Baxter and L. Graham. Characterization of random composites using moving-window technique. *Journal of Engineering Mechanics*, 126(4):389–397, 2000.

[6] G. Becker, C. Geuzaine, and L. Noels. A one field full discontinuous galerkin method for kirchhofflove shells applied to fracture mechanics. *Computer Methods in Applied Mechanics and Engineering*, 200(45-46):3223 – 3241, 2011.

[7] A. Bensoussan, J.-L. Lions, and G. Papanicolaou. *Asymptotic analysis for periodic structures*, volume 374. American Mathematical Soc., 2011.

[8] H. Cho, D. Venturi, and G. Karniadakis. Karhunenlove expansion for multi-correlated stochastic processes. *Probabilistic Engineering Mechanics*, 34(0):157 – 167, 2013.

[9] A. Clément, C. Soize, and J. Yvonnet. Computational nonlinear stochastic homogenization using a nonconcurrent multiscale approach for hyperelastic heterogeneous microstructures analysis. *International Journal for Numerical Methods in Engineering*, 91(8):799–824, 2012.

[10] E. Coenen, V. Kouznetsova, and M. Geers. Computational homogenization for heterogeneous thin sheets. *International Journal for Numerical Methods in Engineering*, 83(8-9):1180–1205, 2010.

[11] Y. Cong, S. Nezamabadi, H. Zahrouni, and J. Yvonnet. Multiscale computational homogenization of heterogeneous shells at small strains with extensions to finite displacements and buckling. *International Journal for Numerical Methods in Engineering*, 104(4):235–259, 2015.

[12] S. Das and R. Ghanem. A bounded random matrix approach for stochastic upscaling. *Multiscale Modeling & Simulation*, 8(1):296–325, 2009.

[13] G. Deodatis and R. C. Micaletti. Simulation of highly skewed non-gaussian stochastic processes. *Journal of Engineering Mechanics*, 127(12):1284–1295, 2001.

[14] A. Der Kiureghian and J. Ke. The stochastic finite element method in structural reliability. *Probabilistic Engineering Mechanics*, 3(2):83 – 91, 1988.

[15] S. Devanarayanan, R. S. Krishnan, and R. Srinivasan. Thermal expansion of crystals. In *International Series in the Science of the Solid State*, volume 12 of *International Series in the Science of the Solid State*, pages ii –. Pergamon, 1979.

[16] A. Duwel, J. Gorman, M. Weinstein, J. Borenstein, and P. Ward. Experimental study of thermoelastic damping in MEMS gyros. *Sensors and Actuators A: Physical*, 103(12):70 – 75, 2003. Micromechanics section of Sensors and Actuators, based on contributions revised from the Technical Digest of the 15th IEEE International conference on Micro Electro mechanical Systems (MEMS 2002).

[17] G. J. Dvorak and Y. Benveniste. On transformation strains and uniform fields in multiphase elastic media. In *Proceedings of the Royal Society of London A: Mathematical, Physical and Engineering Sciences*, volume 437, pages 291–310. The Royal Society, 1992.

[18] J. D. Eshelby. The determination of the elastic field of an ellipsoidal inclusion, and related problems. *Proceedings of the Royal Society of London. Series A. Mathematical and Physical Sciences*, 241(1226):376–396, 1957.

[19] F. Feyel. Multiscale fe 2 elastoviscoplastic analysis of composite structures. *Computational Materials Science*, 16(1):344–354, 1999.

[20] J. Fish and W. Wu. A nonintrusive stochastic multiscale solver. *International Journal for Numerical Methods in Engineering*, 88(9):862–879, 2011.

[21] M. Geers, V. Kouznetsova, and W. Brekelmans. Multi-scale computational homogenization: Trends and challenges. *Journal of Computational and Applied Mathematics*, 234(7):2175 – 2182, 2010.

[22] M. G. Geers, V. G. Kouznetsova, and W. Brekelmans. Multi-scale computational homogenization: Trends and challenges. *Journal of Computational and Applied Mathematics*, 234(7):2175–2182, 2010.

[23] C. Geuzaine and J.-F. Remacle. Gmsh: A 3-d finite element mesh generator with built-in pre- and post-processing facilities. *International Journal for Numerical Methods in Engineering*, 79(11):1309–1331, 2009.

[24] R. Ghanem and P. Spanos. *Stochastic Finite Elements: A Spectral Approach*. Springer Verlag, 1991.

[25] M. Grigoriu. On the spectral representation method in simulation. *Probabilistic Engineering Mechanics*, 8(2):75–90, 1993.

[26] J. Guilleminot, A. Noshadravan, C. Soize, and R. Ghanem. A probabilistic model for bounded elasticity tensor random fields with application to polycrystalline microstructures. *Computer Methods in Applied Mechanics and Engineering*, 200(17 - 20):1637 – 1648, 2011.

[27] V. Gusella and F. Cluni. Random field and homogenization for masonry with nonperiodic microstructure. *Journal of Mechanics of Materials and Structures*, 1(2):357–386, 2006.

[28] T. Harada and M. Shinozuka. The scale of correlation for stochastic fields–technical report. *Department of Civil Engineering and Engineering Mechanics, Columbia University, New York, NY*, 1986.

[29] S. Hazanov and C. Huet. Order relationships for boundary conditions effect in heterogeneous bodies smaller than the representative volume. *Journal of the Mechanics and Physics of Solids*, 42(12):1995 – 2011, 1994.

[30] R. Hill. Elastic properties of reinforced solids: Some theoretical principles. *Journal of the Mechanics and Physics of Solids*, 11(5):357 – 372, 1963.

[31] R. Hill. A self-consistent mechanics of composite materials. *Journal of the Mechanics and Physics of Solids*, 13(4):213–222, 1965.

[32] T. Hoang, M. Guerich, and J. Yvonnet. Determining the size of RVE for nonlinear random composites in an incremental computational homogenization framework. *Journal of Engineering Mechanics*, page Accepted, 2015.

[33] M. Hopcroft, W. Nix, and T. Kenny. What is the young's modulus of silicon? *Microelectromechanical Systems, Journal of*, 19(2):229–238, April 2010.

[34] B. Houston, D. Photiadis, J. Vignola, M. Marcus, X. Liu, D. Czaplewski, L. Sekaric, J. Butler, P. Pehrsson, and J. Bucaro. Loss due to transverse thermoelastic currents in microscale resonators. *Materials Science and Engineering: A*, 370(12):407 – 411, 2004. 13th International Conference on Internal Friction and Ultrasonic Attenuation in Solids.

[35] C. Huet. Application of variational concepts to size effects in elastic heterogeneous bodies. *Journal of the Mechanics and Physics of Solids*, 38(6):813 – 841, 1990.

[36] E. T. Jaynes. Information theory and statistical mechanics. *Physical review*, 106(4):620, 1957.

[37] Ł. Kaczmarczyk, C. J. Pearce, and N. Bićanić. Scale transition and enforcement of rve boundary conditions in second-order computational homogenization. *International Journal for Numerical Methods in Engineering*, 74(3):506–522, 2008.

[38] A. L. Kalamkarov, I. V. Andrianov, V. V. Danishevsâ, et al. Asymptotic homogenization of composite materials and structures. *Applied Mechanics Reviews*, 62(3):030802, 2009.

[39] T. Kanit, S. Forest, I. Galliet, V. Mounoury, and D. Jeulin. Determination of the size of the representative volume element for random composites: statistical and numerical approach. *International Journal of Solids and Structures*, 40(13-14):3647–3679, 2003.

[40] P. Kanouté, D. Boso, J. Chaboche, and B. Schrefler. Multiscale methods for composites: a review. *Archives of Computational Methods in Engineering*, 16(1):31–75, 2009.

[41] J. N. Kapur and H. K. Kesavan. *Entropy optimization principles and their applications.* Springer, 1992.

[42] M. Kleiber, T. Hien, and D. Tran. The stochastic finite element method: basic perturbation technique and computer implementation. 1992.

[43] V. Kouznetsova, W. A. M. Brekelmans, and F. P. T. Baaijens. An approach to micro-macro modeling of heterogeneous materials. *Computational Mechanics*, 27(1):37–48, 2001.

[44] V. Kouznetsova, M. Geers, and W. Brekelmans. Multi-scale second-order computational homogenization of multi-phase materials: a nested finite element solution strategy. *Computer Methods in Applied Mechanics and Engineering*, 193(4851):5525 – 5550, 2004. Advances in Computational Plasticity.

[45] V. Kouznetsova, M. G. Geers, and W. M. Brekelmans. Multi-scale constitutive modelling of heterogeneous materials with a gradient-enhanced computational homogenization scheme. *International Journal for Numerical Methods in Engineering*, 54(8):1235–1260, 2002.

[46] C. Lanczos. Dan iteration method for the solution of the eigenvalue problem of linear differential and integral operators. *Journal of Research of the National Bureau of Standards*, 45(4):255, 1950.

[47] O. Lemaitre and O. Knio. *Spectral methods for uncertainty quantification - with applications to computational fluid dynamics*. Springer, 2010.

[48] S. Lepage. *Stochastic finite element method for the modeling of thermoelastic damping in micro-resonators*. Leloup, 2007.

[49] A. Liebscher, C. Proppe, C. Redenbach, and D. Schwarzer. Uncertainty quantification for metal foam structures by means of image analysis. *Probabilistic Engineering Mechanics*, 28:143 – 151, 2012. Computational Stochastic Mechanics.

[50] R. Lifshitz and M. L. Roukes. Thermoelastic damping in micro- and nanomechanical systems. *Phys. Rev. B*, 61:5600–5609, Feb 2000.

[51] J. LLorca, C. González, J. M. Molina-Aldareguía, J. Segurado, R. Seltzer, F. Sket, M. Rodríguez, S. Sádaba, R. Muñoz, and L. P. Canal. Multiscale modeling of composite materials: a roadmap towards virtual testing. *Advanced Materials*, 23(44):5130–5147, 2011.

[52] V. Lucas, J.-C. Golinval, S. Paquay, V.-D. Nguyen, L. Noels, and L. Wu. A stochastic computational multiscale approach; application to mems resonators. *Computer Methods in Applied Mechanics and Engineering*, 294:141–167, 2015.

[53] J. Ma, S. Sahraee, P. Wriggers, and L. De Lorenzis. Stochastic multiscale homogenization analysis of heterogeneous materials under finite deformations with full uncertainty in the microstructure. *Computational Mechanics*, pages 1–17, 2015.

[54] S. Mariani, R. Martini, A. Ghisi, A. Corigliano, and M. Beghi. Overall elastic properties of polysilicon films: A statistical investigation of the effects of polycrystal morphology. *International Journal for Multiscale Computational Engineering*, 9(3), 2011.

[55] S. Mariani, R. Martini, A. Ghisi, A. Corigliano, and B. Simoni. Monte carlo simulation of micro-cracking in polysilicon mems exposed to shocks. *International Journal of Fracture*, 167(1):83–101, 2011.

[56] H. G. Matthies, C. E. Brenner, C. G. Bucher, and C. Guedes Soares. Uncertainties in probabilistic numerical analysis of structures and solids-stochastic finite elements. *Structural Safety*, 19(3):283 – 336, 1997. Devoted to the work of the Joint Committee on Structural Safety.

[57] G. A. Maugin. *The Thermomechanics of Nonlinear Irreversible Behaviors*, volume 27 of *World Scientific Series on Nonlinear Science Series A*. World Scientific, 1999.

[58] A. McConnell, S. Uma, and K. E. Goodson. Thermal conductivity of doped polysilicon layers. *Microelectromechanical Systems, Journal of*, 10(3):360–369, Sep 2001.

[59] C. Miehe and A. Koch. Computational micro-to-macro transitions of discretized microstructures undergoing small strains. *Archive of Applied Mechanics*, 72(4-5):300–317, 2002.

[60] M. Mignolet and C. Soize. Nonparametric stochastic modeling of linear systems with prescribed variance of several natural frequencies. *Probabilistic Engineering Mechanics*, 23(23):267 – 278, 2008. 5th International Conference on Computational Stochastic Mechanics.

[61] D. Moens and D. Vandepitte. A fuzzy finite element procedure for the calculation of uncertain frequency-response functions of damped structures: Part 1procedure. *Journal of Sound and Vibration*, 288(3):431–462, 2005.

[62] T. Mori and K. Tanaka. Average stress in matrix and average elastic energy of materials with misfitting inclusions. *Acta metallurgica*, 21(5):571–574, 1973.

[63] M. C. Morris, H. F. McMurdie, E. H. Evans, B. Paretzkin, J. H. de Groot, and S. J. Hubbard, Camden R. andCarmel. Section 13. data for 58 substances. In E. van der Giessen and T. Y. Wu, editors, *Standard X-ray Diffraction Powder Patterns*, Technical Report Archive and Image Library. UNT Library, 1976.

[64] H. Moulinec and P. Suquet. A numerical method for computing the overall response of nonlinear composites with complex microstructure. *Computer Methods in Applied Mechanics and Engineering*, 157(1):69–94, 1998.

[65] S. Mulay, G. Becker, R. Vayrette, J.-P. Raskin, T. Pardoen, M. Galceran, S. Godet, and L. Noels. Multiscale modelling framework for the fracture of thin brittle polycrystalline films: application to polysilicon. *Computational Mechanics*, 55:73–91, 2015.

[66] V.-D. Nguyen, E. Béchet, C. Geuzaine, and L. Noels. Imposing periodic boundary condition on arbitrary meshes by polynomial interpolation. *Computational Materials Science*, 55:390–406, 2012.

[67] V.-D. Nguyen, G. Becker, and L. Noels. Multiscale computational homogenization methods with a gradient enhanced scheme based on the discontinuous galerkin formulation. *Computer Methods in Applied Mechanics and Engineering*, 260:63–77, 2013.

[68] L. Noels and R. Radovitzky. A new discontinuous galerkin method for kirchhoff–love shells. *Computer Methods in Applied Mechanics and Engineering*, 197(33):2901–2929, 2008.

[69] A. Noshadravan, R. Ghanem, J. Guilleminot, I. Atodaria, and P. Peralta. Validation of a probabilistic model for mesoscale elasticity tensor or random polycrystals. *International Journal for Uncertainty Quantification*, 3(1):73–100, 2013.

[70] M. Ostoja-Starzewski. Material spatial randomness: From statistical to representative volume element. *Probabilistic Engineering Mechanics*, 21(2):112 – 132, 2006.

[71] M. Ostoja-Starzewski and X. Wang. Stochastic finite elements as a bridge between random material microstructure and global response. *Computer Methods in Applied Mechanics and Engineering*, 168(14):35 – 49, 1999.

[72] I. Özdemir, W. A. M. Brekelmans, and M. G. D. Geers. Computational homogenization for heat conduction in heterogeneous solids. *International Journal for Numerical Methods in Engineering*, 73(2):185–204, 2008.

[73] D. Pivovarov and P. Steinmann. Modified sfem for computational homogenization of heterogeneous materials with microstructural geometric uncertainties. *Computational Mechanics*, 57(1):123–147, 2016.

[74] R. Popescu, G. Deodatis, and J. Prevost. Simulation of homogeneous nongaussian stochastic vector fields. *Probabilistic Engineering Mechanics*, 13(1):1 – 13, 1998.

[75] R. Popescu, G. Deodatis, and J. Prevost. Simulation of homogeneous nongaussian stochastic vector fields. *Probabilistic Engineering Mechanics*, 13(1):1 – 13, 1998.

[76] R. Popescu, G. Deodatis, and J. Prevost. Simulation of non-gaussian stochastic fields with applications to soil liquefaction: two case studies. In *Proceedings of the 12th ASCE Engineering Mechanics Speciality Conference, Reston, Va*, 1998.

[77] Z. Qiu, L. Ma, and X. Wang. Non-probabilistic interval analysis method for dynamic response analysis of nonlinear systems with uncertainty. *Journal of Sound and Vibration*, 319(1):531–540, 2009.

[78] S. S. Rao and L. Berke. Analysis of uncertain structural systems using interval analysis. *AIAA journal*, 35(4):727–735, 1997.

[79] J. Reddy. On locking-free shear deformable beam finite elements. *Computer Methods in Applied Mechanics and Engineering*, 149(1 - 4):113 – 132, 1997. Containing papers presented at the Symposium on Advances in Computational Mechanics.

[80] M. P. Sena, M. Ostoja-Starzewski, and L. Costa. Stiffness tensor random fields through upscaling of planar random materials. *Probabilistic Engineering Mechanics*, 34:131–156, 2013.

[81] E. Serra and M. Bonaldi. A finite element formulation for thermoelastic damping analysis. *International Journal for Numerical Methods in Engineering*, 78(6):671–691, 2009.

[82] C. Shannon. Ba mathematical theory of communication,[bell system tech, 1948.

[83] M. Shinozuka. Simulation of multivariate and multidimensional random processes. *The Journal of the Acoustical Society of America*, 49(1B):357–368, 1971.

[84] M. Shinozuka and G. Deodatis. Response variability of stochastic finite element systems. *Journal of Engineering Mechanics*, 114(3):499–519, 1988.

[85] M. Shinozuka and C.-M. Jan. Digital simulation of random processes and its applications. *Journal of Sound and Vibration*, 25(1):111 – 128, 1972.

[86] C. Soize. Random matrix theory for modeling uncertainties in computational mechanics. *Computer Methods in Applied Mechanics and Engineering*, 194(12 - 16):1333 – 1366, 2005. Special Issue on Computational Methods in Stochastic Mechanics and Reliability Analysis.

[87] C. Soize. Non-gaussian positive-definite matrix-valued random fields for elliptic stochastic partial differential operators. *Computer Methods in Applied Mechanics and Engineering*, 195(13):26 – 64, 2006.

[88] G. Stefanou. The stochastic finite element method: Past, present and future. *Computer Methods in Applied Mechanics and Engineering*, 198(912):1031 – 1051, 2009.

[89] G. Stefanou and M. Papadrakakis. Stochastic finite element analysis of shells with combined random material and geometric properties. *Computer Methods in Applied Mechanics and Engineering*, 193(1):139–160, 2004.

[90] G. Stefanou, D. Savvas, and M. Papadrakakis. Stochastic finite element analysis of composite structures based on material microstructure. *Composite Structures*, 132:384 – 392, 2015.

[91] I. Temizer and P. Wriggers. Homogenization in finite thermoelasticity. *Journal of the Mechanics and Physics of Solids*, 59(2):344 – 372, 2011.

[92] P. Trovalusci, M. L. De Bellis, M. Ostoja-Starzewski, and A. Murrali. Particulate random composites homogenized as micropolar materials. *Meccanica*, 49(11):2719–2727, 2014.

[93] P. Trovalusci, M. Ostoja-Starzewski, M. L. De Bellis, and A. Murrali. Scale-dependent homogenization of random composites as micropolar continua. *European Journal of Mechanics-A/Solids*, 49:396–407, 2015.

[94] E. Vanmarcke. *Random fields: analysis and synthesis.* World Scientific, 2010.

[95] G. N. Wells and N. T. Dung. A {C0} discontinuous galerkin formulation for kirchhoff plates. *Computer Methods in Applied Mechanics and Engineering*, 196(3536):3370 – 3380, 2007.

[96] T. Wright. *The Physics and Mathematics of Adiabatic Shear Bands*. Cambridge Monographs on Mechanics. Cambridge University Press, 2002.

[97] F. Yamazaki, A. Member, M. Shinozuka, and G. Dasgupta. Neumann expansion for stochastic finite element analysis. *Journal of Engineering Mechanics*, 114(8):1335–1354, 1988.

[98] F. Yamazaki and M. Shinozuka. Digital generation of non-gaussian stochastic fields. *Journal of Engineering Mechanics*, 114(7):1183–1197, 1988.

[99] F. Yamazaki and M. Shinozuka. Digital generation of nongaussian stochastic fields. *Journal of Engineering Mechanics*, 114(7):1183–1197, 1988.

[100] K. Yasumura, T. Stowe, E. Chow, T. Pfafman, T. Kenny, B. Stipe, and D. Rugar. Quality factors in micron- and submicron-thick cantilevers. *Microelectromechanical Systems, Journal of*, 9(1):117–125, March 2000.

[101] X. Yin, W. Chen, A. To, C. McVeigh, and W. Liu. Statistical volume element method for predicting microstructureconstitutive property relations. *Computer Methods in Applied Mechanics and Engineering*, 197(43 - 44):3516 – 3529, 2008. Stochastic Modeling of Multiscale and Multiphysics Problems.

[102] X. Yin, S. Lee, W. Chen, W. K. Liu, and M. F. Horstemeyer. Efficient random field uncertainty propagation in design using multiscale analysis. *Journal of Mechanical Design*, 131(2), 2009.

[103] L. A. Zadeh. Fuzzy sets. *Information and control*, 8(3):338–353, 1965.

[104] C. Zener. *Elasticity and Anelasticity of Metals*. University of Chicago Press, 1948.

[105] H.-W. Zhou, B. Kharas, and P. Gouma. Microstructure of thick polycrystalline silicon films for mems application. *Sensors and Actuators A: Physical*, 104(1):1–5, 2003.